HAL
open science

Electronic quantum optics

Charles Grenier

To cite this version:

Charles Grenier. Electronic quantum optics. Physics [physics]. Ecole normale supérieure de lyon - ENS LYON, 2011. English. NNT : 2011ENSL0627 . tel-00617869v2

HAL Id: tel-00617869

https://theses.hal.science/tel-00617869v2

Submitted on 5 Jan 2012 (v2), last revised 31 Jan 2012 (v3)

HAL is a multi-disciplinary open access archive for the deposit and dissemination of scientific research documents, whether they are published or not. The documents may come from teaching and research institutions in France or abroad, or from public or private research centers.

L'archive ouverte pluridisciplinaire **HAL**, est destinée au dépôt et à la diffusion de documents scientifiques de niveau recherche, publiés ou non, émanant des établissements d'enseignement et de recherche français ou étrangers, des laboratoires publics ou privés.

THÈSE

en vue d'obtenir le grade de

Docteur de l'Université de Lyon - École Normale Supérieure de Lyon

spécialité: Physique

LABORATOIRE DE PHYSIQUE

École Doctorale de Physique et Astrophysique De Lyon

présentée et soutenue publiquement le 30 juin 2011

par M. Charles Grenier

Optique quantique électronique
-
Electronic quantum optics

Directeur de thèse: M. Pascal Degiovanni

Après avis de:

Monsieur Frank Hekking

Monsieur Christian Glattli

Devant la comission d'examen formée de:

Monsieur Markus Büttiker

Monsieur Frank Hekking

Monsieur Christian Glattli

Monsieur Peter Holdsworth

Monsieur Pascal Degiovanni

Remerciements

Cete partie du manuscrit étant souvent rédigée en tout dernier, et à une heure pas forcément avouable, on n'échappe que très rarement à une certaine confusion. Les prochaines lignes ne feront malheureusement pas exception. La pauvreté d'un style tardif n'ôtera toutefois rien à la sincerité de ces remerciements.

Je tiens tout d'abord à remercier les membres du jury, en les personnes de Markus Büttiker, Peter Holdsworth, Frank Hekking, Christian Glattli et Pascal Degiovanni. Parmi eux, Frank Hekking et Christian Glattli ont accepté d'être rapporteurs de ce manuscrit. Merci beaucoup à eux d'avoir accepté cette charge supplémentaire de travail.

Pascal a supervisé ce travail avec flegme, enthousiasme, et sympathie. Sa très grande gentillesse, sa disponibilité et ses compétences étendues en font un encadrant de tout premier ordre. Depuis les tréfonds de la mécanique quantique (et autres choses en physique) jusqu' aux moindres détails de l'apocalypse prochaine[1], on apprend beaucoup à son contact.

Les travaux présentés ici doivent énormément aux collaborations et discussions menées ces trois dernières années. En particulier, le LPA fut un lieu de séjour régulier. Merci à Gwendal Fève, Erwann Bocquillon, François Parmentier, Adrien Mahé, Takis Kontos, Bernard Plaçais, Jean-Marc Berroir, Christian Glattli, Nicolas Regnault et Christophe Mora pour leur accueil et pour nous avoir laissés, Pascal et moi, nous incruster à intervalles réguliers. Merci également à Carles Altimiras, Hélène Le Sueur et Frédéric Pierre, ainsi qu'à Thierry Martin, Thibaut Jonckheere et Jérôme Rech. Merci à tous, poour tout.
Le laboratoire de physique de l'ENS Lyon a été un endroit particulièrement agréable pendant trois ans, que ce soit pour travailler, ou pour le reste. Je remercie donc Jean - François Pinton ainsi que Jean-Michel Maillet pour leur accueil respectivement dans le laboratoire et au sein de l'équipe de théorie. Merci à Nadine, Laurence et Laure de rappeler aux physiciens les contraintes matérielles avec le sourire. Merci beaucoup à Éric Freyssingeas pour m'avoir confié des enseignements pendant trois ans. Merci à tous les compagnons de bureau, ainsi qu'aux invités réguliers et passagers du bureau-avec-la-pin-up-sur-la-porte : Arnaud, Maïté, Quentin, Louis-Paul, François Delduc, Marc Magro et Ludovic "Herr doktor" Jaubert, pour son accueil à Dresde et ses visites du Berlin underground. Enfin, merci à Eric[2], Sébastien, Arnaud, Cendrine, Nicolas, Pascal, Pierre parce qu'après tout, on s'est quand même bien marrés.

Ce fut un plaisir de fréquenter les bancs du fond d'amphi en compagnie d'Arnaud, François, Pierre, Sylvain, Martin, et Soumaya. Merci également à tous ceux que je ne croise pas assez souvent, mais qui sont toujours les bienvenus chez moi pour partager une bière ou un verre de rouge : Romain, Thomas, Boule Jaune, Martin, Julien, Romain... Que ceux que j'oublie veuillent bien me pardonner, et qu'ils n'hésitent pas à venir quand même.
Ces remerciements étant téléphonés jusqu'au bout, j'ai donc laissé le plus important pour la fin. Merci énormément à Marie, Louise, mon père, ma mère, ainsi qu'à Michel, Sébastien et aux nouveaux venus : Timothée, Juliette, et Alice.
Enfin, merci à Amélie pour son amour, sa gentillesse et pour avoir patiemment attendu que je sorte de mon bureau.

[1] http://ayearinboston.canalblog.com

Contents

1 Introduction **1**

1 Quantum coherence . . . 2

1.1 State evolution in the presence of an environment . . . 2

1.2 Decoherence in electronic systems . . . 4

2 The quantum Hall effect . . . 4

2.1 Quantum Hall edge channels . . . 4

2.2 Current transport in the integer quantum Hall regime . . . 5

3 Experimental context . . . 6

3.1 The experimental toolbox for electron quantum optics . . . 7

3.2 A Mach-Zehnder interferometer for electrons . . . 9

4 Thesis outlook . . . 10

2 Quantum optics in quantum Hall edge channels **13**

1 Quantum coherence of photons . . . 14

1.1 Photon first order coherence . . . 14

1.2 Photon second order coherence . . . 19

2 Definition and properties of electron coherence functions . . . 22

2.1 First order electronic coherence . . . 22

2.2 Quantum electronic coherence at second order . . . 31

3 Conclusion . . . 37

3 Single electron tomography **39**

1 Tomography protocol . . . 40

1.1 The Hanbury Brown and Twiss effect . . . 40

1.2 Single electron tomography protocol . . . 43

2 Modelling of the SES . . . 48

2.1 Floquet scattering theory . . . 48

2.2 Single particle coherence from Floquet theory . . . 51

3 Numerical results . . . 53

3.1 Occupation number and coherence function . . . 53

3.2 Current pulse . . . 59

3.3 Accuracy of the quantum capacitor as a single electron source . . . 59

4 Conclusion . . . 63

4 Energy exchange between coupled channels **65**
1 Experimental study of edge channel equilibration . . . 66
1.1 Experimental protocol . . . 66
1.2 Results and interpretation . . . 69
2 Plasmon scattering approach to edge channel equilibration . . . 71
2.1 Bosonization and plasmon scattering . . . 71
2.2 Plasmon scattering from general considerations . . . 76
2.3 Predictions for experimental quantities . . . 77
3 Confrontation to experimental results . . . 79
3.1 Evolution with respect to bias voltage . . . 80
3.2 Dependence with the QPC transmission . . . 81
3.3 Noise measurements to probe plasmon scattering . . . 81
4 Conclusion . . . 84

5 Relaxation of a single electron **85**
1 Relaxation of an energy resolved single electron excitation . . . 86
1.1 Statement of the problem . . . 86
1.2 General results for a wavepacket . . . 87
1.3 Relaxation of a single electronic excitation . . . 91
2 Low energy relaxation . . . 95
2.1 Elastic scattering probability . . . 96
2.2 Occupation number . . . 98
2.3 Conclusion . . . 99
3 Relaxation at higher energy . . . 101
3.1 The dynamical Coulomb blockade regime . . . 101
3.2 Drowning of the quasiparticle . . . 101
3.3 Energy interpretation . . . 103
4 Conclusion . . . 105

6 Decoherence and relaxation of time resolved excitations **107**
1 A source of minimal excitations . . . 108
1.1 Driving an edge channel with a classical voltage source . . . 108
1.2 Coherence function of minimal excitations . . . 109
2 Effects of the interactions on the coherence function . . . 111
2.1 Plugging the interactions into the Floquet formalism . . . 112
2.2 Coherence function and interactions . . . 112
3 HBT signals and HOM experiment in the interacting regime . . . 115
3.1 Electron/hole pair counting in HBT interferometry . . . 115
3.2 Hong Ou Mandel effect in the interacting regime . . . 117
4 Conclusion . . . 120

7 Conclusion and perspectives **121**
1 Main conclusions . . . 121
2 Perspectives . . . 124

A Tomography : complements **127**

B Plasmon scattering matrices 131

C Complements on relaxation 143

List of figures 152

Bibliography 163

Chapter 1

Introduction

During the last decade, a significant experimental effort has been done towards the realization of quantum optics experiment with electrons [74, 68, 131, 133, 132]. These experiments underlined the analogy between photons propagating in the vacuum and electrons in ballistic conductors. By showing the importance of electronic decoherence, they also stressed the importance of many body correlations in quantum transport and have then motivated an important theoretical activity [89, 88, 146, 21, 79, 80] to explain quantitatively the decoherence observed in interferometry experiments.
In this context, the recent demonstration of an on demand single electron source [38] has opened the way to quantum optics experiments with single electron excitations. These in turn offer new possibilities to perform quantitative decoherence and relaxation studies. This experimental achievement also raises the problem of the measurement of a single electron wavefunction.

This thesis is a contribution to the physics of single to a few electronic excitations in the integer quantum Hall regime. Its main objective was to provide an appropriate framework for electron quantum optics able to render the analogy between electronic excitations in quantum Hall edge channels and photons propagating in the vacuum and which also takes into account electronic features such as the fermionic statistics and Coulomb interactions.
This formalism has been developed during this thesis and has conducted to experimentally testable predictions. By doing so, the modelling for the dynamics of the systems under consideration could be tested.

A central concept in this thesis is, as in Glauber's quantum optics, the notion of single particle coherence. A significative part of this work has been devoted to the alteration of single electron coherence by interactions and coupling to an external environment : this is the problem of single electron decoherence which is closely related to the problem of electronic relaxation.

We will first present general statements about quantum coherence. This first part will explain how the coupling to an environment affects the dynamics of a quantum system, and what are the related questions that naturally arise in a many electron system. Then, we will present the context in which these ideas on quantum coherence will be applied, by describing current transport in quantum Hall edge channels. A third section will give a short overview of the experimental context of this thesis, and present some recent experimental achievements,

together with a presentation of current fluctuations measurements. Finally, we will give an outline of the ideas developed in this manuscript.

1 Quantum coherence

Contrary to an isolated quantum system which follows a unitary evolution ruled by Schrödinger's equation, an open quantum system experiences decoherence which turns pure states into statistical mixtures. Decoherence is responsible for the quantum to classical transition in the behaviour of a physical system. Its study, even if present from the very beginning of quantum mechanics [34], really took off in the last fourty years, following the pioneering works of H. D. Zeh [75, 162] and W. Zurek [164, 163]. The original motivation for these works was to find a satisfactory explanation to the superselection rules that forbid linear superpositions of states for macroscopic objects[166, 165].

More precisely, decoherence is responsible for a dynamical selection of certain states (the *pointer states*), and acts contrary to the superposition principle : the superpositions of these dynamically selected states are suppressed in characteristic times short compared to the characteristic dissipation time. Surviving the system/environment interaction, these states can be viewed as the "classical states" that can be repeatedly seen by an external observer. The selection of these priviledged states due to the entanglement between the system and its environment is called *einselection* (for environment induced selection)[124].
From the point of view of the environment, the interaction with the open quantum system will generate correlations between the system's state and the one of the environment : the evolution of the environment will be conditioned to the one of the system.

1.1 State evolution in the presence of an environment

To understand the effects of the coupling of a quantum system to its environment, we will use the influence functional formalism derived by Feynman and Vernon [40, 39].
We will consider a small (in terms of degrees of freedom) system $\mathcal{S}$ coupled to a reservoir $\mathcal{R}$. The generalized coordinates describing the system are denoted q, and the ones for the reservoir are denoted x. We assume that the initial states of the $\mathcal{S}$ and $\mathcal{R}$ are initially uncorrelated, which means that the total density operator describing the state of the system and the reservoir factorizes :

$$\rho_{\mathcal{S}\oplus\mathcal{R}}(t_i) = \rho_{\mathcal{S}}(t_i) \otimes \rho_{\mathcal{R}}(t_i)\,.$$

For an isolated system, the probability to get from the initial state i at t_i to the final state f at t_f is given by the square of the modulus of the sum of probability amplitudes associated with all trajectories connecting the initial and the final state :

$$\mathcal{P}_{i\to f} = \sum_{m,n} \mathcal{A}[q_m]\mathcal{A}^*[q_n]\,.$$

In this sum, the terms corresponding to identical trajectories are of the form $\sum_n |\mathcal{A}[q_n]|^2$: they correspond to classical trajectories. Under the influence of the environment, terms involving

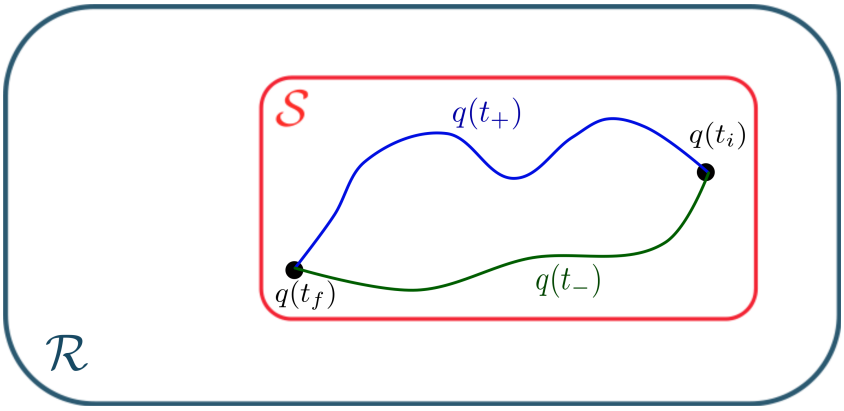

Figure 1.1: Interfering trajectories. The presence of the environment $\mathcal{R}$ is responsible for an attenuation of the visibility of quantum interferences.

interferences between two different trajectories are affected by an influence functional that depends on the system's trajectory $\mathcal{F}[q_+, q_-]$:

$$\mathcal{A}[q_+]\mathcal{A}^*[q_-] \rightarrow \mathcal{A}[q_+]\mathcal{A}^*[q_-]\mathcal{F}[q_+, q_-] \,.$$

In some cases, the expression of the influence functional can be cast in the following form :

$$\mathcal{F}[q_+, q_-] = \langle \xi(q_+)|\xi(q_-)\rangle \,,$$

where $|\xi(q_\pm)\rangle$ denotes the state of the environment conditionned by the system's trajectories $q_\pm$. Depending on the trajectory and on the coupling between the system and its environment, the states $|\xi(q_+)\rangle$ and $|\xi(q_-)\rangle$ might be totally distinguishable (in this case, they are orthogonal) or not. When the environment is a good "path detector", $\mathcal{F}[q_+, q_-]$ is very small and quantum interferences are killed.

Thus, the influence functional is responsible for the attenuation of the quantum interferences, and consequently, for the loss of coherence. The influence functional formalism underlines the analogy with standard coherence theory in undulatory optics. It can be shown [40] that this functional is also responsible for transitions between stationary states of the system $\mathcal{S}$, and thus for energy exchanges with the environment.

From the experimental point of view, traditional playgrounds where quantum coherence phenomenon are discussed and experimentally observed are atomic physics and quantum optics. For example, in cavity quantum electrodynamics, one can monitor the evolution of mesoscopic quantum superpositions of coherent states of the electromagnetic field (Schrödinger cat states) and visualize their quantum to classical transition [57].
In solid state systems, decoherence effects have been observed for example in superconducting qubits [104, 143] or quantum impurity systems [98]. With the emergence of mesoscopic quantum physics, quantum coherence effects have been discussed in solid state devices involving a macroscopic number of particles. In these systems, the manifestations of quantum coherence are for example Anderson localization [155], or the Aharonov-Bohm phase [105].

In this manuscript, the aforementioned concepts on open quantum systems will be applied to mesoscopic electronic systems.

1.2 Decoherence in electronic systems

The behaviour of electrons in metallic conductors is ruled by coulombic interactions and Fermi statistics. In particular, even in the absence of interactions, the latter can generate entanglement between electronic sources [7].
Throughout this thesis, we will consider electronic systems coupled to their electromagnetic environment via Coulomb interactions. More precisely, we will consider the case of single electron injected in a ballistic conductor, and study the interplay of interactions and many body effects on the dynamics of these electrons.
Such physical situations ask the question of the role played by the indistinguishability of electrons in a metallic environment. Indeed, the supplementary electron is integrated in the electronic fluid, and thus is in principle undistinguishable from the other electrons in the conductor. Thus, the natural question that arises is in which cases is it possible to single out an electron and consider the other ones in the conductor as an effective environment ? In such cases, the typical situation will be :

(i) The "small" system $\mathcal{S}$ under consideration will be the electron injected in the conductor.

(ii) The environment $\mathcal{R}$ will comprise the other electrons in the conductor, and the external electromagnetic environment coupled to the conductor.

In the situations considered in this manuscript, we will study the single particle density operator that encodes the single particle properties of the electronic fluid coupled to an external environment. In the cases where the supplementary electron will be singled out of the Fermi sea, it will correspond to the reduced density operator for the single electron.

The physical situations considered in this thesis are one dimensional balistic conductors called quantum Hall edge channels which, as we shall see in the next section, appear when a two dimensional electron gas formed at an heterojunction between different semiconductors is placed in a high perpendicular magnetic field at low temperature.

2 The quantum Hall effect

Low dimensional systems have attracted a lot of attention in mesoscopic physics. Effective two or one dimensional systems such as graphene or carbone nanotubes are subjects of constant experimental and theoretical activity. Among these low dimensional experimental realizations, our interest will focus on two dimensional electron gases, which exhibit particular transport properties at low temperature and high magnetic field. This section will introduce the integer quantum Hall effect, and current transport in this regime, in a semiclassical picture.

2.1 Quantum Hall edge channels

Semiconductor heterostructures such as AsGa/AlGaAs exhibit a potential well at their interface which is responsible for the formation of a two-dimensional high mobility electron gas (2DEG). In the presence of a strong perpendicular magnetic field ($\simeq 10\,T$), at low temperature (below $1\,K$), this 2DEG enters the quantum Hall regime where the transverse conductance is quantized and the longitudinal one vanishes. This new state of matter has been discovered by K. Von

Klitzing [149] in 1980. In this regime, the bulk of the 2DEG becomes insulating and the electrical current flows along one dimensional channels located at the edges of the sample.

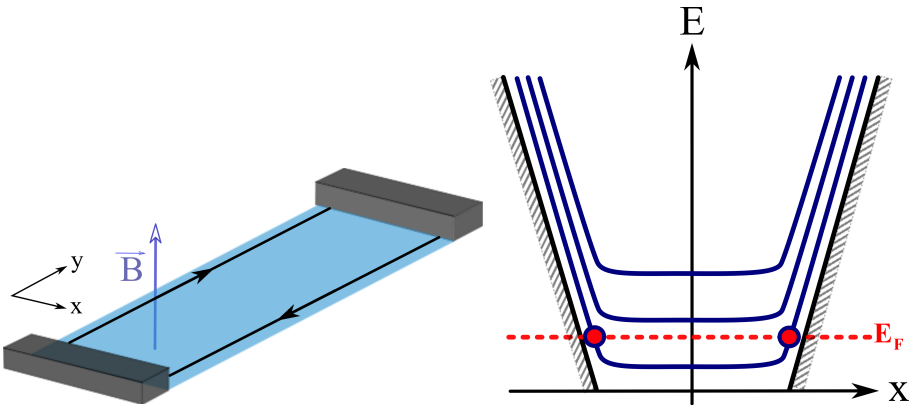

(a) Chiral edge channels (b) Landau levels

Figure 1.2: (a) Chiral quantum Hall edge channels, indicating the electron velocity. (b) The shape of Landau levels is affected by the confinment potential representing the edges of the sample. The intersection of these deformed Landau levels with the Fermi energy gives the edge channels.

Their emergence can be understood within a single particle picture [63, 15] as shown on the figure 1.2 above. The energy levels of electrons in an homogeneous transverse magnetic field are simply given by highly degenerate harmonic oscilator levels called Landau levels, with a characteristic oscillator frequency given by the cyclotron frequency $\omega_c = \frac{eB}{m}$, where m is the electron's mass. In the presence of a confining potential in one direction (y in fig. 1.2), the levels bend according to the confining potential (see fig. 1.2(b)).
The intersection of these bent Landau levels with the Fermi energy will indicate the location of the conduction channels in the system. At the center of the sample, the energy levels of the electrons are harmonic oscillator levels, and consequently the bulk states do not carry electrical current due to the cyclotron gap $\hbar\omega_c$.
A classical image can illustrate this last feature : at the center of the sample, the electrons follow closed circular orbits, that are localized states, and thus do not participate to the electrical current. On the contrary, at the edge of the sample, electrons can move in the y direction by successive bounces.
The number of conduction channels is equal to the number of filled Landau levels at the Fermi energy. This number is called the *filling factor* ν. It is equal to :

$$\nu = n\frac{h}{eB} ,$$

where n is the electronic density and $\frac{h}{eB}$ is the area threaded by one flux quantum. At constant electron density, the filling factor depends on the magnetic field : integer values of ν correspond to an integer number of filled Landau levels .

2.2 Current transport in the integer quantum Hall regime

A key point is that each of the edge channels is chiral : the direction of the current flow depends on the edge of the sample. This comes from the relation between the average velocity of the

carriers (the drift velocity) at the Fermi level and their energy :

$$\langle v \rangle \equiv v_F = \frac{1}{\hbar}\left(\frac{\partial E_n}{\partial k}\right)_{k=k_F} ,$$

where E_n is the energy of the $n-th$ Landau level. The figure 1.2(a) illustrates the dependence of the velocity's sign on the edge under consideration.
Chirality is at the origin of the robustness of current propagation against disorder or interactions. Indeed , in a typical configuration, the only possibility for an electron propagating in an edge channel to be backscattered is to reach the other edge via the tunnel effect. When the sample edges are separated by more than a few magnetic lengths, tunnelling processes from one edge to the other are strongly suppressed. This explains why, in the integer quantum Hall regime, the longitudinal resistivity vanishes. Furthermore, when a current I is applied to the sample, a voltage difference appear between the edges of the samples. This voltage difference is the Hall voltage V_H. The latter is related to the total current I (see fig. 1.3) flowing through the edge channels through :

$$V_H = \frac{h}{\nu e^2} I \, .$$

The Hall voltage is typically measured in a quantum Hall bar between metallic contacts located at opposite edges, as shown in fig.1.3.

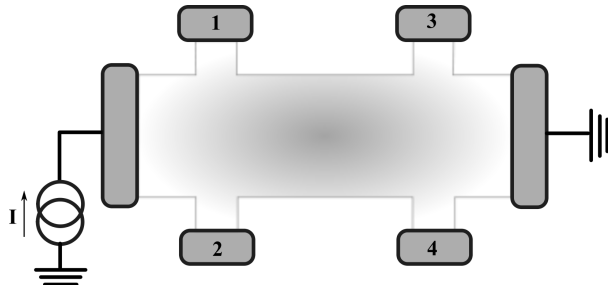

Figure 1.3: A quantum Hall bar. Measurements of longitudinal and transverse resistances are performed with voltage difference measures between respectively contacts 1 and 3 and 1 and 2 when the current I flows through the sample.

The absence of backscattering suggests that chiral quantum Hall edge channels can be viewed as coherent waveguides for electrons similar to optical fibers for photons, an image initially developed by M. Büttiker [15]. This intuition has received a striking experimental illustration in Mach-Zehnder interference experiments, which have shown that electrons remain coherent over distances of a few to 20 μm, greater than the typical size of the samples [132].

3 Experimental context

After this short introduction to the integer quantum Hall effect let us now focus on the experimental aspects of current transport in this particular regime, and discuss how one can realize quantum optics experiments with electrons propagating along chiral quantum Hall edge channels.

3.1 The experimental toolbox for electron quantum optics

We have seen in the previous section that integer quantum Hall edge channels are, at first glance, good analogues of optical fibers. This analogy suggests to extend this comparison to other nanostructures, so as to build a complete toolbox to perform electron quantum optics experiments. Basically, we need pieces able to perform wave separation, which are beamsplitters, we need mirrors, classical light sources, and single photon sources.

An electron beamsplitter : the quantum point contact

The electronic analogue of a beamsplitter is the quantum point contact (QPC). This nanostructure consists in two metallic gates deposited on the surface of the sample and connected to DC voltage sources. Then, when this DC voltage is switched on, electrostatic repulsion is responsible for the creation of a constriction in the 2DEG. When the width w of the constriction becomes comparable to the Fermi wavelength, the number of electronic modes transmitted through the potential barrier becomes quantized in units of $\frac{\lambda_F}{2w}$, where λ_F is the Fermi wavelength[17]. When the system enters the quantum Hall regime, tuning the gate voltage will change the number of edge channels transmitted through the barrier. Starting from zero gate voltage to large negative values, the edge channels are reflected one by one at the QPC. Thus, the conductance of the QPC and so the number of transmitted edge channels can be modified by tuning the gate voltage[150]. Fig. 1.4(b) illustrates that the increase in the magnetic field lowers the number of channels transmitted at the QPC. Consequently a quantum point contact mimicks a channel selective beam splitter with tunable transmission. This peculiarity will be of first importance in designing protocols of electron quantum optics experiments.

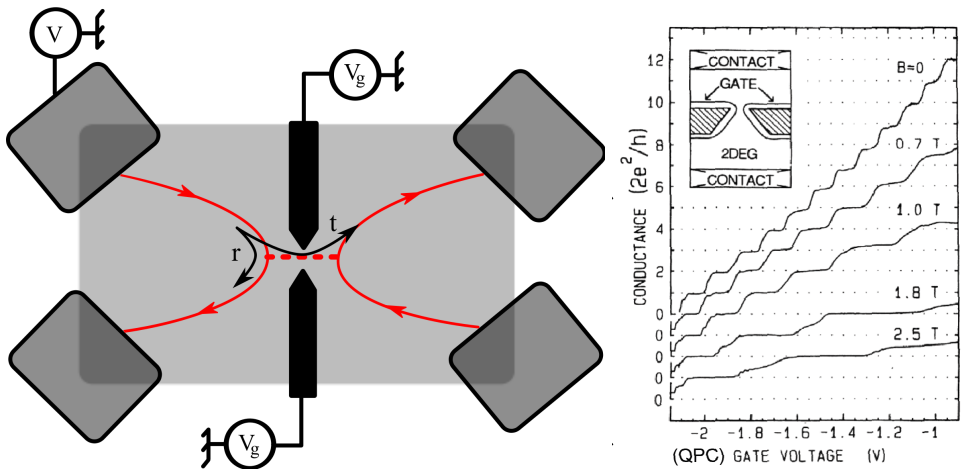

(a) (b)

Figure 1.4: (a) Sketch of a quantum point contact : the gate voltage drives the transparency of the tunnel barrier, and so the conductance of the constriction. (b) Evolution of the conductance of a quantum point contact with the gate voltage, taken from [152].

Noise measurements as probes

Pioneering works on current fluctuations in mesoscopic systems by R. Landauer, Th. Martin and M. Büttiker [103, 85, 86, 10] have shown that current noise contains information about the

dynamics of charge carriers.
On the experimental side, the measurement of partitioned current noise after a quantum point contact has shown that the statistics of electrical current in an ideal quantum conductor is sub-Poissonian [138], as a direct consequence of the Pauli exclusion principle.
Current noise measurements in an Hanbury Brown and Twiss configuration (see fig. 1.5) has also allowed, for example, to measure the charge of fractional excitations in the $\nu = 1/3$ regime [82]. The extraction of the change of quasiparticle from shot noise measurements illustrated in a spectacular way the relevance of studying the noise to obtain information on the current carriers. As we shall see in chapter 3, this idea popularized by Landauer through his sentence " The noise is the signal " [86] will be central in our single electron tomography proposal that aims at reconstructing the single particle coherence of a single electron source.

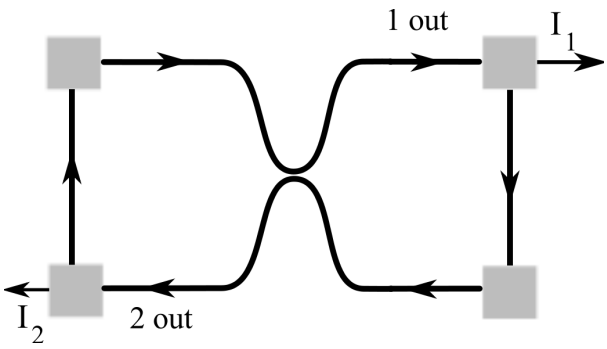

Figure 1.5: Hanbury Brown and Twiss configuration for noise measurements. The quantum point contact mixes the incoming currents, and the correlations between output electrical current I_1 and I_2 are measured.

Electron sources

A DC bias applied to a quantum point contact will create a stationnary electron stream that will populate an edge channel with a macroscopic nonequilibrium distribution. An oscillating voltage bias can alsso be used to create a standing wave on output of an ohmic contact.
To perform quantum optics experiments with single quanta, a single electron source is necesary. Several propositions have been made to realize such an electron source in 2DEG at zero magnetic field or in the quantum Hall regime, relying on tunnel junctions [9], surface acoustic waves [147, 27, 130], charge pumping [159] or the use of a properly designed voltage [87]. Nevertheless, up to now, the only available experimental realization that ensures good control of the emission time together with energy resolution of the emitted electron relies on another technique that we will now describe.

This recently demonstrated single electron source takes benefit on electron confinement in a quantum dot [38]. The latter is an isolated portion of the 2DEG created electrostatically or by changing the shape of the 2DEG during its fabrication. This confinement is responsible for a discrete level structure in the quantum dot. The typical energy level separation Δ is chosen to be well above to the charging energy E_C of the dot.
The application of a periodic square voltage V_{exc} (see fig. 1.6) on the quantum dot will shift the energy levels accordingly to the voltage. By choosing the appropriate amplitude and frequency

for V_{exc}, one can emit a single electron per cycle. In this case, the emitted electron has an energy $eV \leq \Delta$ above the Fermi level. For such a source, the emission of an electron goes together with the emission of a hole in the following half period : it is an AC source. A sketch of the source together with a cartoon of its functioning is given in fig. 1.6.

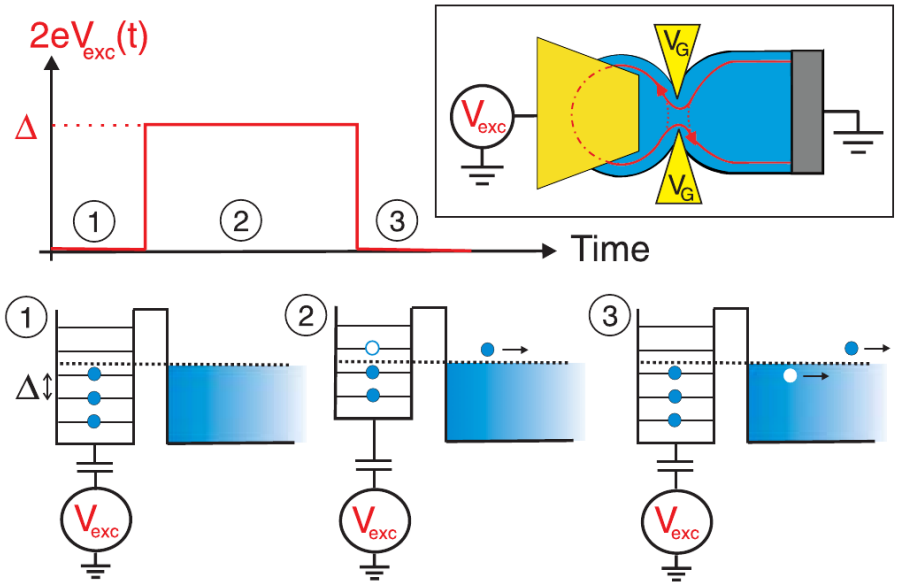

Figure 1.6: Up : Sketch of the single electron source built in the LPA, and shape of the excitation voltage. Each phase of the driving voltage corresponds to a different processus in the emission. Down : the sequential processes in the emission are synchronized with the driving voltage. These figures are taken from [38].

3.2 A Mach-Zehnder interferometer for electrons

The first striking evidence of the quantum coherence of electrons propagating in quantum Hall edge channels came with the demonstration of a Mach Zehnder interferometer in 2003 by the group of M. Heiblum [74] in the Weizmann institute. In this setup, depicted in 1.7, two quantum point contacts are operated as electronic beamsplitters. A first ohmic contact emits electrons towards the first quantum point contact. The reflected and transmitted paths are then recombined at the second quantum point contact.

Since we are in the quantum Hall regime, the whole system in submitted to a strong perpendicular magnetic field $\vec{B}$. Thus, the phase difference between the reflected and transmitted paths is given by the Aharonov-Bohm phase $\varphi = 2\pi\mathcal{A} \times |\vec{B}|/\Phi_0$, where $\mathcal{A}$ is the area of the loop delimited by the two arms of the iterferometer. Here, $\Phi_0 = h/e$ is the flux quantum. The phase difference can be changed by changing the magnetic field or by the backgates G_1 and G_2 which change the area.
The electrical current after recombination is measured at the ohmic contacts D_i. This current presents oscillations when plotted against the magnetic field or the gate's voltage, which are clear signatures of quantum interferences. The visibility reduction (see fig. 1.8) is due to decoherence mechanisms, for which several competing explanations have been proposed. Some of

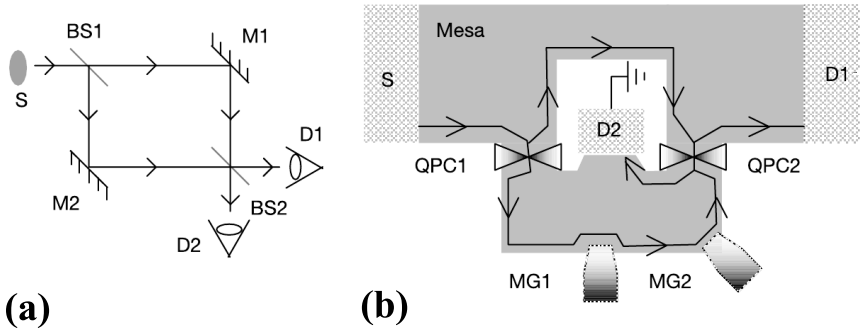

Figure 1.7: Figures taken from [74]. (a) Optical Mach-Zehnder interferometer. (b) Electronic analogue : the quantum point contacts are beamsplitters, in which the electron beams, namely the edge channels, split up and recombine.

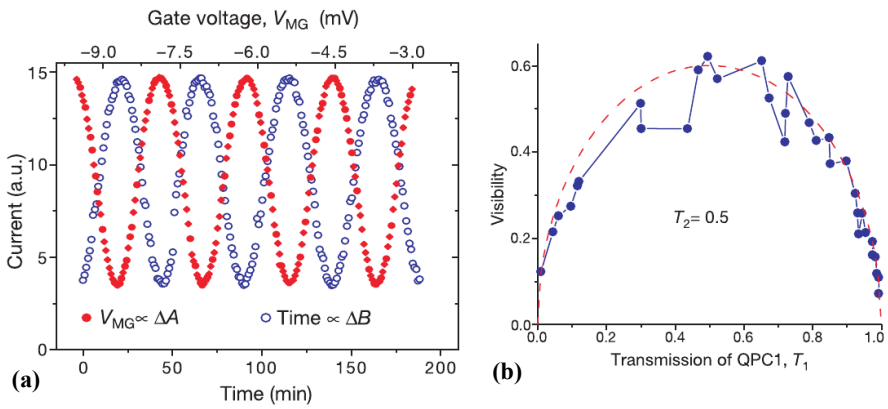

Figure 1.8: Figures taken from [74]. (a) Oscillations in the output current are manifestations of quantum coherence. (b) Visibility of the interference pattern. The reduction of the visibility is a manifestation of the decoherence of electronic excitations, and have motivated a significative amount of theoretical propositions.

them [102, 42, 24, 100, 101, 111, 133] involve sources of dephasing that are exterior to the edge channels, which can be the movement of charge impurities, or radiation emitted by the samples surroundings. Other explanations [21, 114, 88, 79] rely on electron/electron interactions in the edge channels. This departure from the electron quantum optics picture of free electrons "flying" on top of the Fermi sea is at the heart of the work realized in this thesis.

4 Thesis outlook

In the context of Mach-Zehnder interferometry, the Coulomb interaction is responsible for the decoherence of electronic excitations [24, 21, 111, 114, 88, 133, 79]. In particular, this raises the question of the validity of the analogy between current transport in the integer quantum Hall regime and photon propagation in the vacuum : to which extent is this comparison valid, and when do the many body effects mentioned in 1 come into play ?
The single electron source presented in section 3 offers the possibility to probe the one body dynamics in quantum Hall edge channels, but it also demands a reconsideration of the problem of electronic coherence. Indeed, a crucial question would be to understand the deviation from

the noninteracting picture for single electrons excitations due to coulombic interactions and coupling to the electromagnetic environment. As suggested by recent experiments on electron relaxation in $\nu = 2$ quantum Hall edge channels performed by by Frédéric Pierre, Carles Altimiras and Hélène Le Sueur, [2, 145], the effects of interactions seriously challenge the quantum optics paradigm for electrons, which designates the situation in which an electronic wavepacket at an energy high above the Fermi level can propagate freely, as a photon in the vacuum.

This thesis has contributed to push further the understanding of electron transport in the integer quantum Hall regime. The proposed formalism to study the coherence of electrons has shed new light on the relaxation of single electron excitations. This problem is simpler than the relaxation of a general stationary non equilibrium electronic state but is nevertheless conceptually important since it probes the nature of quasiparticle in quantum Hall edge channels. In particular, a unified approach to decoherence and relaxation of single electron has been proposed, which answers the question raised in section 1 concerning many body effects in metallic environments. This approach clearly states at which conditions an electron can be singled out in a conductor when it is submitted to the influence of a linear environment.
We also propose to make use of two particle interferometry experiments (see section 3) to probe the bosonization approach to interactions. This test could be complementary to finite frequency admittances measurements.
Two particle interferences are also the basis of a quantum tomography protocol which aims at probing further the single particle coherence. Indeed, up to now, only spectroscopy of the electron state, namely the measurement of the occupation number, have been performed. Here, the measurement of current correlations that we propose would provide the reconstruction of a single electron's wavefunction, and could be the first step of a whole experimental program to control the state of electrons in quantum Hall edge channels.

This manuscript organizes as follows. The first chapter presents the coherence function formalism for electrons by comparison to the quantum coherence theory of the electromagnetic field. Coherence functions for electrons are nothing but standard correlators encountered in many body condensed matter physics, but the quantum optics interpretation will shed new light on quantum coherence problems in electronic systems.
Then, a protocol aiming at measuring the single particle coherence is presented in chapter 3. It relies on noise measurements similar to those mentioned in section 3. The experimental feasability of this quantum tomography protocol will be assessed by predictions for the single electron source of the Laboratoire Pierre Aigrain [38].
The following three chapters will show how the coherence function formalism together with bosonization can describe decoherence and relaxation of electronic excitations. In chapter 4, a confrontation to experimental results for electron relaxation in the quantum Hall regime is presented. On the basis of bosoonization and a plasmon scattering formalism, predictions for measured quantities are compared to the outcomes of [3, 145].
Chapter 5 describes the decoherence and relaxation of an energy resolved single electron excitation. In this chapter, the relative importance of many body effects and coupling to the external environment are systematically analyzed and propose an answer to the questions concerning the quantum optics paradigm in the presence of interactions.
Finally, chapter 6 provides a study of the interaction effects on the coherence function for sources of minimal excitations proposed by Levitov, Lee and Lesovik [87]. Furthermore, proto-

cols relying on two particle interferences are proposed to investigate interaction mechanisms.

Chapter 2

Quantum optics in quantum Hall edge channels

Contents

1 Quantum coherence of photons **14**

1.1 Photon first order coherence 14

1.2 Photon second order coherence 19

2 Definition and properties of electron coherence functions **22**

2.1 First order electronic coherence 22

2.2 Quantum electronic coherence at second order 31

3 Conclusion **37**

In this chapter, the single particle coherence function for electrons is defined in analogy with the Glauber's functions of quantum optics[51]. To begin with we will recall some elements of Glauber's theory [51], putting the emphasis on the analogies and differences between traditional quantum optics with photons and electron quantum optics. In particular, how these differences manifest themselves in the quantities that we chose to study. Basic concepts will be illustrated on simple examples, both for photons and electrons and will be referenced to extensively throughout this thesis.

In a first part, we will present the first and second order coherence functions, and the associated degrees of .coherence for the electromagnetic field. The second section will be devoted to the study of electron quantum coherence from the quantum optics point of view. In both parts, the coherence functions will be related to experimentally relevant quantities. The similitudes and differences between photons in the vacuum and electrons propagating in quantum Hall edge channels will be illustrated both on experimental and theoretical grounds.

1 Quantum coherence of photons

The quantum theory of optical coherence was elaborated by Glauber [50, 52, 51] in the 1960s. This theory aims at describing the quantum coherence properties of the electromagnetic field and relate them to photodetection signals. The central elements of this theory are correlators of the electric field, which are very similar to the coherences of the electromagnetic field in classical optics. In the case of a quantized field, these correlators are the photon coherence functions.
In this section, we will focus on photon coherence at first and second order. In both cases, the photon coherence functions will be related to photodetection signals, in a similar way as in[25].

1.1 Photon first order coherence

Link with photodetection signals

In his work, Glauber studied the case of an ideal detector insensitive to spontaneous emission, and which measures the intensity of the electric field. The archetypal detector with such properties is the photomultiplier. The basic process at the heart of such an ideal detector is the absorption of a photon : we consider a destructive photon measurement, in opposition with QND measurements performed, for example in cavity quantum electrodynamics (see [67] for a review). In this case, the photon is irreversibly lost during the measurement process.

In a photomultiplier, the absorption of an incoming electron is responsible for the ionization of a photocathode, which then produces a photoelectron [25]. This microscopic current is then amplified to produce the photodetection signal. A schematic illustrations of this process is given in fig. 2.1.

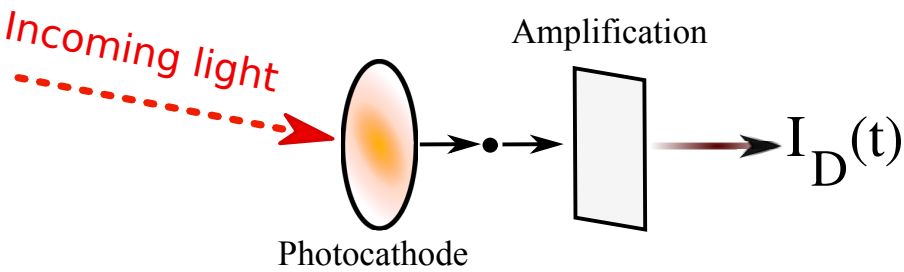

Figure 2.1: A schematic view of a photodetector. The single electron on output of the photocathode is amplified, and generates a measurable output current pulse.

Within a first-order perturbation theory, the instantaneous transition rate of the photodetector from the state $|g\rangle$ to the state $|e\rangle$ is given by the Fermi golden rule .
For the sake of simplicity, we will give the details of the computations for the case of a detector consisting in a single atom localized at the position $\vec{r}$.
The photodetection consists in the absorption of a photon, a process in which the atom undergoes a transition from a state $|g\rangle$ to a state $|e\rangle$, while the field goes from its initial state $|i\rangle$ to a final state $|f\rangle$. The evaluation of the probability of this transition in the time interval $[0, t]$ will give the the associated photocurrent. The atom / field coupling is assumed to be dipolar electric :

$$H_I = \vec{d}(t) \cdot \vec{E}(\vec{r}, t)\,, \tag{2.1}$$

where $\vec{d}(t) = -e\vec{q}(t)$ is the dipole associated to the atomic states $|e\rangle$ and $|g\rangle$. In a first order approximation, the evolution operator between 0 and t is :

$$U(t,0) \simeq \mathbf{1} + \frac{1}{i\hbar}\int_0^t \mathrm{d}t' H_I(t') \tag{2.2}$$

The detector under consideration is sensitive to the positive frequency part of the electric field, which only contains annihilation operators :

$$\vec{E}^+(\vec{r}, t) = i\sum_k \sqrt{\frac{\hbar\omega_k}{2\epsilon_0 V}} a_k e^{i\vec{k}\cdot\vec{r} - i\omega_k t}\vec{e}_\lambda\,, \tag{2.3}$$

V being the volume of the box containing the photons and $\vec{e}_\lambda$ the polarization. The complete electric field is the sum $\vec{E}^+ + \vec{E}^-$, where $\vec{E}^- = (\vec{E}^+)^\dagger$. The transition amplitude is thus :

$$A_{g\to e} = \langle ef|U(t,0)|g\,i\rangle = \frac{ie}{\hbar}\int_0^t \mathrm{d}t' \langle e|\vec{q}(t')|g\rangle\langle f|\vec{E}^+(\vec{r}, t')|i\rangle. \tag{2.4}$$

With $\langle e|\vec{q}(t')|g\rangle = e^{i\omega_{eg}t'}\vec{q}$, one can find the transition probability from state g to e summing over the final states of the electric field [1] and averaging over the possible initial states $|i\rangle$:

$$\begin{aligned}
p_{eg}(t) &= \mathrm{Tr}_i\Big(\sum_f |A_{g\to e}|^2\Big) \\
&= \mathrm{Tr}_i\Big(\sum_f |\langle ef|U(t,0)|gi\rangle|^2\Big) \\
&= \Big(\frac{e}{\hbar}\Big)^2 \int_0^t \mathrm{d}t'\mathrm{d}t'' e^{i\omega_{eg}(t''-t')}||\vec{q}||^2 \mathrm{Tr}_i\Big(\rho_i \vec{E}^-(\vec{r}, t')\vec{E}^+(\vec{r}, t'')\Big) \\
&= \Big(\frac{e}{\hbar}\Big)^2 \int_0^t \mathrm{d}t'\mathrm{d}t'' e^{i\omega_{eg}(t''-t')}||\vec{q}||^2 \mathbf{G_1}(\vec{r}, t'; \vec{r}, t'').
\end{aligned}$$

If one considers a continuum of electronic states with density f, the total transition probability is thus :

$$p(t) = \int \mathrm{d}\omega_{eg} f(\omega_{eg}) p_{eg}(t) \tag{2.5}$$

$$= \Big(\frac{e}{\hbar}\Big)^2 \int_0^t \mathrm{d}t'\mathrm{d}t'' \kappa(t'-t'')\mathbf{G_1}(\vec{r}, t'; \vec{r}, t''), \tag{2.6}$$

where $\kappa(\tau) = \int \mathrm{d}\omega_{eg} e^{i\omega_{eg}\tau} f(\omega_{eg})$.

Thus, in full generality, the photocurrent has the following expression :

$$I_D(t) = \int_0^t \mathrm{d}t'\mathrm{d}t'' \mathbf{G_1}(\vec{r}, t'; \vec{r}, t'') K_D(t'-t''), \tag{2.7}$$

[1] Which is generally unknown.

where K_D takes into account the characteristics of the detector : its efficiency, spectral bandwith, and density of states. $\mathbf{G_1}$ is *the first order photon coherence function* [148] :

$$\mathbf{G}_1(\vec{r}, t; \vec{r}', t') = \mathrm{Tr}\left(\vec{E}^+(\vec{r}, t)\rho\vec{E}^-(\vec{r}', t')\right). \tag{2.8}$$

For a broadband detector,f is almost constant and consequently $p(t)$ is directly given by the integral of $\mathbf{G_1}$: a broadband detector will measure the coherence function at coincident times. For a narrow band detector centered around ω_0 ($f(\omega_{eg}) \simeq \delta(\omega_{eg} - \omega_0)$) the detector will measure its Fourier transform $\mathbf{G_1}(\omega_1; \omega_2)$ for $\omega_1 = \omega_2 = \omega_0$.

The average field intensity is the diagonal part of the one particle coherence function in the time domain :

$$\langle I(\vec{r}, t)\rangle = \mathrm{Tr}\left(\vec{E}^+(\vec{r}, t)\rho\vec{E}^-(\vec{r}, t)\right) = \mathbf{G_1}(\vec{r}, t; \vec{r}, t). \tag{2.9}$$

The values of $\mathbf{G}_1(\vec{r}_1, t_1; \vec{r}_2, t_2)$ for different times and positions are correlations of the light arriving at the photodetector: they account for interferences.

The first order coherence function in the quantum case is very similar to interference terms that come into play in classical interference experiments. For example, the visibility in a Young's interference experiment has the following expression [43] :

$$v = |g^{(1)}(\vec{r}_1, t_1; \vec{r}_2, t_2)|, \tag{2.10}$$

where $g^{(1)}$ is the normalized first order coherence function, defined as :

$$g^{(1)}(\vec{r}_1, t_1; \vec{r}_2, t_2) = \frac{\mathbf{G}_1(\vec{r}_1, t_1; \vec{r}_2, t_2)}{\sqrt{\mathbf{G}_1(\vec{r}_1, t_1; \vec{r}_1, t_1)\mathbf{G}_1(\vec{r}_2, t_2; \vec{r}_2, t_2)}}. \tag{2.11}$$

This function $g^{(1)}$ encodes the coherence properties at the single particle level. Its physical meaning is very similar to the classical case. It discriminates between three different situations:

(i) $|g^{(1)}(\vec{r}_1, t_1; \vec{r}_2, t_2)| = 1$: complete coherence

(ii) $0 < |g^{(1)}(\vec{r}_1, t_1; \vec{r}_2, t_2)| < 1$: partial coherence

(iii) $|g^{(1)}(\vec{r}_1, t_1; \vec{r}_2, t_2)| = 0$: incoherent field.

The next paragraph will illustrate the results on the first order coherence function in simple cases.

Simple examples

For simplicity and without loss of generality, we will from now forget about the vectorial nature of the electric field and we will only consider one spatial dimension. Before going to the electron case, it is useful to give the expression of the first order coherence function in simple cases, such as a wavepacket propagating in the vacuum and also coherent and number states of a single mode electric field.

Single photon field propagating in the vacuum

For an electromagnetic field containing one photon described by a probability amplitude ϕ :

$$\psi^\dagger[\phi]|0\rangle = \int \mathrm{d}k\, \phi(k) a_k^\dagger |0\rangle \,, \tag{2.12}$$

the density operator has the following expression in the position basis :

$$\rho(x,y) = \phi(x)\phi^*(y). \tag{2.13}$$

Using Wick's theorem and the normalization of ϕ, the associated first order coherence function is:

$$\mathbf{G_1}(x,y) = \langle 0|E^-(y)E^+(x)|0\rangle \int \mathrm{d}y_- \mathrm{d}y_+ \phi(y_+)\phi^*(y_-)\langle 0|E^+(y_-)E^-(y_+)|0\rangle + \phi(x)\phi^*(y) \tag{2.14}$$

$$= \phi(x)\phi^*(y)\,. \tag{2.15}$$

Here, the first term in (2.14) vanishes, since the operator a_k annihilates the photon vacuum $|0\rangle$. The vacuum of photons has a vanishing coherence, and does not contribute to the total coherence function. The result is depicted in 2.2 for a lorentzian wavepacket, which models the state of the electromagnetic field emitted by the desexcitation of an atomic level [156].

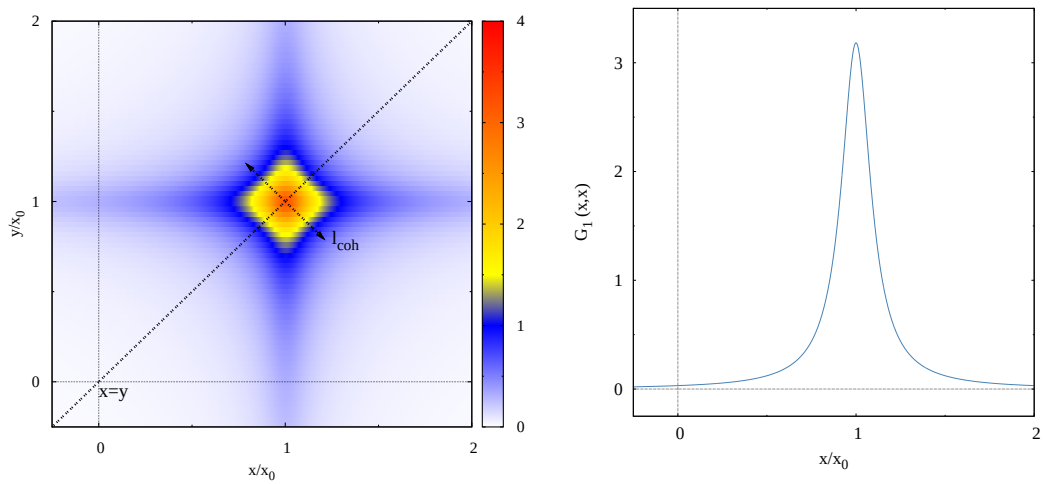

(a) $\mathbf{G_1}(x,y)$ (b) $\mathbf{G_1}(x,x) = \langle I(x)\rangle$

Figure 2.2: (a) Evaluation of the first order coherence function for a wavepacket of the form $\phi(x) = \sqrt{\Gamma/\pi}\frac{1}{x-x_0+i\Gamma}$. The dashed line indicates the diagonal. The extension of the coherence function in the $x-y$ direction gives an estimate of the coherence length l_{coh} of the wavepacket, as suggested by the arrow. (b) Diagonal part of the firt order coherence function, which is the average intensity of the electromagnetic field (2.9).

First order coherence of single mode fields

For a single-mode electric field with wavevector $\vec{q}$ in a volume V, the positive frequency part reads :

$$E^{(+)}(\vec{r},t) = i\sqrt{\frac{\hbar\omega}{2\epsilon_0 V}}\,\hat{a}_{\vec{q}} \text{ with } \omega = c|\vec{q}|\,.e^{i(\vec{q}\cdot\vec{r}-\omega t)}\,, \tag{2.16}$$

For a thermal state, the density operator is a statistical mixing of number states with thermal weights:

$$\rho_{q,th} = \sum_{n_q=0}^{\infty} \frac{e^{-n_q\beta\hbar\omega_q}}{N_q}|n_q\rangle\langle n_q|, \tag{2.17}$$

where n_q is the quanta number in the mode q, and $N_q = \frac{1}{1-e^{-\beta\hbar\omega_q}}$ a normalization constant. For this state, the first order coherence function reads :

$$\mathbf{G_1}(\vec{r}_1,t_1;\vec{r}_2,t_2) = \frac{\hbar\omega}{2\epsilon_0 V}e^{i(\vec{q}\cdot(\vec{r}_1-\vec{r}_2)-\omega(t_2-t_1))}\,\frac{1}{e^{\beta\hbar\omega_q}-1}. \tag{2.18}$$

For a multimode field, one can integrate over k, and making use of the linear dispersion relation in the vacuum, one gets for the reduced first order coherence function:

$$g^{(1)}(x;y) = \frac{6}{\pi^2}\zeta(2,1+i\frac{x-y}{\beta\hbar c})\,, \tag{2.19}$$

where $\zeta(s,z) = \sum_{n\geq 0}\frac{1}{(n+z)^s}$[2]. The characteristic decreasing length $\beta\hbar c$ in (2.19) is the coherence length in the thermal case. This thermal coherence length will allso come into play the case of electron quantum optics in 2.

In the case of a field in a number state $|n\rangle$, the first order coherence function is :

$$\mathbf{G_1}(\vec{r}_1,t_1;\vec{r}_2,t_2) = \frac{\hbar\omega}{2\epsilon_0 V}\,n\,e^{i(\vec{q}\cdot(\vec{r}_1-\vec{r}_2)-\omega(t_2-t_1))}. \tag{2.20}$$

If the field is in an eigenstate of the annihilation operator : $a_q|\alpha_q\rangle = \alpha_q|\alpha_q\rangle$, it is said to be *coherent*[52]. In this case, we have :

$$\mathbf{G_1}(\vec{r}_1,t_1;\vec{r}_2,t_2) = \langle\alpha_q|E^{(-)}(\vec{r}_1,t_1)E^{(+)}(\vec{r}_2,t_2)|\alpha_q\rangle \tag{2.21}$$

$$= \frac{\hbar\omega}{2\epsilon_0 V}|\alpha_q|^2 e^{i(\vec{q}\cdot(\vec{r}_1-\vec{r}_2)-\omega(t_2-t_1))}. \tag{2.22}$$

In the cases of number and coherent states, $g^{(1)}(\vec{r}_1,t_1;\vec{r}_2,t_2) = e^{i(\vec{q}\cdot(\vec{r}_1-\vec{r}_2)-\omega(t_2-t_1))}$. Fig. 2.3 summarizes the results of the last calculations, and compares the obtained first order coherence functions.
$|\mathbf{G_1}(\vec{r}_1,t_1;\vec{r}_2,t_2)| = 1$ for all points in space-time, for both number and coherent states. Thus, coherent and number states (among others) cannot be discriminated on the basis of the information provided by the first order coherence function.
This statement is true in full generality : the first order coherence function cannot distinguish between two sources having the same spectra. We will see in the forthcoming paragraph that being related to photon number statistics, the second order coherence function can distinguish between the two kinds of states. We will thus present the second order coherence for photons in the next paragraph.

[2]In three spatial dimensions, x-y must be replaced by $|\vec{x}-\vec{y}|$.

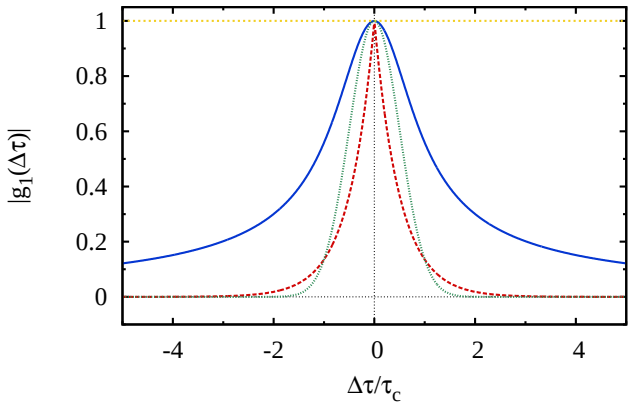

Figure 2.3: Comparison between different first order coherence functions. The solid blue line correspond to the thermal case for a multimode field. The dotted yellow constant line correspond to a coherent state (or to a number state for a single-mode field). The red and green dashed at dash-dotted lines correspond to chaotic (exponential decay) and doppler broadened (gaussian shape) spectra (see, *eg*[91]).

1.2 Photon second order coherence

The first order degree of coherence of the electromagnetic field is appropriate to understand the result of one particle interference experiment, such as Young's experiment. Such an experiment can determine the degree to which a light source is monochromatic, or to determine the coherence length of the light. Nevertheless, it brings no information about the statistical properties of the emitted radiation. More precisely, first order coherence experiments are unable to distinguish between states of light with identical spectral distributions but with quite different photon number distributions as seen previously in the case of number and coherent states of a single mode electrical field.
In the 1950s, Hanbury Brown and Twiss have developped an interferometer [65] involving correlations of intensities instead of fields. The interpretation of intensity interferometry experiments requires the introduction of higher order coherence functions of the electromagnetic field. Chapter 3 will devote more space to the quantum counterpart of the Hanbury Brown and Twiss interferometer in the context of quantum tomography.
In this paragraph, we will focus on the second order coherence function. We will see its relation to photon distribution, and more generally its link to statistical properties of the particles outcoming from a light source.

The second order coherence function is defined by a generalization of the first order coherence:

$$\mathbf{G}_2(\vec{r}_1,t_1;\vec{r}_2,t_2;\vec{r}_3,t_3;\vec{r}_4,t_4) = \mathrm{Tr}\left(\vec{E}^+(\vec{r}_2,t_2)\vec{E}^+(\vec{r}_1,t_1)\rho\vec{E}^-(\vec{r}_3,t_3)\vec{E}^-(\vec{r}_4,t_4)\right). \quad (2.23)$$

Link with photodetection signals

Here, we consider the setup depicted in fig. 2.4. The delay time $\Delta\tau$ between the two detection signals issued from D1 and D2 is controlled. When it is shorter than the coherence time τ_{coh} of

the light source, information about its photon statistics can be obtained.

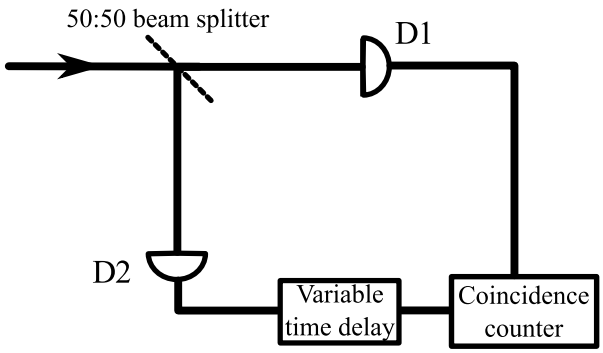

Figure 2.4: Sketch of a coincidence setup. The lengths from the beam splitter to the detectors D1 and D2 are the same. The time delay $\Delta\tau$ is controlled between D2 and the coincidence counter. In practice, the variable time delay is obtained by changing the optical path difference : a $10cm$ difference in length corresponds to $\Delta\tau = 0.3ns$.

The probability amplitude for the absorption of two photons by detectors D_i located at $\vec{r}_i$ is :

$$W_{fi}^{(2)} = |\langle\psi_f|E^{(+)}(\vec{r}_2, t_2)E^{(+)}(\vec{r}_1, t_1)|\psi_i\rangle|^2 \,. \tag{2.24}$$

After summing over the final states and averaging over the initial ones, we obtain the second order coherence function (2.23) by considering the coincidences between two photodetection signals.
At fixed positions,$\mathbf{G_2}$ depends only on the time delay$\Delta\tau$ between photodetections. In this case, it is proportionnal to the probability of absorbing a photon at time t and another at time $t+\Delta\tau$.

To enlighten the relation between the second order coherence function and photon statistics, let us introduce the normalized second order degree of coherence :

$$g^{(2)}(\vec{r}_1, t_1, \vec{r}_2, t_2) = \frac{\mathbf{G_2}(\vec{r}_1, t_1, \vec{r}_2, t_2; \vec{r}_2, t_2, \vec{r}_1, t_1)}{\mathbf{G_1}(\vec{r}_1, t_1; \vec{r}_1, t_1)\mathbf{G_1}(\vec{r}_2, t_2; \vec{r}_2, t_2)}. \tag{2.25}$$

In most cases, we will consider detectors at fixed positions, for which the correlations depend only on the time difference $\Delta\tau$ introduced earlier in fig. 2.4. In the forthcoming examples, we will consequently compute the second order coherence function $g^{(2)}$ as a function of $\Delta\tau$ only. $g^{(2)}$ is positive [91, 121]:

$$0 \leq g^{(2)}(\Delta\tau) \leq \infty. \tag{2.26}$$

For classical electromagnetic fields, it can be shown (see e.g. [121]) that $1 \leq g^{(2)}(\Delta\tau) \leq \infty$. The range of values between 0 and 1 can be reached only by sources that have no classical counterpart. The different behaviours discriminated by the values of $g^{(2)}$ are deeply related to photon statistics.

The second order coherence function at equal position and different times $\mathbf{G_2}(t_1, t_1 + \Delta\tau; t_1 + \Delta\tau + t_1, t_1)$ accounts for the measurement of one photon at time t_1, and another at $\Delta\tau$ later. Thus, the quantity

$$\frac{\mathbf{G_2}(t_1, t_1 + \Delta\tau; t_1 + \Delta\tau + t_1, t_1)}{\mathbf{G_1}(t_1; t_1)} \tag{2.27}$$

can be understood as the joint detection probability to detect a photon at time $t_1 + \Delta\tau$ knowing that one has been detected at t_1. Consequently, $g^{(2)}(t_1, t_1 + \Delta\tau)$ compares the conditional probability (2.27) to the unconditional detection probability $\mathbf{G_1}(t1 + \Delta\tau; t_1 + \Delta\tau)$. At this point, we can distinguish between three characteristic behaviours :

(i) $g^{(2)}(\Delta\tau) = 1$: In this case, the source is coherent. The two photocount events are independent and the second order coherence factorizes into $\mathbf{G_1}(t_1; t_1)\mathbf{G_1}(t_1 + \Delta\tau; t_1+)$.

(ii) $g^{(2)}(\Delta\tau) > 1$: This manifests the tendency of photons to arrive in pairs. This behaviour is called photon bunching.

(iii) $g^{(2)}(\Delta\tau) < 1$: The joint detection probability is less than one, which is the manifestation of photon antibunching.

The behaviour at short $\Delta\tau$ characterizes the light source. If $g^{(2)}(0) > g^{(2)}(\Delta\tau)$, photons will have a tendency to arrive in pairs, and it can be shown [47] that their statistic is superpoissonian. On the contrary, situations where $g^{(2)}(0) < g^{(2)}(\Delta\tau)$, correspond to subpoissonian statistics. The examples in the following paragraph will help to illustrate how the notions of bunching and antibunching are related to photon statistics.

Simple examples

Second order coherence of number and coherent states

As in the case of the first order Glauber's function, we consider a single mode $\vec{q}$ of the electric field. If we evaluate $g^{(2)}$ for this single mode field in an arbitrary state ρ, we find :

$$g^{(2)}(\Delta\tau) = \frac{\langle a^\dagger a^\dagger a a\rangle}{\langle a^\dagger a\rangle} = \frac{\langle n(n-1)\rangle}{\langle n\rangle^2} = 1 + \frac{\langle(\Delta n)^2\rangle - \langle n\rangle}{\langle n\rangle^2}, \tag{2.28}$$

the averages being taken in the state ρ. Here we can see the relation between the degree of second order coherence and photon statistics :

(i) If $g^{(2)} = 1$, then $\langle(\Delta n)^2\rangle = \langle n\rangle$, and the statistics is poisson-like.

(ii) For $g^{(2)} > 1$, then $\langle(\Delta n)^2\rangle > \langle n\rangle$, and the statistics is superpoissonian.

(iii) Conversely, $g^{(2)} < 1 \Rightarrow \langle(\Delta n)^2\rangle < \langle n\rangle$: in this case, the statistics is subpoissonian.

<u>*For a coherent state*</u> $|\alpha_q\rangle$,

$$g^{(2)}_{\text{coh.state}} = 1. \tag{2.29}$$

This result means that coherent states are second order coherent (they also verify $g^{(1)} = 1$). It is also the manifestation of the poissonian nature of the photon statistics in a coherent state, since we have $\langle(\Delta n)^2\rangle = \langle n\rangle$.

<u>*For a number state*</u> $|n\rangle$,

$$g^{(2)}_{\text{numb.state}} = 1 - \frac{1}{n},\ n \geq 2. \tag{2.30}$$

This shows that number states have no classical counterpart. They are truly quantum states, in opposition to coherent states which are semi-classical. It also means that the photon statistics in a number state is sub-poissonian and that photons in a number state will have a tendency to antibunch.

A more general connection between photon collective behaviour (bunching or antibunching) and photon statistics can be made through the Mandel formula [99], which is valid for stationary fields :

$$\langle n^2\rangle - \langle n\rangle^2 - \langle n\rangle = \frac{\langle n\rangle^2}{T^2}\int_{-T}^{T}(T-|\Delta\tau|)[g^{(2)}(\Delta\tau)-1]\,\mathrm{d}\Delta\tau\,. \tag{2.31}$$

In (2.31), the averages are taken over the photon state, which is no longer a number state. This formula states that when a field has $g^{(2)}(\Delta\tau) < 1$ for all $\Delta\tau$ in the time interval $[-T, T]$, it exhibits subpoissonian statistics [3].

Second order coherence of thermal light

Finally, we will show that even if light is treated quantum-mechanically, the second order coherence function of a thermal field has classical features.
The density operator associated to a thermal state of the electric field reads, has been given in the previous paragraph (2.19). The coherence function at second order has the form [91] :

$$g^{(2)}(\Delta\tau) = 1 + |g^{(1)}(\Delta\tau)|^2, \tag{2.32}$$

where $g^{(1)}(\Delta\tau)$ is given in (2.19).
The expression (2.32) shows that $g^{(2)} > 1$ for a thermal state, which means that the thermal photons have a super-poissonian statistics. Furthermore, having $g^{(2)}(\Delta\tau) < g^{(2)}(0)$ for all $\Delta\tau$ indicates that the photons outcoming from a thermal source always bunch [4].

In the next section we present electronic first and second order degrees of coherence, in analogy with what has been done for photons.

2 Definition and properties of electron coherence functions

2.1 First order electronic coherence

At the first order level, the analogues of photon first order correlation functions are the electron (and hole) nonequilibrium Keldysh Green's functions, whose expressions in the state ρ are :

$$\mathcal{G}^{(e)}_{\rho}(x,t;y,t') = \mathrm{Tr}\left(\psi(x)\rho\,\psi^{\dagger}(y)\right) = \langle\psi^{\dagger}(y)\psi(x)\rangle_{\rho} \tag{2.33}$$

$$\mathcal{G}^{(h)}_{\rho}(x,t;y,t') = \mathrm{Tr}\left(\psi^{\dagger}(x)\rho\,\psi(y)\right) = \langle\psi(y)\psi^{\dagger}(x)\rangle_{\rho}. \tag{2.34}$$

[3] We may however be confronted to the case of an antibunching field that exhibits superpoissonian statistics in a finite time interval [121].

[4] This result is also true for sources admitting (2.32) as a second order coherence function. In particular, this is the case of sources having spectra broadened by collisions or Doppler effect.

Due to fermionic anticommutation relations, these two functions fulfil the relation at equal time :

$$\mathcal{G}_\rho^{(e)}(x,y) + \mathcal{G}_\rho^{(h)}(y,x) = \delta(x-y), \tag{2.35}$$

which implies that we will essentially focus on electronic coherence for most cases.
The coherence function for coinciding points $\mathcal{G}_\rho^{(e)}(x,x)$ is the average charge density, and its integral is the total average number of electrons in the system.
The coherence function also satisfies

$$\mathcal{G}_\rho^{(e)}(x,y)^* = \mathcal{G}^{(e)}(y,x), \tag{2.36}$$

making $\mathcal{G}_\rho^{(e)}$ the representation of an hermitian operator in the Hilbert space of single particle states.

In a metallic conductor, due to the presence of the Fermi sea, the vacuum is not void from particles. This is one of the major differences between photons propagating in the true vacuum and electrons in quantum Hall edge channels. A chemical potential μ is associated to the Fermi sea. This chemical potential is assumed to be homogeneous in the system. The Fermi sea has a nonvanishing nonvanishing contribution $\mathcal{G}_\mu^{(e)}$ to the coherence function.

In most case, we will study the single particle coherence of a source emiiting electrons on top a Fermi sea vacuum. We are thus interested to the deviation of the single particle function to the Fermi sea contribution :

$$\Delta\mathcal{G}_\rho^{(e)}(x,y) = \mathcal{G}_\rho^{(e)}(x,y) - \mathcal{G}_\mu^{(e)}(x,y). \tag{2.37}$$

The quantity $\Delta\mathcal{G}_\rho^{(e)}(x,x)$ represents the average excess particle density at the point x and its integral gives the average excess number of charges in the system. Formally, $\Delta\mathcal{G}_\rho^{(e)}(x,x)$ is the normal ordered density with respect to the Fermi sea : $\Delta\mathcal{G}_\rho^{(e)}(x,x) = \langle : \psi^\dagger(x)\psi(x) : \rangle_\rho$.

For a translation invariant state ρ, $\mathcal{G}_\rho^{(e/h)}(x,y)$ only depends on $x-y$ and can be expressed in terms of fermion occupation numbers:

$$\mathcal{G}_\rho^{(e)}(k) = \int \mathcal{G}_\rho^{(e)}(x-y)\, e^{ik(x-y)}\, \mathrm{d}(x-y) = \bar{n}_\rho(k)\,. \tag{2.38}$$

In (2.38), it has been assumed that the density of states is the one of free electrons. In particular, for the Fermi sea $|F_\mu\rangle$ where $\mu \equiv \mu(\rho)$, the occupation number is the Fermi distribution corresponding to the Fermi momentum k_F at the corresponding chemical potential. Since we are considering chiral systems, we will take for convenience $k_F = 0$: All energies and momenta will be measured from the Fermi level.

For any state, the single electron coherence depends in general on x and y, or equivalently on $x-y$ and $\bar{x} = (x+y)/2$. Its Fourier transform $\mathcal{G}_\rho^{(e)}(k_+,k_-)$ defined as

$$\mathcal{G}_\rho^{(e)}(k_+,k_-) = \int \mathcal{G}_\rho^{(e)}(x,y)\, e^{i(k_+x-k_-y)}\, \mathrm{d}x\, \mathrm{d}y \tag{2.39}$$

has non zero values away from the diagonal $k_+ = k_-$. The (k_+,k_-) plane can be divided into four quadrants, as shown on fig. 2.5. The positive energy quadrant $k_+, k_- > 0$ accounts

for electronic excitations. Correspondingly, the negative energy quadrant $k_+, k_- < 0$ represent hole excitations. the off diagonal contributions $k_+ k_- < 0$ to the coherence function in Fourier space account for electron/hole coherences. The examples given below will illustrate this separation.

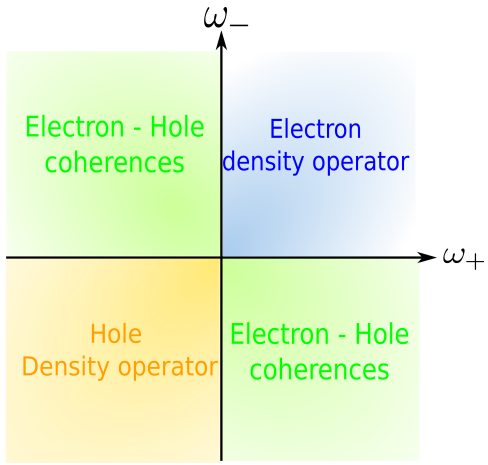

Figure 2.5: The quadrant defined by $k_+ > 0$ and $k_- > 0$ (in blue) corresponds to positive energy states which are electron excitations whereas the red quadrant, defined by $k_+ < 0$ and $k_- < 0$ corresponds to hole excitations (negative energy states). The off diagonal quadrants (in green) defined by $k_+ k_- < 0$ encode the information on electron/hole coherence.

The shape of the charge density wave associated to any state ρ can be recovered by integrating this double Fourier transform along parallels to the diagonal:

$$\int \mathcal{G}_\rho^{(e)}(q + \frac{k}{2}, q - \frac{k}{2}) \frac{\mathrm{d}q}{2\pi} = \int e^{ikx} \mathcal{G}_\rho^{(e)}(x, x) \, \mathrm{d}x. \tag{2.40}$$

In the same way, spatial coherence around a classical position $\bar{x}$ is recovered by integrating along antidiagonal lines in Fourier space:

$$\int \mathcal{G}_\rho^{(e)}(\bar{x} + \frac{\Delta}{2}, \bar{x} + \frac{\Delta}{2}) \, e^{ik\Delta} \, \mathrm{d}\Delta = \int \mathcal{G}_\rho^{(e)}(\frac{k}{2} + q, \frac{k}{2} - q) e^{-iq\bar{x}} \frac{\mathrm{d}q}{2\pi} \, . \tag{2.41}$$

Simple examples

To illustrate clearly the aforementioned general concepts on the single electron coherence function, we will derive its expression in a few simple cases. The first example will show the electron quantum optics paradigm of a single electron waveoacket injected well above the Fermi level. Then, we will illustrate some of the features evocated in the previous part by looking at a superposition of a hole and an electron, and the supersposition of two electronic wavepackets on top of the Fermi sea.

Electronic wavepacket on top of the Fermi sea

Introducing an electronic wavepacket on top of the Fermi sea is equivalent to the action of a wavepacket creation operator on the vacuum :

$$\psi^\dagger[\phi] = \int \mathrm{d}y \phi(y)\psi^\dagger(y)\,, \tag{2.42}$$

with $\int |\phi|^2 = 1$. The associated density operator is $\rho_\phi = \psi^\dagger[\phi]|F\rangle\langle F|\psi[\phi]$. The first order coherence function is thus :

$$\mathcal{G}^{(e)}(x,y) = \langle \psi^\dagger(y)\psi(x)\rangle_{\rho_\phi} \tag{2.43}$$

$$= \int \mathrm{d}y_+ \mathrm{d}y_- \phi(y_+)\phi^*(y_-)\langle F|\psi(y_-)\psi^\dagger(y_-)\psi(y_+)\psi^\dagger(y_+)|F\rangle. \tag{2.44}$$

With the help of Wick's theorem [73], for an electronic wavepacket [5], the coherence function reduces to :

$$\mathcal{G}^{(e)}(x,y) = \mathcal{G}^{(e)}_\mu(x-y) + \Delta\mathcal{G}^{(e)}(x,y) = \mathcal{G}^{(e)}_\mu(x-y) + \phi(x)\phi^*(y). \tag{2.45}$$

The $\Delta\mathcal{G}^{(e)}(x,y)$ term is identical to the coherence function (2.14) for a photonic wavepacket, but here the coherence function of the vacuum (here the Fermi sea) no longer vanishes. For a Fermi sea at chemical potential μ, it has the following expression at finite temperature :

$$\mathcal{G}^{(e)}_\mu(x-y) = \int_{-\infty}^{+\infty} \mathrm{d}k\, \bar{n}_\mu(k) e^{ik(x-y)} = \frac{i\pi}{\beta h} \frac{e^{i\mu(x-y)/\hbar v_F}}{\sinh\left(\pi(x-y)/\beta\hbar v_F\right)}, \quad \beta = \frac{1}{k_B T}\,. \tag{2.46}$$

In the case of a wavepacket well separated from the Fermi sea, eq. (2.45) illustrates the electron quantum optics paradigm (see chapter 1).
In the following example we will evaluate the single particle coherence function for two electrons on top of the Fermi sea.

Two electrons on top of the Fermi sea

This example is quite similar from the previous one, except that we are now considering the injection of two electronic wavepackets. This will illustrate how the Pauli principle comes into play in the coherence function.The state resulting from the action of two operators creating electronic wavepackets ϕ_1 and ϕ_2 on the Fermi sea is a Slater determinant[6] :

$$\frac{1}{\sqrt{\mathrm{Det}\left(\langle\phi_i|\phi_j\rangle_{i,j=1,2}\right)}} \psi^\dagger[\phi_1]\psi^\dagger[\phi_2]|F\rangle\,. \tag{2.47}$$

The wavepackets considered here only have strictly positive momentum Fourier components. The computations to find the associate coherence function are quite similar to the previous case, and we obtain, in Fourier space :

$$v_F^2 \Delta\mathcal{G}^{(e)}(k_+,k_-) = \frac{\tilde{\phi}_1(k_+)\tilde{\phi}_1^*(k_-) - \langle\phi_1|\phi_2\rangle\tilde{\phi}_2^*(k_-)\tilde{\phi}_1(k_+) + \tilde{\phi}_2(k_+)\tilde{\phi}_2^*(k_-) - \langle\phi_2|\phi_1\rangle\tilde{\phi}_1(k_-)^*\tilde{\phi}_2(k_+)}{\mathrm{Det}\left(\langle\phi_i|\phi_j\rangle_{i,j=1,2}\right)} \tag{2.48}$$

[5] This implies that the wavepacket has a nonvanishing spectrum for positive energies only.
[6] The prefactor ensures correct normalization.

For non overlapping wavepackets, each one contributes independently to the excess coherence. But when their overlap is nonzero, the supplementary terms that appear will bear the effects of the Pauli principle.
To illustrate the behaviour of the electronic coherence function in this case, we will choose ϕ_1 and ϕ_2 such that $\tilde{\phi}_1(k) = \sqrt{2l_0}\theta(k)e^{-l_0 k}$ and $\tilde{\phi}_2(k) = \sqrt{2l_0}\theta(k)e^{-l_0 k}e^{ikv_F\Delta t}$, which represents a situation where two identical lorentzian wavepackets [76, 87] are separated by a time Δt. By varying this time interval, we will illustrate the effects of the Pauli principle. As seen in fig. 2.6, the shape of the single particle coherence function is significantly different for the different values of Δt. In particular, when $\Delta t \to 0$, $\mathcal{G}^{(e)}$ is no longer the sum of two identical coherence functions for one electron.

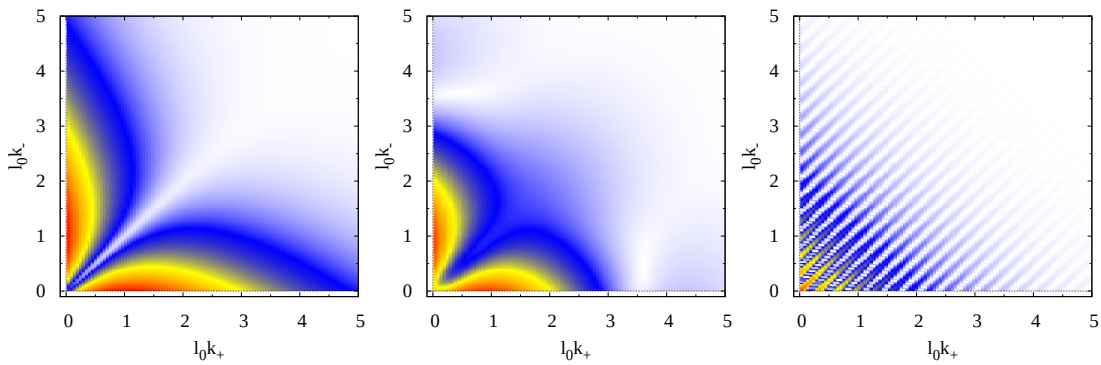

(a) $\Delta t = 0.05 l_0/v_F$ (b) $\Delta t = l_0/v_F$ (c) $\Delta t = 20 l_0/v_F$

Figure 2.6: Modulus of the Fourier transform of first order electronic coherence function for two identical electronic wavepackets separated by Δt. As this time difference goes to zero, oscillations occur in the frequency plane, resulting from interferences between the two wavepackets. On the contrary, as the difference in the emission times increases, the oscillating contribution to the coherence function vanishes.

In position space, the coherence function is also the sum of the same four contributions:

$$v_F^2 \Delta\mathcal{G}^{(e)}(x,y) = \frac{\phi_1(x)\phi_1^*(y) - \langle\phi_1|\phi_2\rangle\phi_2^*(y)\phi_1(x) + \phi_2(x)\phi_2^*(y) - \langle\phi_2|\phi_1\rangle\phi_1(y)^*\phi_2(x)}{\mathrm{Det}\left(\langle\phi_i|\phi_j\rangle_{i,j=1,2}\right)}, \tag{2.49}$$

where $\phi_1(x) = \frac{\sqrt{2l_0}}{l_0 - ix}$ and $\phi_2(x) = \phi_1(x - v_F\Delta t)$. The effect of the overlap is illustrated in 2.7.

In the newt two examples, we will present situations that have no optical counterpart, since they involve hole excitations. More precisely, we will first look at the case of an electron/hole pair, and then at a state that generate electron/hole coherences.

Electron / hole pair

The operator acting on the Fermi sea to create a single electron/hole pair is :

$$\psi^\dagger[\phi_e]\psi[\phi_h] = \int \mathrm{d}y_1\mathrm{d}y_2\phi_h(y_1)\phi_e(y_2)\psi^\dagger(y_2)\psi(y_1)\,. \tag{2.50}$$

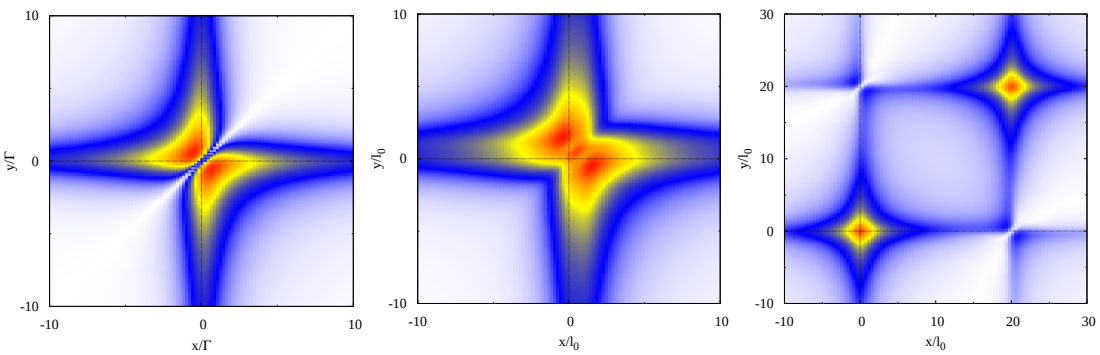

(a) $\Delta t = 0.05 l_0/v_F$ (b) $\Delta t = l_0/v_F$ (c) $\Delta t = 20 l_0/v_F$

Figure 2.7: Modulus of the first order coherence function in position space for two electronic wavepackets separated by a time interval Δt. As the emission time increases, the effects of the overlap vanish, as expected. At short Δt, the Pauli principle imposes the vanishing of the coherence function at equal times.

The excess coherence due to the introduction of the pair is :

$$\Delta\mathcal{G}^{(e)}(x,y) = \langle\psi^\dagger[\phi_h]\psi_x\rangle\left(\langle\psi[\phi_e]\psi_y^\dagger\rangle\langle\psi^\dagger[\phi_e]\psi[\phi_h]\rangle - \langle\psi[\phi_e]\psi^\dagger[\phi_e]\rangle\langle\psi_y^\dagger\psi[\phi_h]\rangle\right) + \tag{2.51}$$

$$\langle\psi_x\psi^\dagger[\phi_e]\rangle\left(-\langle\psi_y^\dagger\psi[\phi_h]\rangle\langle\psi^\dagger[\phi_h]\psi[\phi_e]\rangle + \langle\psi[\phi_e]\psi_y^\dagger\rangle\langle\psi^\dagger[\phi_h]\psi[\phi_h]\rangle\right) \tag{2.52}$$

For any wavepackets ϕ_1 and ϕ_2 :

$$\langle\psi^\dagger[\phi_1]\psi_x\rangle = \int_{-\infty}^{+\infty}\frac{\mathrm{d}q}{2\pi v_F}\bar{n}_F(q)\tilde{\phi}_1(q)e^{iqx} \tag{2.53}$$

$$\langle\psi_y^\dagger\psi[\phi_1]\rangle = \int_{-\infty}^{+\infty}\frac{\mathrm{d}q}{2\pi v_F}\bar{n}_F(q)\tilde{\phi}_1^*(q)e^{-iqy}. \tag{2.54}$$

$$\langle\psi[\phi_1]\psi^\dagger[\phi_2]\rangle = \int_{-\infty}^{+\infty}\frac{\mathrm{d}k}{2\pi v_F}(1-\bar{n}_F(k))\tilde{\phi}_1^*(k)\tilde{\phi}_2(k) \tag{2.55}$$

$$\langle\psi^\dagger[\phi_1]\psi[\phi_2]\rangle = \int_{-\infty}^{+\infty}\frac{\mathrm{d}k}{2\pi v_F}\bar{n}_F(k)\tilde{\phi}_2^*(k)\tilde{\phi}_1(k) \tag{2.56}$$

The expressions (2.55) and (2.56) reduce respectively to $\langle\phi_1|\phi_2\rangle$ and $\langle\phi_1|\phi_2\rangle$ in the case of wavepackets whose Fourier components are only in the $k > 0$ or $k < 0$ interval. Thus, in the case of an electron hole pair, these terms vanish.
Therefore, for electron and hole wavepacket, the excess coherence in Fourier space is:

$$v_F^2\Delta\mathcal{G}^{(e)}(k_+,k_-) = -\tilde{\phi}_h(k_+)\tilde{\phi}_h^*(k_-) + \tilde{\phi}_e(k_+)\tilde{\phi}_e^*(k_-). \tag{2.57}$$

In this expression, the second and fourth term respectively account for hole and electron contribution to the coherence function (red and blue quadrants in 2.5). The other terms are the electron/hole coherences.

Note that in the case of an electron (resp. a hole) wavepacket with Fourier components only in the $k > 0$ (resp. $k < 0$) interval, the electron/hole coherences vanish. This modulus of this excess coherence function is depicted in 2.8 in the particular case of electron and hole lorentzian

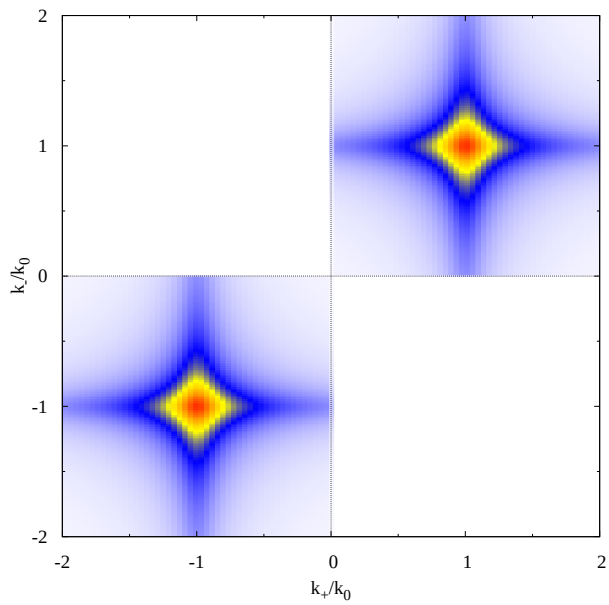

Figure 2.8: Modulus of the first order coherence function in the case of electron and hole wavepackets coherent superposition. The expressions of the wavepackets are : $\tilde{\phi}_e(k) = \theta(k)\frac{\phi_0}{k-k_0+i\Gamma/\hbar v_F}$ and $\tilde{\phi}_h(k) = \theta(k)\frac{\phi_0}{k+k_0+i\Gamma/\hbar v_F}$. Here, Γ is taken to be $v_F k_0/10$.

wavepackets centered at opposite energies. This particular shape of electronic wavepacket is encountered in [76].

Electron/hole coherences

For a state of the form

$$\frac{1}{\sqrt{2}}\left(|F\rangle + \psi[\phi_h]\psi^\dagger[\phi_e]|F\rangle\right) , \tag{2.58}$$

the coherence function contains contributions in the electron/hole quadrants :

$$v_F^2\Delta\mathcal{G}^{(e)}(k_+,k_-) = -\tilde{\phi}_h(k_+)\tilde{\phi}_h^*(k_-) + \tilde{\phi}_e(k_+)\tilde{\phi}_e^*(k_-) - (1-\bar{n}_F(k_+))\bar{n}_F(k_-)\tilde{\phi}_e(k_+)\tilde{\phi}_h^{\ *}(k_-) \tag{2.59}$$

$$+ (1-\bar{n}_F(k_-))\bar{n}_F(k_+)\tilde{\phi}_e^{\ *}(k_-)\tilde{\phi}_h(k_+) . \tag{2.60}$$

The result is illustrated in fig. 2.9 for the previous form of electron and hole wavepackets. In general, the appearance of electron/hole coherences in $\Delta\mathcal{G}^{(e)}$ is associated with the presence of coherent superpositions of electron/hole pairs.

Tunnel detection and first order coherence

In this last part, in analogy with the first section, we will make a link between the electronic coherence function and the detection signal (an electric current) for an ideal tunneling detector coupled to an edge channel. For electronic systems, the analogous of photodetection consist of a device that could extract one electron from the electronic channel and detect the corresponding charge, as depicted in fig. 2.10. The coupling between the edge channel and the detector is assumed to be of the form :

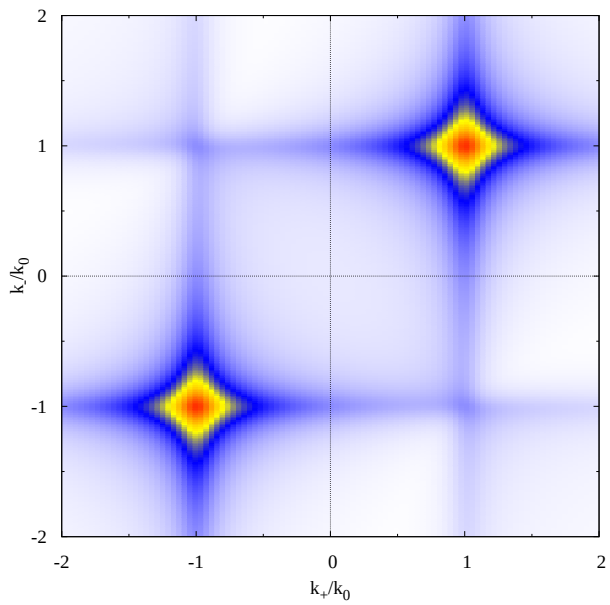

Figure 2.9: Modulus of the first order coherence function in the case of two wavepackets exhibiting electron/hole coherences. The expressions of the wavepackets are : $\tilde{\phi}_e(k) = \frac{\sqrt{\Gamma/\pi}}{k-k_0+i\Gamma/\hbar v_F}$ and $\tilde{\phi}_h(k) = \frac{\sqrt{\Gamma/\pi}}{k+k_0+i\Gamma/\hbar v_F}$. Here, Γ is taken to be $v_F k_0/10$.

$$H_{\mathrm{t}} = \hbar(\psi^\dagger(x_D)\, O + O^\dagger \psi(x_D)) \tag{2.61}$$

where O only acts on the detector and x_D is the position of the detector which is assumed to be local. In this context, the operator O is the analogue of the dipolar operator encountered in the case of photons.

Perturbative approach

As for the case of photodetection, we will consider an ideal two level detector which will be treated in a first order perturbation theory. This detector is initially in the state $|g\rangle$, and the detection of an electron during time t will cause a transition to an excited state $|e\rangle$ containing an extra charge :

$$P_{g\to e}(t) = \int_0^t \langle g|O^\dagger(\tau)|g\rangle\langle g|O(\tau')|e\rangle\, \mathcal{G}^{(e)}_{\rho_0}(x_D,\tau|x_D,\tau')\, d\tau d\tau' \tag{2.62}$$

where ρ_0 is the many body density operator describing the electron channel coupled to the detector. Differences between electrons and photons lie in the detection process. Indeed, contrarily to photons, an electron cannot be destroyed. Therefore, one has to consider also emission processes, where an electron is sent back from the detector into the conductor. The probabilty that such a process occurs, leading to a transition from a state e to g is:

$$P_{e\to g}(t) = \int_0^t \langle g|O(\tau)|e\rangle\langle e|O^\dagger(\tau')|g\rangle\, \mathcal{G}^{(h)}_{\rho_0}(x_D,\tau|x_D,\tau')\, d\tau d\tau' \tag{2.63}$$

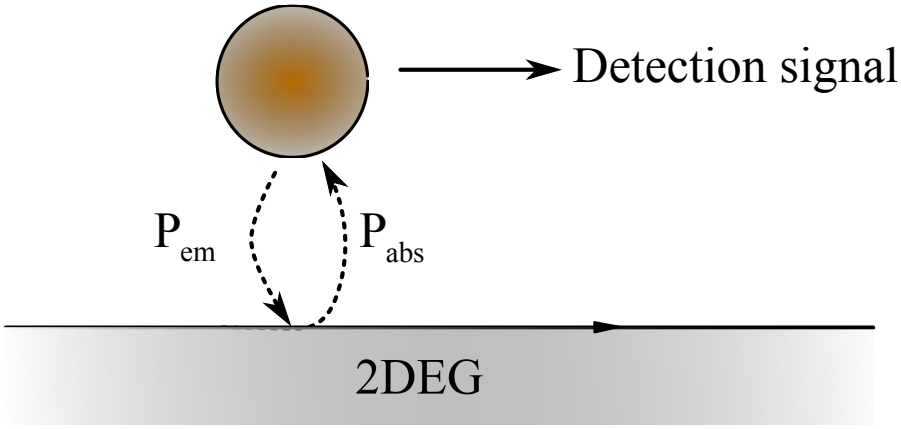

Figure 2.10: Schematic electrodetection setup. The detector is coupled to the conductor via a weak tunnel effect. The detection signal is associated to the absorption process, which has a probability P_{abs} to occur.

and involves the hole coherence function $\mathcal{G}^{(h)}$, suggesting the underlying symmetry between absorption and emission processes in the detection.

We are considering tunneling detection, so the measured signal is the tunneling current flowing from the conductor into the detector. The corresponding absorption operator O can be written as :

$$O(\tau) = \sqrt{\mathrm{v}_F} \int f_d(\omega)\, e^{-i\omega t} c(\omega)\, \frac{d\omega}{\sqrt{\omega}} \tag{2.64}$$

where v_F (taken for simplicity to be equal to the Fermi velocity in the conductor) has been introduced for dimensionality reasons and $f_d(\omega)$ is a dimensionless function that encodes the density of states within the detector as well as any possible energy dependence of tunneling. Summing over all the final states:

$$P_{\mathrm{abs}}(t) = \int_0^t K_D^{(\mathrm{abs})}(\tau - \tau') \mathcal{G}_{\rho_0}^{(e)}(x_D, \tau | x_D, \tau')\, d\tau d\tau' \tag{2.65}$$

$$P_{\mathrm{em}}(t) = \int_0^t K_D^{(\mathrm{em})}(\tau - \tau') \mathcal{G}_{\rho_0}^{(e)}(x_D, \tau | x_D, \tau')\, d\tau d\tau' \tag{2.66}$$

where the detector's functions are expressed in terms of the electron occupation number $\bar{n}_d(\omega)$ within the detector:

$$K_D^{(\mathrm{abs})}(\tau) = \mathrm{v}_D \int e^{i\omega\tau} |f_d(\omega)|^2 (1 - \bar{n}_d(\omega))\, \frac{d\omega}{2\pi} \tag{2.67}$$

$$K_D^{(\mathrm{em})}(\tau) = \mathrm{v}_D \int e^{-i\omega\tau} |f_d(\omega)|^2 \bar{n}_d(\omega)\, \frac{d\omega}{2\pi}\,. \tag{2.68}$$

Stationary regime

In the stationary regime, the coherence functions depend on the time difference $\tau - \tau'$. They are thus related to the electron occupation number in the conductor :

$$\mathcal{G}^{(e)}_{\rho_0}(x_D, \tau | x_D, \tau') = \int e^{i\omega\tau} \bar{n}_e(\omega) \frac{d\omega}{2\pi v_F} \tag{2.69}$$

$$\mathcal{G}^{(h)}_{\rho_0}(x_D, \tau | x_D, \tau') = \int e^{i\omega\tau} (1 - \bar{n}_e(\omega)) \frac{d\omega}{2\pi v_F} \,. \tag{2.70}$$

The probabilities in (2.65) are then increasing linearily with time and can then be replaced by transition rates:

$$\Gamma_{\text{abs}} = \int |f_d(\omega)|^2 \bar{n}_e(\omega)(1 - \bar{n}_d(\omega)) \frac{d\omega}{2\pi} \tag{2.71a}$$

$$\Gamma_{\text{em}} = \int |f_d(\omega)|^2 (1 - \bar{n}_e(\omega)) \bar{n}_d(\omega) \frac{d\omega}{2\pi} \,. \tag{2.71b}$$

The current from the conductor to the detector is finally obtained as : $\bar{I} = -e(\Gamma_{\text{abs}} - \Gamma_{\text{em}})$ and is given by:

$$\bar{I} = e \int |f_d(\omega)|^2 (\bar{n}_d - \bar{n}_e)(\omega) \frac{d\omega}{2\pi} \,. \tag{2.72}$$

In the case of a broadband detector, we consider that $|f_d(\omega)|^2$ is constant over the frequency range under consideration and denote its value by g_D. Then, assuming that n_e and n_d are two Fermi distributions differing by their chemical potential, the average current is given by $\bar{I} = (e^2/h).\, g_D.\, (\mu_d - \mu_e)$ and therefore g_D can be interpreted as the dimensionless conductance between the conductor and the detector.

An interesting case is obtained when considering tunneling from a chiral edge channel into a drain reservoir through an energy filter such as a quantum dot with well defined single particle energy levels. In this case, $|f_d(\omega)|^2 = \gamma_D\, \delta(\omega - \omega_0)$ where γ_D has the dimension of a rate. Then, the average current is a direct measurement of the difference of the electron distribution function within the detector and the system at ω_0:

$$\bar{I} = e\gamma_D\, (\bar{n}_d - \bar{n}_e)(\omega_0) \,. \tag{2.73}$$

Such a detection scheme has been used by Frédéric Pierre and his collaborators at the Laboratoire de Photonique et Nanostructures to study the interaction induced relaxation processes occuring in the quantum Hall regime [2].

Although this is not the subject of this section, nor of this thesis, this approach to electrode-detection could be envisioned to measure the information encoded in the spin degree of freedom [129].

In the following part, we introduce the second order electronic coherence and discuss its relation to current fluctuations in the context of electronic transport.

2.2 Quantum electronic coherence at second order

The forthcoming discussion of second order electronic coherence will be very similar to the one for photons in section 1.

Definition and properties

By analogy with the case of photons, the second order coherence function is defined as :

$$\mathcal{G}_\rho^{(e,2)}(x_1, x_2|y_1, y_2) = \mathrm{Tr}\left(\psi(x_2)\psi(x_1)\,\rho\,\psi^\dagger(y_1)\psi^\dagger(y_2)\right). \tag{2.74}$$

In the following paragraphs, we will essentially consider $\mathcal{G}_\rho^{(e,2)}(x_1, x_2|x_1, x_2) \equiv \mathcal{G}^{(e,2)}(x_1, x_2)$, and see how this function is related to particle number fluctuations and statistics of the electrical current.

We now turn to density correlations $\langle n(x)\,n(y)\rangle_\rho$ where $n(x) = (\psi^\dagger\psi)(x)$. Using the canonical commutation relations [7],then:

$$n(x)\,n(y) = \delta(x-y)\,\psi^\dagger(y)\psi(x) + \psi^\dagger(x)\psi^\dagger(y)\psi(y)\psi(x) \tag{2.75}$$

thus relating density fluctuations to first and second order coherences :

$$\begin{aligned}\langle n(y)\,n(x)\rangle_{c,\rho} &= \langle n(y)n(x)\rangle_\rho - \langle n(y)\rangle_\rho\langle n(x)\rangle_\rho &(2.76)\\ &= \delta(x-y)\,\mathcal{G}_\rho^{(1)}(x,y) + \mathcal{G}_\rho^{(e,2)}(x,y|x,y) - \mathcal{G}_\rho^{(e)}(x,x)\mathcal{G}_\rho^{(e)}(y,y)\,. &(2.77)\end{aligned}$$

Thus, the fluctuations of the total number of particles N_D within a domain D are a sum of two contributions:

$$\langle\delta N_D^2\rangle_\rho = \langle N_D\rangle_\rho + \int_{D^2}\langle n(x)\rangle_\rho\langle n(y)\rangle_\rho\left(g_\rho^{(2)}(x,y) - 1\right)\,dx\,dy\,. \tag{2.78}$$

In a similar way to photons [52], $g_\rho^{(2)}(x,y)$ denotes the degree of second order for electrons :

$$g_\rho^{(2)}(x,y) = \frac{\mathcal{G}_\rho^{(e,2)}(x,y|x,y)}{\mathcal{G}_\rho^{(e)}(x,x)\,\mathcal{G}_\rho^{(e)}(y,y)}\,. \tag{2.79}$$

In the case of free quantum particles at equilibrium, Wick's theorem immediately leads to:

$$\mathcal{G}^{(2)}(x,y|x,y) = \mathcal{G}^{(e)}(x,x)\,\mathcal{G}^{(e)}(y,y) - \mathcal{G}^{(e)}(x,y)\mathcal{G}^{(e)}(y,x)\,. \tag{2.80}$$

Consequently:

$$\langle\delta N_D^2\rangle = \langle N_D\rangle - \int_{D^2}\left|\mathcal{G}^{(e)}(x,y)\right|^2\,dx\,dy\,. \tag{2.81}$$

The first term in the r.h.s corresponds to the usual Gaussian or Poissonian particle number fluctuation arising in classical mechanics. It reflects the discrete nature of particles. The second one arises from quantum coherence and will thus be called the quantum contribution to fluctuations. Note that this contribution reflects the wave nature of quantas. This interpretation has already been proposed by A. Einstein in [35] (reprinted in [4], and also discussed in [55]).

To pursue the parallel between photons and electrons from the point of view of the particle statistics,let us relate the degree of second order coherence (2.79) to the coincidence probability for electrons.

[7] The result is the same for electrons or photons.

Since $\mathcal{G}_\rho^{(e,2)}(x,y|x,y)$ represents the probability density to find a particle at position x and then, immediately after, at position y, the conditional probability to detect a particle at position y knowing one has just been detected at position x is of the form

$$\mathcal{P}(y|x) = \frac{1}{\mathcal{N}_2}\frac{\mathcal{G}^{(e,2)}(x,y|x,y)}{\mathcal{G}^{(e)}(x,x)}\,. \tag{2.82}$$

where $\mathcal{N}_2$ is a normalization constant ensuring $\int \mathcal{P}(y|x)\,dy = 1$. The probability distribution for a single particle is $\mathcal{P}(y) = \langle N\rangle_\rho^{-1}\mathcal{G}^{(e)}(y,y)$ [8]. $\mathcal{P}(y|x)/\mathcal{P}(y) = (\langle N\rangle_\rho/\mathcal{N}_2)\,g_\rho^{(2)}(x,y)$ and it can easily be shown[9] that in the thermodynamic limit, the prefactor goes to 1 and so

$$\frac{\mathcal{P}(y|x)}{\mathcal{P}(y)} = g^{(2)}(x,y)\,. \tag{2.83}$$

Therefore, the degree of second order coherence directly measures the tendency to bunch or antibunch of the particles. The interpretation of the second order of coherence for electrons is the same as in the photon case. Equation (2.82) thus expresses how bunching or antibunching influence particle number fluctuations. The rhs of (2.81) show for example that noninteracting electrons have a tendency to antibunch.

Let us now relate the average number of electron and hole excitations, and their statistical properties to the coherence function. Here we consider the single coherence in the time domain at a given point. Let us assume that its double Fourier transform with respect to time is of the following form:

$$\mathcal{G}_\rho^{(e)}(\omega_+,\omega_-) = \frac{2\pi}{v_F}\,n_F\left(\frac{\omega_+ + \omega_-}{2}\right)\delta(\omega_+ - \omega_-) + \Delta\mathcal{G}_\rho^{(e)}(\omega_+,\omega_-) \tag{2.84}$$

where the first term represents the Fermi sea contribution and $\Delta\mathcal{G}_\rho^{(e)}(\omega_+,\omega_-)$ represents the contribution of the excitations created by a source. It is interesting to consider the operators counting electron-like excitations as well as hole-like excitations with respect to $\mu = 0$:

$$N_+ = \int_0^{+\infty} c^\dagger(\omega)c(\omega)\,d\omega \tag{2.85a}$$

$$N_- = \int_{-\infty}^{0} c(\omega)c^\dagger(\omega)\,d\omega\,. \tag{2.85b}$$

With these conventions N_+ and N_- are positive operators. Their average values obtained from the single electron (resp. hole) coherences by integration over the positive (resp. negative) single particle energy states :

$$\langle N_+\rangle_\rho = \frac{v_F}{2\pi}\int_0^{+\infty}\mathcal{G}_\rho^{(e)}(\omega,\omega)\,d\omega \text{ and } \langle N_-\rangle_\rho = \frac{v_F}{2\pi}\int_{-\infty}^{0}\mathcal{G}_\rho^{(h)}(\omega,\omega)\,d\omega\,. \tag{2.86}$$

[8] Normalized in this way, $\mathcal{G}^{(e)}(x,y)$ represents the one particle density operator. Its diagonal part is consequently the probability density to find an electron at a given position.

[9] This follows from the fact that $\int \mathcal{G}_\rho^{(e,2)}(x,y|x,y)\,dy = \langle N\rangle_\rho - 1 + \int\langle n(x)\,n(y)\rangle_{c,\rho}\,dy$. Assuming that in the thermodynamic limit, the relative fluctuation of the total particle number is subdominant with respect to $\langle N\rangle_\rho$, $\langle N\rangle_\rho/\mathcal{N}_2 \mapsto 1$ in the thermodynamic limit.

The total charge present within the system with respect to the Fermi sea is $Q = -e(N_+ - N_-)$. An AC source will satisfy $Q = 0$ at the operator level (see chapter 3 for the discussion of a periodically driven system).

An AC single electron source is expected to produce $\langle N_+\rangle_\rho = \langle N_-\rangle_\rho = 1$ implying that within each operating cycle, it emits on average a single electron and a single hole. But an indicator of the quality of the source is given by the fluctuation of these numbers: $\langle(\Delta n_+)^2\rangle_\rho = \langle N_+^2\rangle_\rho - \langle N_+\rangle_\rho^2$. Note that for an AC single electron source, we have $\langle(\Delta n_+)^2\rangle_\rho = \langle(\Delta n_-)^2\rangle_\rho = \langle(\Delta n_+)(\Delta n_-)\rangle_\rho$. Then for states such that Wick theorem applies, we have:

$$\langle(\Delta n_+)(\Delta n_-)\rangle_\rho = -\frac{v_F^2}{(2\pi)^2}\int_{\omega_+\geq 0\,\omega_-\leq 0} \mathcal{G}_\rho^{(e)}(\omega_-,\omega_+)\mathcal{G}_\rho^{(h)}(\omega_-,\omega_+)\, d\omega_- d\omega_+ \tag{2.87}$$

Using the anticommutation relations for fermion operators $\{c(\omega), c^\dagger(\omega')\} = \delta(\omega-\omega')$, we find[10]:

$$\langle(\Delta n_+)^2\rangle_\rho = \frac{v_F^2}{(2\pi)^2}\int_{\substack{\omega_+\geq 0\\ \omega_-\leq 0}} \left|\mathcal{G}_\rho^{(e)}(\omega_-,\omega_+)\right|^2 d\omega_- d\omega_+\,. \tag{2.88}$$

This shows that, when Wick's theorem applies, the fluctuation of the number of electron excitations is precisely given by the single electron coherence in the electron/hole sector ($\omega_+\omega_- \leq 0$). For an AC source, the vanishing of these fluctuations is equivalent to the vanishing of $\mathcal{G}_\rho^{(e)}(\omega_+,\omega_-)$ for $\omega_+\omega_- \leq 0$.

We also have the following general expression for the number fluctuations:

$$\langle(\Delta n_+)^2\rangle_\rho = \langle N_+\rangle_\rho - \frac{v_F^2}{(2\pi)^2}\int_{\substack{\omega_+\geq 0\\ \omega_-\geq 0}} \left|\mathcal{G}_\rho^{(e)}(\omega_+,\omega_-)\right|^2 d\omega_+ d\omega_- \tag{2.89}$$

which emphasizes the correction to the Poissonnian result $\langle N_+\rangle_\rho$ as a reduction of the noise due to the single particle coherence of positive energy excitations.

Relation to current noise

Relation between current noise and coherence functions

In this last paragraph, we discuss the relation of temporal second order coherence to current fluctuations. Indeed, the previous discussion on particle number fluctuations are equivalent to a discussion of current noise, since the electrical current is linked to the particle density via :

$$I(x) = -ev_F : \psi^\dagger(x)\psi(x) : \,. \tag{2.90}$$

The general expression of current noise is :

$$\begin{aligned} S(t,t') &= \langle I(t)I(t')\rangle_\rho - \langle I(t)\rangle_\rho\langle I(t')\rangle_\rho \\ &= e^2 v_F \langle n(t)n(t')\rangle_{c,\rho} \end{aligned} \tag{2.91}$$

[10]The boundary of the domain $\omega_+ \geq 0$ and $\omega_- \leq 0$ does not contribute.

where ρ is the many body state generated by the source. Thus current noise and particle fluctuations can be expressed in terms of the first and second order coherences as :

$$(ev_F)^{-2}S(t,t') = \mathcal{G}^{(e)}(t,t)\delta(t-t') - |\Delta\mathcal{G}^{(e)}(t,t')|^2 - \mathcal{G}_F^{(e)}\Delta\mathcal{G}^{(e)}(t,t') - \mathcal{G}_F^{(e)}(t',t)\Delta\mathcal{G}(t',t)\,. \tag{2.92}$$

We now define the quantity :

$$S(\omega) = \int \mathrm{d}\Delta\tau\, \overline{S(t,t+\Delta\tau)}^{t} e^{i\omega\Delta\tau}\,, \tag{2.93}$$

which corresponds to finite frequency noise accessed in experiments. In this expression, the overline represents an average over the time t and corresponds to the signal acquisition time which is much larger than the characteristic dynamical times of the system (time of flight and decoherence time).
The evaluation of noise (2.93) can be done in any state. Here, for simplicity, we illustrate the relation between two particle coherence and current noise on the example of a source producing a single electron in a wavepacket φ_e. In this case, the different contributions arising in (2.92) will have a clear interpretation.

Illustration with a source of single electron wavepackets

We now analyze the case of a single electronic wavepacket propagating in an edge channel from the point of view of current fluctuations. The manybody state is given by (2.42) and the single particle excess wavefunction is given by (2.45).The different contribution to finite frequency noise (2.93) are :

- A term $\overline{\mathcal{G}^{(e)}(t,t+\Delta\tau)}\delta(\Delta\tau)$, which accounts for the poissonian term in (2.92), and which gives a white noise contribution.
- The second term in (2.92) is the Fourier transform of $\overline{\langle I(t)\rangle\langle I(t+\Delta\tau)\rangle}$. This contribution is accessed through finite frequency noise measurements, and is responsible for the antibunching of electrons. In the case of an electronic wave packet on top of the Fermi sea, its expression is

$$-\int_{-\infty}^{+\infty} \mathrm{d}\Delta\tau\, e^{i\omega\Delta\tau} \left(\int_{-\infty}^{+\infty} \mathrm{d}t\, |\varphi_e(t)|^2 |\varphi_e(t+\Delta\tau)|^2\right)\,. \tag{2.94}$$

- The last two terms account for the interference processes occuring between the supplementary electron and the Fermi sea. Consequently, they have no optical counterpart. Remembering that the Fermi sea coherence function is

$$\mathcal{G}^{(e)}(t,t+\Delta\tau) = \hbar\int_{-\infty}^{+\infty} \mathrm{d}\omega\, \bar{n}_\mu(\omega)\, e^{i\omega\Delta\tau}\,, \tag{2.95}$$

  we have the third and fourth contributions for an electronic wavepacket :

$$-\int_{-\infty}^{+\infty} \mathrm{d}\omega_1\, \bar{n}_\mu(\omega_1)|\varphi_e(\omega_1 + \pm\omega)|^2\,. \tag{2.96}$$

  If the wavepacket φ_e centered at the energy $\frac{\Delta}{2}$ is well separated from the Fermi sea, these last two terms vanish for $|\hbar\omega| \leq \Delta/2$.

The total expected noise in the case of a lorentzian wavepacket is depicted in fig. 2.11. The time dependence of the wavepacket is :

$$\varphi_e(t) = \sqrt{\frac{1}{\tau_0}}\, e^{-2i\hbar t/\Delta} e^{-|t|/\tau_0} \,. \tag{2.97}$$

The two first terms in (2.92) are responsible for the low frequency behaviour of $S(\omega)$. Notably, they combine so that the current fluctuations vanish at zero frequency. On the experimental side, this observation coincides with noise measurements [123, 95, 94] performed for the single electron sources of the LPA at optimal transparency (see chapter 3) : the noise related to the uncertainty on the emission time of the emitted electron (the quantum jitter noise) is responsible for the low frequency behaviour of current correlations.

The last two terms involving the Fermi sea are responsible for the high frequency cutoff : the Fermi sea prevents the emission of photons having an energy greater than the energy of the emitted electron.

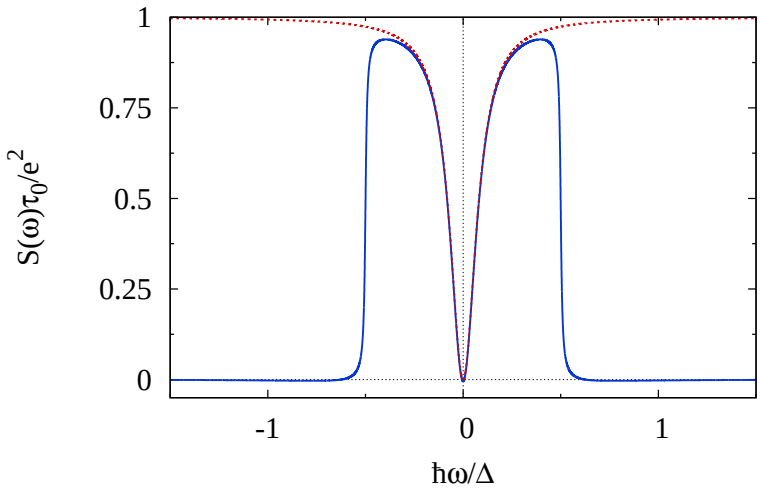

Figure 2.11: Current noise as a function of the measurement frequency at zero temperature, for single electron emission. Here, the current noise is represented in units of the average current transported by a single electron excitations. For a periodic system, it would be proportionnal to the driving frequency. The red dashed curve models the quantum jitter noise, which coincides with the total noise at low frequency.

3 Conclusion

In this chapter, we have presented an approach to quantum coherence of single to few electron and hole excitations in metallic conductors canalogous to quantum optics. This approach is based on electron and hole coherence functions analogous to the ones introduced by Glauber for the electromagnetic field [50, 51]. These coherence functions appear in detection signals and can be related to fluctuation properties of the charge density.
Through simple examples, we have underlined the similitudes and differences between electron quantum optics and the usual photon quantum optics. The first important difference comes from the Pauli principle, which forbids two electrons to be in the same quantum state. It also implies that electron quantum optics does not have a classical Thelimit as the usual quantum optics, and thus there are strictly speaking no coherent states for the electron field $\psi(x)$. The other main difference comes from the nonvanishing coherences in the vacuum : contrary to photon vacuum, the Fermi sea is not empty of particles and contributes to the total electronic coherence. This particular vacuum state also allows the creation of neutral excitations.
In this chapter, we have not considered interaction effects which are responsible for decoherence and relaxation of electronic excitations. This important issue will be studied in details in chapters 4, 5 and 6 of this manuscript.

However, before dealing with interactions, the natural question that arises concerns the measurement of the single electron coherence function. Actually, the detection scheme presented in this chapter only concerns the occupation number, namely the diagonal part of the coherence function in Fourier space. In other words, it performs the spectroscopy of the quantum state.
The complete characterization of the single particle quantum state requires a measurement of the off diagonal part of the coherence function. Reconstructing the ful single electron coherence is called a single electron quantum tomography. This is the subject of the next chapter, in which we propose a tomography protocol based on current noises measurements in an HBT interferometer.

Chapter 3

Single electron tomography

Contents

1 Tomography protocol **40**

1.1 The Hanbury Brown and Twiss effect 40

1.2 Single electron tomography protocol 43

2 Modelling of the SES **48**

2.1 Floquet scattering theory 48

2.2 Single particle coherence from Floquet theory 51

3 Numerical results **53**

3.1 Occupation number and coherence function 53

3.2 Current pulse 59

3.3 Accuracy of the quantum capacitor as a single electron source 59

4 Conclusion **63**

In this chapter, we propose a protocol to measure the first order electronic coherence function. Such a measurement, which aims at reconstructing a quantum state is called a quantum tomography experiment. For this purpose, we propose once again to apply ideas from quantum optics for photons to electrons propagating in quantum Hall edge channels. Although the tomography protocol is analogous to homodyne tomography in quantum optics, differences will arise from the nature of the particles involved.

In a first section, we briefly recall the basics of homodyne tomography which relies on the Hanbury Brown and Twiss effect [12, 13]. We then present a possible realization of homodyne tomography for electrons in quantum Hall edge channels. A second part will be devoted to the study and modelisation of the single electron source built in the Laboratoire Pierre Aigrain in Paris [38]. This part will show that the single electron coherence function can be extracted through current noise measurements. In particular, we will predict the expected experimental signals of a tomography experiment in the case of this single electron source. The feasability of the HBT tomography experiment will be discussed based on these estimations of the expected experimental signals. In this last part, we will also address the question of the quality of the electron emission from the point of view of quantum coherence and statistics of the emitted charge.

1 Tomography protocol

In full generality, tomography designates an imaging technique based on sectionning. By sending waves on the object of interest, one can obtain images of different sections of the object, which are combined to recover the total picture by the mean of tomographic reconstruction. Tomography protocols are of common use in various fields such as geological and medical sciences for example [110].
Quantum state tomography is the process by which a quantum state is reconstructed using measurements on an ensemble of quantum states described by a given density operator [93]. Because of the no cloning theorem[158], quantum tomography requires many copies of the state to be reconstructed. It after involves the measurement of a set of observables. The outputs of these measurements are compared to several test density operators and density matrix that reaches the best agreement is claimed to describe the unknown quantum state [20]. Quantum tomography protocols have been implemented succesfully for one or two qubits[113] or for example in cavity quantum electrodynamics with Rydberd atoms [32] or with superconducting circuits [70, 66].
The goal of this section is to show how the ideas about quantum state tomography that have been developped in atomic physics can be adapted in a tomography protocol for electronic excitations in quantum Hall edge channels. This protocol makes use of the HBT effect so we will first introduce it, and present its experimental aspects in the context of quantum optics. Then, we will describe the tomography protocol for single electron sources [56].

1.1 The Hanbury Brown and Twiss effect

In 1956, R. Hanbury Brown and R.Q. Twiss designed a new kind of interferometer based on intensity interferometry [12, 13]. In this seminal experiment, they made use of the correlations between two photodetection signals to extract the apparent angular diameter of Sirius [65]. More than the final result, this new type of interferometry, which is known as intensity interferometry, inspired a lot of experiments to probe the second order coherence of the electromagnetic field[78, 106]. For the rest of the discussion, we will focus on the quantum aspects of the Hanbury Brown Twiss effect.

HBT effect and homodyne tomography in optics

A typical HBT protocol is depicted in fig. 3.1.

Such a protocol measures the second order function $\mathbf{g_2}(\Delta\tau)$ described in the previous chapter, in 1. The number of photocounts is proportional to the field intensity [43]:

$$N = \frac{\eta T}{\hbar\omega}\,, \tag{3.1}$$

where η is the quantum efficiency of the detector, and $\hbar\omega$ the energy of the measured mode of the electromagnetic field. Thus, the second order photon coherence function can be rewritten in terms of photocounts in detectors D_i at different times :

$$\mathbf{g_2}(\Delta\tau) = \frac{\langle N_1(t)N_2(t+\Delta\tau)\rangle}{\langle N_1(t)\rangle\langle N_2(t+\Delta\tau)\rangle}\,. \tag{3.2}$$

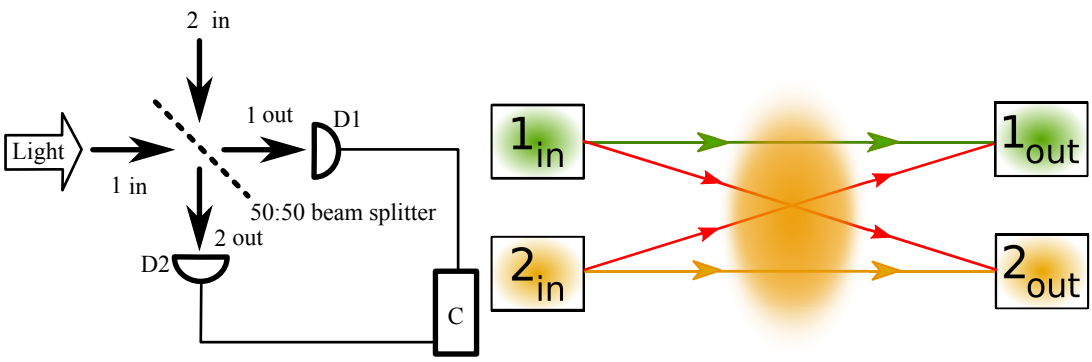

(a) Sketch of a HBT interferometer (b) Interference paths

Figure 3.1: (a) Sketch of a HBT type interferometer. The detectors D1 and D2 absorb photons from the output (w.r.t. the beam splitter) electric fields $E_{i,out}$. The counter C measures the correlation between photodetection events. (b) Direct (orange and green) and exchange (red) paths in a HBT interferometer.

In quantum optics, HBT-like setups can be used to measure the quantum state of a mode of the electromagnetic field. Such a measurement implements a homodyne detection technique, and is thus called a homodyne tomography experiment. In these experiments, the mode of the electromagnetic field that one wants to measure (denoted by a) are sent onto a beam splitter together with a local oscillator (the b mode), typically a laser. The modes on output are linear combinations of the input ones. For a $50:50$ beamsplitter :

$$a^{(out)} = \frac{1}{\sqrt{2}}(a+b) \tag{3.3}$$

$$b^{(out)} = \frac{1}{\sqrt{2}}(b-a) \ . \tag{3.4}$$

Thus, the outcoming photon number in output branches 1 and 2 are

$$N_1^{(out)} = \frac{1}{2}\left(a^\dagger a + b^\dagger b + a^\dagger b + b^\dagger a\right) \tag{3.5}$$

$$N_2^{(out)} = \frac{1}{2}\left(a^\dagger a + b^\dagger b - a^\dagger b - b^\dagger a\right) \tag{3.6}$$

By chosing the state of the local oscillator to be coherent $|z\rangle$, $z = re^{i\phi}$, one can show that

$$N_1^{(out)} - N_2^{(out)} = r\sqrt{2}\left(q\cos\phi + p\sin\phi\right) \ , \tag{3.7}$$

where p and q are the position and impulsion of the oscillator describing the electromagnetic field. Thus, by measuring $N_1^{(out)} - N_2^{(out)}$ for a ensemble of identical systems, one can recover the probability distribution of $q_\phi = q\cos\phi + p\sin\phi$. Finally, varying the phase ϕ of the local oscillator gives the complete probability distribution function, and then the Wigner function of the electromagnetic field mode via a Radon transform [93, 5]. Then, accessing the Wigner function is sufficient to recover the density matrix of the electromagnetic field mode.

Before presenting an homodyne detection quantum tomography protocol for electrons propagating in quantum Hall edge channels, let us discuss in more details the Hanbury Brown and Twiss effect.

The HBT effect in quantum Hall edge channels

From a general point of view, the HBT effect arises from two particle interferences between direct and exchange paths sketched in fig. 3.1 b. These interferences lead to bunching for indistinguishible bosons and antibunching for indistinguishible fermions, as expected from their quantum statistics. Consequently, when indistinguishible particles particles from two independent sources collide on a beamsplitter, the outcoming particle current fluctuations and correlations bear information on the single particle content of the two incoming beams. In mesoscopic physics, the HBT effect has already been observed for electrons in a two dimensional electron gas issued by two reservoirs at equilibrium [90, 68, 119]. Here, we discuss the HBT effect for single electron sources.

In fig. 3.3, the quantum point contact acts as a beamsplitter for electrons, which means that the fermion fields on incoming and outcoming sides of the constriction are related in the following way :

$$\begin{pmatrix} \psi_1(t) \\ \psi_2(t) \end{pmatrix}_{\text{out}} = \begin{pmatrix} \sqrt{\mathcal{R}} & i\sqrt{\mathcal{T}} \\ i\sqrt{\mathcal{T}} & \sqrt{\mathcal{R}} \end{pmatrix} \cdot \begin{pmatrix} \psi_1(t) \\ \psi_2(t) \end{pmatrix}_{\text{in}} \tag{3.8}$$

where the "in" (resp "out") fields are taken right before (resp. right after) the QPC. The probability for an electron to be transmitted in the same (resp. the other) channel is $\mathcal{R}$ (resp. $\mathcal{T}$).
The experimentally relevant quantities are current correlations on the outcoming channels of the interferometer :

$$S^{(out)}_{\alpha,\beta}(t,t') = \langle i^{(out)}_\alpha(t)\, i^{(out)}_\beta(t')\rangle - \langle i^{(out)}_\alpha(t)\rangle\langle i^{(out)}_\beta(t')\rangle \tag{3.9}$$

where $i_\alpha(t)$ denotes the edge current operator propagating along the α ouput channel. This current operator is $i_\alpha(t) = -ev_\alpha : (\psi^\dagger_\alpha\psi_\alpha)(t) :$ where the normal ordering is taken with respect to the Fermi sea corresponding to the chemical potential of the edge channel at the position of the detector.
The goal is to extract information on the source by measuring the outcoming noises of the interferometer. For this purpose, we express the outcoming currents in terms of the incoming fields :

$$i^{\text{out}}_1(t) = \mathcal{R}\, i_1(t) + \mathcal{T}\, i_2(t) - iev_F\sqrt{\mathcal{RT}}(\psi^\dagger_1\psi_2 - \psi^\dagger_2\psi_1)(t) \tag{3.10}$$

$$i^{\text{out}}_2(t) = \mathcal{T}\, i_1(t) + \mathcal{R}\, i_2(t) + iev_F\sqrt{\mathcal{RT}}(\psi^\dagger_1\psi_2 - \psi^\dagger_2\psi_1)(t) \tag{3.11}$$

where "in" superscripts have been removed in the r.h.s for simplicity. These outcoming current correlators can be written as :

$$S^{\text{out}}_{11}(t,t') = \mathcal{R}^2 S_{11}(t,t') + \mathcal{T}^2 S_{22}(t,t') + \mathcal{RT}\, Q(t,t') \tag{3.12}$$

$$S^{\text{out}}_{22}(t,t') = \mathcal{T}^2 S_{11}(\omega) + \mathcal{R}^2 S_{22}(t,t') + \mathcal{RT}\, Q(t,t') \tag{3.13}$$

$$S^{\text{out}}_{12}(t,t') = S^{\text{out}}_{21}(t',t) = \mathcal{RT}\left(S_{11}(t,t') + S_{22}(t,t') - \mathcal{Q}(t,t')\right) \tag{3.14}$$

where $Q(t,t')$ is defined as

$$\mathcal{Q}(t,t') = (ev_F)^2\left(\mathcal{G}^{(e)}_1(t',t)\mathcal{G}^{(h)}_2(t',t) + \mathcal{G}^{(e)}_2(t',t)\mathcal{G}^{(h)}_1(t',t)\right) . \tag{3.15}$$

The $\mathcal{R}^2$ and $\mathcal{T}^2$ contributions in (3.12) to (3.14) correspond to the scattering of electron/hole pairs from one incoming channel into the another one as a whole. They correspond to classical partitioning of noise.
The terms proportional to $\mathcal{RT}\ \mathcal{Q}(t,t')$ probe the single electron and hole coherences at different times within the incoming channels. For classical particles partitionned by the beam splitter, these terms would be absent. Indeed these are the two particle interference contributions to the output noise of the HBT interferometer.

The next paragraph will show that these HBT correlations can give information on the single particle coherence and thus how can the latter be reconstructed.

1.2 Single electron tomography protocol

By analogy with traditional quantum optics, the driven ohmic contact on channel 2 in fig. 3.3 will be used as a local oscillator since its chemical potential μ_2 can be varied to explore the single particle space.
Contrary to quantum optics, it is not possible to access time resolved quantities in electronic transport experiments. Thus, our protocol will rely on the zero frequency Fourier component of the average over $\bar{t}$ of current correlations :

$$S_{\alpha\beta} = 2\int \overline{S^{\text{out}}_{\alpha,\beta}(\bar{t}+\tau/2,\bar{t}-\tau/2)}^{\bar{t}}\,\mathrm{d}\tau. \tag{3.16}$$

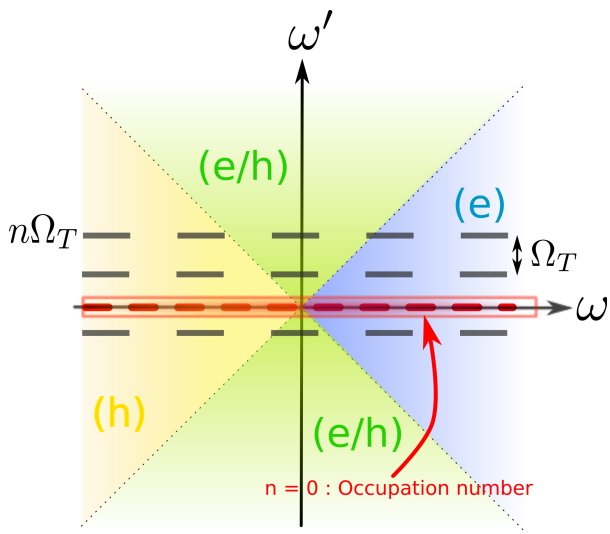

Figure 3.2: Sketch of the coherence function in Fourier space. The frequencies ω and ω' are respectively associated to $t-t'$ and $\bar{t}=\frac{t+t'}{2}$. The harmonics are parallel to the horizontal axis. The $n=0$ harmonic corresponds to the excess occupation number δn introduced by the source. The different quadrants are identical to those in 2.5 in chapter 2.

We would like to measure the excess coherence introduced by a periodic AC source of period $T=\frac{2\pi}{\Omega_T}$ at a given position. This quantity $\Delta\mathcal{G}^{(e)}$ depends on two times t and t' and thus can be viewed as a function of the time average $\bar{t}=\frac{t+t'}{2}$ and difference $t-t'$. In Fourier space, itdepends on two frequencies ω and ω', the first being the conjugate variable to $t-t'$, and the

other being conjugate to $\bar{t}$. The periodicity with respect to $\bar{t}$ implies that the coherence function will be nonzero for values of ω' that are multiples of Ω_T, as suggested in fig. 3.2.

The aim of the forthcoming electronic quantum tomography protocol is thus to measure the ω dependence of each harmonic of the coherence function ($\omega' = n\Omega_T$).

Coherence function and noise signals

The electronic quantum tomography experimental setup is depicted in fig. 3.3 . Here, the quantum point contact plays the role of a beamsplitter for electrons. We measure the low frequency current correlations S_{11}^{out} and S_{22}^{out} defined by eqs. (3.12) and (3.13).

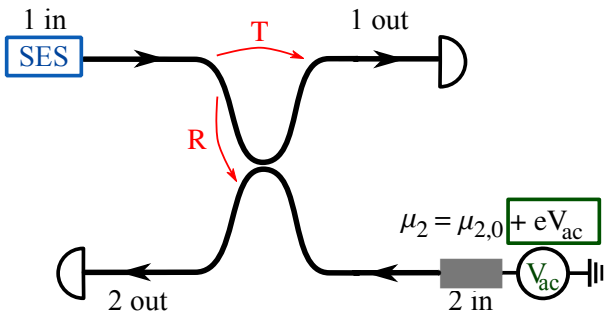

Figure 3.3: The tomography experimental setup for periodic single electron sources. The incoming channel 1 is populated with the output state of the single electron source. The incoming channel 2 is populated with a driven ohmic contact. Current correlations are measured on the outputs of the interferometer. The transparency of the quantum point contact is denoted by $\mathcal{T}$.

The ohmic contact plays here the role of the local oscillator. By changing the frequency of the AC voltage by multiples of the driving frequency, one can access the various harmonics of $\Delta\mathcal{G}^{(e)}$. From a graphical point of view, the homodyning is equivalent to an exploration in the vertical direction in fig. 3.2.
By changing the stationnary part $\mu_{2,0}$ of the chemical potential, one can explore the single particle space, and thus reconstruct the frequency dependence of each harmonic of the coherence function. Changing $\mu_{2,0}$ corresponds to an horizontal displacement in fig. 3.2 .

In the next section, we will see more precisely how these general considerations can be expressed to exprimental noise signals, and what are the quantities that are precisely related to the harmonics of the coherence function.

Single particle coherence function from noise measurements

Summing (3.12) to (3.14) leads to:

$$\sum_{\alpha,\beta} S^{\text{out}}_{\alpha,\beta}(t,t') = S_{11}(t,t') + S_{22}(t,t')\,, \tag{3.17}$$

reflecting particle number conservation. Another relation :

$$\mathcal{Q}(t,t') = (S^{\text{out}}_{11} + S^{\text{out}}_{22})(t,t') - \frac{1-2\mathcal{RT}}{2\mathcal{RT}}(S^{\text{out}}_{12} + S^{\text{out}}_{21})(t,t'), \tag{3.18}$$

shows that the HBT quantum contribution can be extracted from outcoming current noises and correlations measurements.

We now go into the details of the tomography protocol. As stated in the previous chapter, the first order coherences can be split into two parts, the first one $\mathcal{G}_{\mu}^{(e)}$ corresponding to the Fermi sea and the second one, noted $\Delta\mathcal{G}^{(e)}$, representing the excess coherence due to excitations on top of this vacuum state. Here, the contribution that we want to reconstruct is the excess contribution due to the presence of the single electron source in the first incoming channel : $\Delta\mathcal{G}_1^{(e)}$.

The electron and hole coherence functions for the single electron source (denoted 1) and the driven ohmic contact (denoted 2) split into:

$$\mathcal{G}_{1,2}^{(e/h)}(t,t') = \mathcal{G}_{\mu_{1,2}}^{(e/h)}(t-t') + \Delta\mathcal{G}_{1,2}^{(e/h)}(t,t'). \tag{3.19}$$

The excess coherence for the driven ohmic contact $\Delta\mathcal{G}_2^{(e)}$ is due to the AC driving. We now have an expression for $\mathcal{Q}$ in terms of Fermi sea coherence functions and excess contributions :

$$\begin{aligned}\mathcal{Q}(t,t') = {} & \mathcal{G}_{\mu_1}^{(e)}(t',t)\mathcal{G}_2^{(h)}(t',t) + \mathcal{G}_{\mu_1}^{(h)}(t',t)\mathcal{G}_2^{(e)}(t',t) \\ & + \mathcal{G}_{\mu_2}^{(h)}(t',t)\Delta\mathcal{G}_1^{(e)}(t',t) + \Delta\mathcal{G}_1^{(h)}(t',t)\Delta\mathcal{G}_2^{(e)}(t',t).\end{aligned} \tag{3.20}$$

The terms containing $\Delta\mathcal{G}_1^{(e)}$ are isolated in an excess contribution to noise $\Delta\mathcal{Q}$:

$$\Delta\mathcal{Q}(t,t') = \mathcal{G}_2^{(h)}(t',t)\Delta\mathcal{G}_1^{(e)}(t',t) + \mathcal{G}_2^{(e)}(t',t)\Delta\mathcal{G}_1^{(h)}(t',t). \tag{3.21}$$

In eq. (3.20), the terms involving the Fermi sea coherence $\mathcal{G}_{\mu_1}$ describe two different physical effects. First, the expressions of the form $\mathcal{G}_{\mu_1}\mathcal{G}_{\mu_2}$ contribute to the stationnary excess noise [10] which is due to the difference in the chemical potentials $\mu_2 - \mu_1$. The terms containing $\mathcal{G}_{\mu_1}\Delta\mathcal{G}_2$ are present only when the ohmic contact is driven and describe the photoassisted noise [10].
An evaluation of their orders of magnitude shows that the excess noise terms go like (μ_1 is assumed to be zero here) $\frac{e^2\mu_2}{h}$. The photoassisted noise is of the order of $\frac{e^2\mu_2}{h}\frac{eV_0}{\hbar\omega_d}$, where V_0 and ω_d are respectively the amplitude and frequency of the AC drive.
In the same way (3.21) contains contributions associated with $\mathcal{G}_{\mu_2}^{(e/h)}$ and a contribution associated with $\Delta\mathcal{G}_{\mu_2}^{(e/h)}$. A similar evaluation gives: $\mathcal{G}_{\mu_2}\Delta\mathcal{G}_1 \propto \frac{e^2\Omega_T}{2\pi}$ and $\Delta\mathcal{G}_2\Delta\mathcal{G}_1 \propto \frac{e^2\Omega_T}{2\pi}\frac{eV_0}{\hbar\omega_d}$. In these evaluations, the contribution of the source to the noise is taken to be at its maximal value $e^2 f$ [123].
For realistic experimental values (For example $\mu_2 \simeq 50\,\mu$eV, $V_0 \simeq \mu eV$ and $f = \frac{1}{T} = 3\,$GHz), we have :

- Excess noise contribution $\mathcal{G}_{\mu_1}\mathcal{G}_{\mu_2} \propto \frac{e^2\mu_2}{h} \simeq 10^{-26}\mathrm{A}^2/\mathrm{Hz}$
- Photoassisted noise $\mathcal{G}_{\mu_1}\Delta\mathcal{G}_2 \propto \frac{e^2\mu_2}{h}\frac{eV_0}{\hbar\omega_d} \simeq 10^{-27}\mathrm{A}^2/\mathrm{Hz}$
- $\mathcal{G}_{\mu_2}\Delta\mathcal{G}_1 \propto \frac{e^2\Omega_T}{2\pi} \simeq 10^{-28}\mathrm{A}^2/\mathrm{Hz}$
- $\Delta\mathcal{G}_2\Delta\mathcal{G}_1 \propto \frac{e^2\Omega_T}{2\pi}\frac{eV_0}{\hbar\omega_d} \simeq 10^{-29}\mathrm{A}^2/\mathrm{Hz}$.

- Thermal noise at zero frequency $S_{th} \propto 2e^2 \frac{k_B T}{h} \simeq 10^{-30}\mathrm{A}^2/\mathrm{Hz}$ for $T = 50\,mK$.

The expected noises corresponding to the single electron source's coherence function are above the levels of sensibilities that have already been reported with the single electron source under examination or more generally with quantum pumps [97, 96, 49]. Recovering the source's noise requires the implementation of high sensitivity noise measurements and powerful amplification techniques.The source's contribution will be extracted from the difference of noise measurements performed in the presence and absence of the source.

The expression of the noise signals in terms of the harmonics of the coherence function is detailed in the next section. The obtained expressions will be suitable for a numerical evaluation of these signals in the last part of this chapter.

Extraction of the single electron coherence

The tomography protocol aims at reconstructing the harmonics $\Delta\mathcal{G}_n$ of the excess single particle coherence function which are defined by:

$$\Delta\mathcal{G}_1^{(e)}(t,t') = \sum_{n=-\infty}^{+\infty} e^{-2\pi i n \bar{t}/T} \int \Delta\mathcal{G}_{1,n}^{(e)}(\omega) e^{-i\omega\tau} \frac{d\omega}{2\pi}\,. \tag{3.22}$$

The harmonics of $\Delta\mathcal{Q}$ are defined by:

$$\Delta\mathcal{Q}(t,t') = \sum_{n\in\mathbb{Z}} e^{-in\Omega_T(t+t')/2} \int e^{i\Omega(t-t')} \Delta Q_n(\Omega) \frac{d\Omega}{2\pi}\,. \tag{3.23}$$

In the next two paragraphs, we will show precisely how to extract the harmonics of the coherence function from the measurements of the harmonics of $\Delta\mathcal{Q}$. We will first show how to obtain the occupation number, and then how the higher order harmonics can be extracted from an homodyne detection scheme.

Obtention of the excess occupation number

When the AC voltage on the ohmic contact is switched off, the ohmic contact's coherence function does not depend on $\bar{t}$. Thus,in this case, averaging eq. (3.23) over $\bar{t}$ leads to:

$$\overline{\Delta\mathcal{Q}(t,t')}^{\bar{t}} = \Delta\mathcal{Q}_0(t-t') = \Delta\mathcal{G}_{1,0}^{(e)}(t'-t)\mathcal{G}_{\mu_2}(t'-t) + \Delta\mathcal{G}_{1,0}^{(h)}(t'-t)\mathcal{G}_{\mu_2}(t'-t). \tag{3.24}$$

The Fourier transform of this expression is :

$$\Delta\mathcal{Q}_0(\Omega) = e^2 v_F \int \left((1 - n_{\mu_2}(-\omega))\, \Delta\mathcal{G}_{1,0}^{(e)}(\Omega-\omega) - n_{\mu_2}(\omega)\, \Delta\mathcal{G}_{1,0}^{(e)}(\omega-\Omega) \right) \frac{\mathrm{d}\omega}{2\pi}\,. \tag{3.25}$$

Taking the derivative w.r.t. μ_2 [1] leads to the relation between the $n=0$ harmonic of the noise at zero frequency and the excess occupation number $\delta\bar{n}_1$:

[1] Recall that $\frac{d}{dx}\frac{1}{e^x+1} = \frac{1}{4\mathrm{ch}^2(x/2)}$

$$-\frac{R_K}{2}\left(\frac{\partial\Delta\mathcal{Q}_0(\Omega=0)}{\partial\mu_2}\right)_{\mu_2=\hbar\omega_2}=\int_{-\infty}^{+\infty}\delta\bar{n}_1(\omega_2+k_BT_{\text{el}}x/\hbar)\,\frac{dx}{4\cosh^2(x/2)}\,. \tag{3.26}$$

At zero temperature, this equation reduces to:

$$\frac{\partial\Delta\mathcal{Q}_0(\Omega=0)}{\partial\mu_2}=-\frac{2}{R_K}\delta\bar{n}_1(\omega_2)\,,\hbar\omega_2=\mu_2. \tag{3.27}$$

Thus, the remaining integral over x in eq. (3.26) accounts for the thermal smearing in the measurement process. An equivalent result for this spectroscopy of the single electron source has been derived in [108]. In the numerical evaluations presented in the last section of this chapter, this thermal smearing has been taken into account. The thermal effects deteriorate the resolution on noise measurements, and thus the resolution on the single particle coherence. Thus, the electronic temperature must be as low as possible.

Higher order of the single particle coherence : homodyne detection

To access the higher order harmonics of the single particle coherence function, a homodyning method is needed. This means that the ohmic contact in the output way 2 of the HBT interferometer is driven by a small[2] AC voltage $V_{ac}(t)=V_0\cos(\omega_d t+\phi)$ at the frequency corresponding to the one of the harmonic to be measured : recovering the n-th harmonic of the coherence function needs an homodyning at a frequency $\frac{n\Omega_T}{2\pi}$. Looking at the linear response to V_0 :

$$\chi_{\omega_d}(t,t')=\frac{\partial\Delta Q(t,t')}{\partial(eV_0/\hbar\omega_d)}|_{V_0=0}. \tag{3.28}$$

leads to the extraction of the harmonic of the source's coherence function at $n\Omega_T$.

Technical details of the reasoning are given in appendix A. By considering the average over $\bar{t}$ of the response function at the appropriate frequency :

$$\chi_N(t-t')\equiv\overline{\chi_{\omega_d=n\Omega_T}(t,t')}^{\bar{t}}\,, \tag{3.29}$$

we get the final expression relating the linear harmonic response to the harmonics of the coherence function :

$$\left(\frac{\partial\chi_n}{\partial\mu_2}\right)(\Omega,T_{el},\mu_2,\phi)=\int_{-\infty}^{+\infty}\left(\frac{\partial\chi_N^{(0)}}{\partial\mu_2}\right)(\Omega,\mu_2+xk_BT_{el},\phi)\,\frac{dx}{4\cosh^2(x/2)}\,,\text{where} \tag{3.30}$$

$$\left(\frac{\partial\chi_n^{(0)}}{\partial\mu_2}\right)(\Omega,\mu_2,\phi)=\frac{e^2}{h}\Re\left[e^{i\phi}\left(v_F\Delta\mathcal{G}_{1,N}^{(e)}(\frac{\mu_2}{\hbar}+\frac{N\Omega_T}{2})-v_F\Delta\mathcal{G}_{1,N}^{(e)}(\frac{\mu_2}{\hbar}-\frac{N\Omega_T}{2})\right)\right]. \tag{3.31}$$

[2]The amplitude V_0 must be small compared to μ_2/e to remain in the linear response regime.

This equation plays the same role for $n \neq 0$ harmonics than eq.(3.26) for the occupation number. These two equations constitute the main results of this chapter. They make explicit the relation between the single particle coherence function characterizing the source and experimental signals. The inversion of these relations leads to the reconstruction of the single electron coherence in the frequency plane : this inversion constitutes the single electron tomography protocol.
To recover the source's coherence from noise measurements, one can proceed in two steps :

(i) First, a derivative of the experimental with respect to μ_2 must be taken.

(ii) Then, starting from a region where $\Delta\mathcal{G}_n^{(e)}(\omega)$ is expected to vanish, and then proceed by steps of $2\pi nf$ using (3.31) to get $\Delta\mathcal{G}^{(e)}(\omega + 2\pi nf)$ for positive p.

To limit the total reconstruction time, an optimization strategy must be devised to choose the measurement points (i.e. the values of μ_2) so that regions where the coherence is expected to vary most are covered with maximal resolution. To identify this regions of maximal variation, we will then make predictions for the expected experimental signals. Thus, in the next section, we will present a model for the single electron source. This model will be used in section 3 to make predictions for the single particle coherence and the associated signals.

2 Modelling of the SES

To model the functioning of the mesoscopic capacitor operated as a single electron source, former predictions based on noninteracting models for the average current [37] and current noise [94, 123] have been verified experimentally. So far, this suggests that a noninteracting scattering theory can be used to describe the mesoscopic capacitor in the experimentally relevant range of parameters. The suitable formalism is the Floquet scattering formalism for electrons [107, 109, 41].
In this section, we will present the basics of Floquet scattering theory and derive the expression of the Floquet scattering matrix in the case of the mesoscopic capacitor. Then, the single particle coherence will be expressed in terms of Floquet scattering matrix elements.

2.1 Floquet scattering theory

Generalities

For a periodically driven quantum system, Floquet theorem states that there exists a basis of the space of single particle states $|\varphi_\alpha(t)\rangle$, called Floquet states, that are T-periodic solutions of the time dependent Schrödinger equation :

$$|\varphi_\alpha(t+T)\rangle = e^{-i\omega_\alpha T}\,|\varphi_\alpha(t)\rangle\,. \tag{3.32}$$

Consequently, they can be expanded as a Fourier series:

$$|\varphi_\alpha(t)\rangle = e^{-i\omega_\alpha t}\sum_{n\in\mathbb{Z}} e^{-in\Omega_T t}|\varphi_{\alpha,n}\rangle\,. \tag{3.33}$$

Therefore, the Floquet state $|\varphi_\alpha(t)\rangle$ is a linear combination of states with eigenfrequencies $\omega_\alpha + n\Omega_T$. Considering that the time dependent potential is applied within a limited region of the system, Floquet theorem enables us to find the scattering matrix relating outcoming electronic modes to the incoming ones under the form :

$$c_\alpha^{(\mathrm{out})}(\omega) = \sum_{n\in\mathbb{Z}} \sum_{\beta} S_{\alpha,\beta,n}(\omega)\, c_\beta^{(\mathrm{in})}(\omega + n\Omega_T). \tag{3.34}$$

Eq. (3.34) simply states that an output mode at a given frequency ω is a linear combination of those at frequencies $\omega + n\Omega_T$. The coefficients of this linear combination are the elements of the Floquet scattering matrix. In other words, the photoassisted transitions induced by the periodic driving occur only at multiples of the pumping frequency, with transition amplitudes given by the Floquet scattering matrix elements.

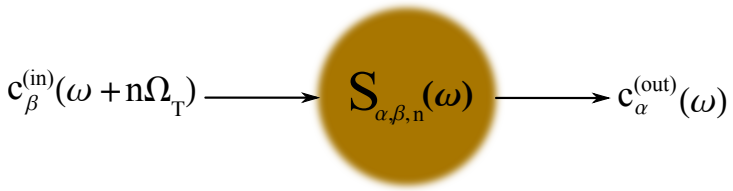

Figure 3.4: Sketch of the action of the Floquet scattering matrix. An electronic mode at energy $\hbar\omega$ in channel α on output of the scattering region is a linear combination of incoming modes from all the incoming channels β at energies $\hbar(\omega + n\Omega_T)$.

Since the outcoming modes satisfy the same (anti)commutation relations as the incoming ones, the Floquet scattering matrix must satisfy the unitarity relation:

$$\sum_{n\in\mathbb{Z}} \sum_{\beta} S_{\alpha,\beta,n}(\omega)\, S_{\alpha',\beta,n}(\omega')^* = \delta_{\alpha,\alpha'}\, \delta(\omega - \omega')\,. \tag{3.35}$$

We now compute the Floquet scattering matrix in the case of the single electron source, following the ideas developed in [94, 123].

Floquet scattering matrix for the SES

In the case of the single electron source under consideration, indexes concerning edge channels in the equation (3.34) can be forgotten and equation (3.34) reduces to:

$$c_\omega^{(out)} = \sum_{n\in\mathbb{Z}} S_n(\omega) c_{\omega+n\Omega_T}^{(in)}. \tag{3.36}$$

For the mesoscopic capacitor, the Floquet scattering originates from the presence of a quantum dot driven by a T-periodic voltage V.

Usually, one already knows the scattering matrix $S_{\mathrm{dot}}(\omega)$ of the mesoscopic capacitor in the absence of interactions and external voltage. It is defined by:

$$\varphi^{(\mathrm{out})}(\omega) = S_{\mathrm{dot}}(\omega)\, \varphi^{(\mathrm{in})}(\omega) \tag{3.37}$$

so that $S_{\rm dot}(\omega)$ represents the amplitude for an electron to go through the mesoscopic capacitor.

We will now derive the Floquet scattering matrix in the presence of a time dependent voltage $V(t)$ applied to the mesoscopic capacitor. The idea is to use gauge invariance which states the physical equivalence of two situations (see fig. 3.5):

(a) The edge channel is connected to reservoirs at fixed chemical potential whereas a time dependent voltage $V(t)$ is applied to the dot.

(b) A global potential $-V(t)$ is applied to the system so that no voltage is applied to the dot but the reservoirs are driven by a voltage $-V(t)$.

Note that in our case $V(t)$ has zero average over its period. Therefore, in situation (b), the reservoirs chemical potentials are the same as in situation (a). Here, the effect of a non zero potential applied to the dot is assumed to be equivalent to a shift of the energy levels within the mesoscopic capacitor and therefore can be accounted for by a suitable frequency shift in the undriven scattering matrix $S_{\rm dot}$ for the capacitor.

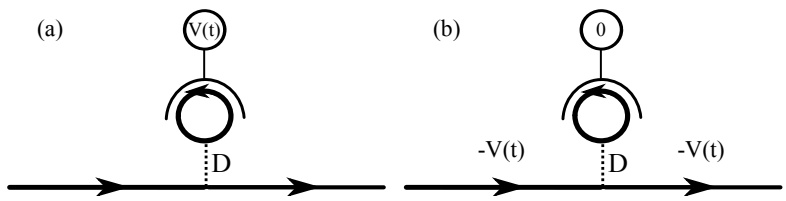

Figure 3.5: Schematic representaion of the driven mesoscopic capacitor. The edge channel is coupled to the quantum dot via a tunnel barrier of transparency D. The two depicted situations (a) and (b) are physically equivalent due to gauge invariance.

The undriven scattering matrix $S_{\rm dot}$ relates the outcoming wavefunction right after the mesoscopic capacitor to the wavefunction right before. In situation (b), the wavefunction injected by the reservoir at $x = -\infty$ (denoted by $\varphi^{(\rm in)}(t)$) leads to the following time dependence of the wavefunction at the entrance of the mesoscopic capacitor :

$$\varphi_{0^-}(t) = \exp\left(\frac{-ie}{\hbar}\int_{-\infty}^{t} V(\tau)\,d\tau\right)\varphi^{(\rm in)}(t)\,. \tag{3.38}$$

Consequently, the wavefunction arriving at the $x = +\infty$ reservoir is:

$$\varphi^{(\rm out)}(t) = \int \exp\left(\frac{ie}{\hbar}\int_{t'}^{t} V(\tau)\,d\tau\right) S_{\rm dot}(t-t')\,\varphi^{(\rm in)}(t')\,dt'\,, \tag{3.39}$$

which directly leads to the Floquet scattering in real time:

$$S(t,t') = S_{\rm dot}(t-t')\,\exp\left(\frac{ie}{\hbar}\int_{t'}^{t} V(\tau)\,d\tau\right). \tag{3.40}$$

Going to Fourier space gives the following expression for the Floquet scattering matrix:

$$S_n(\omega) = \sum_{k\in\mathbb{Z}} c_k[V]\,c_{k+n}[V]^* S_{\rm dot}(\omega - k\Omega_T)\,. \tag{3.41}$$

where $c_n[V]$ denotes the n-th Fourier coefficient of the T-periodic phase factor [3]:

$$\exp\left(\frac{ie}{\hbar}\int_{-\infty}^{t} V(\tau)\,d\tau\right) = \sum_{n\in\mathbb{Z}} c_n[V]\,e^{-in\Omega_T t}\,. \tag{3.42}$$

To achieve a complete description of the driven mesoscopic capacitor in terms of Floquet scattering, we must now compute the zero-drive scattering matrix S_{dot}. To do so, one can use two different models for the quantum dot :

- A first model in which the dot is described as a single resonant level. This model has been used by Keeling *et al.* in [77].
- The second one takes into account the transit time of an electron within the quantum dot, and leads to a Fabry-Perot geometry.

For the rest of the discussion, and notably for numerical evaluations, we will use the second model which is parametrized by the mean level spacing Δ and transparency D of the tunnel barrier between the edge channel and the quantum dot.
In the time domain, the Fabry-Perot scattering matrix represents the probability amplitude to arrive at a time t' at the quantum dot and to escape it after an arbitrary number of turns. Thus, the total probability amplitude is simply a sum over the number of turns (which represents the time an electron spends in the dot) :

$$S_{\text{dot}}(t,t') = \sqrt{D}\,\delta(t-t') - 1 - D\sum_{n=1}^{+\infty} D^{n/2}\,\delta(t-t'-nl/v_F). \tag{3.43}$$

In frequency space, we obtain :

$$S_{\text{dot}}(\omega) = \sqrt{D} - (1-D)\sum_{n=1}^{+\infty} D^{n/2}\,e^{-inl\omega/v_F} = \frac{\sqrt{D} - e^{i\omega l/v_F}}{1-\sqrt{D}\,e^{i\omega l/v_F}}\,. \tag{3.44}$$

The time independent density of states of the quantum dot can be found using the zero-drive scattering matrix S_{dot} [19, 45, 37, 44] :

$$\mathcal{N}(\epsilon=\hbar\omega) = \frac{1}{2i\pi\hbar}S^*_{dot}(\omega)\frac{dS_{\text{dot}}}{d\omega} = \frac{1}{\Delta}\frac{D}{2-D-2\sqrt{1-D}\,\cos(2\pi\epsilon\Delta)}, \tag{3.45}$$

where $\Delta = \hbar v_F/l$. When the tunnel barrier is completely opened, the density of states is flat and equal to $\frac{1}{\Delta}$. As the transparency D goes to zero, it is a sum of well separated lorentzian peaks, as can be seen in fig. 3.6. In this last situation, the two models to describe the dot are expected to give the same results.

2.2 Single particle coherence from Floquet theory

The single particle electronic coherence on output of the driven quantum dot is :

$$\mathcal{G}^{(e)}(t,t') = \langle\psi^\dagger_{out}(t')\psi_{out}(t)\rangle. \tag{3.46}$$

[3] We recall that $\int_t^{t+T} V(\tau)\mathrm{d}\tau = 0$.

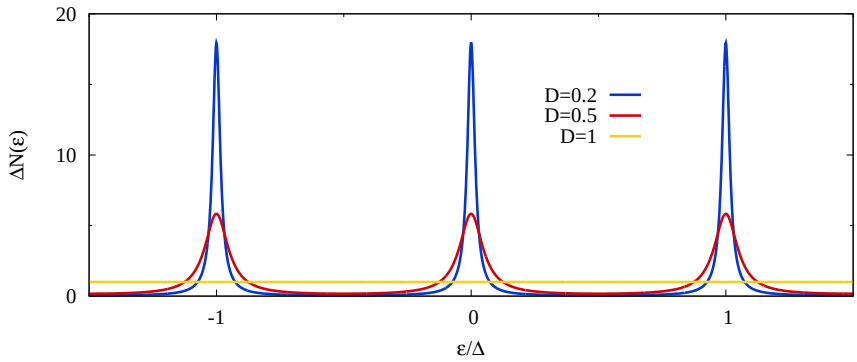

Figure 3.6: Density of states of the quantum dot as a function of ϵ/Δ (in units of Δ), for different values of the transparency D of the tunnel barrier.

The fermionic operators on output of the scattering region are related to the input operators via the Floquet scattering matrix (3.36) :

$$\psi_{out}(t) = \sum_{n\in\mathbb{Z}} \int_{\mathbb{R}} \frac{\mathrm{d}\omega}{\sqrt{2\pi v_F}} e^{-i(\omega-n\Omega_T)t} S_n(\omega - n\Omega_T) c_\omega^{(out)} \tag{3.47}$$

$$\psi_{out}^\dagger(t) = \sum_{n\in\mathbb{Z}} \int_{\mathbb{R}} \frac{\mathrm{d}\omega}{\sqrt{2\pi v_F}} e^{i(\omega-n\Omega_T)t} S_n^*(\omega - n\Omega_T) c_\omega^{(out)\dagger}. \tag{3.48}$$

The source is periodic. Consequently, the coherence function is periodic in $\bar{t} = \frac{t+t'}{2}$. Formally, this means that it can be written as a Fourier sum with respect to $\bar{t}$:

$$\mathcal{G}^{(e)}(t,t') = \mathcal{G}_\mu^{(e)}(t-t') + \sum_{n\in\mathbb{Z}} \Delta\mathcal{G}_n(t-t') e^{-ni\Omega_T\bar{t}}. \tag{3.49}$$

Using the decomposition of the fermion operators (3.47) in terms of the input modes and the Floquet scattering matrix elements, we can obtain the Fourier transform w.r.t. $t-t'$ of the harmonics $\Delta\mathcal{G}_n$ of the coherence function :

$$\begin{aligned} v_F\Delta\mathcal{G}_n(\omega) &= \int \mathrm{d}(t-t') e^{i\omega(t-t')} \Delta\left(v_F\mathcal{G}_n(t-t')\right) \\ &= \sum_{k\in\mathbb{Z}} S_{n+k}^*(\omega - \frac{n}{2}\Omega_T) S_k(\omega + \frac{n}{2}\Omega_T) \bar{n}_\mu(\omega + (k + \frac{n}{2}) \end{aligned} \tag{3.50}$$

In the above equation, $\bar{n}_\mu$ designates the equilibrium occupation number of a Fermi sea at a chemical potential μ.

Extracting the physical content of (3.50) requires a numerical evaluation of its r.h.s. The forthcoming section presents numerical results for the coherence function and the associated noise signals. This numerical work has also been the occasion to study the statistics of the emitted charge and the purity properties emitted electronic excitations.

3 Numerical results

This section is devoted to the numerical study of the mesoscopic capacitor operated as a single electron source, using the analytical results given by the Floquet scattering theory. More than formulae evaluation, this numerical work provides an efficient tool for predicting single particle coherence and other experimentally or theoretically relevant quantities. The methods presented here will be also be useful in chapter 6 for computing the relaxation of minimal excitations.
All the formulae that have been used in the numerics are recalled in appendix A, where we also describe the checks that have been done to ensure the validity of the numerical evaluation.

We will first study the $n = 0$ harmonic, namely the excess occupation number $\delta\bar{n}$, and continue by examining the complete single particle coherence function. We will finally consider the issue of the quality of the source by studying the statistics of the emitted charge and its coherence properties. The computation of the expected experimental signal will argue in favour of the experimental feasability of the single electron quantum tomography protocol.

3.1 Occupation number and coherence function

Occupation number

The excess occupation number is defined as $\delta\bar{n} = \bar{n} - \bar{n}_\mu$, where $\bar{n}_\mu$ is the equilibrium occupation number in the edge channel. This excess occupation number has the following expression in terms of Floquet matrix elements :

$$\delta\bar{n}(\omega) = \sum_{k\in\mathbb{Z}} |S_k(\omega)|^2 \bar{n}_\mu(\omega + k\Omega_T) - \bar{n}_\mu(\omega)\,. \tag{3.51}$$

Its integral over the positive (resp. negative) frequencies gives the average electron excitation number emitted per cycle $\bar{n}_+$ (resp. the average number of hole excitations emitted per cycle $\bar{n}_-$). The source under consideration is an AC source : the average output charge added to the Fermi sea is zero. In other words, the average numbers of emitted electron and hole excitations are opposite : $\bar{n}_+ = -\bar{n}_-$.
These quantities are linked to the excess occupation number. For example, for the average number of electrons, we have, from chapter 2 :

$$\bar{n}_+ = \int_0^{+\infty} \langle : c_\epsilon^\dagger c_\epsilon : \rangle \, \mathrm{d}\epsilon = \int_0^{+\infty} \delta\bar{n}(\epsilon)\, \mathrm{d}\epsilon. \tag{3.52}$$

Thus, the neutrality condition $\bar{n}_+ = -\bar{n}_-$ becomes :

$$\int_{-\infty}^{+\infty} \delta\bar{n}_\mu(\epsilon)\, \mathrm{d}\epsilon = 0\,.$$

The relevant experimental parameters are the electronic temperature, the amplitude and frequency of the driving voltage, as well as the transparency of the tunnel barrier. The temperature must be as low as possible, and will be chosen at a realistic although already challenging value of $50mK$.
The frequency of the driving voltage V must be such that the electron has the time to escape,

and sufficiently high to keep a significative noise signal (as noted in the previous section, the relevant noises are proportional to the driving frequency). Here, f is fixed at $3\,GHz$. Numerically, all these quantities are expressed in units of the mean level spacing $\Delta/k_B = 4.7\,K$.
The position of the dot's level with respect to the Fermi level ϵ_0 must be symmetric to operate in the particle/hole symmetric regime, as seen in fig.3.7. Furthermore, the voltage's amplitude must correspond exactly to the mean level spacing Δ.

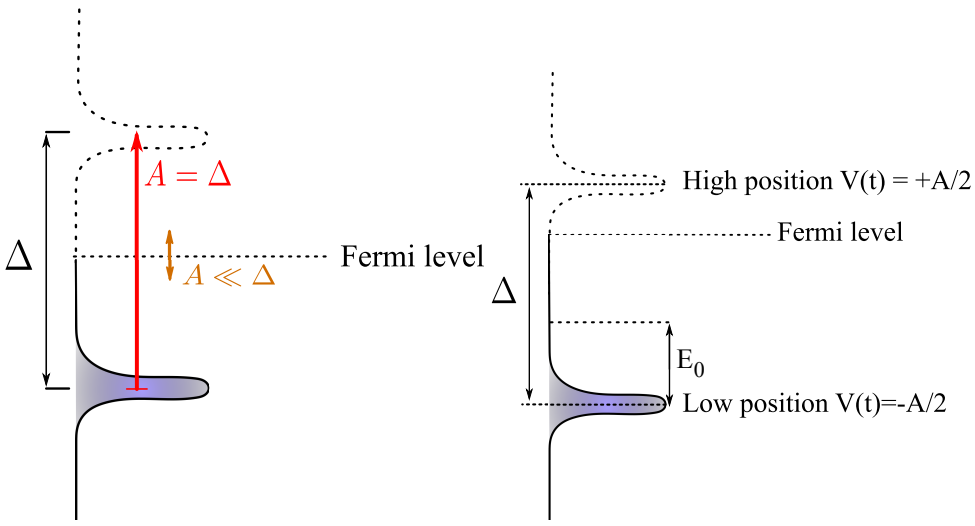

(a) Choice of the voltage amplitude (b) Position of the dot level wrt the Fermi sea

Figure 3.7: The position of the dot's levels are chosen to be symmetric around the Fermi energy. The effect of the initial position E_0 of the dot's level wrt the symmetric configuration is illustrated at the end of this paragraph.

Occupation number in the symmetric configuration

Figures 3.8 and 3.9 display the excess occupation number for different values of the trabsparency D.

From these plots, we can infer the following conclusions :

D=1 When the tunnel barrier is completely open, the source emits a coherent superposition of particle/hole pairs. No energy resolved electron and hole excitation are produced. Actually, in this regime, the result essentially probes the response of the chiral edge channel to a periodic square voltage. The particle/hole pair production is, in this regime, responsible for important charge fluctuations. Lastly, we observe that $\bar{n}_+$ differs from one.

D=0.44 In this case, energy resolved excitations appear but are accompanied by particle hole pairs, as seen from the nonzero values of the occupation number near the Fermi level. The associated noise signal has jumps corresponding to the peaks in the occupation number.

D=0.2 In this regime, electron and hole excitations are energy resolved, and no remarkable electron/hole production occurs. The corresponding noise signal displays a shape close

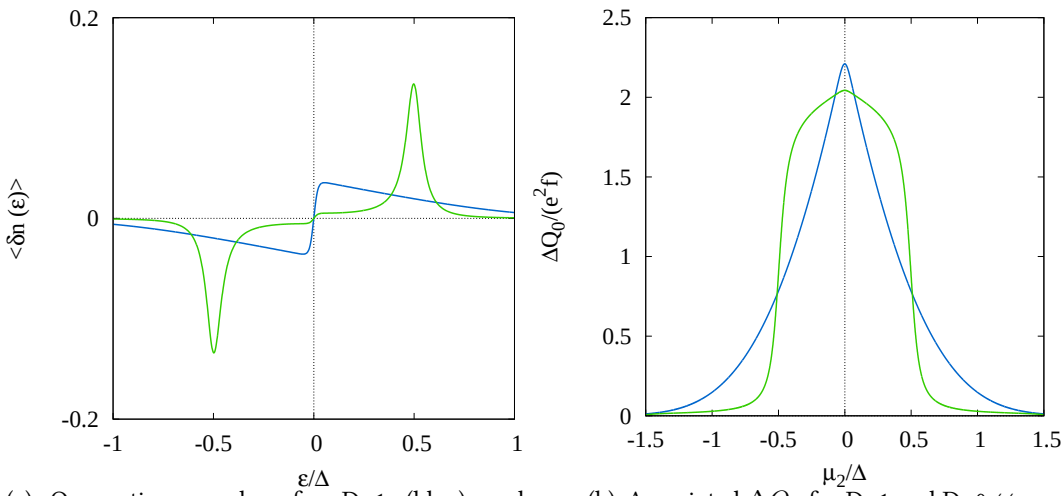

(a) Occupation number for D=1 (blue) and D=0.44 (green)

(b) Associated ΔQ_0 for D=1 and D=0.44

Figure 3.8: Excess occupation number and associated noise for D=1 and D=0.44.

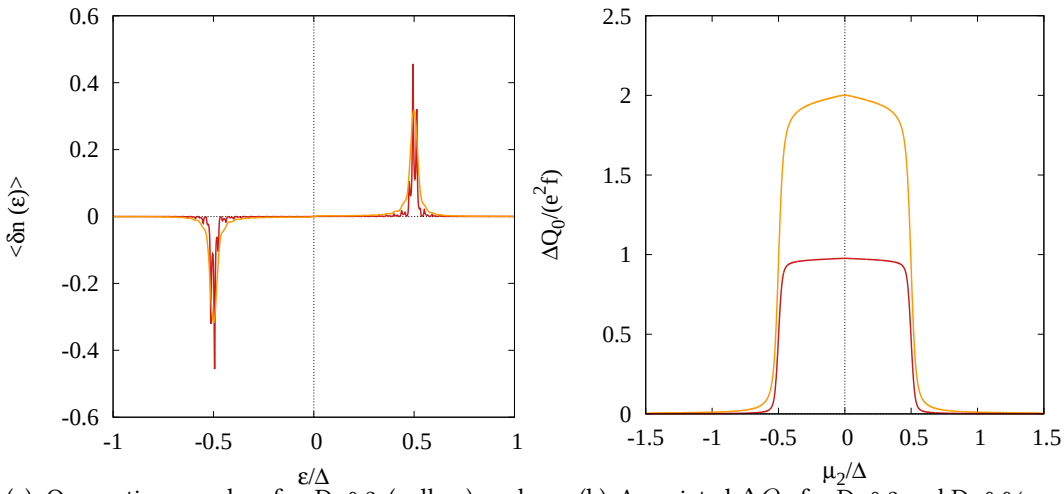

(a) Occupation number for D=0.2 (yellow) and D=0.04 (red)

(b) Associated ΔQ_0 for D=0.2 and D=0.04

Figure 3.9: Excess occupation number and associated noise for D=0.2 and D=0.04. The spurious pikes for $D = 0.04$ are numerical artefacts.

to a square : the jumps at $\mu_2 = \pm\Delta/2$ are linked to the electron and hole emission at precise energies. Furthermore, the almost flat shape of the noise signal means that the electron/hole pair production close to the Fermi level has almost disappeared. Finally, having $\Delta\mathcal{Q}(\mu_2 = 0) = 2$ means that $\bar{n}_+ = -\bar{n}_- = 1$.

D=0.04 When the transparency is too low, the escape time of the electron and hole becomes too long compared to the period of the driving voltage (as can be seen in the current pulse fig. 3.15). As a consequence, $\Delta\mathcal{Q}_0(\mu_2 = 0)$ is reduced by a half. In this regime, the output state is expected to be a linear superposition of the Fermi sea and a particle/hole pair :

$$|\Psi_{out}\rangle = \frac{1}{\sqrt{2}}\left(|F\rangle + \psi[\varphi_h]\psi^\dagger[\varphi_e]|F\rangle\right). \tag{3.53}$$

The evaluation of the supplementary charge in this state explains the value $\Delta\mathcal{Q}_0(\mu_2 = 0)$.

We will now see how these result have a manifestation in the full coherence function, and which other information can be extracted.

Effect of nonsymmetric configurations and transition to the adiabatic regime

Fig. 3.10 depicts the excess occupation number for different values of the initial position E_0 of the dot's levels w.r.t the Fermi energy (in units of Δ). As the energy shift goes away from the symmetric configuration value $E_0 = 0$, the source emits an increasing number of particle/hole pairs, since the values of the excess occupation number around $\epsilon = 0$ are increasing. The total number of electrons emitted per cycle does not experience significant modification, but the energy repartition of the emitted excitations is drastically modified. Thus, this analysis shows that the symmetric configuration is optimal for energy resolved electron emission. Furthermore, it makes the source less sensible to voltage fluctuations.

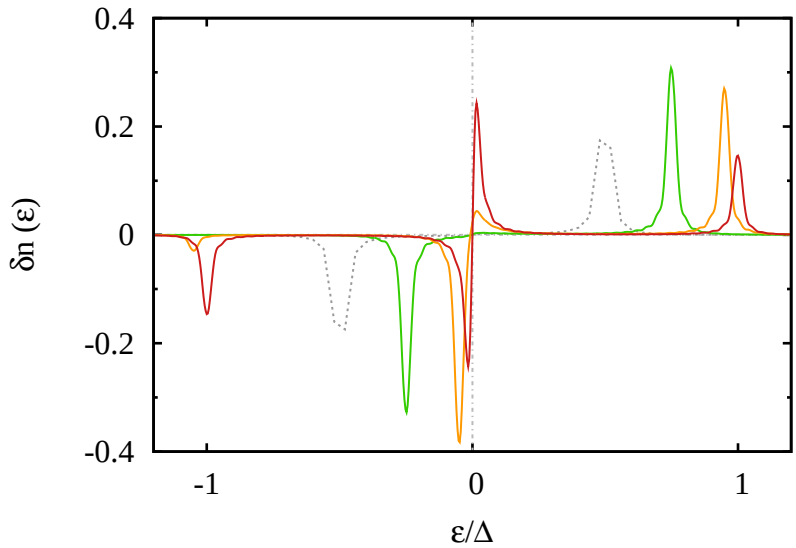

Figure 3.10: Excess occupation number for different configurations of the dot's levels, for an amplitude of the driving voltage equal to Δ, $f = 3\,Ghz$, and $T = 50\,mK$. Green, yellow, and red curve correspond respectively to a shift of $\frac{\Delta}{4}$, 0.45Δ and $\frac{\Delta}{2}$. The gray dashed curve corresponds to the symmetric configuration. The energy shift E_0 is linked to the quantity ϕ_0 in [123] by $\phi_0 = 2\pi\frac{E_0}{\Delta}$.

The effect of the driving frequency for a sine voltage on the excess occupation number is shown in fig. 3.11. The emission regime tends to the adiabatic limit [108] as the frequency decreases. In this asymptotic regime, the electron / hole emission takes place at the surface of the Fermi sea, and the energy repartition is exponentially decreasing over an energy scale $\hbar\Omega_T$.

The next paragraph will focus on the impact of the transparency D of the tunnel barrier on the full coherence function, and on the associated noise signals. This study will be done at fixed temperature and voltage characteristics.

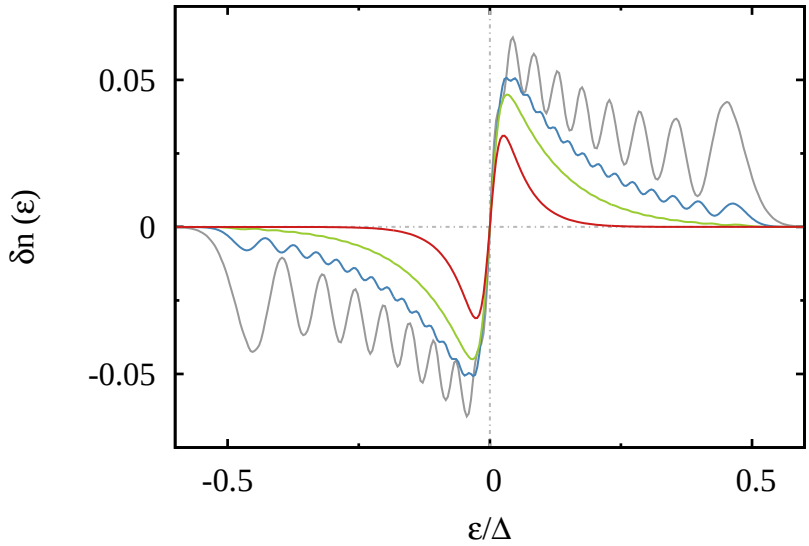

Figure 3.11: Excess occupation number for different values of the driving frequency, for a sine voltage, with an amplitude of the driving voltage equal to Δ, $D = 0.2$ and $T = 50\,mK$. Gray, blue, green and red curve correspond respectively to a frequency of $f \equiv f_0 = 3\,GHz$, $f_0/2$, $f_0/3$ and $f_0/6$.

Complete coherence function

Along the same lines as for the occupation number, we now focus on the behaviour of the complete single particle coherence function as a function of the transparency of the tunnel barrier between the quantum dot and the edge channel.

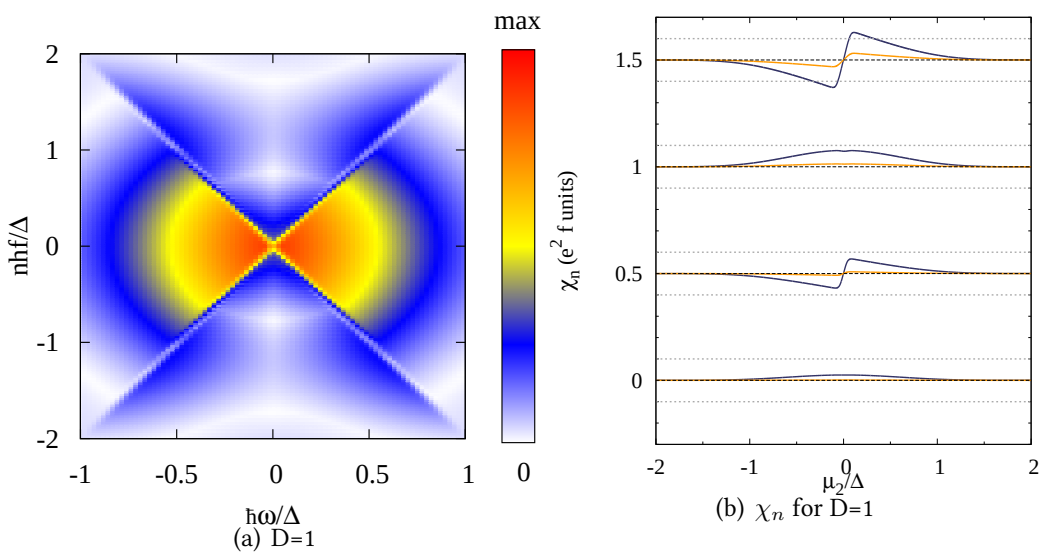

Figure 3.12: Coherence function (modulus) and the first four harmonics of the associated noise signal for D=1. In (b), grey lines indicate the minimal measurable level of noise ($0.1e^2 f$). The blue lines corresponds to $\Re(\chi_n)$ and the orange ones to $\Im(\chi_n)$.

When the dot is completely open, the source emits particle/hole pairs close to the Fermi level. This can be seen in the coherence function depicted on fig. 3.12 (a) : the highest values of $|\Delta\mathcal{G}|$ are in the vicinity of the origin. Furthermore, the strong electron/hole coherences (in blue

in 3.12) indicate large fluctuations of the number of emitted electron per cycle as pointed out in chapter 2. For most of the harmonics, the expected signal is close to the minimal experimental sensitivity. Nevertheless, we see that it is essentially localized close to $\mu_2 = 0$.

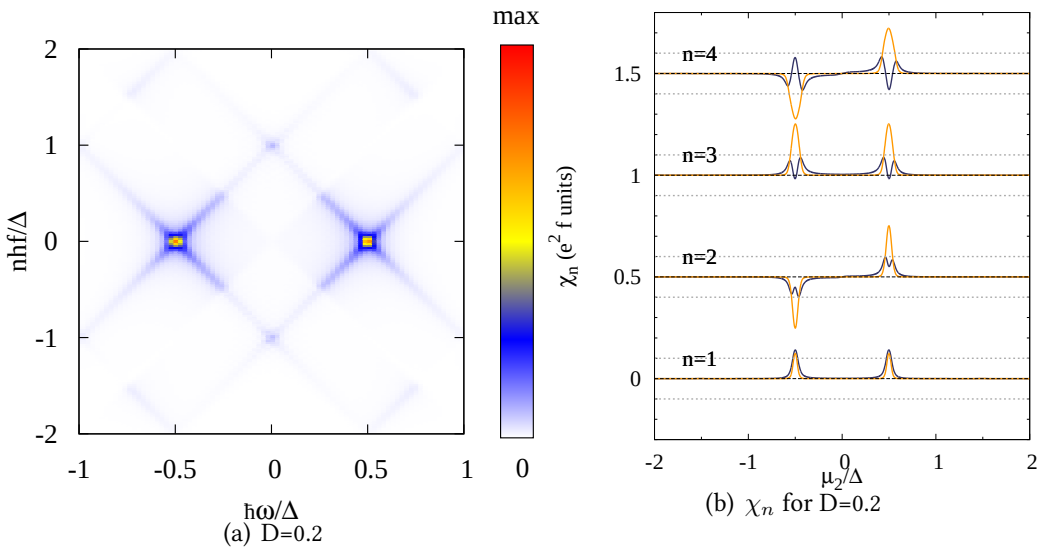

Figure 3.13: Coherence function and the first four harmonics of the associated noise signal for D=0.2.

At $D = 0.2$, we see in fig. 3.13 that electron and hole excitations are localized in energy space. The crosses around the spots represent the electron's and hole's wavefunctions. This localization in Fourier space goes along with a disppearance of the electron/hole coherences : the small values of $|\Delta\mathcal{G}^{(e)}|$ in the off diagonal quadrants indicate weak fluctuations of the number of emitted electrons $\bar{n}_+$.
The experimental signal is essentially nonzero around $\mu_2 = \pm\Delta/2$ corresponding to the energies of the emitted electron and hole excitations.

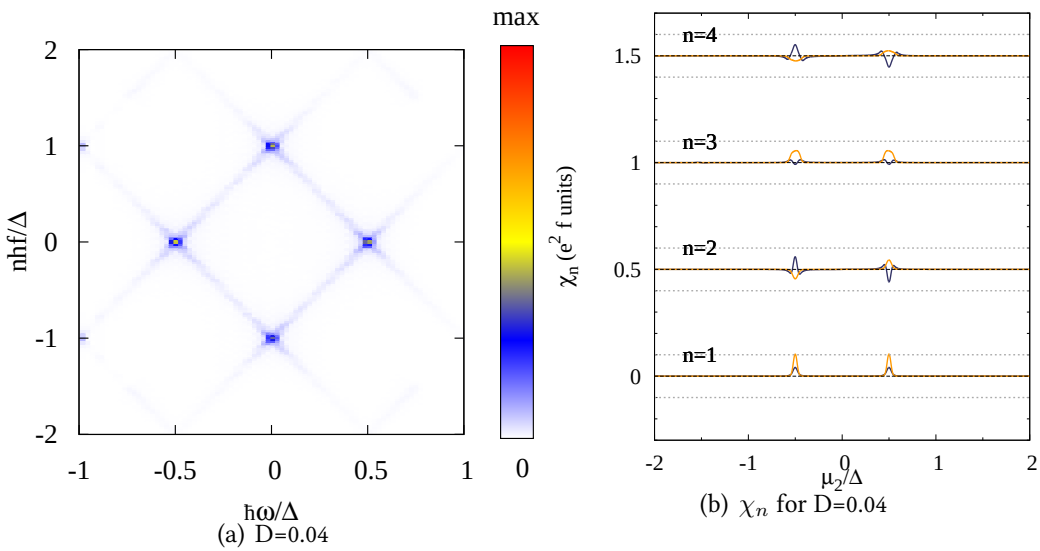

Figure 3.14: Coherence function and the first four harmonics of the associated noise signal for D=0.04.

If the transparency of the tunnel barrier is too low, the electron/hole coherences reappear implying that the fluctuations of $\bar{n}_+$ number are greater in this regime than in the $D = 0.2$ case. The consequences of such a long escape time in the low-D regime are more clearly seen in the current pulse as we will now discuss.

3.2 Current pulse

The average current can expressed in terms of the harmonics of the excess coherence function :

$$\langle I(t)\rangle = -ev_F \sum_{n\in\mathbb{Z}} \Delta \left(v_F \int_{-\infty}^{+\infty} \frac{\mathrm{d}\omega}{2\pi} \Delta \mathcal{G}_n^{(e)}(\omega) \right) e^{-in\Omega_T t}, \tag{3.54}$$

Thus, as noted in chapter 2 in eq.(2.40), integrating the coherence function over lines parallel to its diagonal gives the average current.

Fig. 3.15 depicts the current pulse for different values of the transparency of the tunnel barrier. In these plots, the current pulse has been obtained by performing an inverse Fourier transform of the current pulse's Fourier coefficients in (3.54).

When D tends to 0.2, the current pulse tends to an exponential decay form, with a decay time given by the escape time $\tau_{esc} = \frac{h}{D\Delta}$. But when the transparency of the tunnel barrier is too low, the pulse does not have the time to decay completely (see fig. 3.15)because the escape time becomes too long compared to the driving period. In this regime, due to the decrease of $\bar{n}_+$, the relative second order fluctuations of the emitted charge are more important, as we will see in the next part.

3.3 Accuracy of the quantum capacitor as a single electron source

The optimal value of the driving amplitude corresponds exactly to the mean level spacing Δ : such a voltage ensures that and only one of the dot's levels will cross the Fermi energy. The driving frequency is chosen as a compromise between noise power (which increases with Ω_T) and the experimental possibilities (microwave generators only give access to frequencies up to $20\,\mathrm{GHz}$) and has been fixed at $f = \frac{\Omega_T}{2\pi} = 3\,\mathrm{GHz}$. Thus, the remaining parameter is the transparency of the tunnel barrier connecting the quantum dot to the edge channel.
To find the optimal value of the transparency D, we evaluate the quality of the emitted electron for the full range of the transparency [4]. This evaluation consists in fulfilling two criteria:

(a) The average number of emitted electrons per cycle must be one, and the fluctuations around this average number must be minimal.

(b) The output state must be pure.

Statistics of the emitted charge

Formally, the criterion (a) is equivalent to:

$$\bar{n}_+ \to 1 \text{ and } \frac{(\Delta n_+)^2}{\bar{n}_+^2} \ll 1, \tag{3.55}$$

[4]This study is done at fixed frequency. For another value of f, the results will be different. Nevertheless, the principle remains the same.

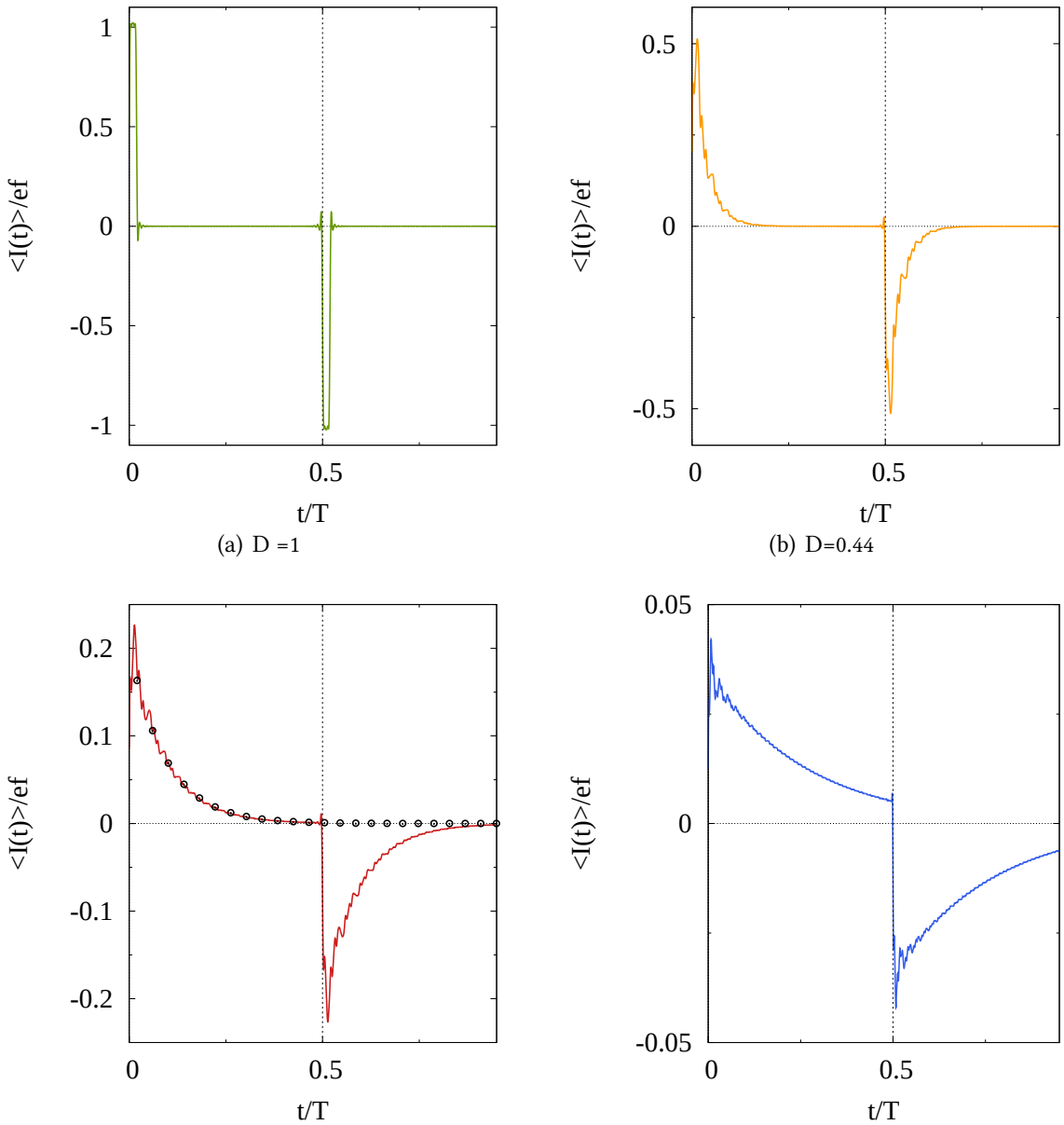

(a) D =1 (b) D=0.44 (c) D=0.2 (d) D=0.04

Figure 3.15: Current pulse for different values of D. In these curves, $k_B T/\Delta = 1/100$, $hf/\Delta = 0.019$, corresponding to $T = 50\,mK$ and $f = 3\,Ghz$. The black dots in (c) represent an exponential decay with characteristic constant $\tau_{esc} = \frac{h}{\Delta}\left(\frac{1}{D} - \frac{1}{2}\right) \simeq \frac{h}{D\Delta}$ [38]. Rapid oscillations (Stokes phenomenon) near $t = 0$ and $t = T/2$ are due to the finite number of terms in Fourier sums.

where $(\Delta n_+)^2$ is the fluctuation of the number of emitted electrons $\bar{n}_+$. These two quantities can be extracted from the single particle coherence function (see Chapter 2, section 2) :

$$\bar{n}_+ = T \int_0^{+\infty} v_F \Delta \mathcal{G}_0^{(e)}(\omega) \frac{d\omega}{2\pi} \tag{3.56}$$

$$(\Delta n_+)^2 = T \sum_{n=1}^{+\infty} \int_{-n\Omega_T/2}^{+n\Omega_T/2} \left| v_F \Delta \mathcal{G}_n^{(e)}(\omega) \right|^2 \frac{d\omega}{2\pi} \tag{3.57}$$

The evolution of $\bar{n}_+$ and $\frac{\Delta n_+}{\bar{n}_+} = \sqrt{\frac{(\Delta n_+)^2}{\bar{n}_+^2}}$ with the transparency D are given in 3.16.

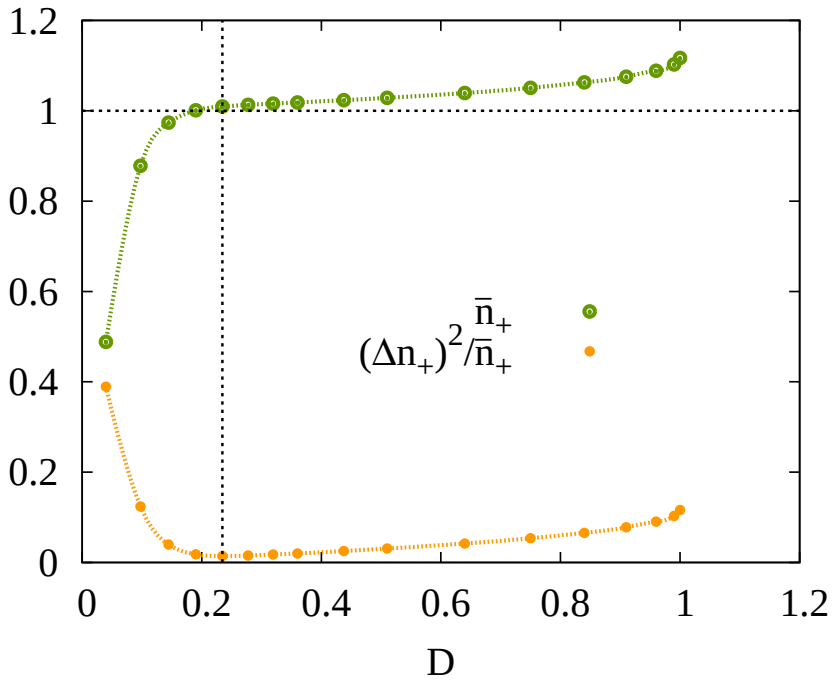

Figure 3.16: Average number of electrons emitted per cycle $\bar{n}_+$ (yellow curve) and corresponding fluctuations $\frac{\Delta n_+}{\bar{n}_+}$ (green curve).

The curve representing $\bar{n}_+$ displays a plateau at $\bar{n}_+ \simeq 1$ for values of the transparency close to $D = 0.2$. Apart from this value, the output charge falls to zero when the quantum point contact is closed, as expected. When the transparency of the tunnel barrier is too high, charge quantization is lost : the average number of electron excitations emitted per cycle becomes slightly greater than one [5]. These observations on the average electron number can be confirmed by looking at its fluctuations.
If we turn to $\Delta n_+/\bar{n}_+$ we see that it exhibits a minimum close to $D = 0.2$. Away from this minimum, when the transparency increases, $\Delta n_+/\bar{n}_+$ becomes more important due to electron hole pairs. Thus, when $D \to 1$, the relative fluctuations $\Delta n_+/\bar{n}_+$ increase since we essentially create electron hole pairs. When $D \to 0$, the fluctuations are due to the weak values of the average electron number. In this regime, the escape time $h/D\Delta$ of the electron is too long compared to the period, and then the electron could not escape the confined region before the dot level is sunk again under the Fermi level.

Coherence properties of the output electron

To estimate the purity of the output electronic state, we use the linear entropy S_{lin} [125]. This quantity is obtained by linearizing the Von-Neumann entropy around the identity

$$S_{VN}(\rho) = -\text{Tr}\big(\rho \log \rho\big) \quad : \quad S_{\text{lin}}(\rho) = 1 - \text{Tr}(\rho^2)\,, \tag{3.58}$$

[5] Here, $\bar{n}_+$ is obtained as an integral of the occupation number in the positive energies, and so could be greater than one.

and is consequenctly easier to evaluate numerically. Tt is linked to another relevant quantum information quantity : the purity $\gamma = 1 - S_{\text{lin}}$ [116]. Here, we compute the linear entropy of the one body electronic density operator ρ_e, extracted from the single particle coherence function in Fourier space [6] :

$$\rho_e(\omega_+, \omega_-) = \frac{1}{\bar{n}_+}\theta(\omega_+)\theta(\omega_-)\Delta\mathcal{G}^{(e)}(\omega_+, \omega_-). \tag{3.59}$$

In our case, $S_{\text{lin}} \in [0, 1]$ and reaches 0 only for a pure state. For our purpose, we must identify the value of D that corresponds to the minimal linear entropy. For that value of the transparency, the emitted state will be the purest. The linear entropy has the following expression in terms of the excess coherence function[7] :

$$S_{\text{lin}} = 1 - \frac{T}{\bar{n}_+}\sum_{n\in\mathbb{Z}}\int_{|n|\Omega_T}^{+\infty}\frac{\mathrm{d}\omega}{2\pi}|v_F\Delta\mathcal{G}_n^{(e)}(\omega)|^2. \tag{3.60}$$

The remaining question concerns the characterization of this state. For this purpose, we compute the overlap of the output electronic state to a trial wavefunction. In the present context, it is natural to consider the wavefunction predicted by the resonant level coupled to a semi-infinite continuum model [26] :

$$\phi_{test} = \theta(\omega)\frac{\sqrt{2\hbar/D\Delta}}{\omega - \Delta/2\hbar + iD\Delta/h}. \tag{3.61}$$

At low transparency, the typical escape time $h/D\Delta$ is expected to be small compared to the driving period T. In this case, the dot level that has been displaced at an energy $\Delta/2$ over the Fermi energy at $t = 0$ has the time to deliver a single electron into the edge channel, which plays the role of the continuum. To quantify how close the output state is from (3.61), we compute its overlap [116] with ϕ_{test} :

$$\mathcal{O}(\rho|\phi_{test}) = \langle\phi_{test}|\rho|\phi_{test}\rangle, \tag{3.62}$$

which becomes, in terms of the coherence function :

$$\mathcal{O}(\mathcal{G}^{(e)}|\phi_{test}) = \sum_{n\in\mathbb{Z}}\int\Delta\mathcal{G}_n^{(e)}(\omega)\,\phi_{test}^*\left(\frac{\omega + n\Omega_T/2}{v_F}\right)\phi_{test}\left(\frac{\omega - n\Omega_T/2}{v_F}\right)\frac{d\omega}{2\pi}. \tag{3.63}$$

The numerical evaluation of (3.63) together with the linear entropy is plotted in fig. 3.17. It shows that S_{lin} has a minimum for D close to 0.2, which is the same value as in 3.16. When the transparency goes to zero, the emitted state is no more pure due to the revival of electron/hole pair production. When D increases from its optimal value, the purity decreases, as electron/hole coherences (and electron/hole pairs) appear. The optimal regime also corresponds to a maximal overlap with the trial wavefunction (99%). In this regime, the emitted electron is emitted with probability 99 % in a lorentzian wavefunction in energy space and the corresponding current pulse is an exponential decay.

We can then infer the following results:

- In the optimal regime, the emitted state is pure and this optimal operating point also corresponds to the optimal in terms of statistical indicators $\bar{n}_+$, $\Delta n - +$.
- The wavefunction describing the emitted electron is predicted by a model of a resonant level coupled to a semi-continuum (3.61).

[6] A hole density operator can be defined in an equivalent way.

[7] The Von-Neumann entropy cannot be expressed simply in terms of the single electron coherence

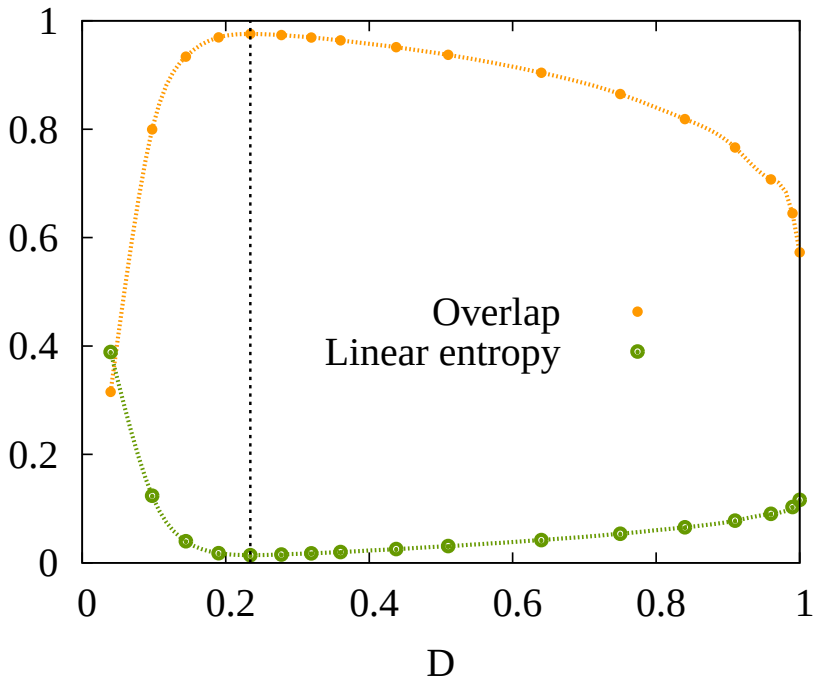

Figure 3.17: Overlap of the electron density operator to the resonant level model (orange curve) and linear entropy S_{lin} (green curve). The vertical dotted line indicates the optimal operating point.

4 Conclusion

This chapter was devoted to the presentation of a single electron quantum tomography protocol based on current noise measurements in an Hanbury Brown and Twiss configuration. This protocol is an electronic analogue of homodyne tomography in photonic quantum optics.

In order to evaluate the feasability of its implementation in the case of the single electron source built in the LPA, we have obtained numerical predictions for the expected noise signals based on the noninteracting Floquet scattering theory.
This quantum tomography protocol could be envisioned to characterize the state of other types of sources, such as time resolved sources envisioned by Keeling *et. al* [76].
Another proposition [108] has been recently done to perform the spectroscopy of the state of a single electron source. This other protocol relies on two particle interferences. It has also been illustrated in the case of the mesoscopic capacitor [38], but is adaptable for other kinds of sources. Contrarily to the proposition of this chapter, it does not rely on homodyne detection, but on the suppression of current noise due to the overlap of the incoming states of the interferometer.

Interaction effects are a major issue in electron quantum optics. Understanding them in a controlled decoherence experiment may lead to new ideas to minimize the decoherence. In this chapter, we have considered the issue of source characterization but performing single electron tomography after an interaction region as depicted on fig. 3.18 is a very interesting perspective. As we shall see in the next chapters, the HBT protocol could also be implemented to study the single electron decoherence and relaxation [30], or the production of noise induced by interac-

tions, as proposed in the chapter 6.

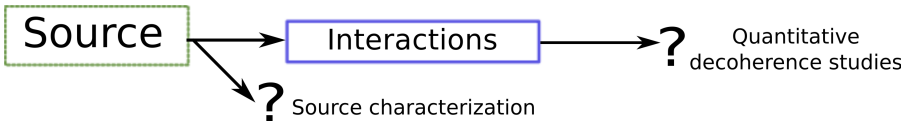

Figure 3.18: The different situations in which the tomography protocol depicted in this chapter can be useful. Here, we illustrated the first possibility, which is the characterization of an unkwnown source. In chapter 6, we will see that it could also be useful for characterizing interaction effects.

These experiments could bring new elements to the study of energy exchange mechanisms in quantum Hall edge channels. The extracted information would be complementary to those obtained using tunneling spectroscopy [2, 3, 145], which only measure the stationnary contribution to single particle coherence .
The following chapter is devoted to the study of some of the results of this spectroscopy experiment in the $\nu = 2$ regime. This chapter will explain how electron transport in the interacting regime can be understand by the mean of the bosonization technique. It will also explain predictions that will be compared to experimental results.

Chapter 4

Energy exchange between coupled channels

Contents

1 Experimental study of edge channel equilibration . . . 66

1.1 Experimental protocol . . . 66

1.2 Results and interpretation . . . 69

2 Plasmon scattering approach to edge channel equilibration . . . 71

2.1 Bosonization and plasmon scattering . . . 71

2.2 Plasmon scattering from general considerations . . . 76

2.3 Predictions for experimental quantities . . . 77

3 Confrontation to experimental results . . . 79

3.1 Evolution with respect to bias voltage . . . 80

3.2 Dependence with the QPC transmission . . . 81

3.3 Noise measurements to probe plasmon scattering . . . 81

4 Conclusion . . . 84

In the previous chapters we have neglected the effects of interactions in current transport in the quantum Hall regime. Nevertheless, although some experimental results [112, 152] agree remarkably well with noninteracting theoretical predictions [140], the results of Mach-Zehnder interferometry experiments [74, 68, 131, 133, 132] have shown that studying interactions is crucial to understand relaxation and decoherence. Here, we illustrate this general statement on the example of energy exchange in the $\nu = 2$ quantum Hall regime, a situation which has been recently studied experimentally [145, 3, 2].
In a first section, we will briefly describe the experimental setup and results. In the second part, we will present an approach based on bosonization and plasmon scattering to understand the effect of interactions. We will finally show how this approch to interactions can be tested using current noise measurements at finite frequency.

1 Experimental study of edge channel equilibration

In this section, we review recent results obtained by Frédéric Pierre and his collaborators on the energy exchanges in the $\nu = 2$ regime [145, 3, 2]. We will first describe the experimental setup, and then analyze briefly the experimental results, showing which information on energy exchange can be extracted from the datas.

1.1 Experimental protocol

Experimental setup

The experimental setup is described in [2] and its schematic view is shown on fig. 4.1. A nonequilibrium electronic distribution is created by mixing two equilibrium distributions at the same temperature and different chemical potentials μ_1 and μ_2 :

$$f_1(\epsilon) = \tau f_{in,1}(\epsilon) + (1-\tau) f_{in,2}(\epsilon). \tag{4.1}$$

The electrons of this nonequilibrium distribution in the channel (1) in fig.4.1 copropagate along with the other edge channel (2), which has been populated by an equilibrium distribution at the chemical potential μ_2. The aim of this experiment is twofold :

(i) Elucidate which mechanisms are responsible for the relaxation of the nonequilibrium state in the edge channel (1).

(ii) Find the final equilibrium electronic distribution.

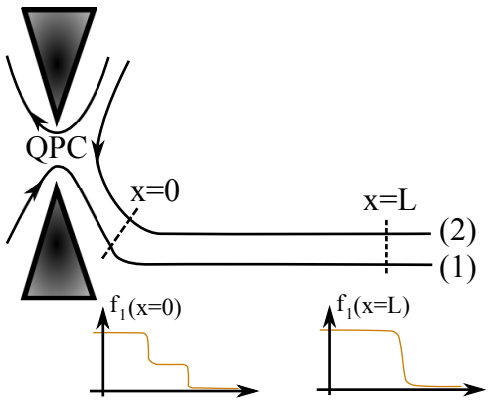

Figure 4.1: Sketch of the energy relaxation setup. A nonequilibrium electronic distribution is injected in the outer edge channel (1) at $x = 0$ by mixing two equilibrium distributions $f_{in,1}$ and $f_{in,2}$ at different chemical potentials μ_1 and μ_2 with a quantum point contact of transmission τ. The electronic distribution is measured at $x = L$. The inner edge channel (2) is populated by an equilibrium distribution at chemical potential μ_2.

We look at the temporal coherence after copropagation over a distance L. This length is varied using different paths in the sample (see fig.4.3). The path in which the current propagates is chosen by opening the appropriate quantum point contacts. The distribution function is measured by the mean of a quantum dot operated as an energy filter.
Experimental data consist in the variation of the electric current flowing through the dot I_D

with respect to V_G, where V_G is the external voltage that shifts the dot's energy levels. Assuming that, at the measurement point, the density of states is the one of free chiral fermions, $\frac{\partial I_D}{\partial V_G}$ is related to the Fermi function in channel (1) and in the reference channel (see. fig. 4.2):

$$\frac{\partial I_D}{\partial V_G} \propto \frac{\partial}{\partial E}(f_1 - f_{ref}), \tag{4.2}$$

a result that directly follows from eq. (2.73) in chapter 2.

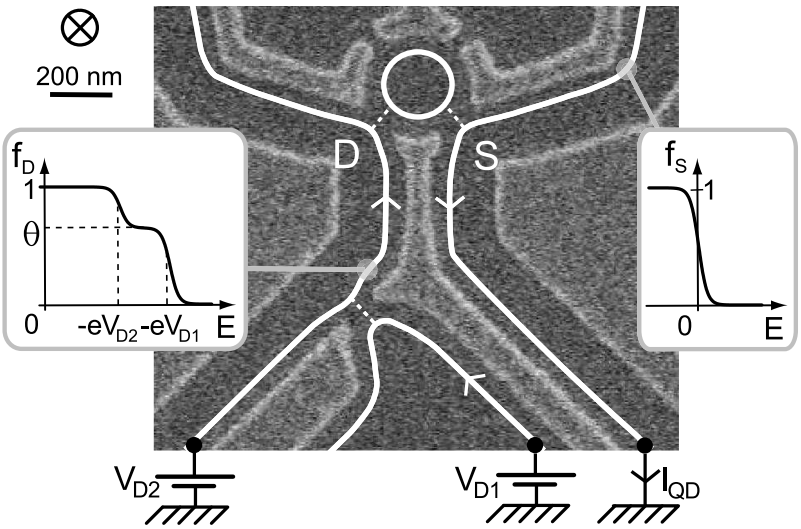

Figure 4.2: Measurement point in the relaxation setup (from [2]). The measured electronic distribution is f_D. The dot (white circle) acts as an energy filter. The measured current I_{QD} has variations w.r.t V_G proportional to $f_1 - f_{ref}$.

The next discussion shows how information on energy exchange can be extracted from electronic distribution measurement.

Energy exchange from electronic distribution

The total energy current along an edge channel α is the sum of an electrochemical contribution due to the chemical potential and of a heat contribution due to electron excitations with respect to the cold Fermi sea at the local EC chemical potential.
The electrochemical energy current has the following expression [31] (supplementary material) :

$$J_\alpha^{(ec)} = \frac{\mu_\alpha^2}{2h}. \tag{4.3}$$

The heat current is expressed in terms of the electron distribution function $f_\alpha(\epsilon, x)$ in channel α at position x as

$$J_{qp} = \rho_\alpha v_\alpha \int (f_\alpha(\epsilon, x) - \theta(\mu_\alpha - \epsilon))\, \mathrm{d}\epsilon \tag{4.4}$$

ρ_α being the density of states per unit length end energy, which verifies $\rho_\alpha\, v_\alpha = 1/h$. In the case of an equilibrium state at temperature T,

$$J_{qp} = \frac{\pi^2}{6h}(k_B T)^2. \tag{4.5}$$

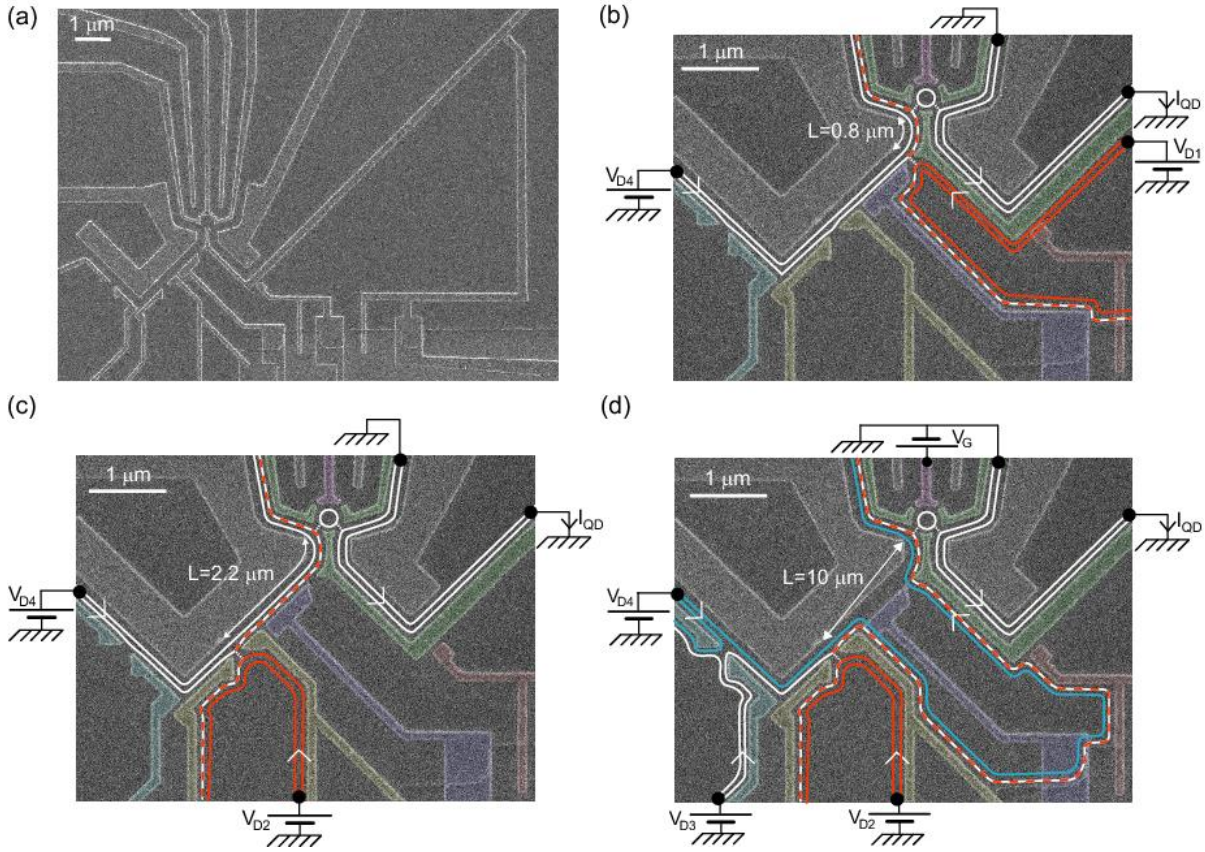

Figure 4.3: (from [145]) (a) : Overview of the setup for relaxation studies. Here, the different paths having different propagation lengths are represented in (b), (c) and (d).

In the experiment described in [2], the measured energy current along the edge channel α is the one of quasiparticles. It can be expressed in terms of an effective temperature using (4.5) :

$$J_{qp} = v_\alpha E_{qp} = \frac{\pi^2}{6h} \left(k_B T_{qp}\right)^2 \ . \tag{4.6}$$

At $x = 0$, we thus obtain : T_{qp} :

$$k_B T_{qp} = \sqrt{\frac{6(E_{qp}/\rho)}{\pi^2}} \tag{4.7}$$

$$= \sqrt{T^2 + 3\tau(1-\tau)\left(\frac{\mu_2 - \mu_1}{\pi k_B}\right)^2} \tag{4.8}$$

$$= \sqrt{T^2 + T_{exc}^2}\,, \tag{4.9}$$

where T_{exc} is the excess temperature equivalent to the quasiparticle energy injected at $x = 0$. In the next part, we show the experimental results for the measurement of the energy current flowing through the quantum dot, together with the extracted excess temperature. A short interpretation of these observations will be presented, and will lead us to the most probable relaxation process.

1.2 Results and interpretation

Experimental datas and analysis

Raw measurement datas are presented in fig. 4.4(b). Integration of these datas provides the nonequilibrium electronic distribution function. This distribution function gives access to the heat current E_{qp} using (4.4), which is represented as an excess temperature in fig. 4.4(c).

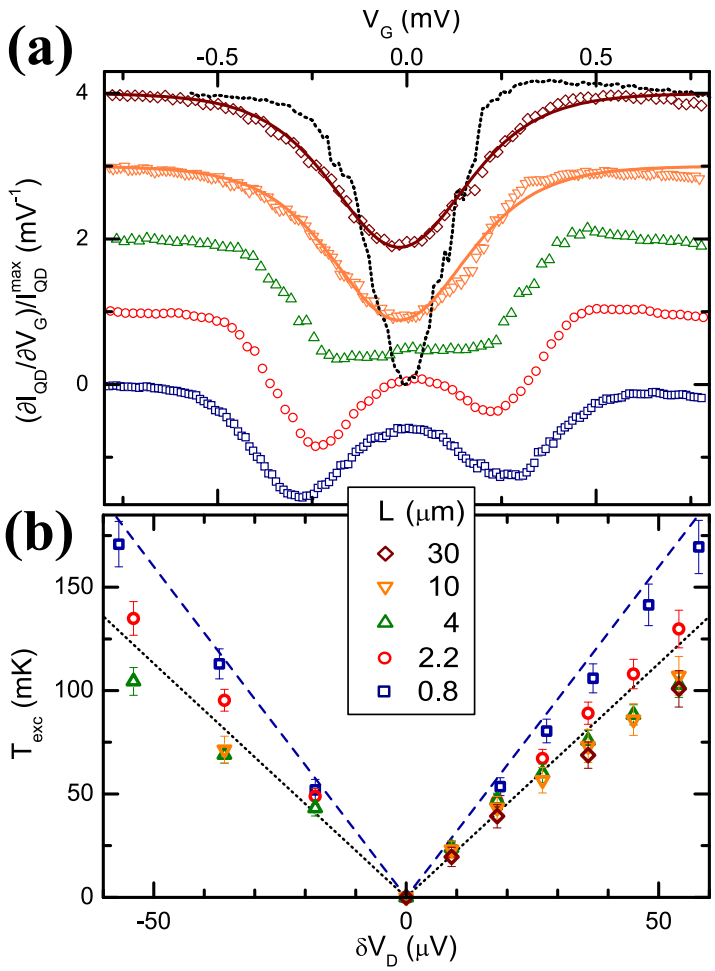

Figure 4.4: (from [145]) (b) Raw data for $\partial I_D/\partial V$ for different propagation lengths and at fixed QPC bias ($36\,\mu V$). Solid lines accompanying datas for $L = 10$ and $30\mu m$ are expected dips for Fermi electronic distribution at $85\,mK$. The dotted line is the measured dip in the absence of QPC bias. It corresponds to a Fermi distribution at $40\,mK$. (c) Extracted excess temperature as a function of the QPC bias for various propagation length.

The results presented in fig. 4.4 organize as follows for increasing propagation length:

$\mathbf{L = 0.8\,\mu m}$ For the shortest propagation length (blue squares), the double dip in $\partial I_D/\partial V_D$ associated to the double step in the electronic distribution is close to noninteracting predictions, and thus shows that energy exchanges are small at short lengthscales.

L = 2.2 to 30 μm As the copropagation length is increased, the double dip in the experimental signal evolves toward a single dip. This is the manifestation of the relaxation of the nonequilibrium distribution injected at $x = 0$ towards a state close to a Fermi distribution, for which a single dip is expected. The temperature characterizing this distribution is higher than the equilibrium temperature as can be seen by comparing the dip for $L = 30\,\mu m$ and the dotted line presenting the measured signal for a Fermi distribution at the equilibrium temperature. For the chosen value of the QPC bias ($36\,\mu V$), the characteristic relaxation length is $L_{inel} = 3\,\mu m$. [1]

L = 10 and 30 μm For the two longest paths, the experimental signal is the same, showing that the relaxation process saturates at long propagation lengths.

This information extracted from the raw experimantal datas provide some insight on the relaxation mechanism.

Interpretation : finding the relaxation mechanism

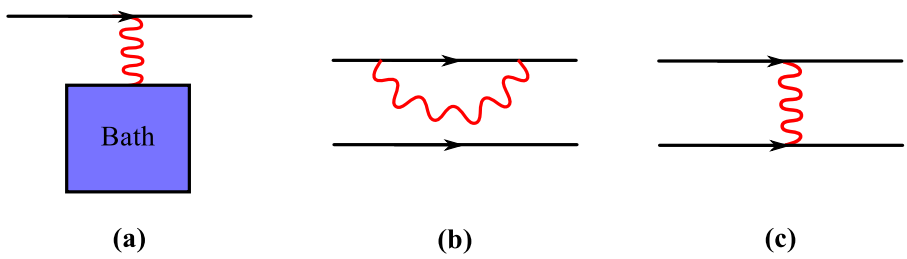

Figure 4.5: The different possible mechanisms for energy exchange . (a) : Exchange with a thermalized bath. (b) : Intrachannel interaction. (c) : Interchannel interaction.

The different mechanisms that could be proposed to explain these results are schematized in fig. 4.5. Neglecting the possibility of charge tunneling between the edge channels [145, 151], three mechanisms can be proposed to explain the observed energy exchange:

(a) Coupling to a thermalized bath such as the excitations of metallic gates or phonons ;

(b) Intrachannel interactions ;

(c) Electrostatic coupling between charge densities in different edge channels.

These different possibilities can be discriminated on experimental grounds [145] by analyzing the results for the energy contained in the probed edge channel.
The saturation of energy redistribution at long propagation lengths is incompatible with the scenario (a). Indeed, a coupling with a thermalized bath of excitations would instead imply a relaxation towards an equilibrium state identical to the one at zero QPC bias.
Experimental data in 4.4 (c) suggest a repartition of quasiparticle energy between the two edge channels. Thus, the measured evolution of the excess temperature reflects an energy exchange between the two copropagating edge channels, which is incompatible with the possibility of dominant intrachannel coupling (b).

[1] The procedure to extract this characteristic length is described in [145] (supplementary material).

Consequently, the best candidate to explain the energy exchange observed in this experiment is electrostatic coupling between charge densities propagating in the two channels. More precisely, this interchannel coupling arises from the Coulomb interaction screened by the gates that design the shape of the 2DEG.

In the next section, we will present a model that describes the coupling between edge channels in terms of scattering of bosonic modes. This approach will be used to make predictions for the excess temperature that will be compared to the experimental results [31].

2 Plasmon scattering approach to edge channel equilibration

Our modeling of interactions is based on bosonization. This technique describes a one-dimensional electronic fluid in terms of its long-range charge density fluctuations and thus allows a nonperturbative treatment of interactions. After a brief introduction to the bosonization of chiral electrons, we will describe interaction effects within a scattering formalism for bosonic excitations. We will finally see how the predictions from this model can be used to extract experimentally relevant quantities and how they compare with experimental data.

2.1 Bosonization and plasmon scattering

Short introduction to bosonization

Electrons in one dimension can be described in terms of charge density oscillations. The bosonization technique focuses on low energy excitations and provides an effective theory of electronic excitations. A complete account of the bosonization technique can be found in refs. [142, 53, 48, 154, 144]. Here, we focus on specific points that will be used to understand the description of electrons propagating in chiral edge channels as bosonic modes called the edge magnetoplasmons. The electron/electron interactions in finite regions will be described in terms of plasmon scattering. This hydrodynamical approach is similar to [157].

Bosonization of chiral electrons

As pointed out in chapter 1, the current flow in integer quantum Hall edge channels is chiral. Thus, in fig. 4.6, we consider only one branch of the dispersion relation with electrons having positive momenta (right movers) [2]. Furthermore, we consider only low energy excitations. Consequently, the spectrum is linearized around the Fermi energy. Finally, we do not consider the spin of electron here. We are thus left with spinless chiral electrons with a linear dispersion relation.

These assumptions lead to the following free electron hamiltonian :

$$\mathcal{H}_0^{(F)} = -i\hbar v_F \int_{\mathbb{R}} \mathrm{d}x\, \psi^\dagger(x)\partial_x\psi(x)\,. \tag{4.10}$$

[2] In a quantum Hall bar, the edge of the sample have different moving directions, but the spatical separation prevents any backscattering from one edge to the other. The two chiralities are decoupled.

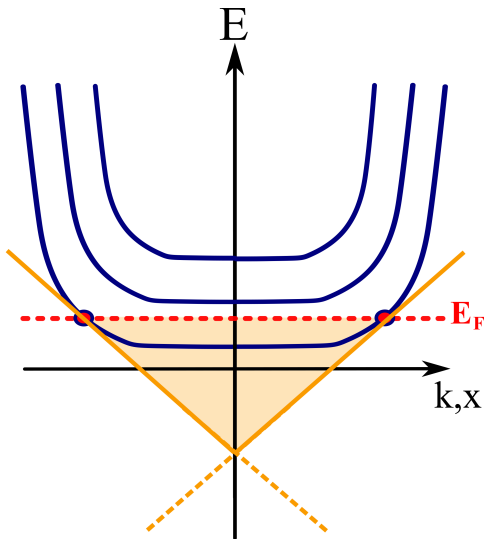

Figure 4.6: Linearized spectrum for electrons in one dimension. The quadratic dispersion relation is linearized around the two Fermi points $\pm k_F$. This linearization gives birth to chiral electron modes, propagating in the right and left directions. In our case, we only consider right moving electrons, corresponding to positive momenta.

The expression of the electronic field in terms of a bosonic field [3] relies on the fact that the electron density is a bosonic object, since it is the product of two fermion fields. If we assume that the electron density is the derivative of a bosonic field ϕ, $n(x) \propto \partial_x \phi$, then

$$\phi(x) = \lambda \int_x^\infty \mathrm{d}y\, n(y) \quad n(x) = \frac{1}{\lambda}\partial_x \phi, \tag{4.11}$$

where λ is a constant to be determined. Creating an electron at the position x' increases $\phi(x)$ by a value λ if $x < x'$. Because of the commutation relation between ϕ and its conjugate field $\Pi(x) = \frac{1}{v}(\partial_t \phi)(x)$:

$$\left[\phi(x), \int_{-\infty}^{x'} \mathrm{d}y\, \Pi(y)\right] = i\theta(x' - x), \tag{4.12}$$

creating an electron at the position $x' < x$ necesarily involves the action of the following shift operator:

$$\exp\left[-i\lambda \int_{-\infty}^{x'} \mathrm{d}y\, \Pi(y)\right]. \tag{4.13}$$

Thus, the electron creation operator $\psi^\dagger(x)$ can be written in terms of ϕ as :

$$\psi^\dagger(x) = A e^{2i\lambda\phi(x)} \tag{4.14}$$

$$\tag{4.15}$$

Ensuring that the electron field fulfils the appropriate anticommutation relations imposes A and λ :

$$\psi^\dagger(x) = \frac{U^\dagger}{\sqrt{2\pi\alpha}} e^{i\sqrt{4\pi}\phi(x)} \text{ and } \psi(x) = \frac{U}{\sqrt{2\pi\alpha}} e^{-i\sqrt{4\pi}\phi(x)}, \tag{4.16}$$

[3] We ignore spin here. Its inclusion would be equivalent to the introduction of another boson type.

where U is an operator which lowers the number of particles by one, called a Klein factor. It also ensures the fermionic nature of ψ. In (4.16),α is a short distance cutoff.
Then, the free electron hamiltonian (4.10) can be written as an hamiltonian for the free chiral bosonic field ϕ :

$$\mathcal{H}_0^{(B)} = \hbar v \int \mathrm{d}x \, (\partial_x \phi)^2, \tag{4.17}$$

where the bosonic field admits the following mode decomposition [4] :

$$\phi(x - vt) = \int_{k>0} \frac{\mathrm{d}k}{2\pi} \frac{1}{\sqrt{2k}} [b_R(k) e^{ik(x-vt)} + b_R^\dagger(k) e^{-ik(x-vt)}] \tag{4.18}$$

Before using the formulae (4.16) to express the interacting hamiltonian in bosonic terms, it will be useful for the next chapters to notice that operators of the form $e^{i\sqrt{4\pi}\phi}$ are displacement operators for the bosonic modes. More precisely, their action on the vacuum creates a coherent state of bosonic modes with a position-dependent parameter :

$$e^{i\sqrt{4\pi}\phi(x)}|0\rangle = \bigotimes_{\omega>0} D(\lambda_\omega(x))|0\rangle = \bigotimes_{\omega>0} |\lambda_\omega(x)\rangle, \tag{4.19}$$

where $D(\lambda_\omega(x))$ is a displacement operator of parameter $\lambda_\omega(x) = -\frac{1}{\sqrt{\omega}} e^{i\omega x/v_F}$, where the latter is the coherent state parameter for the bosonic mode at energy $\hbar\omega$ (see appendix C). The tensorial product over all positive frequencies reflect the independence of bosonic modes.
Here, the zero temperature Fermi sea is seen as a boson vacuum :

$$|F\rangle = \bigotimes_{\omega>0} |0_\omega\rangle, \tag{4.20}$$

where $|0_\omega\rangle$ is the vacuum state for the boson mode at frequency ω. In $\lambda_\omega(x)$, the phase encodes the position of the single electron excitation. Using eq. (C.14) shows that an n fermion excitation of the form $\psi_R^\dagger(x_1) \ldots \psi_R^\dagger(x_n) \, |F\rangle$ also corresponds to a plasmonic coherent state on top of a Fermi sea corresponding to $N + n$ particles [5].

A coherent wave packet introduced on top of the Fermi sea is now described as a Schrődinger cat state of plasmonic coherent states:

$$\psi^\dagger[\varphi_0] \, |F\rangle = \int \varphi_0(x) \bigotimes_{\omega>0} |\lambda_\omega(x)\rangle \, dx \, . \tag{4.21}$$

Note that in general, the coherent state description presented here is well suited to the description of states that are obtained by adding a few electrons or holes above the Fermi sea. On the other hand, a stationnary state corresponding to a non equilibrium electron distribution such as the one created by a Fermi sea is a very complicated object in this language since it is obtained from a Fermi vacuum by adding a macroscopic number of particles. Nevertheless, the basics of bosonization such as the expression for the electron density and the fermion operators are still valid.

[4] We disregard the zero mode here

[5] For an infinite system, adding a finite number of electrons will not change the chemical potential. this is no longer true for a finite system.

Coupling of the 1D channel under consideration to an external linear environment will produce entanglement which has a simple description in the plasmonic coherent state basis. Exactly as in cavity or circuit QED, this entanglement will induce decoherence of the quantum many body state of the 1D chiral electronic fluid turning it from a pure state into a statistical mixture (see chapter 5). This point of view [29] will be at the heart of our discussion of single electron decoherence in Quantum Hall edges.

Bosonization and interactions

In the situations under consideration here, we will stay in the linear response regime. An example of nonlinear response in a mesoscopic sysem can be found in [117] for a mesoscopic capacitor.
Chiral propagation prevents electrons from experiencing interaction induced backscattering. Furthermore, we do not take into account the spin degree of freedom here. The interaction hamiltonian consequently have the general form of a coupling between charge densities propagating in the same direction[6] :

$$\mathcal{H}_{int} = \int \mathrm{d}x \int \mathrm{d}y\, \rho(x) V(x,y) \rho(y)\,. \tag{4.22}$$

The total hamiltonian can be written in a simple bosonic form :

$$\mathcal{H} = \pi v_F \int \mathrm{d}x\, (\partial_x \phi(x))^2 + \frac{e^2}{\pi} \int \mathrm{d}x\, \mathrm{d}y\, (\partial_x \phi(x)) V(x,y) (\partial_y \phi(y))\,, \tag{4.23}$$

and leads to the following equations of motion for the chiral field ϕ :

$$(\partial_t + v_F \partial_x)\, \phi(x,t) = \frac{e\sqrt{\pi}}{h} \int \mathrm{d}y (\partial_y \phi(y))\, .V(x,y) \tag{4.24}$$

Plasmon scattering

Throughout this manuscript we will consider situations in which an edge channel is coupled to an arbitrary linear environment over a length L. Before and after the interacting region $|x| < L/2$, the bosonic field ϕ describing the edge channel propagates freely, and thus defines *in* (for $x < -L/2$) and *out* (for $x > L/2$) plasmon modes b :

$$\phi^{(in/out)}(x,t) = -\frac{i}{\sqrt{4\pi}} \int_0^{+\infty} \frac{\mathrm{d}\omega}{\sqrt{\omega}} \big(b_\omega^{(in/out)} e^{i\omega(x/v - t)} + h.c. \big). \tag{4.25}$$

The total system { edge channel $\oplus$ environment } is described by an set of bosonic fields $\{\phi_\alpha\}$. Since the dynamics is time translation invariant and ruled by linear equations, the *in* and *out* fields are related via a scattering matrix [7] :

$$\mathbf{\Phi}^{(out)}(\omega) = \mathcal{S}(\omega, L) \mathbf{\Phi}^{(in)}(\omega), \tag{4.26}$$

[6] In standard g-ology terminology [48], it means that we only consider the g_4 term.

[7] This definition for scattering takes the free propagation into account : In the case of noninteracting channels, the scattering matrix is diagonal : $\mathcal{S}_{\beta\alpha}(\omega, L) = \delta_{\alpha\beta} e^{i\omega L/v_\alpha}$.

where $\mathbf{\Phi}^{(in/out)} = (\phi_\alpha)_\alpha$ contains the in and out bosonic fields describing the edge channel and its environment. The properties of the plasmon scattering matrix are detailed in appendix B.

Relation to finite frequency admittances

For a mesoscopic conductor connected to electron reservoirs by external leads (indexed by α), the finite frequency admittance matrix relates the current I_α flowing into the conductor through lead α to the time dependent voltage $V_\beta(t)$ applied to the reservoir connected to the lead β. In the linear response regime:

$$I_\alpha(\omega) = \sum_\beta G_{\alpha\beta}(\omega)\, V_\beta(\omega)\,. \tag{4.27}$$

The plasmon scattering matrix can be related to the linear response of the edge channel to an external classical voltage V. Solving the equation of motion for the bosonic field ϕ, we find that such a voltage creates in the edge channel a coherent state $\mu(\omega)$ of the plasmon modes b. The parameter of this coherent state is related to the Fourier transform of V :

$$\mu(\omega) = -\frac{e}{h}\frac{V_s(\omega)}{\sqrt{\omega}}. \tag{4.28}$$

The particle density is related to the bosonic field :

$$n(x,t) = \frac{1}{\sqrt{\pi}}(\partial_x\phi)(x,t), \tag{4.29}$$

so the total charge stored in the region $[-L/2, L/2]$ is:

$$Q_L(t) = -e\int_{-L/2}^{L/2} \mathrm{d}x\, n(x,t) = -\frac{e}{\sqrt{\pi}}\left(\phi(L/2,t) - \phi(-L/2,t)\right). \tag{4.30}$$

Using the decomposition (4.25) of the bosonic fields in modes, and the definition (B.2) of the scattering matrix, we find the relation between the admittance matrix and the plasmon scattering [136, 137, 135] :

$$G_{\alpha\beta}(\omega) = \frac{e^2}{h}\left(\delta_{\alpha\beta} - \mathcal{S}_{\alpha\beta}(\omega)\right). \tag{4.31}$$

A low frequency expansion of (4.31) provides the value of the circuit element representing the environment in terms of the plasmon scattering matrix's parameters, as will be illustrated in the next chapter.

The following part is devoted to the derivation of the plasmon scattering matrix in the specific case of two edge channels coupled by a short-range Coulomb interaction.

2.2 Plasmon scattering from general considerations

Now, we turn to the specific case of two edge channels coupled over a finite length L. Here, we derive the plasmon scattering matrix on the basis of general considerations. This will lead to an expression for $\mathcal{S}(\omega, L)$ in terms of only three parameters which play in the present case the same role as the Luttinger or Fermi liquid liquid parameters. In appendix B, we also show how the plasmon scattering matrix can be derived from a microscopic model of short range interactions thus relating these three parameters to the microscopic parameters describing interactions.
Each channel $\alpha = 1, 2$ is described by a chiral bosonic field ϕ_α related to the particle density :

$$\rho_\alpha(x,t) =: (\psi^\dagger\psi)(x,t) := \frac{1}{\sqrt{\pi}}\partial_x\phi_\alpha(x,t). \tag{4.32}$$

The equation for this bosonic field in the presence of an external voltage $U_\alpha(x,t)$ is (see appendix B):

$$(\partial_t + v_\alpha\partial_x)\phi_\alpha(x,t) = \frac{e\sqrt{\pi}}{h}U_\alpha(x,t), \tag{4.33}$$

where v_α is the Fermi velocity in the channel α. The scattering matrix relates the bosonic fields ϕ_α on input and output of the interaction region :

$$\phi_\beta^{(out)}(\omega, L/2) = \mathcal{S}_{\beta\alpha}(\omega, L)\phi_\alpha(\omega, -L/2). \tag{4.34}$$

We will now try to infer as much as possible $\mathcal{S}(\omega, L)$ from its physically expected properties. First of all, $\mathcal{S}(\omega, L)$ being a unitary matrix, it can be written as the product of a phase and a $SU(2)$ matrix :

$$\mathcal{S}(\omega, L) = e^{if(\omega,L)}e^{-i\vec{a}(\omega,L)\cdot\vec{\sigma}}, \tag{4.35}$$

where $f(\omega, L)$ and $\vec{a}(\omega, L)$ only depend on ω and L.
The previous paragraph has shown the relation (4.31) between the plasmon scattering and admittance matrices. The applied magnetic field being perpendicular to the plane of the 2DEG, the Onsager-Büttiker relations [14] (see appendix B) impose that the scattering matrix is symmetric :

$$\mathcal{S}_{21}(\omega, L) = \mathcal{S}_{12}(\omega, L)\,. \tag{4.36}$$

Consequently, $a_y(\omega, L) = 0$.

Finally, interactions being short range, we expect the scattering matrix to satisfy the following composition relation :

$$\mathcal{S}(\omega, L_1 + L_2) = \mathcal{S}(\omega, L_1)\mathcal{S}(\omega, L_2)\,, \tag{4.37}$$

which implies that $\vec{a}(L, \omega) = L\vec{b}(\omega)$, and $f(\omega, L) = Lg(\omega)$.

The coupling between the edge channel and its environment being purely capacitive, the admittance must vanish at low frequency. As a consequence, the plasmon scattering matrix tends to the identity at zero frequency :

$$\mathcal{S}(\omega) \to \mathbf{1} \text{ as } \omega \to 0. \tag{4.38}$$

Thus, $\vec{b}(\omega) \to \vec{0}$ and $g(\omega) \to 0$ when $\omega \to 0$. The simplest dependence for $\vec{b}$ and g is linear in ω corresponding to capacitances. this leads to the following expressions for $\vec{a}$ and f :

$$a_x(\omega) = \omega\tau \sin(\theta) \tag{4.39}$$
$$a_z(\omega) = \omega\tau \cos(\theta) \tag{4.40}$$
$$f(\omega) = \omega\tau_0 \,. \tag{4.41}$$

where θ is a fixed angle independent of L. The times τ and τ_0 can be interpreted as times of flight, and have the following expressions:

$$\tau_0(L) = \frac{L}{v_0} \text{ and } \tau(L) = \frac{L}{v}, \tag{4.42}$$

where v_0 and v are characteristic velocities. Finally, the scattering matrix admits the following expression :

$$\mathcal{S}(\omega, L) = e^{i\omega L/v_0} e^{-i\omega L/v(\cos\theta\sigma^z + \sin\theta\sigma^x)}. \tag{4.43}$$

Its $v_\pm$ of the previous matrix are the velocities of the plasmonic eigenmodes :

$$\frac{1}{v_\pm} = \frac{1}{v_0} \pm \frac{1}{v} \,. \tag{4.44}$$

Now that we have represented the effects of short-range coupling in a scattering formalism, we will now seehow it could lead to predictions for experimentally measurable quantities.

2.3 Predictions for experimental quantities

To make quantitative predictions for energy exchange, we make use of the previously described bosonization formalism to evaluate the excess temperature (4.60). Our approach relies on the identification between the heat current carried by quasiparticles and the energy current of the plasmon modes. Then, using the plasmon scattering approach to account for interactions, we can find the evolution of the plasmon occupation number with respect to the copropagation length.

Relation between injected noise and energy current

The heat current in channel α is defined in eq. (4.4), with the help of the electronic distribution $f_\alpha(x, \epsilon)$ at the position x along the edge channel α . In (4.4), the energy ϵ is measured from the chemical potential μ_α of the edge channel. Since there is no tunnelling between the two edge channels, this chemical potential is not expected to vary with the position x. The heat current can also be expressed in terms of plasmons :

$$J_\alpha(x) = \int_0^{+\infty} \frac{\mathrm{d}\omega}{2\pi} \hbar\omega\, \bar{n}_\alpha(x, \omega), \tag{4.45}$$

where $\bar{n}_\alpha(x, \omega)$ is the average plasmon occupation number at the position x along the channel α. This relation holds here since we are dealing with DC transport. Thus, the plasmon modes

are not populated on average : $\langle b_{\alpha,\omega}\rangle = 0$ for all frequencies and the only remaining contributions to the heat current are given by (4.45).
The plasmon occupation number is related to the excess current noise:

$$\bar{n}_\alpha(x,\omega) = \frac{2\pi}{e^2}\frac{S_{i_\alpha(x)}(\omega) - \frac{e^2}{4\pi}\omega}{\omega}, \tag{4.46}$$

where $S_{i_\alpha(x)}(\omega)$ is the finite frequency unsymmetrized current noise at position x. In (4.46), the zero point fluctuations have been substracted.
For an equilibrium state at temperature T, the occupation number does not depend on x :

$$\bar{n}_{\alpha,eq}(\omega) = \frac{1}{e^{\hbar\omega/k_BT} - 1}, \tag{4.47}$$

and substituting (4.47) in (4.45) we recover the equilibrium value of the heat current already found in (4.5) : $J_{\alpha,eq} = (k_BT)^2\frac{\pi^2}{6h}$.

Before extracting the excess temperature, we will evaluate the excess noise created at a quantum point contact operated at a transparency $\mathcal{T}$. The result will provide the evaluation of the excess noise right after the QPC creating the nonequilibrium distribution in the experiment. The noises in the external and internal channels right after the QPC are given by (3.12), (3.13) and (3.14), as seen in chapter 3, section 1. Here, since the incoming channels are populated by reservoirs at fixed chemical potentials, the current correlators as well as $\mathcal{Q}(t,t')$ (see chapter 3) are stationary and thus only depend on $t-t'$. Their Fourier transform with respect to $t-t'$ can then be expressed in term of the reservoir's electron distribution $n_\alpha(\omega)$. In particular:

$$\mathcal{Q}(\Omega) = \frac{e^2}{2\pi}\int \left(\bar{n}_1(\Omega+\omega)(1-\bar{n}_2(\omega)) + \bar{n}_2(\Omega+\omega)(1-\bar{n}_1(\omega))\right)\, d\omega\,. \tag{4.48}$$

Rewriting $\bar{n}_1(1-\bar{n}_2)+\bar{n}_2(1-\bar{n}_1) = \bar{n}_1(1-\bar{n}_1)+\bar{n}_2(1-\bar{n}_2)+(\bar{n}_1-\bar{n}_2)(n_1-\bar{n}_2)$, the finite frequency noises can then be rewritten as follows:

$$S_{11}^{\text{out}}(\omega) = \mathcal{R}^2 S_{11}(\omega) + \mathcal{T}^2 S_{22}(\omega) + \mathcal{RT}\, S^{\text{exc}}(\omega) \tag{4.49}$$

$$S_{22}^{\text{out}}(\omega) = \mathcal{T}^2 S_{11}(\omega) + \mathcal{R}^2 S_{22}(\omega) + \mathcal{RT}\, S^{\text{exc}}(\omega) \tag{4.50}$$

$$S_{12}^{\text{out}}(\omega) = S_{21}^{\text{out}}(\omega) = -\mathcal{RT}\, S^{\text{exc}}(\omega) \tag{4.51}$$

where the excess noise is given by :

$$S^{\text{exc}}(\Omega) = \frac{e^2}{2\pi}\int (\bar{n}_1-\bar{n}_2)(\Omega+\omega)(\bar{n}_1-\bar{n}_2)(\omega)\, d\omega\,. \tag{4.52}$$

The terms proportional to $\mathcal{R}^2$ and $\mathcal{T}^2$ account for the classical repartition of electrons at the quantum point contact. The $\mathcal{RT}$ contribution account for truly nonequilibrium effects.

In the case of two reservoirs at the same temperature and with different chemical potential, the integral can be evaluated explicitely and this leads to the excess noise at finite temperature and bias voltage V:

$$S^{\text{exc}}(\omega) = \frac{e^2}{2\pi}\left(\frac{\omega+\omega_V}{e^{\beta_{\text{el}}\hbar(\omega+\omega_V)}-1} + \frac{\omega-\omega_V}{e^{\beta_{\text{el}}\hbar(\omega-\omega_V)}-1} - \frac{2\omega}{e^{\beta\hbar\omega}-1}\right) \tag{4.53}$$

where $\omega_V = eV/\hbar$ and $\beta_{\rm el}^{-1} = k_B T_{\rm el}$. Eq. (4.53) is depicted in fig. 4.10 (black dashed line). This expression for the excess noise on output of a quantum point contact has been probed experimentally in [161].

Extraction of the excess temperature

The incoming and outcoming plasmon modes of edge channel α are related by the plasmon scattering matrix :

$$b_{\alpha,\omega}^{(out)} = \mathcal{S}_{\alpha\beta}(\omega, L) b_{\beta,\omega}^{(in)} \,. \tag{4.54}$$

Since $\langle b_{\alpha,\omega}^\dagger b_{\beta,\omega}\rangle = 0$ for $\alpha \neq \beta$, the plasmon occupation numbers in the edge channels on output of a scattering region of length L are given by :

$$\bar{n}_1(\omega, L) = T(\omega, L)\bar{n}_1(\omega, 0) + R(\omega, L)\bar{n}_2(\omega, 0) \tag{4.55}$$

$$\bar{n}_2(\omega, L) = T(\omega, L)\bar{n}_2(\omega, 0) + R(\omega, L)\bar{n}_1(\omega, 0), \tag{4.56}$$

where $T(\omega, L)$ (resp. $R(\omega, L)$) is the probability for a plasmon at energy $\hbar\omega$ to be transmitted in the same channel (resp. sent to the other channel) after a length L. The expression (4.43) of the plasmon scattering matrix gives the following expression for T and R :

$$T(\omega, L) = 1 - R(\omega, L) = \frac{1 + \cos^2\theta}{2} + \frac{1 - \cos^2\theta}{2} \cos\left(\frac{2\omega L}{v}\right). \tag{4.57}$$

We now have all the necessary ingredients to make a prediction for the excess temperature. The total energy current in channel α is the sum of two contributions. The first one is a thermal contribution, which is left intact by the propagation in the interacting region. The second one is a nonequilibrium contribution, which will be affected by the interactions :

$$J_{\alpha,qp} = \frac{\pi^2}{6h}(k_B T)^2 + \frac{R_K}{2}\left(\frac{e^2}{2\pi}\right)^2 \tau(1-\tau) \int_{-\infty}^{+\infty} T(\omega, L) F(\omega, \mu_2 - \mu_1, \beta)\, \mathrm{d}\omega \,, \tag{4.58}$$

where

$$F(\omega, \Delta\mu, \beta) = \frac{\omega + \Delta\mu/\hbar}{e^{\beta(\hbar\omega + \Delta\mu)} - 1} + \frac{\omega - \Delta\mu/\hbar}{e^{\beta(\hbar\omega - \Delta\mu)} - 1} - \frac{2\omega}{e^{\beta\hbar\omega} - 1}. \tag{4.59}$$

Now, if we express the energy current in terms of an effective temperature using (4.5), we associate a nonequilibrium temperature T_{exc} to the nonequilibrium contribution in (4.58) :

$$\left(\frac{k_b T_{exc}}{\Delta\mu}\right)^2 = \frac{3}{\pi^2}\tau(1-\tau)\left(T_\infty + (1 - T_\infty)\frac{\mathrm{sinc}^2(L/L_{\Delta\mu})}{\mathrm{sinhc}^2(L/L_{th})}\right), \tag{4.60}$$

with $L_{\Delta\mu} = \hbar v/e|\Delta\mu|$, $L_{th} = \hbar v\beta$, $\mathrm{sinc}(x) = \frac{\sin x}{x}$ and $\mathrm{sinhc}(x) = \frac{\sinh x}{x}$.

This prediction for the excess temperature will be now compared to experimental datas.

3 Confrontation to experimental results

Here, we test the dependence of the excess temperature on the propagation length L and bias voltage $V = \frac{\mu_2 - \mu_1}{2}$ at fixed QPC transmssion (see fig. 4.7). We also consider its dependence on the transmission of the QPC at fixed length and bias voltage (see fig. 4.8).

3.1 Evolution with respect to bias voltage

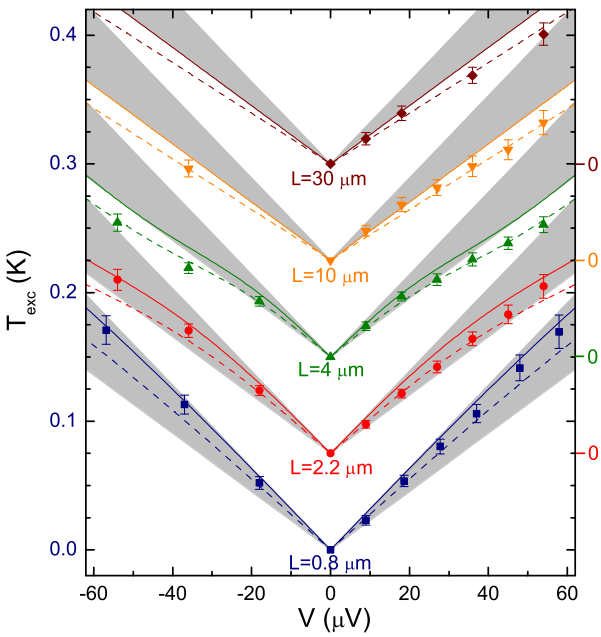

Figure 4.7: Evolution of the excess temperature as a function of the bias voltage applied to the QPC, for a fixed QPC transmission $\tau = 0.5$ (taken from [31]). The excess temperature for different lengths are shifted vertically by $75mK$ for clarity. Solid lines show raw prediction for T_{exc} from (4.60) by taking $T_\infty = 1/2$, and dashed lines the predictions scaled down by 13%. Grey areas show the values of T_{exc} accessible at fixed length and QPC transmission by varying the coupling. All the quantities are calculated with a Fermi velocity of $10^5 m/s$.

The experimental results for $T_{exc}(\Delta\mu, L, \tau, \theta)$ presented in 4.7 agree well with the prediction (4.60) at strong coupling ($\theta = \frac{\pi}{2}$, or equivalently $T_\infty = \frac{1}{2}$). The nonlinear shape of T_{exc} at low $|V|$ is well reproduced, together with the characteristic relaxation length L_{th}.

Nevertheless, we can see that the data points fall off the grey areas that represents the possible values for T_{exc} reachable from our model. Indeed, a systematic scaling down by 13% of the predictions is necessary to reach agreement. This feature can be interpretated as a leak of energy towards other degree of freedom that have not been taken into account. We suggest that these could be the internal modes of the inner edge channel [1]. Indeed, this channel is expected to be wider, and consequently more prone to such phenomena. Another possibility for this energy leak has been proposed in [92]. In this paper, cooperative energy transport between localized states is designated as being responsible for this extra energy exchange. The discussion on this matter remains open, and other contributors [81] have since suggested that the discrepancy actually comes from a renormalization of the density of states at the measurement point by the interactions.

This discrepancy also appears in the dependance of the excess temperature with respct to the QPC transmission which we now discuss.

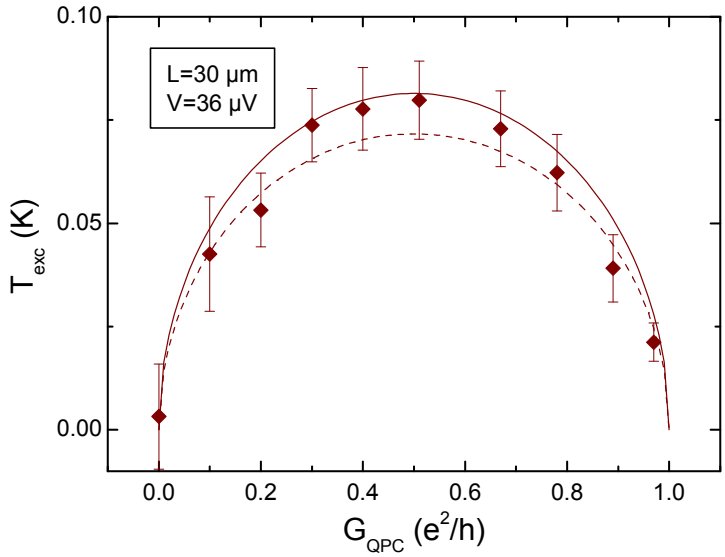

Figure 4.8: Evolution of the excess temperature with the conductance of the QPC (from [31]). Here, the length is set to $L = 30\mu m$ and the bias voltage V is $V = 36\mu V$. The solid line represents the prediction of (4.60) for $L \to \infty$ at strong coupling $T_\infty = 1/2$, and the dashed line the same prediction with a reduction by 13%.

3.2 Dependence with the QPC transmission

Concerning the dependence of the excess temperature with respect to the QPC transmission, the prediction of eq. (4.60) reproduces quite well the $\sqrt{\tau(1-\tau)}$ shape of the experimental results presented in 4.8, still up to the scaling down evoked earlier.

An experimental test of the plasmon scattering approach would be to measure the frequency dependence of the probabilities $R(\omega, L)$ and $T(\omega, L)$ for a plasmon to be transmitted or reflected. Such a measurement could shed light on the mechanism responsible for the extra energy loss. Moreover, it could help discriminate between our approach and an alternative one relying on iterative corrections to free electron propagation that has been proposed by A.M Lunde, S. Nigg and M. Büttiker in [92]. A possible setup for this kind of measurement is described in the next part, together with the expected results as predicted by the plasmon scattering approach.

3.3 Noise measurements to probe plasmon scattering

Being an integrated quantity, the heat current cannot bring energy resolved information. The electronic distribution neither does. Furthermore, the difficulty to provide results concerning this quantity both from theoretical and experimental sides does not make it an ideal quantity to compare theory and experiment. Finite frequency measurements, on their behalf, are able to provide energy resolved information on the dynamics and could be very helpful tool for testing the various approaches.

Here, we propose to make use of the setup depicted in fig. 4.9 to probe in more details the plasmon scattering approach.

Noise measurement setup

The setup proposed in fig. 4.9 relies on finite frequency noise measurements which are now available in the GHz domain [161, 122]. A first quantum point contact is operated in the same way as in the setup in 1 : it creates a nonequilibrium double step distribution in the external channel which copropagates and interacts with the electrons in the external channel. Contrary to the setup described in the first section, here the two channels are separated by choosing an appropriate operating point of the second quantum point contact. This makes the current noises on each channel accessible separately. The quantities to be measured are the finite frequency excess noises at contacts $1'$ and $2'$:

$$S^{(exc)}_{i_\alpha(L)}(\omega) = S_{I_{\alpha'}}(\omega, V) - S_{I_{\alpha'}}(\omega, V = 0)\,, \tag{4.61}$$

where V is the bias voltage at the first quantum point contact.

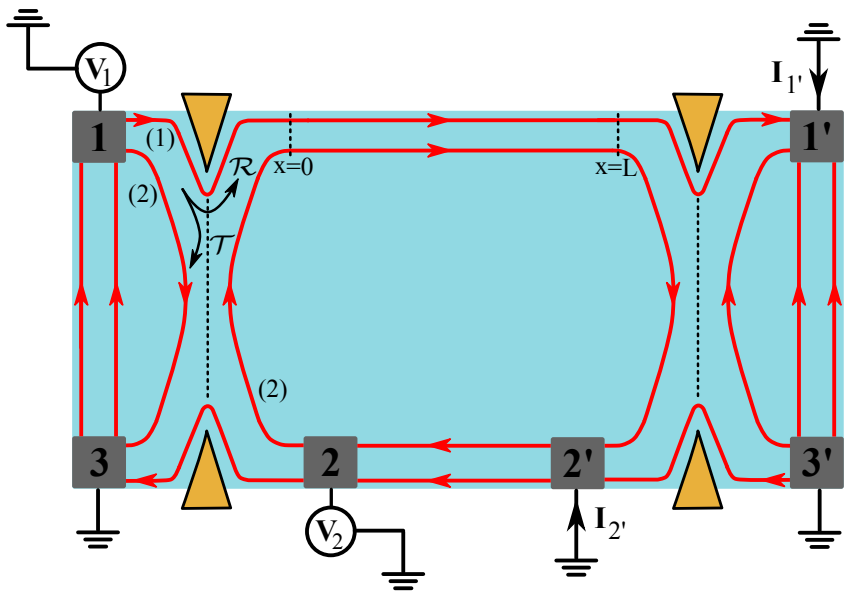

Figure 4.9: Noise measurement setup. The right QPC is set to perfectly reflect the internal channel and perfectly transmit the external one. Voltage drives V_1 and V_2 are applied to the ohmic contacts 1 and 2. The currents $I_{1'}$ and $I_{2'}$ are measured at contacts $1'$ and $2'$.

Expected results for correlation measurements

Figure 4.10 shows the expected results for noise measurements in the configuration depicted in 4.9, using the plasmon scattering matrix (4.43). Indeed, as shown in eq. (4.46), the excess noise is linked to the plasmon occupation number. At $x = L$, the excess noises on channel 1 and 2 are given by :

$$S^{(exc)}_{i_1(L)}(\omega) = T(\omega, L) S^{(exc)}_{i_1(0)}(\omega) \tag{4.62}$$

$$S^{(exc)}_{i_2(L)}(\omega) = R(\omega, L) S^{(exc)}_{i_2(0)}(\omega). \tag{4.63}$$

Thus, the use of the expression (4.57) for T and R implies oscillations in the excess current noise measured on output of the scattering region. The zero frequency excess noise

$$S^{(exc)}_{i_\alpha(L)}(\omega = 0) = e^2\tau(1-\tau)\frac{eV}{h}\left(\coth\left(\frac{eV}{2k_BT}\right) - \frac{2k_BT}{eV}\right) \tag{4.64}$$

is left untouched by the interactions since the scattering matrix for plasmons tends to the identity at low frequencies (see appendix B).

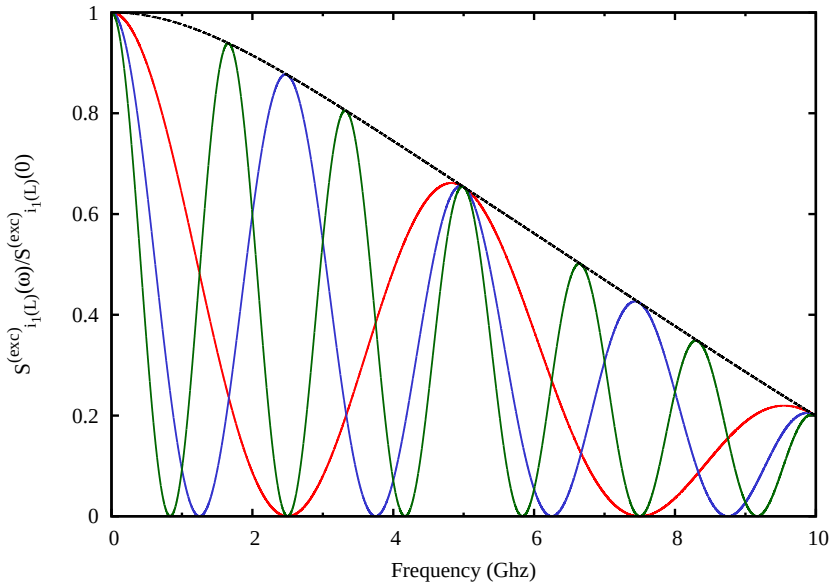

Figure 4.10: Expected excess noise after interchannel coupling over various lengths : $L = 10\mu m$ (red),$L = 20\mu m$ (blue) and $L = 30\mu m$ (green). The dashed black line represents the injected excess noise.

4 Conclusion

In this chapter, we have developped a plasmon scattering approach to interactions in the integer quantum Hall regime. This method will be used throughout the rest of this thesis to deal with interaction effects.
Here, we have applied this approach to a simple model for capacitively coupled copropagating edge channels and have obtained predictions for the excess temperature characterizing the energy exchange between the two channels.
These predictions agree well with the experimental findings [31], up to a systematic energy loss, possibly towards other degrees of freedom (gapless additional modes due to smooth edge confinement, for example [1]). A possible extension of this work could be for example to derive a similar plasmon scattering theory that takes these additional modes into account.
Another approach [92] to the energy relaxation problem has been proposed by Lunde, Nigg & Büttiker which relies on iterative corrections to free electron propagation. These corrections are implemented by the mean of an equation of motion technique. This other proposition also reaches good agreement with experimental data. Furthermore, it also gives predictions for the evolution of the nonequilibrium distribution. In this work, the energy loss is accounted for by the cooperative energy transfer into nonpropagating modes existing in the bulk of the sample.
To get a deeper insight on the relaxation process, we have proposed a finite frequency noise measurement setup. Our design allows the measurement of all the current noises in the system and could bring more information on the mechanism responsible for energy losses and could help discriminating between the plasmon scattering and equation of motion approaches.

One missing point in our study is a prediction for the nonequilibrium occupation number of electrons. The biaised quantum point contact injects a far from equilibrium distribution which contains a macroscopic number of electrons. An adaptation of the ideas of nonequilibrium bosonization [61, 60, 62, 59] would be necessary to deal with the interactions along the same lines.

Our plasmon scattering approach will be used in the next chapters to study the decoherence and relaxation of single elecron excitations. In this case, nonperturbative predictions will be made for the occupation number (in chap.5) and the whole coherence function (in chap.6). From these studies, we will be able to find informations on the regime in which electron quantum optics ideas are valid.

Chapter 5

Decoherence and relaxation of single electron excitations

Contents

1 Relaxation of an energy resolved single electron excitation 86

1.1 Statement of the problem 86

1.2 General results for a wavepacket 87

1.3 Relaxation of a single electronic excitation 91

2 Low energy relaxation 95

2.1 Elastic scattering probability 96

2.2 Occupation number 98

2.3 Conclusion 99

3 Relaxation at higher energy 101

3.1 The dynamical Coulomb blockade regime 101

3.2 Drowning of the quasiparticle 101

3.3 Energy interpretation 103

4 Conclusion 105

In chapter 2, we have left aside the problem of how interactions affect the propagation of single electron excitations. Nevertheless, as we have shown in chapter 4, the coupling of an edge channel to its electromagnetic environment induces energy exchange and is responsible for the relaxation of electronic excitations. Being able to evaluate the effect of interactions in particular situations is of crucial importance to test the validity of the electron quantum optics paradigm described in chapter 1. In particular, it is of crucial importance to study how interactions affect the propagation of a single electron at a given energy above the Fermi level.

Here, we address the problem of decoherence and relaxation of an energy resolved single electronic excitation under the influence of its electromagnetic environment in the spirit of Landau's quasiparticle problem[83]. We will first present a general solution to this problem, underlining the different contributions arising in the coherence function. The two following sections will then describe the relaxation processes at low and high injection energy. In both cases, the study will rely on analytical results and their numerical evaluation.

1 Relaxation of an energy resolved single electron excitation

This part first explains and motivates the study of the relaxation of an energy resolved single electron excitation at zero temperature. Then, details concerning the method adopted for the resolution are given. They preceed the general results for the expected coherence function.

1.1 Statement of the problem

As stated in chapter 2, the injection of a single electron with a wave function φ in a quantum Hall edge channel is equivalent to the action of the following operator on the Fermi sea :

$$\psi^\dagger[\varphi] = \int_{-\infty}^{+\infty} \mathrm{d}x\, \varphi(x)\, \psi^\dagger(x)\,. \tag{5.1}$$

The density operator describing the Fermi sea and this extra particle is :

$$\rho_{in} = \psi^\dagger[\varphi]|F\rangle\langle F|\psi[\varphi] = \int dy_+ dy_- \varphi(y_+)\varphi^*(y_-)\psi^\dagger(y_+)|F\rangle\langle F|\psi(y_-). \tag{5.2}$$

We then assume that the edge channel can be divided in three distinct regions (see Fig. 5.1). The central region, called the interaction region, is where the coupling to the external circuit and/or interactions acts. The two external regions, respectively called the incoming and outcoming regions, are located respectively before and after the interaction region with respect to chiral electron propagation. In these two regions, electrons propagate freely. Equivalently, we assume that in this region long range Coulomb interactions are screened by a suitable set of electrostatic gates.
These assumptions justify the use of a scattering formalism . Furthermore, we will make use of the bosonization technique (see previous chapter) and describe interactions effects by a scattering matrix for edge magnetoplasmons.
Both the incoming and outcoming regions are connected to Ohmic contacts at fixed chemical potentials. Electronic excitations are generated in the input region using for example an AC drive applied to the input Ohmic contact or by another source located deep inside the input region. This source could for example be a tunneling tip connected to an electron reservoir at potential V_0 or a single electron source [38].

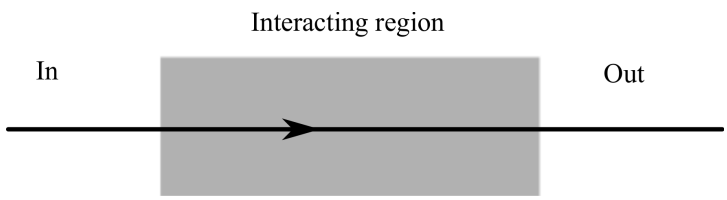

Figure 5.1: Input/output setup : the interaction region is supposed to have a finite extension, from $x = 0$ to $x = L$. The electrons in incoming and outcoming regions propagate freely.

We are then looking for the expression of the single particle coherence $\mathcal{G}^{(e)}_{out}$ in the outcoming region Usually, it is measured at a given position and at different times $\mathcal{G}^{(e)}(x_D, t|x_D, t')$. However, in the geometry considered here, it is equivalent to consider the spatial dependence

of $\mathcal{G}^{(e)}$ in the outcoming region due to the chiral relativistic motion of electrons in this region. Furthermore, we also assume that the density of states is the one of free chiral fermions in the outcoming region :

$$\mathcal{G}^{(e)}_{\text{out}}(x,y) = \text{Tr}\left(\psi_{\text{out}}(x).\,\rho_{\text{in}}.\,\psi^{\dagger}_{\text{out}}(y)\right) \tag{5.3}$$

where the ψ_{out} and $\psi^{\dagger}_{\text{out}}$ fields represent the fields within the outcoming region[1]. The density operator ρ_{in} represents the many body state injected into the system by the source.

To illustrate the physics of electron decoherence following from our results, we will discuss three important examples :

(i) The case of two edge channels coupled by a screened potential, as described in chapter 4.

(ii) A single edge channel coupled to a quantum RC circuit [30]. This illustration is motivated by the modelling of an on the fly detector for qubits travelling along quantum Hall edge channels [36]. The derivation of the associated scattering matrix is given in the appendix B.

(iii) An edge channel capacitively coupled to a closed channel over a length l. Here, the transmission coefficient is a phase : $t_b(\omega) = e^{i\varphi(\omega)}$ where $\varphi(\omega)$ is highly nonlinear. It will illustrate that single electron relaxation and decoherence can also occur in the absence of an external environment for the edge channel. This example has been studied experimentally by F. Pierre and his collaborators [3] and by P. Roche and his collaborators [2]

The next paragraph presents our approach to the relaxation of a single electron wavepacket. In particular, we show how the single particle coherence function can be cast in a form analogous to (2.45) in the presence of interactions. Then, the specific case of a planewave will be discussed in the light of these general principles.

1.2 General results for a wavepacket

Decoherence of an electronic wavepacket

Assuming that the plasmon scattering matrix $\mathcal{S}(\omega)$ is known, the output state produced by the interactions can be computed directly. At zero temperature, the initial state of the total system (edge channel $\oplus$ environment) is factorized and can be written as :

$$|\Psi_i\rangle = \left[\int_{-\infty}^{\infty} \varphi(y) \left(\bigotimes_{\omega>0} |-\lambda_\omega(y)\rangle\right) dy\right] \otimes \left(\bigotimes_{\omega>0} |0_\omega\rangle\right) , \tag{5.4}$$

where the electronic state (5.1) has been written in bosonic terms and $\left(\bigotimes_{\omega>0} |0_\omega\rangle\right)$ denotes the vacuum state for all environment modes. The position dependent coherent state parameter is (see chapter 4):

$$\lambda_\omega(y) = -\frac{1}{\sqrt{\omega}} e^{-i\frac{\omega y}{v_F}} . \tag{5.5}$$

[1]Formally extended to $-\infty$ in order to be able to describe all excitations of a chiral edge channel.
[2]Poster presentation in the "Rencontres de Moriond" 2011 by P.A Huyn.

In quantum optics, classical coherent waves sent onto a beam splitter come out as classical coherent waves whose amplitudes are given by the transmission and reflexion amplitudes of the beam splitter. At the quantum level, this property translates into scattering of coherent states by the beam splitter: at a given frequency $\omega/2\pi$, an initial factorized coherent state $|\alpha_\omega\rangle \otimes |\beta_\omega\rangle$ is sent onto the factorized coherent state $|\alpha'_\omega\rangle \otimes |\beta'_\omega\rangle$ where

$$\alpha'_\omega = t_a(\omega)\alpha_\omega + r_b(\omega)\beta_\omega \tag{5.6a}$$

$$\text{and } \beta'_\omega = r_a(\omega)\alpha_\omega + t_b(\omega)\beta_\omega \,. \tag{5.6b}$$

Applying this to the state $\otimes_{\omega>0}(|-\lambda_\omega(y)\rangle \otimes |0_\omega\rangle)$ appearing in (5.4) leads to the outcoming edge channel / environment entangled state :

$$|\Psi_f\rangle = \int \varphi(y) \bigotimes_{\omega>0} [|-t_b(\omega)\lambda_\omega(y)\rangle \otimes |-r_b(\omega)\lambda_\omega(y)\rangle] \, dy \,. \tag{5.7}$$

The effect of interactions on the electronic dynamics is seen through the many-body reduced density operator for the edge channel. It is obtained by tracing out over the environment's degrees of freedom (see chapter 1) :

$$\begin{aligned} \rho_{1D} &= \int dy_+ dy_- \, \varphi(y_+) \, \varphi(y_-)^* \mathcal{D}_{\text{ext}}(y_+, y_-) \\ &\times \bigotimes_{\omega>0} |-t_b(\omega)\lambda_\omega(y_+)\rangle\langle -t_b(\omega)\lambda_\omega(y_-)| \end{aligned} \tag{5.8}$$

where the extrinsic decoherence coefficient $\mathcal{D}_{\text{ext}}(y_+, y_-)$ is the overlap of the environment's states associated with two different positions $y_\pm$. Its explicit expression is:

$$\mathcal{D}_{\text{ext}}(y_+, y_-) = \exp\left(\int_0^{+\infty} R(\omega) \, (e^{-i\frac{\omega\,\Delta y}{v_F}} - 1) \, \frac{d\omega}{\omega}\right) \tag{5.9}$$

where $\Delta y = y_+ - y_-$ and $R(\omega) = |r_b(\omega)|^2$ denotes the probability that a plasmon at energy $\hbar\omega$ is scattered into the environmental modes. In the case of the RC circuit, this corresponds to photon emission into the transmission line. For the cases of coupled channels, the scattering of a plasmon with a given energy $\hbar\omega$ generates a plasmon at the same energy, since the scattering is elastic for plasmonic modes.

The plasmon transmission coefficient can be written as $t_b(\omega) = e^{i\omega\tau_0}\mathcal{T}(\omega)$, where τ_0 accounts for the total linear dephasing :

$$\tau_0 = -i\frac{d\text{Log}(t_b(\omega))}{d\omega}(\omega = 0) \,. \tag{5.10}$$

The outcoming electronic excitations in (5.8) are not bare electrons. They are collective excitations of the Fermi sea corresponding to an electron dressed by particle hole pairs generated by the interactions :

$$\tilde{\psi}^\dagger(y) = \frac{1}{\sqrt{2\pi a}} U \otimes \left[\bigotimes_{\omega>0} D(-t_b(\omega)\lambda_\omega(y))\right] \tag{5.11a}$$

$$= e^{i\int_0^{+\infty} \Im(t_b(\omega))\frac{d\omega}{\omega}} \, \psi^\dagger(y) \left[\bigotimes_{\omega>0} D_{b_\omega}\left(\lambda_\omega(y)(1 - t_b(\omega))\right)\right] \,. \tag{5.11b}$$

The linear phase $e^{i\omega\tau_0}$ in $t_b(\omega)$ represents a time delay for the electron, and thus does not lead to decoherence. This linear phase reflects the ambiguity on the choice of the position y in the decomposition (5.11b). As shown in appendix C, the appropriate choice corresponds to $t_b(\omega) \to 1$ at high energies. When the dressed electron operator (5.11b) acts on the Fermi sea, it generates the state

$$\tilde{\psi}^\dagger(y)|F\rangle = e^{i\int_0^{+\infty}\frac{d\omega}{\omega}\Im(t_b(\omega))}\,\psi^\dagger(y_\pm)|g(y)\rangle \tag{5.12}$$

where

$$|g(y)\rangle = \bigotimes_{\omega>0}|(1-t_b(\omega))\lambda_\omega(y)\rangle \tag{5.13}$$

contains all e/h pairs created during the interaction between the edge channel and the environment. This leads to the following expression for the outcoming single particle coherence :

$$\mathcal{G}^{(e)}_{out}(x,y) = \int \varphi(y_+)\varphi^*(y_-)\langle F|\widetilde{\psi}(y_-)\psi^\dagger(y)\psi(x)\widetilde{\psi}^\dagger(y_+)|F\rangle\mathcal{D}_{\text{ext}}(y_-,y_+)\,dy_+dy_- \ . \tag{5.14}$$

We will now see how to separate this expression into two contributions with clear physical interpretation.

Different contributions to the coherence function

An electronic wavepacket φ introduced on top of the Fermi sea admits the following first order coherence function in the absence of interactions (see chapter 2, eq. (2.45)) :

$$\mathcal{G}^{(e)}(x,y) = \mathcal{G}^{(e)}_\mu(x,y) + \varphi(x)\varphi^*(y)\,. \tag{5.15}$$

The aim of the following paragraphs is too show that an analogous separation can be done also in the interacting regime. Such a decomposition will make the evaluation of $\mathcal{G}^{(e)}_{out}$ in Fourier space easier, and it will also provide a clear physical interpretation to the two arising contributions.

A generalized Wick theorem proved in appendix C naturally provides a suitable decomposition of the coherence function. It shows that $\mathcal{G}^{(e)}(x,y)$ can be decomposed into a *wavepacket* contribution $\mathcal{G}^{(e)}_{\text{wp}}(x,y)$ analogous to the second term in (5.15) and another which we call the *modified vacuum* contribution and denote by $\mathcal{G}^{(e)}_{\text{mv}}(x,y)$, which is the analogue of $\mathcal{G}^{(e)}_\mu(x,y)$ in the interacting regime.

Wavepacket contribution

Detailed computations given in appendix C lead to the following exact expression for the wave packet contribution to $\mathcal{G}^{(e)}_{\text{out}}(x,y)$:

$$\mathcal{G}^{(e)}_{\text{wp}}(x,y) = \int \varphi(y_+)\,\varphi(y_-)^*\,\langle\psi(y_-)\,\psi^\dagger(y)\rangle\langle\psi(x)\psi^\dagger(y_+)\rangle\,C_{y_+}(x,y)\,C_{y_-}(y,x)^*\,dy_+dy_- \tag{5.16a}$$

$$C_{y_+}(x,y) = \exp\left\{\int_0^{+\infty}\frac{d\omega}{\omega}(1-t_b(\omega))\left[e^{-\frac{i\omega y_+}{v_F}}\left(e^{\frac{i\omega y}{v_F}} - e^{\frac{i\omega x}{v_F}}\right)\right]\right\} \tag{5.16b}$$

In this expression, $\langle\psi(x)\psi^\dagger(y_+)\rangle_F$ and $\langle\psi(y_-)\psi^\dagger(y)\rangle_F$ are free electron propagators. The interaction effects are contained in the exponential factors $C_{y_+}(x,y)$ and $C_{y_-}(y,x)^*$.

Assuming that the incident wavepacket is still well above the Fermi sea after its interaction with the environment, the two point functions $\langle\psi(x)\psi^\dagger(y_+)\rangle$ and $\langle\psi^\dagger(y)\psi(y_-)\rangle$ can be approximated by their free particle expressions $\delta(x-y_+)$ (resp. $\delta(y-y_-)$) in (5.16a).
This heuristic argument leads to a simplified expression for the wave packet contribution to $\mathcal{G}^{(e)}_{\rm wp}(x,y)$ which is expected to be valid as long as dissipation does not bring the incident wave packet onto the Fermi surface:

$$\mathcal{G}^{(e)}_{\rm wp}(x,y) \simeq \mathcal{D}_{\rm tot}(x,y)\,\varphi(x)\,\varphi(y)^*\,, \tag{5.17}$$

where

$$\mathcal{D}_{\rm tot}(x,y) = \exp\left(\int_0^{+\infty} 2\Re(1-t_b(\omega))(e^{-i\frac{\omega\,(x-y)}{v_F}}-1)\,\frac{d\omega}{\omega}\right). \tag{5.18}$$

The expression above can be interpreted as an effective decoherence coefficient that describes dissipative effects on the injected particle. This decoherence coefficient is indeed the product $\mathcal{D}_{\rm tot}(x,y) = (\mathcal{D}_{\rm ext}\times\mathcal{D}_{\rm int})(x,y)$ of the extrinsic contribution due to the external environment (5.9) and of the intrinsic decoherence coefficient $\mathcal{D}_{\rm int}(x,y) = \langle g(y)|g(x)\rangle$ whose explicit expression is given by:

$$\mathcal{D}_{\rm int}(x,y) = \exp\left(\int_0^{+\infty} |1-t_b(\omega)|^2\,(e^{-i\frac{\omega\,(x-y)}{v_F}}-1)\,\frac{d\omega}{\omega}\right). \tag{5.19}$$

This intrinsic decoherence coefficient accounts for the loss of coherence associated to the particle/hole pairs generated in the Fermi sea by the interactions. The total decoherence coefficient (5.18) is nothing but the influence functional introduced in chapter 1 which contains the effects of the coupling to the external environment and of the many body dynamics. In terms of impedances, the total decoherence coefficient (5.18) depends on the total admittance $\Re(1-t)$ of the electromagnetic environment, including the contribution of the Fermi sea.
In this regime, the Fermi sea appears as an extra dissipation channel which must be taken into account into an effective environment in the spirit of the dynamical Coulomb blockade theory [72, 33]. Note that here, this picture emerges in the high energy limit, when the extra-particle does not relax down to the Fermi surface. This case describes the electron quantum optics paradigm in the presence of interactions (see chapter 1). The section 3 will show under which conditions this picture is valid in the chosen examples.
Nevertheless, in general, the indiscernability of electrons plays an important role and as a consequence the Fermi sea cannot be viewed as an independent dissipation channel. However, the general expression (5.16) contains all these effects and properly accounts for the effects of the Pauli principle.

The manifestations of these two limiting regimes in the occupation number for the relaxation of the quasiparticle will be analyzed in detail in section 3. We will now discuss the remaining contribution to the single particle coherence function.

Modified vacuum contribution

As shown in appendix C, the modified vacuum contribution can always be written as arising from an effective many body operator built out of plasmonic coherent states $|g(y)\rangle$ (see Eq. (C.35)):

$$\rho_{\rm mv}[\varphi] = \int \varphi(y_+)\varphi(y_-)^*\langle\psi(y_-)\,\psi^\dagger(y_+)\rangle\frac{|g(y_+)\rangle\langle g(y_-)|}{\langle g(y_-)|g(y_+)\rangle}dy_+dy_-\,. \tag{5.20}$$

The physical meaning of eq. (5.20) is the following: after travelling through the interaction region, the quantum coherences of the initial wave packet have been imprinted into the modified vacuum through the association of the plasmonic coherent state $|g(y)\rangle$ to every position y.

Using Eq. (C.29), the modified vacuum contribution $\mathcal{G}^{(e)}_{\mathrm{mv}}(x,y)$ is of the form

$$\mathcal{G}^{(e)}_{\mathrm{mv},\varphi}(x,y) = \mathcal{G}^{(e)}_{\mu}(x,y)\,\mathcal{F}_{\varphi}(x-y)\,, \tag{5.21}$$

where $\mathcal{F}_{\varphi}(x-y)$ can be interpreted as the decoherence coefficient for the Fermi sea induced by the extra electron. Its expression is given by:

$$\mathcal{F}_{\varphi}(x,y) = \int \varphi(y_+)\varphi^*(y_-)\langle\psi(y_-)\psi^\dagger(y_+)\rangle_F\, C_{y_+}(x,y)C_{y_-}(y,x)^*\, dy_+dy_-\,. \tag{5.22}$$

where $C_{y_+}(x,y)$ is defined by eq. (5.16b).

Having identified the different contributions in the outcoming coherence function let us now discuss in more details the case of an energy resolved single electron excitation.

1.3 Relaxation of a single electronic excitation

Let us now turn to the problem of the relaxation of an energy resolved single electron excitation originally considered by Laudau in Fermi liquid theory [83]. In this theory, a system of interacting fermions is mapped onto a noninteracting Fermi gas of quasiparticles which bear the same properties as bare fermions except for a renormalized mass. In particular, this theory assesses the survival of the quasiparticle close to the Fermi level. Here, the results that we present bring a solution to this issue in the context of chiral quantum Hall edge channels.

To do so, we consider a single electronic excitation $c^\dagger_{k_0}$at energy $\epsilon_0 = \hbar v_F k_0$ above the Fermi level :

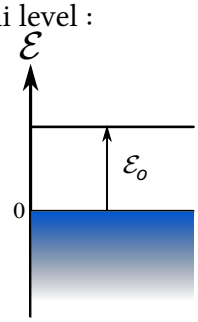

$$|in\rangle = c^\dagger_{k_0}|F\rangle. \tag{5.23}$$

In position space, it is equivalent to the introduction of an electron with a plane wave wavefunction φ_{k_0}:

$$|in\rangle = \psi^\dagger[\varphi_{k_0}]|F\rangle = \int e^{ik_0x}\,\psi^\dagger(x)|F\rangle\,\mathrm{d}x\,.. \tag{5.24}$$

As can be explicitely checked using eq. (5.14) this restores the translation invariance of the single electron coherence $\mathcal{G}^{(e)}_{\mathrm{out}}(x,y)$ since $\varphi_{k_0}(y_+)\,\varphi_{k_0}(y_-)^*$ now only depends on $y_+ - y_-$. Moreover, both the wavepacket and modified vacuum contributions only depend on $x-y$ in this case, as pointed out in chapter 2. In the stationary state under consideration here, the coherence lies in the $k_- = k_+$ line in fig.2.5). Translation invariance of $\mathcal{G}^{(e)}(x,y)$ translates into the absence of coherences in momentum space for electrons: $\langle c^\dagger_k c_{k'}\rangle = 0$ for $k \neq k'$.

At this point, one should remember that the wavepacket φ_{k_0} is not normalized. To regularize the infrared behaviour of the quantities under consideration, we assume that the edge

channel has a finite length L. As a consequence, φ_{k_0} is divided by $\sqrt{L}$ and the incoming coherence is found to be

$$\mathcal{G}^{(e)}(x,y) = 2\pi L\, \mathcal{G}^{(e)}_{\mu}(x,y) + e^{ik_0(x-y)}\,. \tag{5.25}$$

In this expression, the L factor reflects that we are studying single to few electron excitations on top of the Fermi sea which contains a macroscopic number of electrons. In fact, this approach is perturbative in the number of excess electronic excitations introduced on top of the Fermi sea but nonperturbative in the interactions.
Rewriting eq. (5.25) in Fourier space makes this point explicit:

$$L^{-1}\mathcal{G}^{(e)}(x,y) = \int e^{ik(x-y)} \left(\bar{n}_{\mu}(k) + L^{-1}\delta(k-k_0)\right)\, dk\,. \tag{5.26}$$

In the previous equation, $\bar{n}_{\mu}(k)$ is the equilibrium occupation number for a Fermi sea at chemical potential μ .
In the same way, the outcoming electron distribution will consists into the Fermi sea and, on top of this, a $1/L$ perturbation that reflects the relaxation of the extra single electron excitation :

$$\mathcal{G}^{(e)}_{\text{out}}(x,y) = L\int e^{ik(x-y)} \left(\bar{n}_{\mu}(k) + L^{-1}\delta n_{k_0}(k)\right)\, dk \tag{5.27}$$

In the equation above, δn_{k_0} is the deviation of the occupation number from the equilibrium. It is the same quantity as in chapter 3, where the supplementary index k_0 recalls its dependence on the initial wavevector.
Thus, taking the Fourier transform with respect to $x-y$ of $\mathcal{G}^{(e)}_{\text{out}}(x,y)$ for incoming φ_{k_0} and substracting the Fermi sea contribution gives a direct access to the single electron relaxation $\delta n_{k_0}(q)$. This quantity satisfies the sum rule

$$\int \delta n_{k_0}(q)\, dq = 1 \tag{5.28}$$

which reflects particle conservation.

At zero temperature, no energy can be given to the electron and therefore, one expects $\delta n_{k_0}(k) = 0$ for $k > k_0$. Note that at zero temperature, $\delta n_{k_0}(k)$ also vanishes for $k < -k_0$ since the incoming extra electron has just enough energy to draw one electron from momentum $-k_0$ to the Fermi level. As we shall see, $\delta n_{k_0}(k)$ can be decomposed into a quasi-particle peak at $k = k_0$ representing elastic scattering through the interaction region and a regular part $\delta n^r_{k_0}(k)$ representing both the electron relaxation as well as the heating of the Fermi sea (see fig.5.2):

$$\delta n_{k_0}(k) = \delta n^r_{k_0}(k) + Z(k_0)\,\delta(k-k_0) \tag{5.29}$$

where $Z(k_0)$ denotes the elastic scattering probability for an electron at incident energy $\hbar v_F k_0$.

The regular part is positive for $k > 0$ and negative for $k < 0$ since in this case, electrons below the Fermi level can only be extracted through electron/hole pair creation. The goal is then to determine $Z(k_0)$ and $\delta n^r(k)$.

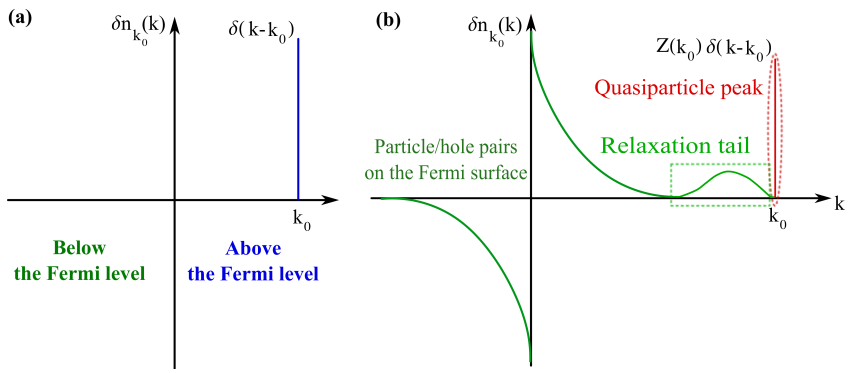

Figure 5.2: Sketch of the excess occupation number. (a) Incoming single electron coherence for an initial energy resolved single electron excitation above the Fermi level. (b) Outcoming single electron coherence $\delta n_{k_0}(k)$: at $k = k_0$, the quasiparticle peak comes is the contribution of electrons ying across the interaction region without loosing energy (elastic scattering probability).

Results

As shown in appendix C, explicit expressions can be obtained for the wavepacket and modified vacuum contributions to the Fourier transform of $\mathcal{G}^{(e)}_{\text{out}}(x, y)$ with respect to $x-y$. The extensive Fermi sea contribution that has to be substracted to obtain $\delta n_{k_0}(q)$ comes from the modified vacuum contribution.

The complete result for $\delta n_{k_0}(q)$ is the sum of a wavepacket contribution $\delta n^{(\text{wp})}_{k_0}(q)$ and of a modified vacuum contribution $\delta n^{(\text{mv})}_{k_0}(q)$ which can be exactly computed from auxiliary functions $A_\pm(q)$ which are solutions of the following equation :

$$\mp q\, A_\pm(q) = 1 - t(-v_F q) + \int_0^{-q} (1 - t_b(v_F k))\, A_\pm(k+q)\, dk\,. \tag{5.30}$$

More precisely, the expressions of the two contributions $\delta n^{(\text{wp})}_{k_0}(q)$ and $\delta n^{(\text{mv})}_{k_0}(q)$are :

$$\delta n^{(\text{wp})}_{k_0}(q) = |\mathcal{Z}(k_0)|^2 \delta(q - k_0) \tag{5.31a}$$

$$+ \; 2\Re(\mathcal{Z}(k_0) J^*(q - k_0)) + \int J(p)^* J(q - k_0 - p)\, dp \tag{5.31b}$$

$$\delta n^{(\text{mv})}_{k_0}(q) = \int_q^{+\infty} G(k_0, k)\, \frac{dk}{2\pi} \tag{5.31c}$$

where $\mathcal{Z}(k_0)$, J and G are expressed in terms of the $A_\pm(q)$ (see appendix C). The complete expressions given in appendix C show that, as expected $\delta n_{k_0}(q)$ has a discontinuity at $q = 0$ associated with the Fermi level and also a delta singularity at $q = k_0$ associated with the elastic scattering of the extra electron through the interaction region.

Elastic scattering probability

At zero temperature, a quasi particule peak of the form $Z(k_0)\, \delta(q - k_0)$ subsists. The weight $Z(k_0)$ represent the probability for the electron to remain at the same energy. This is the amplitude for elastic scattering of the electron across the interacting region. Its explicit expression

is :

$$Z(k_0) = |\mathcal{Z}(k_0)|^2 = \left|1 - \int_0^{k_0} A_-(k)\,\frac{dk}{2\pi}\right|^2 . \tag{5.32}$$

This result can indeed be recovered more directly. Let us consider the amplitude for a single electron excitation of momentum k_0 to be scattered elastically. This amplitude is nothing but the scalar product $\langle \text{out}|\text{in}\rangle$ where the $|\text{in}\rangle$ and $|\text{out}\rangle$ states take into account the environmental modes :

$$|\text{in}\rangle = \int \mathrm{d}y_+\, e^{ik_0 y_+} \left[\bigotimes_{\omega>0} |-\lambda_\omega(y_+)\rangle \otimes |0_\omega\rangle\right]_{\text{in}} \tag{5.33}$$

$$|\text{out}\rangle = \int \mathrm{d}y_+\, e^{ik_0 y_-} \left[\bigotimes_{\omega>0} |-\lambda_\omega(y_-)\rangle \otimes |0_\omega\rangle\right]_{\text{out}} \tag{5.34}$$

Indeed, this quantity represents the overlap between an energy resolved electron in the outcoming region $c^\dagger_{k_0,out}|F\rangle$ and the state $U_{int}c^\dagger_{k_0,in}|F\rangle$, where U_{int} is the evolution operator accounting for the interactions.

Expressing $|\text{in}\rangle$ in terms of the out modes leads to:

$$|\text{in}\rangle = \int dy_+ e^{ik_0 y_+} \left[\bigotimes_{\omega>0} |-t_b(\omega)\lambda_\omega(y_+)\rangle \otimes |-r(\omega)\lambda_\omega(y_+)\rangle\right]_{\text{out}} \tag{5.35}$$

and using eq. (C.19) and $|r(\omega)|^2 + |t_b(\omega)|^2 = 1$, the scalar product becomes:

$$\langle \text{out}|\text{in}\rangle = \int dy_+ dy_- e^{ik_0(y_+ - y_-)} \exp\left(\int_0^{+\infty} (t_b(\omega) e^{i\frac{\omega}{v_F}(y_- - y_+)} - 1)\,\frac{d\omega}{\omega}\right) \tag{5.36}$$

The scalar product is proportional to size of the system as expected from the norm of the wavepacket φ_{k_0}. Dividing by this divergent normalization factor leads to the amplitude for the electron to scatter elastically:

$$\mathcal{Z}(k_0) = \int e^{-ik_0 z} \exp\left(\int_0^{+\infty} (t_b(\omega) e^{i\frac{\omega z}{v_F}} - 1)\,\frac{d\omega}{\omega}\right) dz\,. \tag{5.37}$$

This expression can be shown to be equal to (C.46). This discussion provides a supplementary interpretation to $\mathcal{Z}(k_0)$ as the overlap of the input and output states of the system made of the edge channel and the environment.
The elastic scattering probability also appears naturally as the reduction factor of the visibility in Mach-Zehnder experiments (see chapter 1) for energy resolved single electron excitations. In this context, the interference terms in this case are multiplied by products of amplitudes of the form (5.37). The effect of the coupling to the environment is similar to the one of a voltage probe [16], which has been illustrated experimentally in [134]. In this work, the reduction of the visibility of the interference fringes when the gate voltage is increased is understood as the lowering of the probability to go out of the interferometer without transiting to the voltage probe.

In the next two sections, a detailed analysis of the low and high energy regimes will be presented. The discussion will focus first on the weight of the residual quasiparticle peak and then on the full electron occupation number δn_{k_0}.

2 Low energy relaxation

The plasmon scattering coefficients for the models under consideration here are derived in appendix B. Each model is characterized by a set of dimensionless parameters :

RC circuit The different regimes of this model are parametrized by $\mathcal{R} = R/R_K$, which compares the resistance of the circuit to the resistance quantum, and $\alpha = l/v_F R_K C$ which compares the time of flight l/v_F to the characteristic response time of the circuit.

Coupled channels The coupling strength is represented through an angle $\theta \in [0, \pi/2]$, and the energies will be measured in units of $\hbar v/L$.

Closed channel In this model, the propagative and closed channel are capacitively coupled by short range interactions. Once again, the angle θ accounts for the strength of interactions. The new dimensionless parameter that comes into play is the ratio between the dipolar and charge mode velocities $\gamma = v_+/v_- \leq 1$, which represents the dephasing between the eigenmodes after a copropagation length L.

The real and imaginary parts of these transmission coefficients for different values of the parameters are represented in fig.5.3.

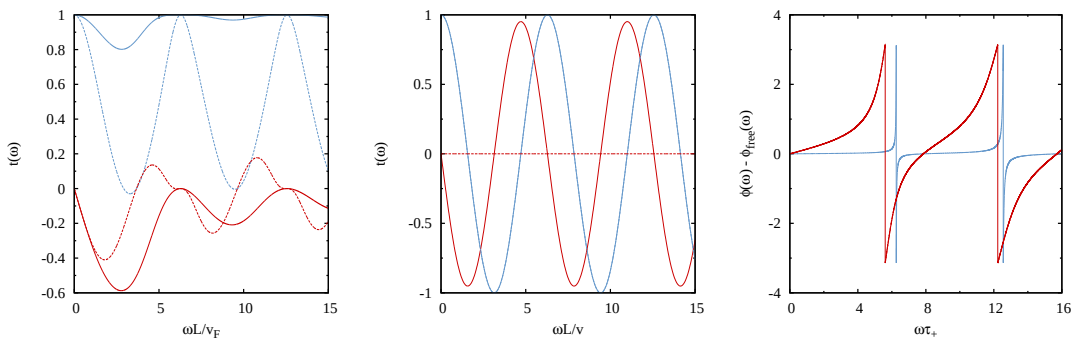

(a) RC circuit (b) Coupled channels (c) Closed channel

Figure 5.3: (a) Real (blue) and imaginary part (red) of the transmission coefficient for the RC circuit for $\alpha = 1/2$, and low resistance ($\mathcal{R} = 0.002$ or $R = 50\,\Omega$,solid lines) or high resistance ($\mathcal{R} = 0.5$ or $R = R_K/2$,dashed lines). From the detection point of view, a fast detector is expected to have a short response time compared to the time of flight L/v_F under the capacitor's influence. This coresponds to high values of α. (b) Real (blue) and imaginary part (red) of the transmission coefficient for coupled channels for low coupling ($\theta = \pi/10$, solid lines) or strong coupling ($\theta = \pi/2$, dashed lines).(c) Nonlinear part of the phase in the case of a closed loop channel for $\gamma = 1/5$. The green curve corresponds to $\theta = \pi/10$ (low coupling) and the orange one to strong coupling $\theta = \pi/2$.

Before going any furher, two remarks on these transmission coefficients must be made:

- The scattering for coupled edge channels ($\nu = 2$ and closed channel cases) does not present a finite spectral bandwidth [3].

[3]This observation is not surprising, since these transmission coefficients are obtained through low energy considerations or a short range interaction model, see appendix B.

- The transmission for the RC circuit has richer features from this point of view : the low $\mathcal{R}$ scattering converges rapidly to 1 but at higher relaxation resistance, the scattering matrix does not trivializes on the same energy scales.

2.1 Elastic scattering probability

At low energy, the elastic scattering probablity tends to one : the quasiparticles are not sensitive to decoherence and relaxation mechanism when they are injected close to the Fermi level, as expected when metallic reservoirs dominate the dynamics. This common feature to all the models under consideration in this thesis originates in the low energy behaviour of the scattering matrix, which tends to the identity as $\omega \to 0$ [4].

Circuit equivalent at low energy

At low energies, it is interesting to describe the quantum circuit formed by the edge channel coupled to the environment in terms of discrete circuit elements. This discrete circuit elements approach was developed by Prêtre, Thomas & Büttiker in [128, 18] to study quantum transport at finite frequency. It is valid as long as the frequency is low compared to the inverse of the longest time of flight in the system. This description is contained within the low frequency expansion of the admittance $y(\omega) = 1 - e^{i\omega l/v} t_b(\omega)$ which is of the form

$$y(\omega) = -iR_K C_\mu \omega + R_K R_q (C_\mu \omega)^2 - i(R_K C_\mu \omega)^3 \left[\frac{L_q/C_\mu}{R_K^2} - \frac{R_q^2}{R^2} \right] + y_4 (R_q C_\mu \omega)^4 + \dots \quad (5.38)$$

where $C_\mu^{-1} = \frac{1}{C} + \frac{v_F R_K}{l}$ denotes the electrochemical capacitance of the complete circuit that takes into account the density of states, $R_q = R + R_K/2$ its total relaxation resistance and L_q its total kinetic inductance that accounts for the dynamical effects [22, 127]. These three parameters are sufficient for describing the expansion up to order three. Pushing the expansion one step further requires one extra parameter y_4.
This approach is very similar to the one adopted by Blanter, Hekking and Büttiker [11], in which the finite frequency admittance is related to the interaction parameter of the Luttinger liquid. In this work, it is suggested that a better understanding of electron/electron interactions can be reached via low frequency admittance measurements. The recent progresses in this direction in the GHz range [46, 45] have already confirmed earlier predictions on the quantum RL and RC circuits, and provide a good opportunity to probe experimentally plasmon scattering properties.

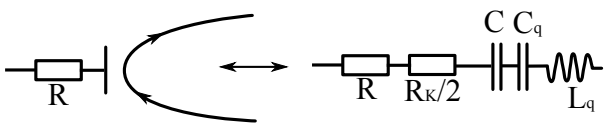

Figure 5.4: Sketch of the quantum circuit equivalent to the system comprising the edge channel and its environment. R_q is the total relaxation resistance, C_μ the quantum capacitance, and L_q the kinetic inductance.

[4] This comes from the capacitive capacitive coupling, see appendix B.

As shown in appendix C, the single electron coherence does not change when multiplying $t_b(\omega)$ by a phase linear in ω. Therefore, one could replace $t_b(\omega)$ by $t_{\text{eff}}(\omega)$ defined by

$$1 - t_{\text{eff}}(\omega) = e^{iC_\mu R_K \omega} y(\omega)\,. \tag{5.39}$$

The low frequency expansion of the admittance (5.38) then leads to a low frequency expansion for $t_{\text{eff}}(\omega)$ which can in turn be used to obtain an expansion of $A_-(q)$ in powers of $-q$ for $q < 0$.

Using the expression for the elastic scattering probability from $A(q)$ as detailed in the appendix C finally leads to the low energy expansion of the elastic scattering probability in powers of $R_K C_\mu \omega$ of the form :

$$Z(\omega) = 1 - Z_2 (R_K C_\mu \omega)^2 - Z_4 (R_K C_\mu \omega)^4 - \dots \tag{5.40}$$

where the coefficients are given by ($R_q = R + R_K/2$):

$$Z_2 = \frac{R}{R_K} = \frac{R_q}{R_K} - \frac{1}{2} \tag{5.41a}$$

$$Z_4 = \frac{1}{2}\left(\Re(y_4) + \frac{5}{12}\left(\frac{R_q}{R_K}\right)^2 + \frac{1}{12}\frac{R_q}{R_K} - \frac{L_q/C_\mu}{R_K^2} - \frac{1}{96}\right)\,. \tag{5.41b}$$

This shows that as soon as $R \neq 0$, the low energy inelastic scattering is dominated by photon emission within the external circuit. The probability for inelastic scattering at a given energy ε thus scales as ε^2 which shows that the quasi particles survives down to the Fermi sea. This result is universal : it does not depend on the particular form of the scattering coefficient. Furthermore, this simple result can be recovered by a perturbative expansion at first order in $1 - t_b$, which gives that $Z(\omega) \simeq 1 - t_b''(0)\omega^2$.

In the case of a passive gate described as an RC circuit with $R = 0$, the relaxation resistance is given by the relaxation resistance of the edge channel: $R_q = R_K/2$ and this leads to $Z_2 = 0$. The kinetic inductance is also fixed and given by $L_q = R_K^2 C_q$ where $C_q = \frac{l}{v_F R_K} = le^2\nu$ is the edge channel's quantum capacitance (ν is the density of states).
The y_4 coefficient is also determined from the plasmon scattering matrix and substituting these parameters shows that the fourth order vanishes. Indeed, inelastic scattering arises at order six:

$$1 - Z(\omega) = \frac{11\,(C/C_q)^2}{25920}\,(\omega R_K C_\mu)^6\,. \tag{5.42}$$

As expected, the passive gate leads to a much weaker low energy inelastic scattering than a dissipative external circuit. Contrary to the expansion at second order, this result is not universal, since it still depends on the geometrical capacitance C.

In the case of coupled channels, fig. 5.5(b) shows that the elastic scattering probability decays quadratically at low energy for all coupling strengths. As in the case of the quantum RC circuit, the deviation to the quadratic approximation appears more clearly for lower couplings as seen on the red curve in fig. 5.5(b). It could also be seen on this graph that the relaxation resistance increases with the coupling strength, as expected. In the strong coupling case, the equivalent resistance for the conductor made of the two channels is $\frac{R_K}{4}$ corresponding to the

parallel association of two resistances equal to $\frac{R_K}{2}$.

For the case of a closed channel, the resonances observed in the scattering phase 5.3 are responsible for brutal decays of the elastic scattering probability at multiples of the resonance frequency $v_+/2\pi L$. The height of this decay increases with the coupling strength, as expected. As long as the initial energy is lower than the associated energy scale, the elastic scattering probability remains close to one : the quasiparticle remains untouched at low energy.

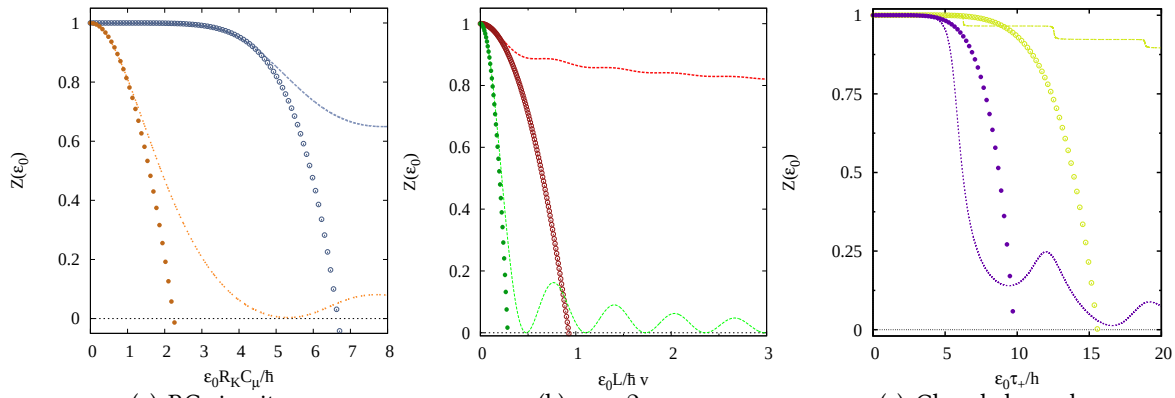

(a) RC circuit (b) $\nu = 2$ (c) Closed channel

Figure 5.5: (a) Low energy behaviour of the elastic scattering probability in the case of the quantum RC circuit for a passive gate (blue) and $\mathcal{R} = 0.5$. Dots represent the low energy expansions in both cases. (b) Low energy behaviour of the elastic scattering probability for the coupled channels model at low ($\theta = \pi/10$,red) and strong coupling ($\theta = \pi/2$, green). Dots represent the low energy expansion (5.40) at order 2. (c) Elastic scattering probability for the coupling to a closed channel at low ($\theta = \pi/10$, yellow) and strong coupling ($\theta = \pi/2$,violet), and $\gamma = 1/5$. The dots show the series expansion up to order 6. The quick departure from the low energy expansion is due to the resonance at L/v_F.

2.2 Occupation number

Relaxation close to the Fermi level can be described using of a simple model which relies on the following two hypothesis :

(i) The Fermi sea is left unaltered by the quasiparticle relaxation : it does not participate to decoherence.

(ii) Quasiparticle relaxation's properties are described by the probability density $p(q)$ to lose momentum q.

Formally, these assumptions are equivalent to assuming that the regular part of the excess occupation number $\delta n_{k_0}(k)$ is nonzero only for $k \in [0, k_0]$, and that it is given by $p(k_0 - k)$. Making use of the normalization condition

$$\int \delta n_{k_0}(k)\, \mathrm{d}k = 1, \tag{5.43}$$

we find that the probability density is given by the derivative of the elastic scattering probability :

$$p(q) = -Z'(q). \tag{5.44}$$

Thus, the excess occupation number is given by[5] :

$$\delta n_{k_0}(k) = -Z'(k_0 - k) + Z(k_0)\delta(k - k_0). \tag{5.45}$$

The figures 5.6 and 5.7 display the low energy behaviour of the excess occupation number for the quantum RC circuit and the coupled channels, in different regimes. The bosonization prediction and the phenomenological expression (5.45) agree well for small injection energies in both cases. The only difference being that the agreement remains at higher energies in low dissipative cases (low resistance or weak coupling between the edge channels). Nevertheless, it is always possible to find an appropriate regime in which the phenomenological expression (5.45) describes the relaxation.

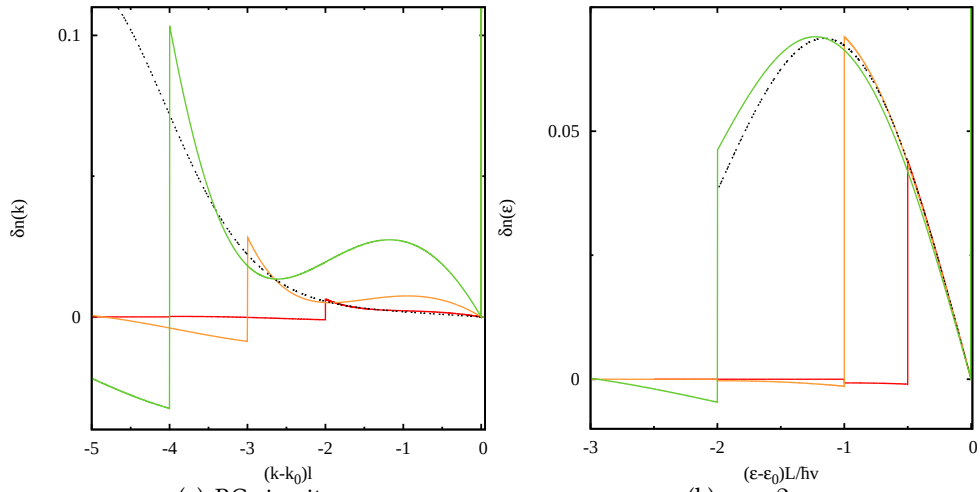

(a) RC circuit (b) $\nu = 2$

Figure 5.6: (a) Low energy limit of the occupation number for $R = 50\,\Omega$ ($\mathcal{R} = 0.002$). Dots represent the low energy phenomenological approximation (5.45). (b) Low energy behaviour of the occupation number for the coupled channels model, at low coupling $\theta = \pi/10$.

In fig. 5.8, the excess occupation number is depicted at low and strong coupling in the closed channel case. In this regime, we can observe no major decrease of $Z(\epsilon_0)$ (see fig. 5.5), which corresponds here to a small creation of electron hole pairs, both in the relaxation tail of the quasiparticle and at the surface of the Fermi sea. This is due to the fact that at low energy, no resonance in the scattering phase has been encountered. When the initial energy of the electron does not reach this energy scale, the excess quasiparticle is almost left untouched. This feature has been probed experimentally in the relaxation experiments described in chapter 4. For this model, the energy associated to the first phase resonance in the plasmon scattering defines the low energy regime [3].

2.3 Conclusion

At low injection energies, relaxation is frozen by the Pauli principle. This result appears both in the elastic scattering probability (which tends to unity at low energies) and in the occupation

[5] This expression can also be reached by a low initial energy expansion of (5.31a), see appendix C.

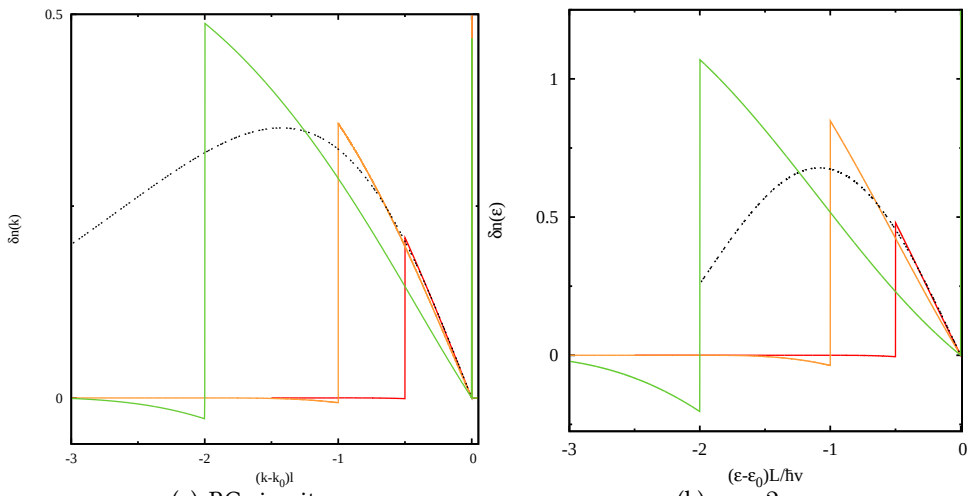

(a) RC circuit (b) $\nu = 2$

Figure 5.7: (a) Low energy limit of the occupation number for $R = \frac{R_K}{2}$ ($\mathcal{R} = 0.5$). Dots represent the low energy phenomenological approximation (5.45). (b) Low energy behaviour of the occupation number for the coupled channels model, at strong coupling $\theta = \pi/2$.

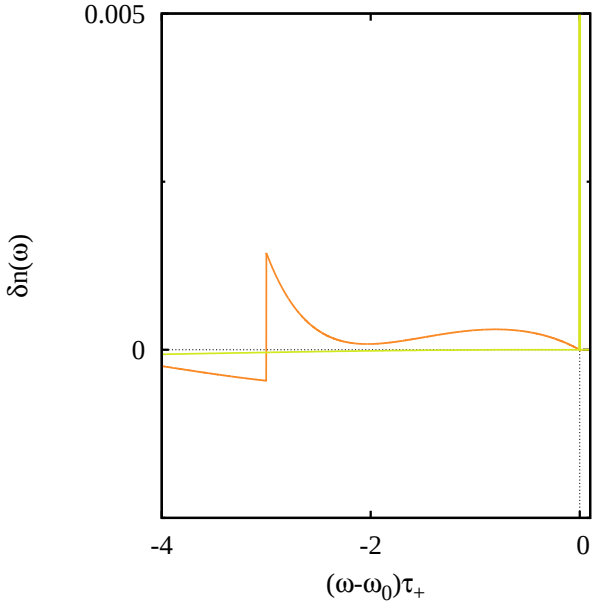

Figure 5.8: Excess occupation number for the closed channel model at low injection energy. At low ($\theta = 0.1$) and strong ($\theta = \pi/2$) coupling. $\gamma = 0.2$ in both cases

number. Close to the Fermi level, the relaxation properties are incoded in the elastic scattering probability and also can be understood through a discrete circuit elements model.

The results at low energy are universal, provided that the injection energy is small compared to the smallest energy scale appearing in plasmon scattering.
The high energy regime displays a richer behaviour, since the results drastically depend on the whole structure of plasmon scattering, and the values of the parameters. The next section will present the different situations that can be encountered at high injection energy.

3 Relaxation at higher energy

In this section, we illustrate the two possible scenarii on the same examples as before. The two limiting situations at high injection energy have already been presented in section 1, and are :

(i) The dynamical Coulomb blockade like regime, where the relaxation tail of the quasiparticle can be separated from the particle/hole pairs at the surface of the Fermi sea. In this case, the coherence function in position space is of the form (5.17).

(ii) The "quasiparticle drowning" case, where the two contributions to the occupation number cannot be separated.

3.1 The dynamical Coulomb blockade regime

When the coupling between the edge channel and its environment is sufficiently low and provided that the bandwidth of the plasmon scattering is finite, the behaviour at high injection energy limit reaches the limiting case formulated by (5.17) in section 1. In this case, the value of the elastic scattering probability at infinite energies is finite (see fig 5.5).

The curves in 5.9 represent δn_{k_0} at high k_0. In the case of the quantum RC circuit at low resistance the coupling to the environment is sufficiently weak and the bandwidth of the scattering is finite so that a simple high energy limit can be reached : the quasiparticle is still defined at high energy and its relaxation tail matches the Fourier transform of the total decoherence coefficient (5.18).
This is no longer the case when the environment consists of a copropagating edge channel. In this situation, the bandwidth of the scattering is not finite and the quasiparticle's relaxation tail merges with the particle/hole pairs at the surface of the Fermi sea, even at low coupling.

3.2 Drowning of the quasiparticle

This paragraph illustrates the consequences of the strong coupling of the edge channel to its environment. In this case, the electron quantum optics limit cannot be reached. The excess quasiparticle is merged into the particle/hole pairs generated at the surface of the Fermi sea by the interactions. The electron gets literally drown into the Fermi sea.

This regime is illustrated in fig. 5.10 and 5.11 in the same cases as before. In the three cases, the regular part of the occupation number cannot be split into clearly separated contributions. This situation is uncompatible with the electron quantum optics paradigm, since the excess quasiparticle cannot be singled out after its travel through the interaction region. In the case of coupled channels at strong coupling the Fourier transform of the total decoherence coefficient (5.17) is negligible compared to the bosonization prediction (see fig.5.10(b)). Relaxation in this case can only be understood by the mean of the complete expressions provided in section 1.

For the closed channel model, the high energy regime is reached when the initial energy exceeds a few resonance energies $\frac{\hbar v_F}{l}$. Even if illustrated at high coupling only in fig. 5.11, the result at high energy in this case is general : the dynamical Coulomb blockade regime cannot be reached. Indeed, the scattering has infinite bandwidth and each resonance is responsible for the creation of particle hole pairs in the Fermi sea. Thus, at high energies, the initial excess

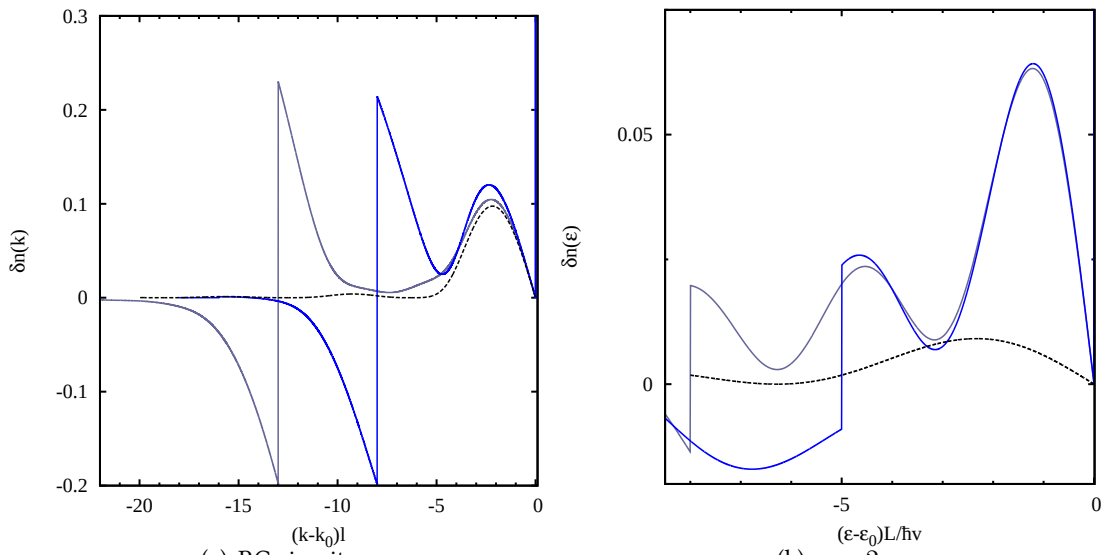

(a) RC circuit (b) $\nu = 2$

Figure 5.9: (a) High injection energy limit of the occupation number for $R = 50\,\Omega$ ($\mathcal{R} = 0.002$). (b) Low energy behaviour of the occupation number for the coupled channels model, at low coupling $\theta = \pi/10$. In both cases, the dashed line represents the Fourier transform of the high energy approximated expression (5.17).

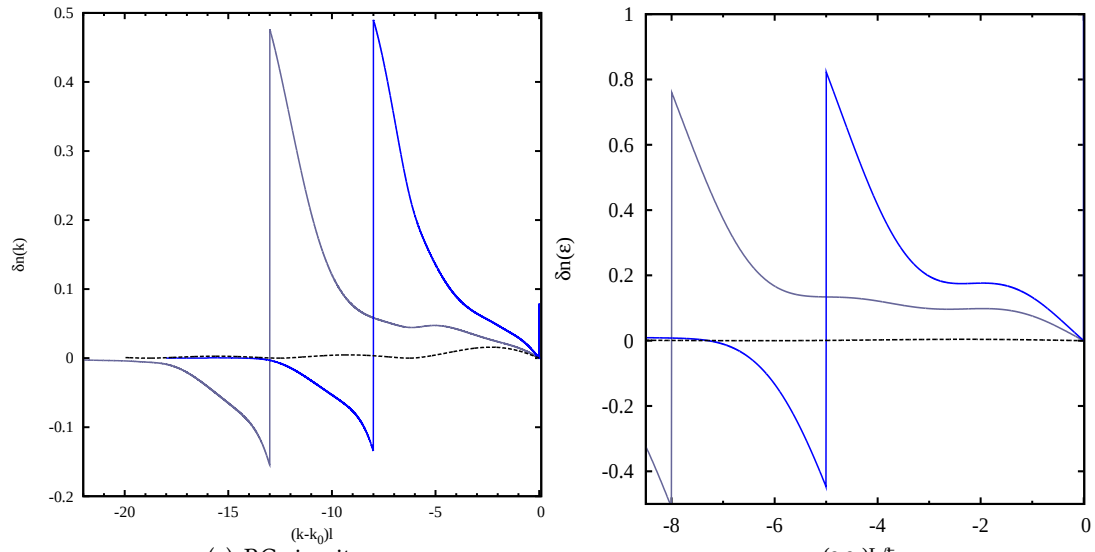

(a) RC circuit (b) $\nu = 2$

Figure 5.10: (a) High injection energy limit of the occupation number for $R = \frac{R_K}{2}$ ($\mathcal{R} = 0.5$). (b) Low energy behaviour of the occupation number for the coupled channels model, at strong coupling $\theta = \pi/2$. In both cases, the dashed line represents the Fourier transform of the high energy approximated expression (5.17).

quasiparticle is destroyed.
Furthermore, this example illustrates the possibility for decoherence and relaxation even in the absence of an external environment. This would also be the case for intrachannel interactions : these would imply a nonlinearity in the dispersion relation (see appendix B), and consequently

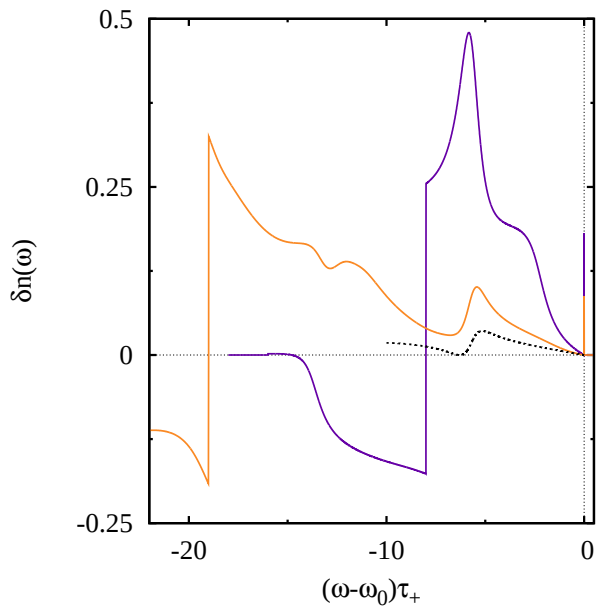

Figure 5.11: Excess occupation number for the closed channel model, at increasing injection energy, for strong coupling $\theta = \pi/2$ and $\gamma = 0.2$. The dashed line indicates the fourier transform of the total decoherence coefficient.

a nonlinear propagation phase (see appendix B). Such a model has been investigated in the high energy limit (ie for an initial energy above the energy scale associated to the interaction range) in [115, 114, 69]. In particular, in [114], a universal power law decay of the spatial coherence at zero temperature is predicted. The approach adopted in these works is very similar to the dynamical Coulomb blockade regime described above, in the sense that the supplementary electron interacts with a fluctuating bath of electrons in the Fermi sea.

The different behaviours previously described can be understood through an interpretation in terms of energy repartition between the edge channel and the environment, as shown in the next section.

3.3 Energy interpretation

The conclusions on quasiparticle's survival can be described in energy terms. This discussion generalizes the low energy circuit expansion for the elastic scattering probability, which concludes to the survival of the quasiparticle close to the Fermi level under the assumptions adopted here [6] .

Up to now, at high energy, it has not been possible to make general expansions of the elastic scattering probability since its behaviour depends on the complete structure of the scattering matrix for plasmons. Nevertheless, numerical evaluations of $Z(\epsilon_0)$ can help to characterize a model depending on its parameters' values.

The injection of a single electron with perfectly resolved energy is equivalent to an energy injection of $E_{init} = \epsilon_0 = \hbar\omega_0$. This energy can be understood as a sum over plasmons energies,

[6] The crucial hypothesis being the low energy limit of the scattering matrix, which must tend to the identity.

since $\langle b_\omega^\dagger b_\omega \rangle = \frac{1}{\omega}$ for $0 < \omega \leq \omega_0$:

$$E_{init} = \int_0^{\omega_0} \mathrm{d}\omega \langle b_\omega^\dagger b_\omega \rangle \hbar\omega \,. \tag{5.46}$$

The plasmon modes within the outcoming region are related to the incoming ones via the plasmon scattering matrix therefore the energy after the interaction region splits into two contributions :

$$E_{after} = E_{init} = E_{ec} + E_{env}, \tag{5.47}$$

where the edge channel (E_{ec}) and environment (E_{env}) energies have the following expression, still in the case of an energy resolved single electron excitation :

$$E_{ec} = \hbar \int_0^{\omega_0} \mathrm{d}\omega |t_b(\omega)|^2 \tag{5.48}$$

$$\text{and } E_{env} = \hbar \int_0^{\omega_0} \mathrm{d}\omega |r_b(\omega)|^2. \tag{5.49}$$

The evaluation of the energy sent into the environment gives a first clue : if the quasiparticle experiences massive energy emission towards the environment during the scattering, it will have only a small probability to come out untouched of the interacting region.
The energy stored in the edge channel can be split into two contributions, one corresponding to the quasiparticle, and another representing the particle/hole pairs in the Fermi sea. Consequently, the fraction of the energy which leaks towards the effective environment (external and the particle/hole pairs) is given by $1 - Z(\epsilon_0)$, and is depicted in fig. 5.12 for incresing circuit resistance, as a function of the injection energy and $\alpha = \frac{l}{v_F R_K C}$.

The analysis of the inelastic scattering probability gives a criterion to determine wether the electron quantum optics limit is reached at high energy or not : if a region in parameter space corresponds to a nonzero elastic scattering probability at infinite energy, then the dynamical Coulomb blockade limit in section 3 can be reached. More precisely, if we consider the elastic scattering probability at very high energy :

$$Z(\epsilon_0 \to \infty) = \exp\left(- \int_0^\infty \frac{\mathrm{d}\omega}{\omega} \Re(y(\omega)) \right), \tag{5.50}$$

where $y(\omega)$ is the dimensionless admittance. If the dissipative part of the admittance is such that the integral on the rhs of (5.50) is finite, then the quasiparticle survives at high energy, and its relaxation properties can be understood via the effective Dynamical Coulomb blockade approach.

At small resistance, a low coupling regime can be found, which corresponds to a finite elastic scattering probability at high energy for nonvanishing α. This suggests the existence of a transition in the behaviour of the model at high resistance. In this case, it is no longer possible to find a value of α for which the elastic scattering probability does not vanish at high energy. Conversely, in this situation, the total energy available in the initial state is totally dissipated towards the external environment and the particle/hole pairs in the Fermi sea.

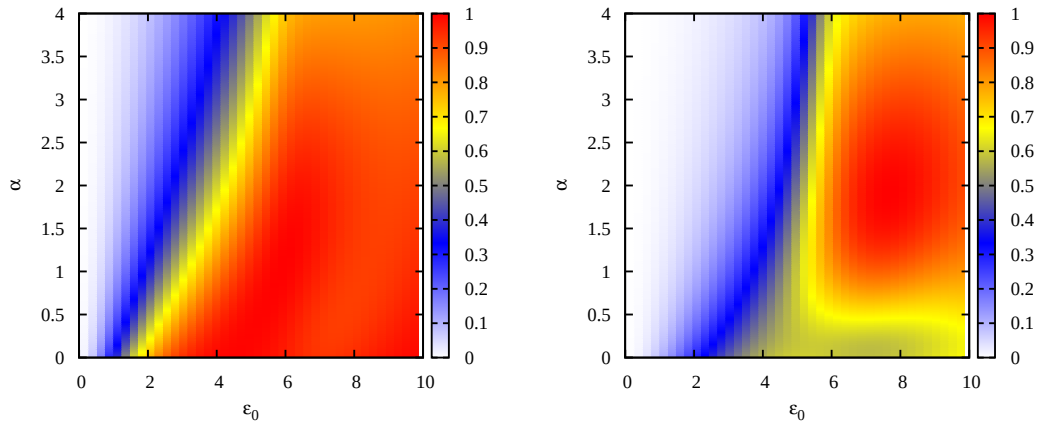

(a) $\mathcal{R} = \frac{1}{2}$

(b) $\mathcal{R} = 0.1$

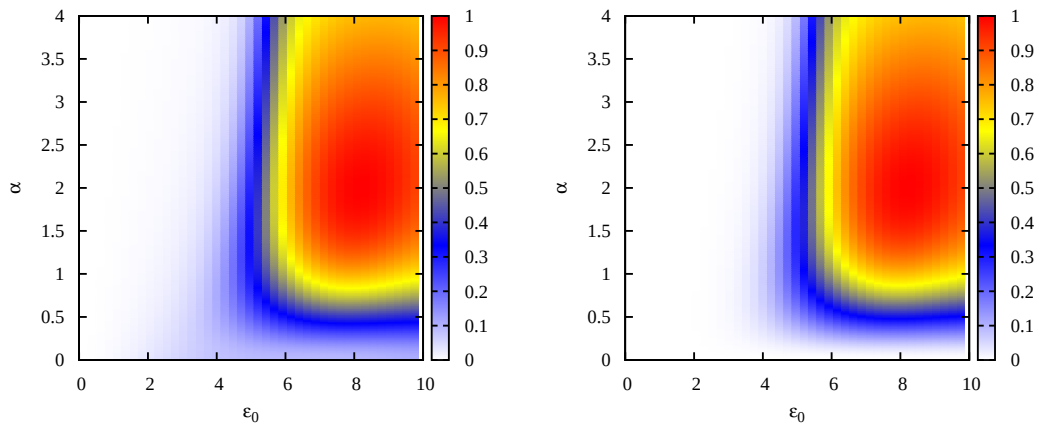

(c) $\mathcal{R} = 0.01$

(d) $\mathcal{R} = 0.001$

Figure 5.12: Energy fraction send to the effective environment (external circuit and edge channel) for the RC circuit model for decreasing resistance from (a) to (d)

4 Conclusion

In this chapter, we have studied the effects of interactions on energy resolved single electron excitations. With the help of the bosonization formalism, nonperturbative evaluations of the occupation number have been made for any of injection energy. Limiting regimes at low and high energies have been discussed and characterized. At low energy, a phenomenological model describes the relaxation properties in which the Fermi sea remains spectator. In this case we are left with a decoherence scenario that can be described using a discrete circuit elements approach in the spirit of Prêtre Thomas & Büttiker [18, 128]. In this regime, the electron relaxation is blocked at very low energy (Pauli blockade) in accordance to what should be expected when Fermi liquid reservoirs dominate the dynamics.

The situation at high energy is more involved. For interactions leading to a scattering matrix with a finite bandwidth, if the injection energy is sufficiently high, the quasiparticle decoheres under the influence of the environment made of the external circuit and the particle/hole pairs generated in the Fermi sea. The relaxation tail of the quasiparticle does not merge with the particle hole pairs at the Fermi level. The relaxation properties are described by an effective model similar to the dynamical Coulomb blockade theory. If the environment does not have a finite bandwidth, the quasiparticle gets drown into the Fermi sea. In this case, no quasiparticle exists at high energy. The typical situations exhibiting this behaviour is the capacitive coupling of $\nu = 2$ edge channels : at low energy, the quasiparticle is well defined, but at high energy, the quasiparticle decays over a length inversely proportional to its energy.

The results obtained from bosonization interpolate between these two limiting regimes and are valid for all injection energy. They are also nonperturbative in the interactions.

From the experimental point of view, the results presented here are relevant for the relaxation of a state emitted by the single electron source depicted in chapter 3 operated in its optimal regime. The predictions could be measured by the mean of the HBT tomography protocol proposed in chapter 3, or by a spectroscopy measurement.

In the last chapter of this manuscript, we will study the effect of the coupling of the edge channel to a linear environment on time resolved excitations for chiral quantum Hall edge channels. This study will show quantitative predictions for interaction induced particle/hole pair generation, together with the interplay of interactions and the Pauli principle in this case.

Chapter 6

Decoherence and relaxation of time resolved excitations

Contents

1 A source of minimal excitations **108**

1.1 Driving an edge channel with a classical voltage source 108

1.2 Coherence function of minimal excitations 109

2 Effects of the interactions on the coherence function **111**

2.1 Plugging the interactions into the Floquet formalism 112

2.2 Coherence function and interactions 112

3 HBT signals and HOM experiment in the interacting regime **115**

3.1 Electron/hole pair counting in HBT interferometry 115

3.2 Hong Ou Mandel effect in the interacting regime 117

4 Conclusion **120**

This last chapter discusses the relaxation of time resolved single electron excitations. These electronic excitations have been described by Levitov, Lee and Lesovik [87] and were further studied by Keeling *et al.* [76]. They are eigenstates of the total number of electron excitations N_+ generated by the application of a classical voltage of appropriate shape on an ohmic contact. They are accompanied by minimal particle/hole pairs. Contrary to the previous chapter, the electronic excitations we will be dealing with are not energy resolved and are indeed produced close to the Fermi level. These excitations being accompanied by minimal charge fluctuations, they are appropriate tools to reveal interaction induced particle/hole pairs production processes. A first part will detail the properties of these excitations, including their coherence properties and discuss how they could be generated. Then, we will see how the effects of interactions can be treated exactly. We then illustrate the effect of the interactions on the coherence function and see how information concerning the electron/hole pair production can be recovered through the HBT setup proposed in chapter 3.

1 A source of minimal excitations

This section describes the source of minimal excitations proposed in [87] by the mean of the coherence function of its emitted state. We first describe the action of a classical voltage on an edge channel, before specifying the discussion to a Lorentzian pulse of quantized action. Then, the properties of the excitations generated by these pulses will be discussed within the coherence function formalism.

1.1 Driving an edge channel with a classical voltage source

General case

The generic setup consist in a classical voltage $V(t)$ driving an ohmic contact or a metallic gate capacitively coupled to the edge channel. This classical potential couples to the charge density and thus becomes the analogue of a classical force for a quantum harmonic oscillator. Consequently, the action of such a classical drive is to generate a plasmonic coherent state in the edge channel. As mentioned in appendix B, the parameter of this coherent state is found solving the equations of motion for the bosonic field ϕ and is :

$$\mu_\omega = -\frac{e}{h}\frac{\hat{V}_\omega}{\sqrt{\omega}}\,. \tag{6.1}$$

Using the general fomulae given in appendix C, the coherence function for a coherent state can be evaluated, and gives :

$$\mathcal{G}^{(e)}(x,y) = \mathcal{G}_F^{(e)}(x,y)\exp\left(4i\int_0^\infty \frac{d\omega}{\sqrt{\omega}}\Re\big(\mu_\omega e^{i\omega\bar{x}/v_F}\big)\sin\left(\frac{\omega(x-y)}{v_F}\right)\right). \tag{6.2}$$

We will now see how these results translate for a particular shape of the voltage pulse.

Case of a Lorentzian pulse of quantized action

We consider now a lorentzian pulse of characteristic time τ_0 centered at a time t_0 :

$$V(t) = \frac{V_0\tau_0^2}{(t-t_0)^2+\tau_0^2}. \tag{6.3}$$

So as to suppress the emission of particle/hole pairs, the action associated to this pulse must be quantized [87] :

$$\int_{-\infty}^{+\infty} eV(t)\mathrm{d}t = nh, \tag{6.4}$$

where n is a stricly positive integer. Thus, this voltage generates a coherent plasmonic state which is also a pure state of the electron number N_+. The expression of the voltage and the associated coherent state parameter are respectively :

$$V(t) = \frac{nh\tau_0/\pi}{(t-t_0)^2+\tau_0^2} \text{ and } \mu_\omega = -\frac{n}{\sqrt{\omega}}e^{-\omega\tau_0}e^{-i\omega t_0}. \tag{6.5}$$

The fact that the emitted state is a coherent plasmonic state will reveal convenient for the inclusion of interactions through the bosonization formalism. These excitations can also be easily described in fermionic terms, as the next paragraph will show. We will now see how the characteristic properties of the n electron pulse manifests in the coherence function formalism.

1.2 Coherence function of minimal excitations

For the rest of this chapter, we will systematically distinguish between single shot and periodic sources. In the first case, the applied voltage has the form (6.5), whereas in the second one the voltage (6.5) is applied repeatedly at each period [1], and is consequently equal to :

$$V_T(t) = \sum_k V(t - kT) = \sum_k \frac{nh\tau_0/\pi}{(t - t_0 - kT)^2 + \tau_0^2} \,. \tag{6.6}$$

Equivalently, in Fourier space :

$$\widehat{V_T}(\omega) = \sum_{n\in\mathbb{Z}} \delta(\omega - n\Omega)\hat{V}(n\Omega). \tag{6.7}$$

A pulsed source

The periodic application of the lorentzian voltage (6.5) generates quantitatively different outcoming state depending on the ratio T/τ_0. At low frequency ($T/\tau_0 \gg 1$), the emitted state is comparable to the single shot source : consecutive wavepackets do not overlap. At high frequency ($T/\tau_0 \ll 1$), the Pauli exclusion principle comes into play, and is responsible for discrete structures, as can be seen in fig. 6.1. In the limit $\tau_0 \gg T$, the application of the voltage (6.6) is only responsible for a shift in the chemical potential correspoding to the charge added in the edge channel. The different situations are illustrated in fig. 6.1.

All these different cases can be taken into acount in a common framework by the mean of the Floquet formalism. We proceed along the same lines as in the case of the single electron source in chapter 3, where the only difficulty arises from the phase associated to the periodic voltage, since here the edge channel has no structure :

$$\exp\left(\frac{ie}{\hbar}\int_0^t \delta V_T(\tau)d\tau\right) = \sum_{k\in\mathbb{Z}} C_k[\delta V_T]e^{ik\Omega t} \,, \tag{6.8}$$

where $\delta V_T(t) = V_T(t) - \bar{V_T}$, where $\bar{V_T}$ is the average of the driving voltage. Contrary to chapter 3, this quantity is nonzero : $\bar{V_T} = \frac{nhf}{e}$. Indeed, the application of this voltage modifies the chemical potential of the Fermi sea by nhf.

The T-periodic coherence function

$$\mathcal{G}^{(e)}(t,t') = \sum_{n\in\mathbb{Z}} \mathcal{G}_n(t-t')e^{ni\Omega\bar{t}}. \tag{6.9}$$

can be decomposed into harmonics depending on $t - t'$, which have the following Fourier decomposition :

$$\widetilde{\mathcal{G}_n}(\omega) = \frac{1}{v_F}\sum_{k\in\mathbb{Z}} C_{n+k}[\delta V_T]C_k^*[\delta V_T]\bar{n}_\mu(\omega + (k+n/2)\Omega) \,. \tag{6.10}$$

[1] The repetition process is assumed to be ideal. Nevertheless, imperfections in the emission process, such as uncertainty on the emission time, can be accounted for.

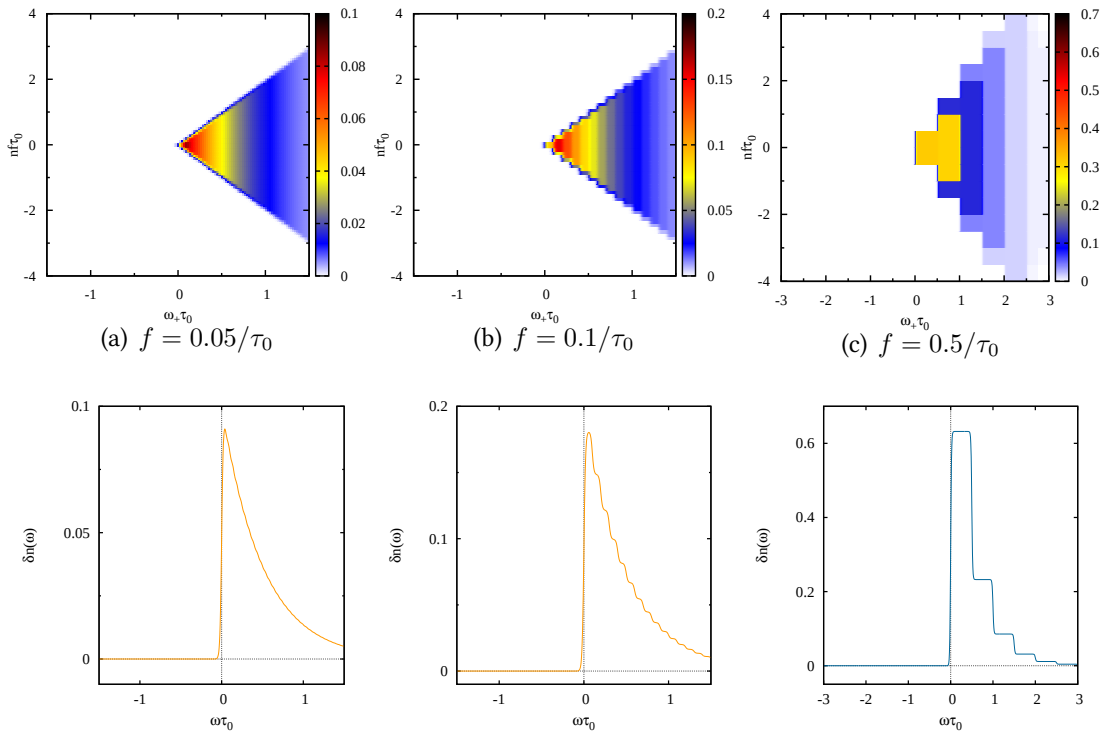

(a) $f = 0.05/\tau_0$ (b) $f = 0.1/\tau_0$ (c) $f = 0.5/\tau_0$

(d) $f = 0.05/\tau_0$ (e) $f = 0.1/\tau_0$ (f) $f = 0.5/\tau_0$

Figure 6.1: Coherence function in Fourier space of the state generated by the repeated application of a Lorentzian pulse containing one electron. The repetition frequency increases from $0.05/\tau_0$ in (a) to $0.5/\tau_0$ in (c). The horizontal and vertical coordinates are frequencies respectively conjugated to $t - t'$ and $\frac{t+t'}{2}$. The temperature is $k_B T = \frac{h}{100\tau_0}$. (d),(e),(f) display the $n = 0$ harmonic (the occupation number) for increasing frequency.

Single shot source

The single shot case corresponds to the zero frequency limit of the periodic source described in the last paragraph. Considering this limit will be of interest when studying interaction effects on time resolved phenomena such as the Hong Ou Mandel effect (see section 3). Furthermore, in this limit, the interactions are conveniently taken into account by the bosonization formalism (see section 2).

The time dependence of the coherence function for an arbitrary number of quanta $n$is obtained by a direct integration of the phase associated to the voltage pulse :

$$\mathcal{G}_n^{(e)}(t,t') = \mathcal{G}_F^{(e)}(t,t') \exp\left(i\frac{e}{\hbar}\int_{t'}^{t} \mathrm{d}\tau V(\tau)\right) \tag{6.11}$$

$$= \mathcal{G}_F^{(e)}(t,t') \left[\frac{1 - it/\tau_0}{1 + it/\tau_0}\right]^n \left[\frac{1 + it'/\tau_0}{1 - it'/\tau_0}\right]^n \tag{6.12}$$

At zero temperature, the coherence function in Fourier space is of the simple form :

$$\widetilde{\mathcal{G}^{(e)}}(\omega,\omega') = \mathcal{G}_\mu^{(e)}(\omega,\omega') + \Phi_n(\omega)\Phi_n^*(\omega'), \tag{6.13}$$

This shows that the output state generated by the Lorentzian voltage is pure. The function Φ_n appearing in (6.13) is nonzero only for positive frequencies : the state is purely electronic. For

$n = 1$, this function can be directly interpreted as the wavefunction of the output electron. In full generality, Φ_n is found by taking the Fourier transform of (6.12) by :

$$\Phi_n(\omega) = -\sqrt{2\tau_0} e^{-\omega\tau_0} \theta(\omega) \mathcal{L}_{n-1}(2\omega\tau_0) \,. \tag{6.14}$$

In (6.14), $\mathcal{L}_N$ is the Laguerre polynomial of order N [54]. In the case $n > 1$, Φ_n cannot be interpreted as the many body wavefunction for the n supplementary electrons : finding the wavefunction of the n supplementary electrons requiresthe evaluation of the electronic coherence function of order n.
The modulus of $\Delta\mathcal{G}^{(e)}(\omega, \omega')$ is depicted in 6.2 for different values of the quanta number n. These plots show that the coherence only lies in the positive part of the energy plane : $\Delta\mathcal{G}^{(e)}(\omega_+, \omega_-) = 0$ for $\omega_\pm < 0$: this reflects the absence of particle /hole pairs in the output state.

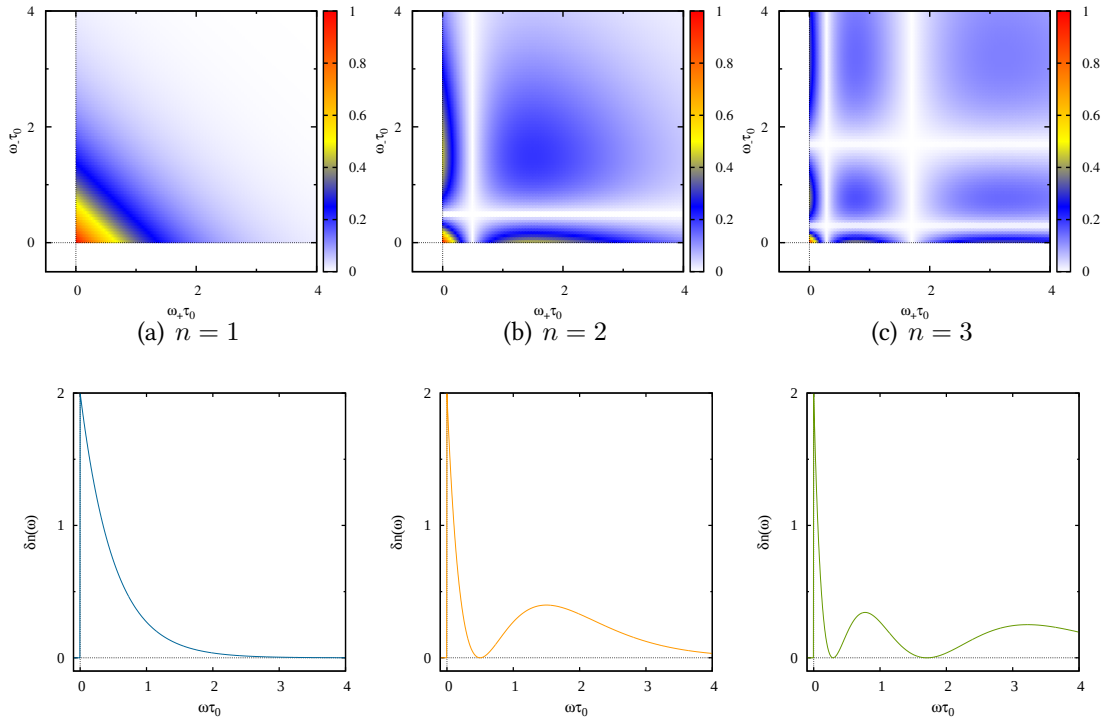

(a) $n = 1$ (b) $n = 2$ (c) $n = 3$

(d) $n = 1$ (e) $n = 2$ (f) $n = 3$

Figure 6.2: Excess coherence function in Fourier space of the state generated by a single Lorentzian pulse. In these plots, ω and ω' are frequencies conjugated respectively to t and t'. (d),(e) and (f) are the occupation number ($\omega = \omega'$) for different n.

We will now see how the interactions affect the output state of the minimal excitation source.

2 Effects of the interactions on the coherence function

In the presence of interactions, two different methods can be used to predict the single particle coherence. Technics developed in the case of the single electron relaxation can be adapted to compute the relaxation function for the single shot excitation.

For the periodic source, there is a way to compute the coherence that does not require the use of bosonization. This method proves to be more convenient for the numerical evaluation of the coherence function after interaction.

2.1 Plugging the interactions into the Floquet formalism

As stated in the first section, driving a region with a classical voltage creates a coherent plasmonic state whose parameter is proportional to the Fourier transform of the voltage. After an interaction region, the outcoming plasmon state is still coherent but its parameter is multiplied by the scattering coefficient $t_b(\omega)$. Therefore, the outcoming state can be viewed as generated by an effective voltage pulse $\widetilde{V}_{out}$ renormalized by the interactions :

$$\hat{\widetilde{V}}_{out}(\omega) = t_b(\omega)\hat{V}(\omega)\,. \tag{6.15}$$

Formally, the coherence function reads :

$$\mathcal{G}^{(e)}(t,t') = \mathcal{G}_\mu(t-t')\exp\big(\frac{ie}{\hbar}\int_t^{\prime t} d\tau \widetilde{V}_{out}(\tau)\big), \tag{6.16}$$

In the periodic case, the expression of the renormalized voltage is :

$$\widetilde{V}_{out}(t) = \sum_{n\in\mathbb{Z}} \widehat{V}(n\Omega)t(n\Omega)e^{-in\Omega t} \tag{6.17}$$

Consequently, the coherence function is obtained through the computation of the Fourier coefficients of the phase associated to the modified voltage, as in the case of the single electron source. Note that because $t_b(\omega) \to 1$ when $\omega \to 0$, the constant part of the voltage and thus the chemical potential are not altered by the interactions.

2.2 Coherence function and interactions

Interaction effects are illustrated on the example of the scattering for $\nu = 2$ edge channels introduced in chapter 4. We will first discuss interaction effects on the single particle function in real time before examining it in Fourier space.

Temporal coherence

Average current

As mentioned in chapter 2, the diagonal part of the real-time coherence function is the average particle density, and, up to a constant $-ev_F$, the average current flowing along the edge channel.

$$\Delta\mathcal{G}^{(e)}(t,t') = \mathcal{G}^{(e)}_\mu(\Delta)\Big[\exp\big(\frac{ie}{\hbar}\int_0^\Delta d\tau \widetilde{V}(\tau+\bar{t}-\Delta/2)\big)-1\Big]. \tag{6.18}$$

Then, with $\Delta = \epsilon,\ \epsilon \to 0$, one finds, with $\mathcal{G}_\mu^{(e)}(\Delta) = \frac{i\pi}{\beta h}\frac{e^{i\mu\Delta/\hbar}}{\sinh(\pi\Delta/\beta\hbar)}$:

$$\lim_{\epsilon\to 0^+}(-ev_F)\Delta\mathcal{G}^{(e)}(\bar{t}+\epsilon/2,\bar{t}-\epsilon/2) = (-ev_F)\langle:\Psi^\dagger(\bar{t}-\epsilon/2)\Psi(\bar{t}+\epsilon/2):\rangle = \langle I\rangle(\bar{t}) = \frac{e^2}{h}\widetilde{V}(\bar{t}). \tag{6.19}$$

Figure 6.3 shows the evolution with respect to the length of the interaction region of the average current over a voltage period . This evolution can be understood analytically : the scattering (4.43) is reponsible for a splitting of the initial voltage peak into two separate peaks with different heights :

$$\widetilde{V}(t) = \frac{1+\cos\theta}{2}V(t-L/v) + \frac{1-\cos\theta}{2}V(t+L/v). \tag{6.20}$$

If the time shift L/v introduced by the scattering is long compared to τ_0, the two peaks are well separated. When the dephasing time L/v eventually reaches a multiple N of $T/2$, the peaks from different periods recombine to restore the initial shape of the current, with an additional dephasing $NT/2$.

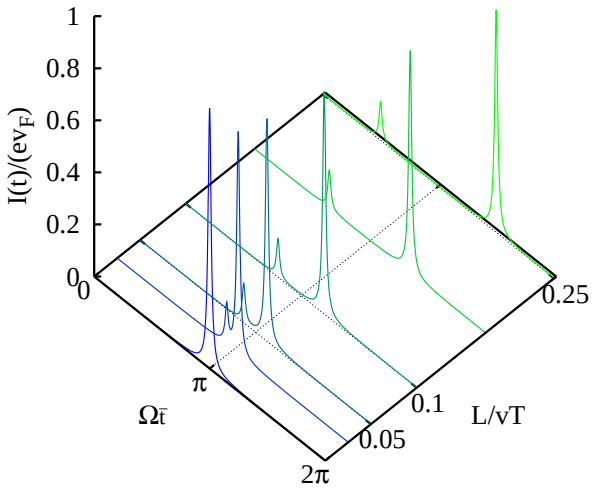

Figure 6.3: Evolution of the current pulse profile with the interaction length, for $\theta = \frac{\pi}{4}$, $k_BT = 0.01h/\tau_0$. Here, only one period of the current pulse is displayed.

Complete coherence function

The complete time dependence of the coherence function is depicted in fig. 6.4, for different values of the time spent in the interacting region. The initial coherence in 6.4 (a) evolves in the same way as the average current (see fig. 6.3). The initial lorentzian peak splits into two lorentzian peaks with different heights. These secondary peaks are manifestations of the propagation of plasmon eigenmodes of the $\nu = 2$ system at different velocities and without dispersion (spin/charge modes) [2]

As noticed in the analysis of the average current, the coherence function has a periodicity in the interaction length : fig. 6.4 (d),(e) and (f) are identical to fig. 6.4 (a), (b) and (c) up to a π dephasing.

We will now see how these features appear in Fourier space.

[2]The spin and charge modes are, in full rigor the eigenmodes of the $\nu = 2$ system only at strong coupling, *ie* $\theta = \frac{\pi}{2}$.

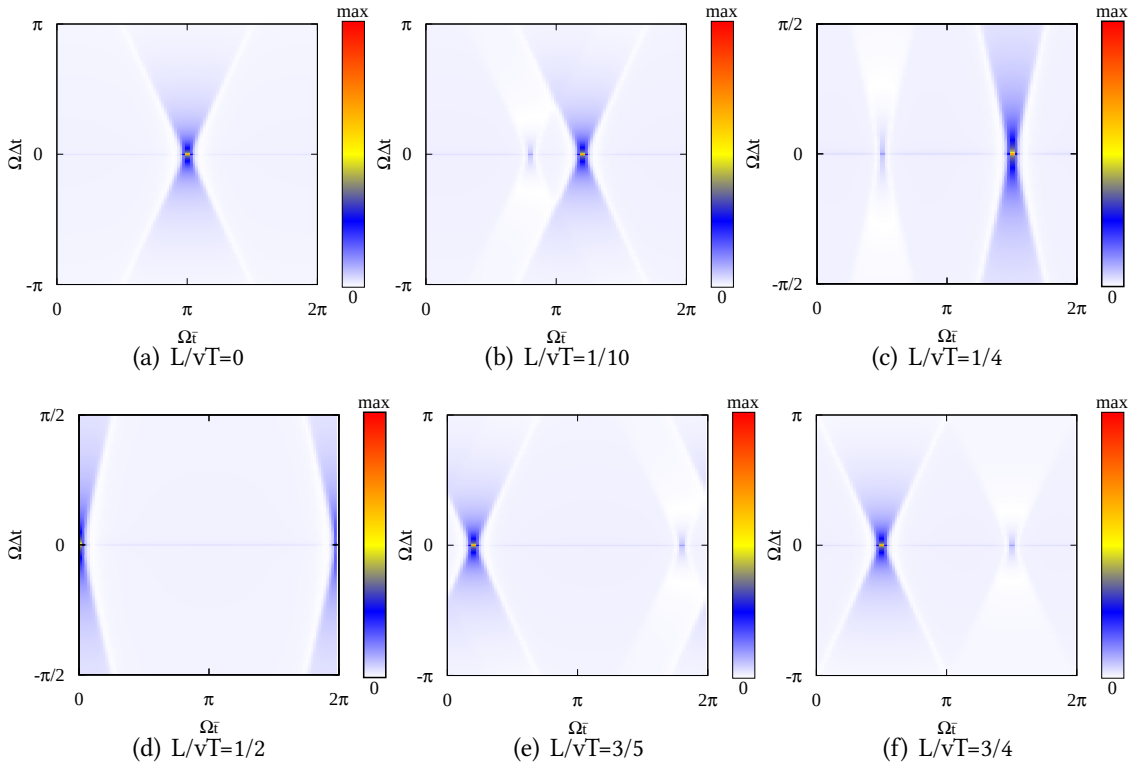

(a) L/vT=0 (b) L/vT=1/10 (c) L/vT=1/4

(d) L/vT=1/2 (e) L/vT=3/5 (f) L/vT=3/4

Figure 6.4: Real time coherence function (modulus) for increasing interaction lengths. The parameters are $f = \frac{1}{20\tau_0}$, $k_B T = \frac{h}{100\tau_0}$, and $\theta = \frac{\pi}{4}$.

Coherence function in Fourier space

The single electron coherence function in the frequency domain is shown on 6.4 for the same values of the interaction length. The two peaks in the real time coherence function interfere and are responsible for the oscillations in Fourier space. Furthermore, we observe that the off diagonal quadrants are no more empty : interactions have generated electron/hole coherences. Also,the hole quadrant is not empty anymore. Coherent electron/hole pairs have thus been generated. A quantitative study of the number of hole excitations generated by the interactions as a function of the coupling and the interactions length will be performed in the forthcoming section.

The periodicity in the interaction length clearly appears in Fourier space : for an interaction time corresponding to half a period, the initial coherence is recovered. This feature originates in the periodicity of the driving voltage and the linear dispersion relation : this is truly a stroboscopic effect. This stroboscopic revival reflects the dispersionless propagation of plasmonic modes within the interacting region. Any deviation to the linear dispersion would destroy this perfect revival of the initial coherence. In different words, this particular effect is a test of the validity of the phenomenological plasmon scattering for two channels (4.43).

In the next section, we will discuss how interactions can be probed using these time resolved excitations in an HBT setup.

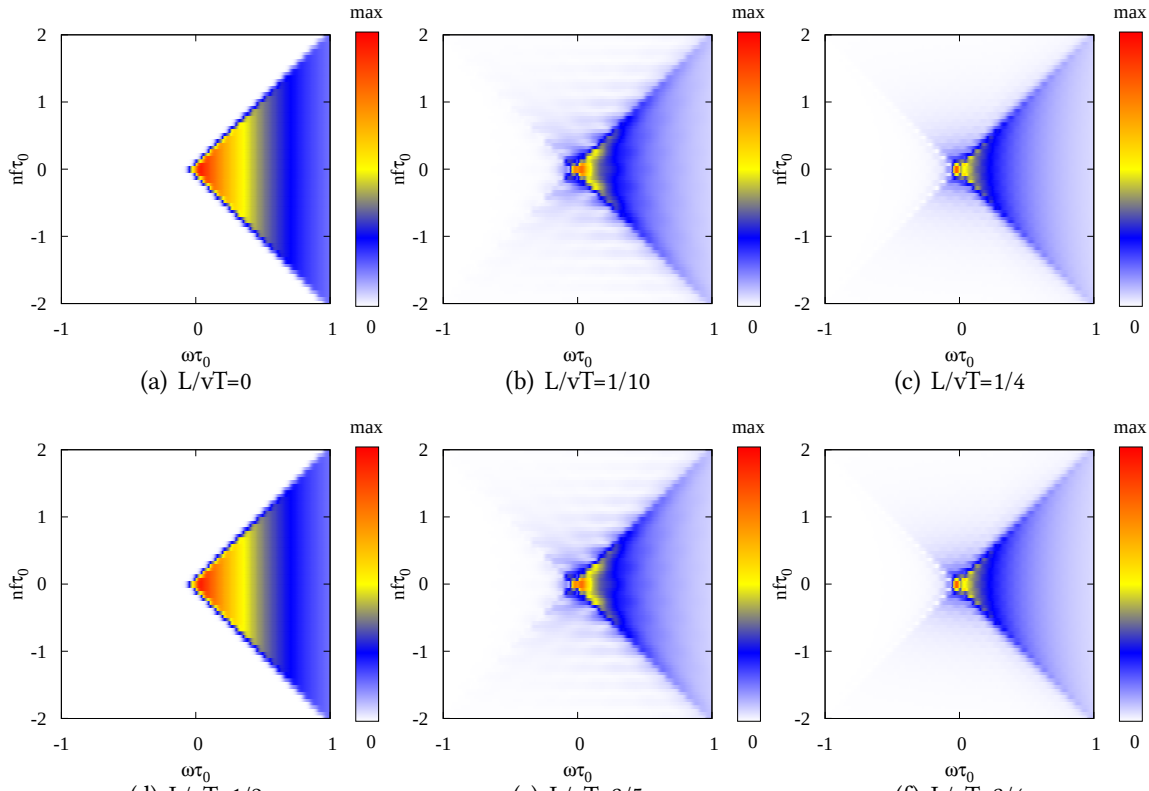

(a) L/vT=0 (b) L/vT=1/10 (c) L/vT=1/4

(d) L/vT=1/2 (e) L/vT=3/5 (f) L/vT=3/4

Figure 6.5: Modulus of the coherence function in Fourier space for increasing interaction lengths. The parameters are $f = \frac{1}{20\tau_0}$, $k_B T = \frac{h}{100\tau_0}$ and $\theta = \frac{\pi}{4}$.

3 HBT signals and HOM experiment in the interacting regime

In this last section, we propose two experiments based on HBT interferometry to probe decoherence mechanisms with the help of noise measurements and quantized lorentzian voltage pulses. In the first proposal, we propose to measure the number of hole excitations generated by interactions using the HBT setup in the same way as in the tomography protocol discussed in chapter 3. The second proposal is a Hong Ou Mandel electronic experiment also used to probe the interactions.

3.1 Electron/hole pair counting in HBT interferometry

Experimental setup

A sketch of the experimental setup is depicted in fig. 6.6. The pulsed Lorentzian voltage source is followed by an interacting region. The modulation of the sources's freqency accounts for the variation of the interaction length. As in the tomography protocol described in chapter 3, we assume that the Coulomb interaction plays no role at the quantum point contact.

In the next paragraph, we will show how quantitative information on electron/hole pair creation can be extracted from HBT measurements.

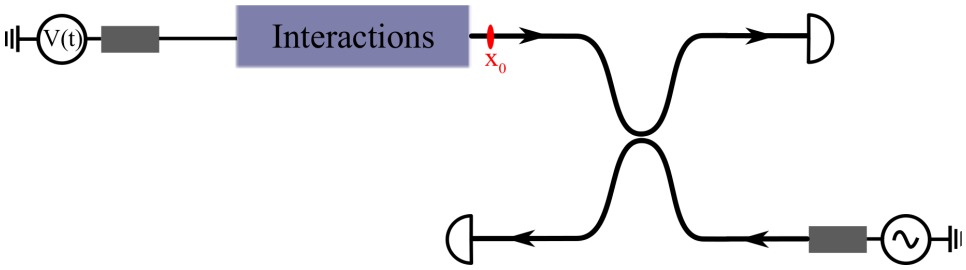

Figure 6.6: HBT setup for the n electron pulses in the presence of interactions. The emitted state of the pulsed lorentzian source is sent into an interacting region. The coherence function is measured by an HBT interferometer at the position x_0 right after the interacting region.

Electron/hole pair counting

The HBT signals contain information about the average number of holes created by the interactions. Up to a thermal smearing, the $n = 0$ contribution to HBT correlations at zero energy is related to the average number of electrons and holes introduced by the source (cf eq. (3.27)) :

$$\Delta\mathcal{Q}_0(\mu_2 = 0) = -\frac{2}{R_K}\int_{-\infty}^{0} \mathrm{d}\epsilon\, \delta n(\epsilon)\,, \tag{6.21}$$

The curves in fig. 6.7 (a) show the evolution of $\Delta\mathcal{Q}_0$ after the interactions have been switched on. If the value at $\mu_2 = 0$ is recorded for different values of the interaction length and different coupling strengths, the evolution of $\Delta Q_0(\mu_2 = 0)$ depicted in 6.7 (b) is obtained. In fig. 6.7(b), the red dashed line indicates the expected noise signal for free propagation. Any deviation from this prediction would imply the presence of interactions. Measuring this quantity is equivalent to monitor the number of holes generated by the interactions.

As expected, the particle/hole production increases with the coupling. Nevertheless, it only reaches experimental noise sensitivity for strong coupling. The periodicity is a manifestation of the stroboscopic reconstruction of the initial pulse as explained in the previous section.

HBT signal predictions

Fig. 6.8 shows the expected noise signals for higher harmonics of the single particle coherence function in the noninteracting case (6.8 (a)) and for $\theta = \pi/4$ (6.8 (b)). A comparison between the two graphs shows that the values associated to negative energies in fig. 6.8 (b) reflect the appearance of electron/hole pairs due to the interactions. These signals assess the relevance of HBT noise measurements to probe interaction mechanisms. In the absence of interactions (fig. 6.8 (a)), the expected noise signals have a typical value of $0.2\, e^2 f$, which is above the experimental noise sensivity. This is not always the case when interactions occur (see fig. 6.8 (b)). In this case, the typical value for the noise signals is closer to $0.1\, e^2 f$.

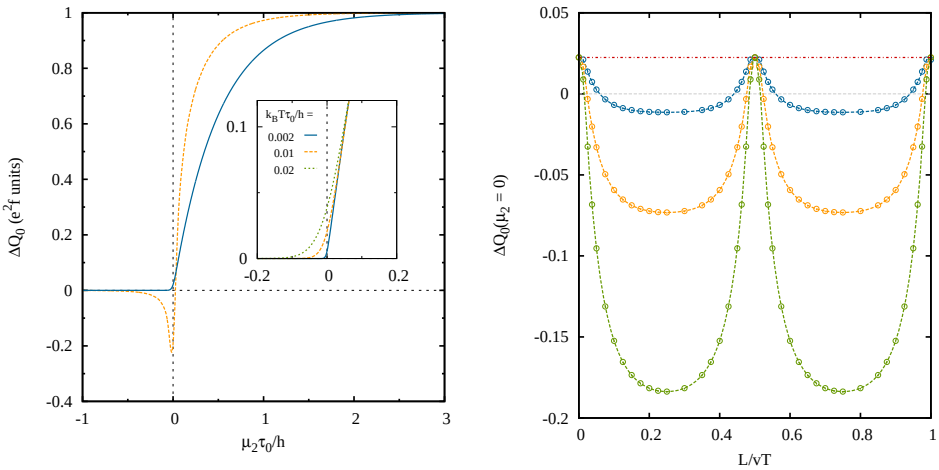

(a) $n = 0$HBT signal (b) e/h pairs number

Figure 6.7: Evolution of the HBT signals for $n = 0$ harmonics in the presence of interactions. (a) HBT signal associated to the occupation number for zero coupling and strong coupling. The Inset shows the evolution of the $\mu_2 = 0$ signal wrt temperature. (b) Evolution of the particle/hole pair number as a function of the interaction length and the coupling strength. The red dashed line indicates the expected noise signal in the absence of interactions. In these predictions, $f = 0.05/\tau_0$ and $k_B T = 0.01h/\tau_0$.

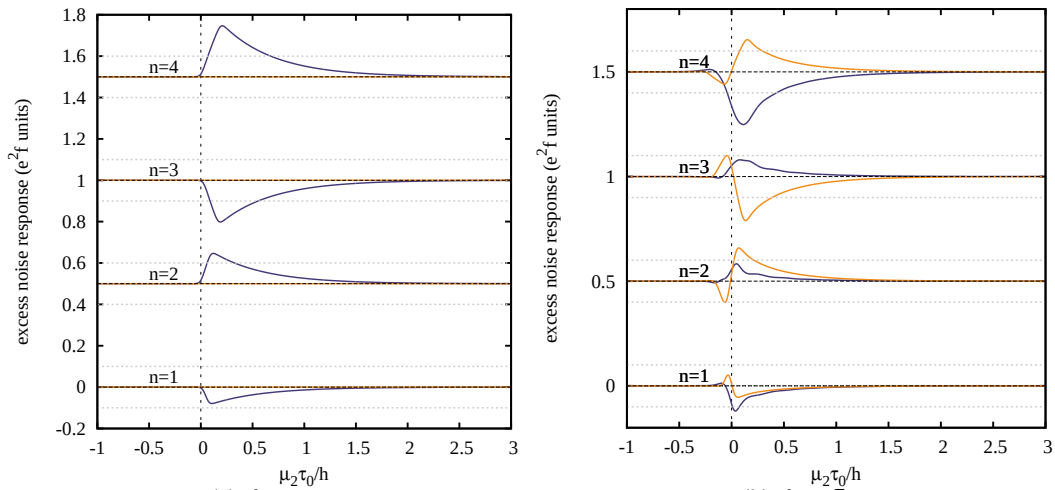

(a) $\theta = 0$ (b) $\theta = \frac{\pi}{4}$

Figure 6.8: Evolution of the HBT signals for $n \neq 0$ harmonics in the presence of interactions. (a) $\theta = 0$: Zero coupling case. (b) $\theta = \frac{\pi}{4}$: Mid coupling case. In these predictions, the length of the interaction region is taken to be $2vT$. The dashed lines indicate the minimal sentivity level for noise measurements. The temperature is $k_B T = 0.01h/\tau_0$, and the frequency is $f = 0.05/\tau_0$.

3.2 Hong Ou Mandel effect in the interacting regime

In this last paragraph, we analyze the effect of the propagation of an electronic excitation in an interacting region on the result of a Hong Ou Mandel experiment [71]. In this experiment, two sources emit identical single particle states which are sent onto a beamsplitter. The time delay between the two arrivals at the beamsplitter is variable and controlled. The output signal is the

correlation between the two output currents.
In the case of photons [71], when the paths lengths are equal, photons arrive at the same time at the 1/2:1/2 beamsplitter. Destructive two particle interferences prevent them to go out on different outcoming channels. Thus, the correlation between the two output intensities vanishes. As the path length (or equivalently the time delay) is varied from zero to values long compared to the source's coherence time, the correlation between the two outcoming channels reappears and reaches its maximal value at long delay times. The shape of the correlation as a function of the delay time is given in 6.9.

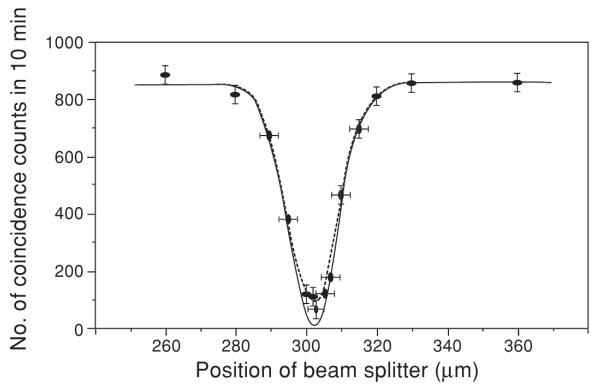

Figure 6.9: Hong Ou Mandel correlation dip for photons at zero delay time (taken from [71]).

We propose here to realize a similar experiment for lorentzian excitations in the presence of interactions in one of the two incoming channels. A sketch of the proposed setup is shown in fig. 6.10. As in the case of the single electron source in chapter 3, we focus on the excess HBT contribution $\Delta\mathcal{Q}(t,t')$ on output of the QPC.

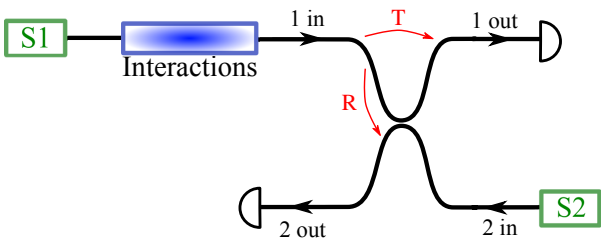

Figure 6.10: Sketch of a Hong Ou Mandel setup in the presence of an interacting region. The two single shot sources S1 and S2 feed the two branches of the interferometer. An interacting region is present in the first incoming channel, and a controlled time delay $\Delta\tau$ is introduced on the second branch. Current correlations are measured on output of the interferometer.

The excess quantum contribution due to both sources can be written as :

$$\Delta\mathcal{Q}(t,t') = \mathcal{G}^{(e)}_{1,F}(t',t)\mathcal{G}^{(h)}_{2,F}(t',t)\left(e^{-i\Phi_1(t,t')}-1\right)\left(e^{i\Phi_2(t,t')}-1\right)+1\leftrightarrow 2\,, \tag{6.22}$$

where

$$\Phi_i(t,t') = \frac{e}{\hbar}\int_{t'}^{t} V_i(\tau)\,\mathrm{d}\tau\,. \tag{6.23}$$

For a quantum point contact with no DC bias, the phase factors in (6.22) combine to give :

$$\Delta\mathcal{Q}(t,t') = 2\mathcal{G}_F^{(e)}(t',t)\mathcal{G}_F^{(h)}(t',t)\left[1-\cos\left(\Phi_1(t,t')\right)\cos\left(\Phi_2(t,t')\right)-\sin\left(\Phi_1(t,t')\right)\sin\left(\Phi_2(t,t')\right)\right] . \tag{6.24}$$

Experimentally, the equivalent of photocounting is the broadband measurement of current fluctuations[3] :

$$\int \langle I(t)I(t)\rangle \,\mathrm{d}t = \int \langle I(\omega)I(-\omega)\rangle \,\mathrm{d}\omega . \tag{6.25}$$

we define the following quantity from the expression (6.24) :

$$\Delta Q(t,t)(t) \equiv \lim_{\epsilon\to 0^+} \Delta\mathcal{Q}(t+\frac{\epsilon}{2}, t-\frac{\epsilon}{2}) = -\frac{e^4}{\hbar^2}V_1(t)V_2(t) . \tag{6.26}$$

Integrating the last expression over t, we get :

$$\overline{\Delta Q}(\Delta\tau) \equiv \int_{-\infty}^{+\infty} \mathrm{d}t\, Q(t,t) = -\frac{e^4}{\hbar^2}\int_{-\infty}^{+\infty} \mathrm{d}t\, V_1(t)V_2(t) . \tag{6.27}$$

This last quantity, which is a function of the delay time $\Delta\tau$, corresponds to the overlap between the two voltages. In the presence of interactions, the voltage V_1 is simply replaced by its renormalized expression :

$$\tilde{V}_1(t) = \int_{-\infty}^{\infty} \frac{\mathrm{d}\omega}{2\pi}\, t_b(\omega)\hat{V}_1(\omega)e^{i\omega t} . \tag{6.28}$$

To make the dependence in $\Delta\tau$ more explicit, we write the voltage V_2 as :

$$\hat{V}_2(\omega) = \hat{W}_2(\omega)e^{-i\omega\Delta\tau} , \tag{6.29}$$

where W_2 does not depend on $\Delta\tau$. Thus, the main result is, in its most general form :

$$\overline{\Delta Q}(\Delta\tau) = -\frac{e^4}{\hbar^2}\int_{-\infty}^{+\infty} \frac{\mathrm{d}\omega}{2\pi}\, \hat{V}_1(\omega)t_b(\omega)\hat{W}_2(-\omega)e^{i\omega\Delta\tau} . \tag{6.30}$$

In the case of two identical lorentzian pulses, (6.30) becomes :

$$\overline{\Delta Q}(\Delta\tau) = -\frac{e^4}{2\hbar^2}\frac{V_0}{\tau_0}\frac{1}{1+\frac{1}{4}\left(\frac{\Delta\tau}{\tau_0}\right)^2} . \tag{6.31}$$

The effect of an ohmic dissipation ($t_b(\omega) = e^{-\omega\tau_1}$, see appendix B) on (6.31) would be the renormalization of τ_0 : $\tau_0' = \tau_0 + \tau_1$. The effect of the $\nu = 2$ channel at different coupling strength and fixed propagation length is illustrated in fig. 6.11, and can be evaluated :

$$\overline{\Delta Q}(\Delta\tau) = -\frac{e^4}{2\hbar^2}\frac{V_0}{\tau_0}\left(\frac{1-\cos\theta}{1+\left(\frac{\Delta\tau}{2\tau_0}\right)^2\left(1+\frac{L}{v\Delta\tau}\right)^2} + \frac{1+\cos\theta}{1+\left(\frac{\Delta\tau}{2\tau_0}\right)^2\left(1-\frac{L}{v\Delta\tau}\right)^2}\right) . \tag{6.32}$$

Interactions are responsible for a drastic change in the shape of the HOM dip. Indeed, in the case of the $\nu = 2$ edge channels, the original dip (blue in fig.6.11) splits into two dips which reflect the plasmon eigenmodes. Their depth is related to the coupling strength (they are identical in the strong coupling limit), and their relative distance accounts for the propagation length.

[3]From the experimental signal, a filter function χ will come into play : the signal becomes $\int\langle I_1(\omega)I_2(-\omega)\rangle e^{i\omega\Delta\tau}\,\chi(\omega)\mathrm{d}\omega$.

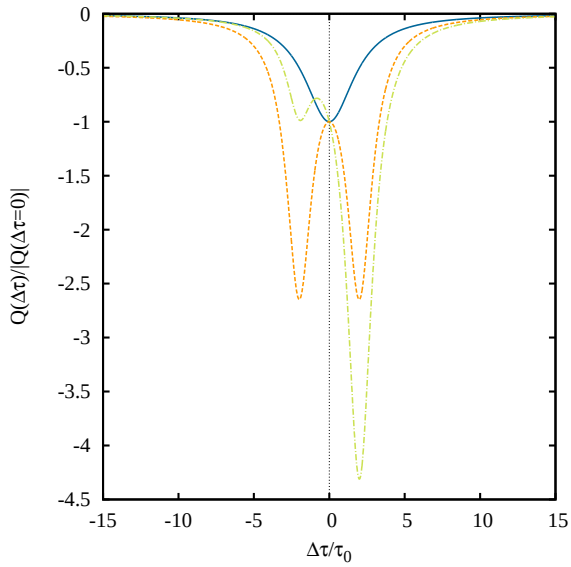

Figure 6.11: HOM dip in the presence of interactions. Blue curve corresponds to free propagation. Orange curve (symmetric wrt the y-axis) corresponds to strong coupling $\theta = \pi/2$ and the green curve corresponds to $\theta = \pi/4$. In both case, the propagation length is such that $L/v\tau_0 = 1$. The temperature is taken to be $0\,K$.

4 Conclusion

In this chapter we have studied the relaxation of electronic excitations generated by voltage pulses of quantized action. Because of the "dual nature" of these excitations (single electron and coherent plasmonic), the Floquet scattering approach can be used to compute the single particle coherence even in the presence of interactions. This remarkable fact has been used to obtain simple predictions in the $\nu = 2$ edge channel system. In particular, we have shown that when plasmonic eigenmodes are dispersionless within the interacting region, a perfect stroboscopic revival of the initial single electron coherence occurs for certain propagation lengths.

We have proposed to test this phenomenon using an HBT setup where the perfect revival would manifest itself through the periodicity of the outcoming noise in the HBT setup.
Finally, we have focused on the effect of interactions in a Hong Ou Mandel experiment, and obtained a simple result describing the evolution of the HOM dip as the overlap between renormalized voltages.

Chapter 7

Conclusion and perspectives

1 Main conclusions

The recent advances in nanofabrication, radiofrequency technology and experimental techniques have paved a way to new experiments aiming at the controlled manipulation of elementary excitations in ballistic quantum conductors similar to what is done with photons in quantum optics[38, 74, 68, 131, 133, 132, 112]. These experiments have already stimulated an important stream of theoretical research on the formulation of electron quantum optics taking into account interactions and discussing the dynamics of single to few electron excitations in the presence of interactions [89, 88, 21, 79, 80, 102, 100]. Furthermore, numerous recent theoretical works [24, 139, 120, 108, 23]contain proposals aiming at pushing these experiments further. This thesis has been realized in this rich experimental and theoretical context.
In this section, we review the results reported in this manuscript. They organize in two main directions. The first one is the definition of the appropriate framework to study electron quantum optics. The other is the analyzis of decoherence and relaxation mechanisms due to the coupling of electronic excitations to their electromagnetic environment.

Building blocks of electron quantum optics

The first part of this manuscript was devoted to the definition of quantum optics correlations for electrons propagating in quantum Hall edge channels, in analogy with the quantum coherence theory of the electromagntic field formulated by Glauber [51].

In full generality, the coherence function for electrons or photons can be split into two parts. The first one is the contribution of the vacuum to the coherence and the other one represents the contributions of the excitations on top of the vacuum. The vacuum of photons being a true vacuum, it does not contribute to the total coherence. In other words, its coherence functions are zero at all orders. This is no longer true for electrons : in this case the vacuum is filled with particles and contributes to the total coherence at all orders. These nonvanishing correlations reflect the possibility to generate particle/hole pairs from the Fermi sea : these contributions to the total coherence have been observed both in the noninteracting (chapter 2 and 3) and interacting cases (chapters 5 and 6). One of the main challenges in the study of the interacting

regime (especially in chap. 5 for this point) has been to show how such a natural decomposition translates in the interacting regime.

The single electron coherence function has been shown in chapter 2 to contain different contributions corresponding to electrons and hole excitations (diagonal blocks in the frequency domain) and electron/hole coherences (off diagonal blocks). These notions are defined with respect to a given chemical potential, the natural choice being the chemical potential of the conductor.

Evaluating the single particle coherence function in simple cases has shown similarities with the photon case. Notably, the expression of the wavepacket contribution in the case of a single electronic wavepacket is totally similar to the result obtained for a coherent light wavepacket. This result illustrates the electron quantum optics paradigm, where an electronic wavepacket well separated in energy propagates freely in the edge channel it has been injected in. The study of single electron relaxation in chap 5 has described in which cases an equivalent situation can be recovered at high injection energy in the presence of an external electromagnetic environment. In situations that do not match this paradigm, the complete many body approach developped in chapter 5 offers a solution to understand the the coherence properties at the single particle level.
The simple examples considered in chapter 2 also give an insight into the strong differences between photonic and electronic quantum optics, even in the noninteracting case. Apart from the nonvanishing coherence of the Fermi sea vacuum, the Pauli principle is ubiquitous when it comes to situations involving several electronic excitations. This fermionic characteristic is one of the sources of the richness of electron quantum optics compared to photon quantum optics. Note that in the interacting case, we have explicitely shown that the Pauli principle prevents the relaxation of the quasiparticle emitted at the surface of the Fermi sea.
Electronic coherence at second order have also been considered. The relation of this correlation to particle fluctuations and current noise have been unveiled, and we have shown that it contains information on the statistics of electron sources. Nevertheless, the analogy with photons is not complete, since the Fermi sea contributes to the second order coherence via two particle interferences.

In chapter 3, we have proposed a protocol to reconstruct the single electron coherence. This single electron quantum tomography is based on the HBT effect and can be viewed as the electron quantum optics analogue of homodyne tomography in quantum optics.
To argue in favor of its experimental feasability, we have considered [56] the case of the mesoscopic capacitor [38] operated as single electron source which we have modelled using the Floquet scattering approach.
Finally, we have introduced quantum information theory notions such as purity and fidelity with respect to a trial wavefunction in order to assess the the quality of such a single electron source at the quantum level.

This HBT protocol has also been proved efficient to characterize the mechanisms responsible for the decoherence and relaxation of single electron excitations. In the case of n electron pulses considered in chapter 6, we have shown that HBT noise measurements can recover information on interactions, such as the average of particle/hole pairs generated .

Interaction induced decoherence and relaxation

The results that have been obtained concerning the propagation in the interacting regime concern both single electron excitations (chapters 5 and 6) and nonequilibrium distributions (chapter 4). They mainly rely on the bosonization formalism and make extensive use of a plasmon scattering approach. In this approach, it is thus crucial that the interaction region is surrounded by free propagation regions. Although limited from this point of view, this approach has proved efficient in many different cases.

In our study of energy relaxation in chapter 4, we have derived a universal low energy plasmon scattering matrix for a system with screened Coulomb interactions [31]. We have also shown that this scattering provides predictions for experimentally relevant quantities. We have compared these predictions with experimental data on energy relaxation[2, 3, 145] and seen that this simple scattering approach captures most of the physics, up to small discrepancies, for which several different explanations can be provided [1, 64, 92, 81, 28]. Our opinion is that further progresses in understanding relaxation in the $\nu = 2$ edge channel system requires new experiments able to probe the dynamics in a frequency resolved way. This is why we have proposed finite frequency noise measurements to get a better insight on these issues.

In chapters 5 and 6, we have presented a complete theory of the relaxation of coherent single electron excitations in integer quantum Hall edge channels. For simplicity, we have focused on the decoherence andrelaxation of an energy resolved single electron excitation. This problem has been originally considered by Landau in the elaboration of the Fermi liquid theory[83].
The scattering between edge plasmonic and environmental modes determines both the finite frequency admittances and relaxation properties of a coherent single electron excitation. The latter can thus be computed exactly from the finite frequency admittances. This approach is very general and can be used to compute the relaxation of a single electron under the influence of any linear environment over a finite length.

In our study, we have considered two physically important regimes.
The low energy regime, which concerns the relaxation properties close to the Fermi level. Investigating this range of energy would provide an answer to the problem of the survival of the quasiparticle at low energy, and consequently answer the question of the nature of the electronic fluid. In the cases we have considered, the inelastic processes are blocked by the Pauli principle at low energy. The results in this regime are universal, and can be captured by a discrete circuit element approach[18, 128].

At high energies, the situation is richer. This regime appears when the initial energy of the electron is higher than the typical energy scale of the plasmon scattering. Our approach to this case relies on bosonization, and is nonperturbative in the interactions. Similarly to the low energy case, this regime also raises the question of the survival of the particle. In this case, the persistence of the electron would ensure the validity of the electron quantum optics paradigm. Here, all the frequency dependence of the plasmon scattering is involved, so the results are not universal.
Our analyzis has unveiled two different possibilities. For interactions that are not too strong, and for an environment with a finite bandwidth, the excess quasiparticle decoheres under the influence of an effective environment including the remaining electrons in the Fermi sea and

the external environment, as in the dynamical Coulomb blockade. In this case, the relaxation tail of the supplementary electron can be separated from the particle/hole pairs generated by the interactions at the surface of the Fermi sea.
On the contrary, if the bandwidth of the scattering matrix or if the coupling is too strong, this simple physical picture is no longer valid. Our study shows that in such cases, the particle/hole wave generated at the Fermi level catches up the excess quasiparticle, which gets literally drown into the Fermi sea. This approach can also be suited for non chiral quantum wires, or for the fractional quantum Hall regime, as we will see in the next section.

Interaction effects on a time resolved electronic excitation have been examined through the example of the source of minimal excitation proposed by Levitov, Lee and Lesovik [87]. Being non stationary, these states require the evaluation of the complete coherence function in the interacting regime. They also provide an example where the interplay between the Pauli principle and interactions can be explored in a simple way. Furthermore, we have used this example to illustrate the relevance of two particle interference experiments in the investigation of relaxation mechanisms. Indeed, the average number of holes generated by interactions has been extracted directly from HBT noise measurements. Then, signals associated to off diagonal coherences have shown the emergence of electron hole coherences, thus assessing the relation between off diagonal coherences and noise generation proposed in chapter 3.

To summarize, the proposed framework fullfils the requirements to study the quantum optics of electronic excitations stated in chapter 1. Indeed, this framework takes into account the specific features of electrons, namely the Pauli principle, and Coulomb interactions. It is also well suited to understand the analogies between photons and electrons in chiral edge channels. Finally, even if the similarities between current transport and light propagation in optical fibers should be stressed, one of the richnesses of electron quantum optics emerges from its departure from the ideal situation : understanding the interplay of Coulomb interactions and of the Fermi statistics in a mesoscopic conductor is a highly non trivial problem which has already attracted a lot of attention[153, 118, 6]. It raises questions concerning the nature and dynamics of quasiparticles in mesoscopic conductors. Future experiments may involve controlled decoherence of single to few electron excitations . They would provide quantitative answers to the aforementioned questions in quantum Hall edge channels.

2 Perspectives

Possible extensions of the results presented in this manuscript are various and go towards different directions, from the answer to questions arising in the condensed matter community, to quantum information perspectives. In both directions, theoretical and experimental works have provided numerous new sources of inspiration.
A first possible extension would be the study of quantum optics with plasmons. These excitations are particularly adapted to deal with interactions, and would consequently be ideal candidates for a preliminary evaluation of their influence on electron quantum optics correlations. Another one is coherent spin transport, which has quantum information implications. In particular, a major issue is to determine to what extent the quantum state can be encoded and then transported using a one dimensional system such as a $\nu = 2$ edge system [1] as a conveyer

[1] Via a superposition of the spin states in the two channels.

belt for an electronic flying qubit.
From a different perspective, far from equilibrium effects and strong interactions regimes are not fully understood. In particular, reconsidering them in the light of electron quantum optics would help clarifying important issues. This requires an adaptation of the coherence function formalism to the case of electronic distributions containing a macroscopic number of electrons, or to the fractional quantum Hall regime.

Quantum optics with plasmons

A first natural possibility is to investigate the plasmonic content of electronic excitations. Indeed, the statistics of the photons emitted by a conductor depends on the current that flows through it. Thus, by accessing the statistics of the radiation emitted by a conductor, one can recover information on the plasmon state, which is directly related to the electrical current. If this current has classical features, the plasmon state is coherent, and so is the photon state. On the contrary, if the plasmon state is non classical, then the photon statistics will exhibit purely quantum features, as noted in [8]. Thus, one can apply a similar reasoning to single electron sources, and question the nature of the plasmon state on output of a single electron source.

The other perspective is more general, and suggests the possibility to realize plasmon quantum optics experiments. We have seen in this manuscript that a classical voltage drive provides a source of coherent plasmons. Furthermore, a natural beamsplitter for plasmons is an interacting region. A clever use of an interaction region in the $\nu = 2$ edge channel system would thus open the possibility of controlled plasmon interference. Finally, a mesoscopic capacitor or a QPC would provide a nonlinear element that can create nonclassical plasmon state.

Coherent spin transport

The elements of electronic quantum coherence described here could be useful to understand the propagation of a quantum superposition in the presence of interaction. In a quantum information perspective, this superposition woud be a superposition of spin state for which the edge state plays the role of a quantum information transport channel, and the supplementary electron acquires the status of a flying qubit.
The ideas presented in this manuscript could bring interesting elements in the study of coherent spin transport, whose natural applications are the manipulation and transport of quantum information. Ongoing experimental efforts aim at developing quantum channels between quantum dots to transport single electron spin qubits. Their perspectives are also fast qubit injection,manipulations, transfer, and readout.
Manipulating the spin of a single electron requires detection schemes based on high frequency transport. Since these experimental works are aimed at transmitting quantum information, one could ask for measurement schemes that do not alter too much the spin state of the qubit. This raises the issue of the feasability of nondestructive measurements in the context of electronic transport, or, at least, how close a realist detection scheme can be from such an ideal detection process.
Besides injection and detection problems, the propagation of a spin superposition in the presence of the interchannel interactions has to be discussed. The formalism proposed for a single

electron excitation injected in one quantum Hall edge channel can be extended to the case of a non-polarized spin superposition. In that case, the coherence function will become a matrix whose elements encode the coherence between each spin component of the excitation. Tracing out orbital degrees of freedom, the spin reduced density matrix can be obtained from the complete coherence function.

Strong interactions and far from equilibrium effects

So far, the formalism developed for electron quantum optics assumed an initial state consisting in single or a few excitations on top of the Fermi sea, together with interactions which do not cause the disapperance of the quasiparticle at low energies. It is consequently natural to think of the potential extension of the results obtained on this context to cases that do not fulfil such preliminary assumptions, namely far from equilibrium electronic distributions, or the fractional quantum Hall regime.
The study of interactions in the $\nu = 2$ regime already sheds light but also raises questions on the strong interacting regime together with far from equilibrium initial states, both from theoretical and experimental points of view. On the basis of recent propositions for the development of a nonequilibrium bosonization formalism [61, 62, 58, 60], the adaptation of the coherence function formalism to far from equilibrium situations will help connecting electron quantum optics and the full counting statistics approach.

Finally, let us mention the extension of electron quantum optics to the fractional quantum Hall regime. In this manuscript, we have only considered situations in which the electronic quasiparticle is preserved at low energy : the vacuum remains a Fermi sea. Considering the effect of strong interactions and going to the Luttinger liquid regime would provide new insights on the behaviour of Laughlin quasiparticles since it would give the opportunity to study their quantum coherence.The strong interactions in this regime are responsible for a change in the behaviour of the electron fluid at low energy. Thus, one can wonder about the modifications induced by this different nature of the vacuum on the coherence function, and more generally on electronic quantum optics.

Appendix A

Quantum tomography : extraction of the coherence function and complements on the driving phase

This appendix first details the derivation of the results for single electron quantum tomography. Then, in a second part, we derive the expression of the Fourier coefficients of the driving phase for simple driving voltages. We also derive analytically the expression of the harmonics of the coherence function in the simple case of a sinusoidal drive. This is one of our reference situations which was compared to the numerical results of the Floquet formalism.

Extraction of the single electron coherence

Generalities

The harmonics of the single particle coherence function are defined by:

$$\Delta\mathcal{G}_1^{(e)}(t,t') = \sum_{n=-\infty}^{+\infty} e^{-2\pi i n \bar{t}/T} \int \Delta\mathcal{G}_{1,n}^{(e)}(\omega) e^{-i\omega\tau} \frac{d\omega}{2\pi} \,. \tag{A.1}$$

The corresponding noise is thus :

$$\Delta\mathcal{Q}(t,t') = (ev_F)^2 \sum_{n\in\mathbb{Z}} e^{-in\Omega_T \frac{t+t'}{2}} \left(\Delta\mathcal{G}_{1,n}^{(e)}(t'-t)\, \mathcal{G}_2^{(h)}(t',t) + \Delta\mathcal{G}_{1,n}^{(h)}(t'-t)\, \mathcal{G}_2^{(e)}(t',t), \right) \tag{A.2}$$

where $\Delta\mathcal{G}_{1,n}^{(e/h)}$ denotes the n-th harmonic of the electron/hole single particle coherence function[1]. If we assume that no interactions are present in the interferometer [2], the anticommutation of fermion fields and chiral motion

$$\{\psi_\alpha^\dagger(t), \psi_\beta(t')\} = \delta_{\alpha,\beta}\, v_F^{-1}\, \delta(t-t') \,. \tag{A.3}$$

[1]The supplementary index 1 indicates that the branch of the HBT interferometer containing the source is the first one

[2]Interactions can be present in the source. If so, they would be responsible for a modification of the predictions for the coherence function, but not for its measurement.

lead in Fourier space to a relation between electron and hole coherence function for a periodic source :

$$\Delta\mathcal{G}^{(e)}_{1,n}(\omega) + \Delta\mathcal{G}^{(h)}_{1,n}(-\omega) = \frac{\delta_{n,0}}{v_F}\,. \tag{A.4}$$

Since $\Delta\mathcal{G}^{(e/h)}_{1,n} = \mathcal{G}^{(e/h)}_{1,n} - \delta_{n,0}\mathcal{G}^{(e/h)}_{\mu_1}$, we obtain $\Delta\mathcal{G}^{(e)}_{1,n}(\omega) = -\Delta\mathcal{G}^{(h)}_{1,n}(-\omega)$. Now, let us express the n-th harmonic of the noise signal $\Delta\mathcal{Q}$ in terms of the harmonics of the coherence function of the source $\Delta\mathcal{G}_1$ and the coherence function of the driven ohmic contact $\mathcal{G}_2$.

The ohmic contact on the input way 2 of the interferometer is driven by a periodic voltage so the coherence function $\mathcal{G}_2$ is periodic in $\bar{t}$.

$$\mathcal{G}^{(e/h)}_2(t,t') = \sum_{k\in\mathbb{Z}} e^{-ik\Omega_T\bar{t}}\mathcal{G}^{(e/h)}_{2,k}(t-t'). \tag{A.5}$$

Thus, the n-th harmonic $\Delta\mathcal{Q}_n(t-t')$ can be expressed as :

$$\Delta\mathcal{Q}_n(t-t') = \sum_{k\in\mathbb{Z}} \Delta\mathcal{G}^{(e)}_{1,k}\mathcal{G}^{(h)}_{2,n-k}(t-t') + \Delta\mathcal{G}^{(h)}_{1,k}\mathcal{G}^{(e)}_{2,n-k}(t-t'). \tag{A.6}$$

In Fourier space, this transforms into, if we take eq. (A.4) into account:

$$\Delta\mathcal{Q}_n(\Omega) = \sum_{k\in\mathbb{Z}} \int \frac{\mathrm{d}\omega'}{2\pi}\Delta\mathcal{G}^{(e)}_{1,n}(\omega')\mathcal{G}^{(h)}_{2,n-k}(\Omega-\omega') - \Delta\mathcal{G}^{(e)}_{1,n}(\omega')\mathcal{G}^{(e)}_{2,n-k}(\Omega+\omega'). \tag{A.7}$$

Higher order harmonics

The electron and hole coherence functions of the driven ohmic contact are ($V_{ac}(t) = V_0\cos(\omega_d t + \phi)$):

$$\mathcal{G}^{(e)}_2(t',t) = \mathcal{G}^{(e)}_{\mu_2}(t',t)\,\exp\left(\frac{ie}{\hbar}\int_t^{t'} V_{\mathrm{ac}}(\tau)\,d\tau\right) \tag{A.8a}$$

$$\mathcal{G}^{(h)}_2(t',t) = \mathcal{G}^{(h)}_{\mu_2}(t',t)\,\exp\left(-\frac{ie}{\hbar}\int_t^{t'} V_{\mathrm{ac}}(\tau)\,d\tau\right). \tag{A.8b}$$

The linear response to V_0 is defined by:

$$\chi_{\omega_d}(t,t') = \frac{\partial\Delta Q(t,t')}{\partial(eV_0/\hbar\omega_d)}|_{V_0=0}. \tag{A.9}$$

It has the following expression in terms of coherence functions :

$$\chi_{\omega_d}(t,t') = 2i(ev_F)^2\,\cos(\omega_d\bar{t}+\phi)\,\sin\left(\frac{\omega_d(t'-t)}{2}\right)\left(\Delta\mathcal{G}^{(h)}_1\mathcal{G}^{(e)}_{\mu_2} - \Delta\mathcal{G}^{(e)}_1\mathcal{G}^{(h)}_{\mu_2}\right)(t',t)\,. \tag{A.10}$$

Taking $\omega_d = n\Omega_T$, and performing the average over $\bar{t}$, we obtain the relation between $\Delta\mathcal{G}_{1,n}$ and the linear response function at $\omega_d = n\Omega_T$:

$$\chi_n(t-t') \equiv \overline{\chi_{\omega_d=n\Omega_T}(t,t')}^{\bar{t}} \tag{A.11}$$

$$= 2i(ev_F)^2\sin\left(\frac{n\Omega_T(t'-t)}{2}\right)\Big\{\mathcal{G}^{(h)}_{\mu_2}(t'-t)\frac{e^{i\phi}\Delta\mathcal{G}^{(e)}_{1,n}(t'-t) + e^{-i\phi}\Delta\mathcal{G}^{(e)}_{1,-n}(t'-t)}{2}$$

$$-\,\mathcal{G}^{(e)}_{\mu_2}(t'-t)\frac{e^{i\phi}\Delta\mathcal{G}^{(h)}_{1,n}(t'-t) + e^{-i\phi}\Delta\mathcal{G}^{(h)}_{1,-n}(t'-t)}{2}\Big\}. \tag{A.12}$$

The remaining steps are similar to the $n = 0$ case, $\chi_n(t-t')$ playing the role of $\Delta\mathcal{Q}_0(t-t')$. The final expression relating the linear harmonic response to the harmonics of the coherence function is:

$$\left(\frac{\partial\chi_n}{\partial\mu_2}\right)(\Omega, T_{el}, \mu_2, \phi) = \int_{-\infty}^{+\infty}\left(\frac{\partial\chi_N^{(0)}}{\partial\mu_2}\right)(\Omega, \mu_2 + xk_BT_{el}, \phi)\,\frac{dx}{4\cosh^2(x/2)} \tag{A.13}$$

$$\left(\frac{\partial\chi_n^{(0)}}{\partial\mu_2}\right)(\Omega, \mu_2, \phi) = \frac{e^2}{h}\Re\left[e^{i\phi}\left(v_F\Delta\mathcal{G}_{1,n}^{(e)}(\frac{\mu_2}{\hbar} + \frac{N\Omega_T}{2}) - v_F\Delta\mathcal{G}_{1,n}^{(e)}(\frac{\mu_2}{\hbar} - \frac{n\Omega_T}{2})\right)\right].$$

Fourier coefficients of the driving phase

The expression of the Fourier coefficients of the driving phase are derived in simple cases, analytically for simple voltage shapes and numerically (via FFT) for more generic voltages. Here, we give the expressions for a square and sine voltages.

Generalities

The driving represents the total phase acquired by an electron travelling under the influence of $V(\tau)$ between times t and t' :

$$\phi(t, t') = \exp\left(\frac{ie}{\hbar}\int_t^{t'} V(\tau)d\tau\right). \tag{A.14}$$

We assume here that the voltage is periodic :

$$V(t) = \sum_{n\in\mathbb{Z}} V_n e^{-in\Omega_T t}. \tag{A.15}$$

For a T-periodic voltage with zero mean, we have :

$$\exp\left(\frac{ie}{\hbar}\int_{-\infty}^{t} V(\tau)d\tau\right) = \sum_{n\in\mathbb{Z}} c_n[V]e^{-in\Omega_T t}, \tag{A.16}$$

where $\Omega_T = \frac{2\pi}{T}$. We will now evaluate this result in simple cases.

Computations in simple cases

Square voltage

For a T-periodic voltage $V(\tau) = +V$ for $\tau \in]0, T/2[$ and $V(\tau) = -V$ for $\tau \in]-T/2, 0[$. Then, we have:

$$\exp\left(\frac{ie}{\hbar}\int_0^t V(\tau)\,d\tau\right) = \exp\left(\frac{ieV}{\hbar}\,|t|\right) \quad \text{for } |t| \leq T/2\,. \tag{A.17}$$

Denoting $\omega_V = eV/\hbar$, computing the integrals leads to the following generic expression, valid when ω_V/Ω_T is not an integer :

$$c_n[V] = \frac{2i\,\omega_V T}{(\omega_V T)^2 - 4\pi^2 n^2}\left(1 - (-1)^n e^{i\omega_V T/2}\right) . \tag{A.18}$$

When $\omega_V/\Omega_T = p \in \mathbb{N}^*$, we have:

$$c_n[V] = \frac{i}{2\pi}\frac{2p}{p^2 - n^2}(1 - (-1)^{n+p}) \quad \text{for } n^2 \neq p^2 \tag{A.19a}$$

$$\text{and } c_p[V] = c_{-p}[V] = \frac{1}{2} . \tag{A.19b}$$

Cosine voltage

In the case of a cosine voltage $V(t) = V_0 \cos(\Omega_T t + \phi)$, we have :

$$c_n[V] = (-1)^n J_n\left(\frac{2eV}{\hbar\Omega_T}\right) e^{-in\phi} , \tag{A.20}$$

where J_n denotes the n-th order Bessel function.

For voltages containing an arbitrary number of harmonics, a numerical evaluation has been performed on the basis of a fast Fourier transform. This method offers the possibility to evaluate the effects of a periodic voltage of any form.

Harmonics of the coherence function in a simple case

So as to verify the numerical evaluation of the harmonics of the coherence function, it is of importance to compare it with analytical results whenever possible. Fortunately, this can be done in the case of a cosine voltage. Here, we derive completely the expression of the single particle coherence function's harmonics for a cosine voltage.
We consider an ohmic contact driven by a voltage $V(t) = V_0 \cos(\Omega_T t + \phi)$. The coherence function generated by this drive is :

$$\mathcal{G}^{(e)}(t,t') = \mathcal{G}^{(e)}_\mu(t-t') \exp\left(\frac{ieV_0}{\hbar\Omega_T}\sin(\Omega_T\frac{t-t'}{2})\cos(\Omega_T\bar{t})\right) , \tag{A.21}$$

with $\bar{t} = \frac{t+t'}{2}$. With [54] $e^{iz\cos\theta} = \sum_{n\in\mathbb{Z}} i^n J_n(z) e^{in\theta}$, we find the n-th harmonic of the coherence function :

$$\mathcal{G}^{(e)}_n(t-t') = i^n e^{ni\phi}\mathcal{G}^{(e)}_\mu(t-t') J_n\left(\frac{2eV_0}{\hbar\Omega_T}\sin(\Omega_T\frac{t-t'}{2})\right) . \tag{A.22}$$

Now, recalling the power series development of Bessel functions [54], we can compute the Fourier transform of $\mathcal{G}_n$:

$$\mathcal{G}_n(\omega) = (-1)^n e^{ni\phi}\sum_{k\in\mathbb{N}}\frac{\gamma^{2k+n}}{k!(n+k)!} f_{n,k}(\omega)$$

$$f_{n,k}(\omega) = \sum_{j=0}^{2k+n} C^j_{2k+n}(-1)^j \bar{n}_F(\omega - (k-j+n/2)\Omega_T) , \gamma = \frac{eV_0}{2\hbar\Omega_T} \text{ and } C^k_n = \frac{n!}{k!(n-k)!} . \tag{A.23}$$

Appendix B

Plasmon scattering

In all models considered throughout the manuscript, the dynamics of the edge channel coupled to its environment is solved within a scattering formalism. The central object of this approach is thus the scattering matrix for bosonic modes $\mathcal{S}(\omega)$ that relates the edge (b) and environmental (a) modes before and after the interacting region :

$$\mathcal{S}(\omega) = \begin{pmatrix} t_a(\omega) & r_b(\omega) \\ r_a(\omega) & t_b(\omega) \end{pmatrix} \tag{B.1}$$

such that

$$\begin{pmatrix} a_\omega^{(out)} \\ b_\omega^{(out)} \end{pmatrix} = \mathcal{S}(\omega). \begin{pmatrix} a_\omega^{(in)} \\ b_\omega^{(in)} \end{pmatrix} . \tag{B.2}$$

Physically, this means that the coupling between the edge and its environment acts as a beam-splitter between the edge and environmental modes. All the physical aspects are contained in the frequency dependence of the reflexion and transmission coefficients.

This appendix presents some of the properties and expressions of the plasmon scattering matrices . In a first part, we present the Onsager-Büttiker relations which enforce the symmetry of the scattering matrix. In a second part, we derive the expression of scattering coefficients that have been used in in chapters 4, 5 and 6.

Consequences of Onsager-Büttiker relations

In the framework of linear response theory, the Onsager-Büttiker relations [14] concern the behaviour of the finite frequency admittance (and consequently of the plasmon scattering) in the presence of a magnetic field. These relations are:

$$G_{\alpha\beta}(\omega, \vec{B}) = G_{\beta\alpha}(\omega, -\vec{B}), \tag{B.3}$$

where $\vec{B} = \vec{B}_\parallel + \vec{B}_\perp$ is the total magnetic field applied to the 2DEG (see fig. B.1). $\vec{B}_\parallel$ (resp. $\vec{B}_\perp$) is the contribution to the magnetic field parallel (resp. perpendicular) to the plane of the 2DEG.
The system is symmetric in a reflexion with respect to the plane of the 2DEG :

$$G_{\alpha\beta}(\omega, \vec{B}_\parallel, \vec{B}_\perp) = G_{\alpha\beta}(\omega, \vec{B}_\parallel, -\vec{B}_\perp). \tag{B.4}$$

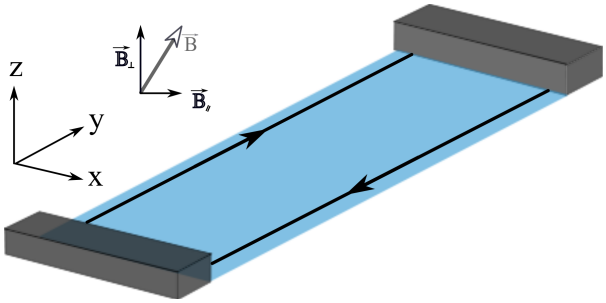

Figure B.1: The different contributions to the total magnetic field. In the absence of the component parallel to the 2DEG plane, the admittance and plasmon scattering matrices are symmetric.

Combining the previous equation with the Onsager-Büttiker relations, we finally have :

$$G_{\alpha\beta}(\omega, \vec{B}_\parallel, \vec{B}_\perp) = G_{\beta\alpha}(\omega, -\vec{B}_\parallel, \vec{B}_\perp). \tag{B.5}$$

In the case of a magnetic field perpendicular to the 2DEG, the admittance and scattering matrices are symmetric.

Derivation of scattering matrices for different models

In this section, we derive explicitely the expression of the scattering matrices for plasmons used in chapter 4, 5 and 6.

The quantum RC circuit

Here, we find the expression of the scattering matrix for the quantum RC-circuit, which is expected to describe the mesoscopic capacitor in the linear response regime [36, 30]. To do so, we consider a chiral edge channel coupled to a perfect conductor, and analyze the role of screening and Coulomb interactions, in the spirit of [128], which will allow an extension of previous works [141] on electron dephasing in such situations.

Electrostatics of edge channels

In the presence of a potential $V(x,t)$, the electron field in the edge channel evolves according to :

$$\psi(t+\tau, x+v_F\tau) = \psi(x,t)\exp\left(\frac{ie}{\hbar}\int_0^\tau V(x+v_F t', t+t')\mathrm{d}t'\right). \tag{B.6}$$

This evolution transposes to the following equation of motion for the bosonic field ϕ:

$$(\partial_t + v_F\partial_x)\phi(x,t) = \frac{e\sqrt{\pi}}{h}V(x,t). \tag{B.7}$$

Now, we must find the voltage in the edge channel as a function of the voltage $V_{cond}(t)$ that drives the conductor, and the density field ϕ. To do so, we have to solve the Poisson equation

for the voltage difference $V(x,t) - \widetilde{V}_{cond}(x,t)$, (see fig. B.2) where $\widetilde{V}_{cond}(x,t)$ is the voltage induced by the conductor's voltage along the edge channel :

$$-\Delta(V - \widetilde{V}_{cond}) = \frac{1}{\epsilon}\left(\rho_{ch} + \rho_{ind}\right), \tag{B.8}$$

where ρ_{ch} is the charge density along the edge channel, and ρ_{ind} the charge density induced in the conductor in the absence of the conductor's voltage.

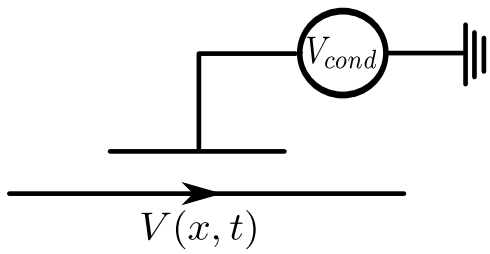

Figure B.2: Edge channel gated by a conductor driven with $V_{cond}(t)$. The voltage along the edge channel is $V(x,t)$, and the voltage induced along the edge channel by the driven conductor is $\widetilde{V}_{cond}(x,t)$.

If we rewrite $\widetilde{V}_{cond}(x,t)$ as $V_{cond}(t)K(x)$, and introducing the conductor's polarisability:

$$\chi_{cond}(x,y) = -\frac{1}{\epsilon}\Big(\frac{\partial \rho_{ind}(x)}{\partial V(y)}\Big)_{V_{cond}=0}, \tag{B.9}$$

we find the voltage along the edge channel:

$$V(x,t) = V_{cond}(t)K(x) - \frac{e}{\epsilon\sqrt{\pi}}\int \mathrm{d}y(-\Delta + \chi)^{-1}(x,y)(\partial_y\phi)(y,t). \tag{B.10}$$

The equations (B.7) and (B.10) describe the dynamics of a chiral edge channel coupled to a perfect conductor. We thus obtained an integrodifferential equation for the bosonic field ϕ, which relates it to the conductor's potential V_{cond}. This result takes into account linear screening effects.

Scattering matrix of the quantum RC circuit

Model from electrostatics

We now replace the preceeding conductor by a quantum RC circuit. In this case, the conductor has its own charge dynamics over a relaxation time RC, and the charge relaxation resistance R is modelled by a semi-infinite transmission line [160] of inductance and capacitance per unit length $\mathcal{L}_{line}$ and $\mathcal{C}_{line}$ such that $R = \sqrt{\frac{\mathcal{L}_{line}}{\mathcal{C}_{line}}}$.
It is also assumed that the characteristic polarization time of the capacitor's plate is much shorter than all other time scales RC and l/v_F. In this case, any charge fluctuation in the edge channel leads to an immediate polarization of the capacitor's plate.
Two neutrality conditions are satisfied:

Circuit neutrality The charge stored in the plate and in the transmission line are opposite.

Capacitor neutrality The edge channel and the plate being in total electrostatic influence, the charge stored in the edge channel and in the plate are opposite.

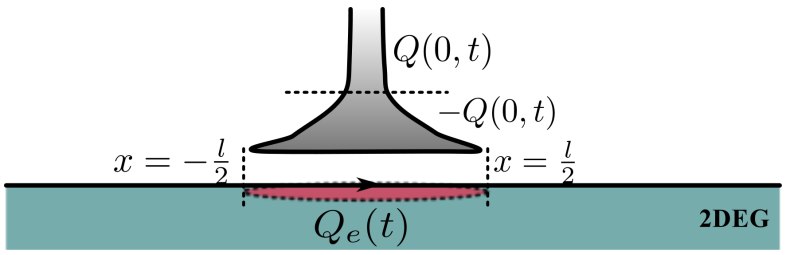

Figure B.3: Sketch of the mesoscopic RC circuit. The conductor made of the capacitor's plate and the associated lead is neutral. The total charge stored in the lead is the total charge of the transmission line. For perfect screening, the charge $Q_e(t)$ stored on the shaded part of the chiral edge channel and the charge stored on the plate facing it are opposite:$Q_e(t) = -(-Q(0,t)) = Q(0,t)$.

The capacitor's plate and the edge channel are coupled over a length L. The charge stored in the circuit is $Q(z,t)$, z being the coordinate along the transmission line (see fig. B.3). The neutrality conditions and the equation of motion for the bosonic field in the presence of an external potential lead to :

$$Q(0,t) = -e\int_{-L/2}^{+L/2} n(y,t)\mathrm{d}y \tag{B.11}$$

$$(\partial_t + v_F\partial_x)\phi(x,t) = \frac{e\sqrt{\pi}}{h}f(x)U_c(t)\,, \tag{B.12}$$

where $f(x) = 1$ if $|x| < L/2$ and 0 otherwise and $U_c(t)$ is the potential seen by the electrons in the edge channel inside the capacitor.

Solution as a plasmon scattering matrix

The distributed charge $Q(z,t)$ along the transmission line satisfies a wave equation for $z > 0$. The distributed charge in the transmission line thus decomposes into ingoing and outgoing waves:

$$Q_{in}(z,t) = \sqrt{\frac{\hbar}{4\pi R}}\int_0^{+\infty}\frac{d\omega}{\sqrt{\omega}}(a_\omega^{(in)}e^{i\omega(z/v-v)} + h.c.) \tag{B.13}$$

$$Q_{out}(z,t) = \sqrt{\frac{\hbar}{4\pi R}}\int_0^{+\infty}\frac{d\omega}{\sqrt{\omega}}(a_\omega^{(out)}e^{-i\omega(z/v-v)} + h.c.), \tag{B.14}$$

where $a^{(in,out)}$ are the input/output modes of the transmission line. The capacitance C appears as a boundary condition :

$$Q(0,t) = C\Big(U_c(t) - \frac{1}{\mathcal{C}_{line}}\left(\frac{\partial Q}{\partial z}\right)(0,t)\Big)\,. \tag{B.15}$$

In (B.15), the second term in the r.h.s. is the voltage at the boundary of the transmission line. The total charge accumulated in the transmission line is $Q(0,t) = Q_{in}(0,t) + Q_{out}(0,t)$. Thus, the voltage on the capacitor's plate is given by :

$$V(0,t) = -R(\partial_t Q)(0,t) = eR\sqrt{\frac{R_K}{2R}}\int_0^{+\infty}\frac{\mathrm{d}\omega}{2\pi}\sqrt{\omega}\left(i(a_\omega^{(in)} - a_\omega^{(out)})e^{-i\omega t} + h.c.\right). \quad \text{(B.16)}$$

The capacitor's potential in eq. (B.15) can be expressed as

$$U_c(t) = \frac{Q(0,t)}{C} + V(0,t), \quad \text{(B.17)}$$

which gives, in the equation of motion for ϕ:

$$(\partial_t + v_F\partial_x)\phi(x,t) = \frac{e\sqrt{\pi}}{h}f(x)\left(\frac{Q(0,t)}{C} + V(0,t)\right). \quad \text{(B.18)}$$

By introducing the spatial Fourier components of the density field along the edge channel:

$$\phi(x,t) = \int\frac{\mathrm{d}\omega}{2\pi}\phi_\omega(x)e^{i\omega(x/v_F - t)}, \quad \text{(B.19)}$$

one can solve eq. (B.18)for $\phi_\omega(x)$:

$$\phi_\omega(x) = \frac{1}{2}\left(\phi_\omega^{(out)} + \phi_\omega^{(in)}\right) + \frac{1}{v_F RC}\sqrt{\frac{2R}{R_K}}\sqrt{\frac{\pi}{\omega}}\left(\Lambda(\omega)a_\omega^{(in)} + \Lambda^*(\omega)a_\omega^{(out)}\right)\left[G_0(x) - \frac{1}{2}G_0(L/2)\right], \quad \text{(B.20)}$$

with $\Lambda(\omega) = 1 + i\omega RC$ and $G_0(x) = \int_{-L/2}^{x} f(y)e^{-i\omega y/L}\mathrm{d}y$. Using the relation between ϕ_ω and the b modes

$$\phi_\omega^{(in/out)} = -i\sqrt{\frac{\pi}{\omega}}b_\omega^{(in/out)}, \quad \text{(B.21)}$$

the specification $x = L/2$ gives a first relation between a and b modes :

$$b_\omega^{(out)} - b_\omega^{(in)} = \frac{i\tilde{f}(\omega/v_F)}{v_F RC}\sqrt{\frac{R}{2R_K}}\left(\Lambda(\omega)a_\omega^{(in)} + \Lambda^*(\omega)a_\omega^{(out)}\right). \quad \text{(B.22)}$$

To obtain a second relation between b and a modes, we must use the neutrality condition (B.11), which rewrites :

$$Q(0,t) = -\frac{e}{\sqrt{\pi}}\int f(y)\frac{d}{dy}\left(e^{i\omega y/v_F}\phi_\omega(y)\right)\mathrm{d}y. \quad \text{(B.23)}$$

Using (B.20), we get :

$$\mu(\omega)a_\omega^{(in)} + \mu(\omega)^* a_\omega^{(out)} = -\frac{\omega}{2v_F}\tilde{f}(-\omega/v_F)\sqrt{\frac{2R}{R_K}}(b_\omega^{(in)} + b_\omega^{(out)}), \quad \text{(B.24)}$$

where :

$$\mu(\omega) = 1 + \frac{l_f(\omega)\Lambda(\omega)}{v_F R_K C} \quad \text{(B.25)}$$

$$l_f(\omega) = \int f^2(x)\mathrm{d}x + \frac{\omega}{v_F}\int_{x\geq y} f(x)f(y)\sin\left(\frac{\omega(x-y)}{v_F}\right)\mathrm{d}x\mathrm{d}y. \quad \text{(B.26)}$$

The two equations (B.22) and (B.24) can be solved to give the out modes as functions of the in modes :

$$\begin{pmatrix} a_\omega^{(out)} \\ b_\omega^{(out)} \end{pmatrix} = \mathcal{S}(\omega) \begin{pmatrix} a_\omega^{(in)} \\ b_\omega^{(in)} \end{pmatrix} , \tag{B.27}$$

where the scattering matrix coefficients admit the following expression :

$$t_b(\omega) = \frac{\mu^*(\omega) - iRC\omega|\beta(\omega)|^2\Lambda^*(\omega)}{\mu^*(\omega) + iRC\omega|\beta(\omega)|^2\Lambda^*(\omega)} \tag{B.28}$$

$$t_a(\omega) = \frac{-\mu(\omega) - iRC\omega|\beta(\omega)|^2\Lambda^*(\omega)}{\mu^*(\omega) + iRC\omega|\beta(\omega)|^2\Lambda^*(\omega)} \tag{B.29}$$

$$r_b(\omega) = \frac{-2i\omega RC\beta^*(\omega)}{\mu^*(\omega) + iRC\omega|\beta(\omega)|^2\Lambda^*(\omega)} \tag{B.30}$$

$$r_a(\omega) = \frac{2i\omega RC\beta(\omega)}{\mu^*(\omega) + iRC\omega|\beta(\omega)|^2\Lambda^*(\omega)}, \tag{B.31}$$

where $\beta(\omega) = \frac{i}{2v_F RC}\sqrt{\frac{2R}{R_K}}\tilde{f}(\omega/v_F)$.
The behaviour of the scattering coefficients is determined by two dimensionless parameters:

$$\mathcal{R} = \frac{2R}{R_K} \tag{B.32}$$

$$\alpha = \frac{L}{v_F R_K C} = \frac{e^2/C}{hv_F/L}. \tag{B.33}$$

$\mathcal{R}$ is the dimensionless relaxation resistance, and α measures the relative importance of Coulomb interactions (which scale as e^2/C) and the kinetic energy hv_F/L. In other words, it compares the time of flight through the circuit L/v_F to the typical response time $R_K C$ in the absence of the resistance. The fast circuit limit is reached when $\alpha \gg 1$. On the contrary, a circuit with slow response will have $\alpha \ll 1$.

In the case of a square gate, the plasmon transmission coefficient [1] admits the following expression :

$$t_b(\omega) = \frac{1 + \alpha\text{sinc}(\omega L/v_F) - \mathcal{R}\sin^2(\omega L/2v_F) - i(\omega L/2v_F)\big(\alpha\text{sinc}^2(\omega L/2v_F) + \mathcal{R}\text{sinc}(\omega L/v_F)\big)}{1 + \alpha\text{sinc}(\omega L/v_F) + \mathcal{R}\sin^2(\omega L/2v_F) + i(\omega L/2v_F)\big(\alpha\text{sinc}^2(\omega L/2v_F) - \mathcal{R}\text{sinc}(\omega L/v_F)\big)} . \tag{B.34}$$

In the UV regime, this expression becomes :

$$t_b(\omega) \simeq \frac{1 - \mathcal{R}\sin^2(\omega L/2v_F) - i\mathcal{R}/2\sin(\omega L/v_F)}{1 + \mathcal{R}\sin^2(\omega L/2v_F) - i\mathcal{R}/2\sin(\omega L/v_F)} . \tag{B.35}$$

At low frequency, (B.34) reduces to:

$$t_b(\omega) \simeq \frac{1 + \alpha - (\omega L/v_F)^2(\alpha/6 + \mathcal{R}/4) - i(\omega L/v_F)(\alpha/2 + \mathcal{R})}{1 + \alpha + (\omega L/v_F)^2(\mathcal{R}/4 - \alpha/6) + i(\omega L/v_F)(\alpha/2 - \mathcal{R})} \tag{B.36}$$

[1] It has been shown in chapter 5 that this coefficient encodes all the relaxation properties.

At low frequency, the plasmon transmission coefficient (B.34) reduces to a phase linear in ω, and gives acces to the Wigner-Smith delay time $\tau = \frac{L}{v_F}\frac{\alpha+2\mathcal{R}}{1+\alpha}$. In other words, this delay time represents the renormalized time of flight under the influence of the capacitor.
Finally, the low frequency expansion of the admittance associated to (B.34) gives the total relaxation resistance and the total electrochemical capacitance of the circuit :

$$R_q = R + \frac{R_K}{2} \text{ and } C_\mu = \frac{1}{\frac{v_F R_K}{L} + \frac{1}{C}} \,. \tag{B.37}$$

Microscopic model for the $\nu = 2$ regime

If we consider short-range coupling in the interacting region :

$$V_{\alpha\beta}(x,y) = V_{\alpha\beta}\delta(x-y) \,, \tag{B.38}$$

with $V_{\beta\alpha} = V_{\alpha\beta}$, the equation of motion for the bosonic field reads:

$$(\partial_t + v_\alpha \partial_x)\phi_\alpha(x,t) = -\frac{e^2}{h} f(x) \sum_\beta V_{\alpha\beta}(\partial_x \phi_\beta)(x,t), \tag{B.39}$$

with $f(x) = 1$ if $|x| < L/2$ and 0 otherwise.

Considering position dependent Fourier modes, we get:

$$\mathcal{V}(x)\frac{\partial \Phi}{\partial x}(x,\omega) = i\omega\Phi(x,\omega). \tag{B.40}$$

with $\mathcal{V}_{\alpha\beta}(x) = \delta_{\alpha\beta}v_\alpha + \frac{e^2}{h}f(x)V_{\alpha\beta}$. We see here that the diagonal terms in V renormalize the Fermi velocities in each channel. The non-diagonal part, which couples the edge channels, is responsible for the interchannel plasmon scattering. It is useful to rewrite $\mathcal{V}$ in the interaction region as :

$$\mathcal{V} = \bar{v}\mathbf{1} + \frac{\Delta v}{2}\sigma^z + W\sigma^x, \tag{B.41}$$

where

$$\bar{v} = \frac{v_1 + v_2}{2} + \frac{e^2}{2h}(V_{11} + V_{22}) \tag{B.42}$$

$$\Delta v = v_1 - v_2 + \frac{e^2}{h}(V_{11} - V_{22}) \tag{B.43}$$

$$\text{and } W = \frac{e^2}{h}V_{12}. \tag{B.44}$$

The plasmon scattering matrix is found by integrating eq. (B.40):

$$\mathcal{S}(\omega, L) = e^{iL\mathcal{V}^{-1}} = e^{i\omega L/v_0} e^{i\omega L/v(\cos\theta\sigma^z + \sin\theta\sigma^x)} \,. \tag{B.45}$$

The eigenmode velocities $v_\pm$ and the angle θ are given by :

$$v_\pm = \frac{1}{\frac{1}{v_0} \mp \frac{1}{v}} = \bar{v} \pm \sqrt{\left(\frac{\Delta v}{2}\right)^2 + W^2} \tag{B.46}$$

$$\cos\theta = \frac{\Delta v/2}{\sqrt{W^2 + (\Delta v/2)^2}} \text{ and } \sin\theta = \frac{W}{\sqrt{W^2 + (\Delta v/2)^2}} \,. \tag{B.47}$$

Requiring the Hamiltonian of the infinite system to be definite positive implies that $v_\pm > 0$ and this gives a constraint on the interaction potentials which we assume to be satisfied : $|v_+ - v_-| < \bar{v}$). As soon as there are interactions, $v_+ < v_-$ and therefore these eigenmodes are called the fast and slow modes depending on their velocities. We thus recover a scattering of the form (4.43) found in chapter 4, where the angle can be interpreted as representing the strength of interactions. Indeed, the value of $\cos\theta$ and $\sin\theta$ depends on the ratio $u = W/\Delta v$:

When W $\to$ 0 then $\theta \to 0$. We are in the weak coupling regime : plasmon modes localized in one channel only acquire a phase during their propagation.

When u $\to \infty$, then $\theta \to \frac{\pi}{2}$: the interchannel coupling is much stronger than the energy scale associated to the renormalized Fermi velocities[2]. This value corresponds to the strong coupling regime, a case that has been considered in [88].

In the strong coupling case, which corresponds to maximal mixing, the eigenmodes correspond to a spinless mode calledspin the charge mode (fast mode of velocity v_+) and a dipolar mode carrying a nonvanishing spin (slow mode of velocity v_-) : this model exhibits the spin/charge separation.
The mesoscopic conductor made of the two edge channels admits the following admittance :

$$R_K\, Y(\omega) = (1 - e^{i\omega l/v_+})(1 - \sin\theta) + (1 - e^{i\omega l/v_+})(1 + \sin\theta)\,. \tag{B.48}$$

If $\theta = \pi/2$, the admittance (B.48) becomes $R_K\, Y(\omega) = 2(1 - e^{i\omega l/v_-})$: in this case, only the symmetric mode carries charge, as expected. If we expand (B.48) at low frequency, we get in the strong coupling regime :

$$R_q = \frac{R_K}{4} \text{ and } R_K C_\mu = 2l/v_+\,. \tag{B.49}$$

Discrete circuit elements model for coupled channels

We would like to see the coupled channels problem in terms of discrete circuit elements describing long range interactions along the same lines as [128]. Within the interaction region $|x| < l/2$, the channel α sees a uniform time dependent potential $U_\alpha(t)$. This potential is in turn related to the charges $Q_\beta(t)$ stored in the interacting region thruogh a capacitance matrix $(\mathcal{C}_{\alpha\beta})_{\alpha\beta}$:

$$Q_\alpha(t) = \sum_\beta \mathcal{C}_{\alpha\beta} U_\beta(t)\,. \tag{B.50}$$

The equations of motion for the bosonic fields describing the density fluctuations in the two edge channels are :

$$(\partial_t + v_F \partial_x)\, \phi_\alpha(x,t) = \frac{e\sqrt{\pi}}{h} f(x) U_\alpha(t)\,. \tag{B.51}$$

where $f(x) = 1$ if $|x| < l/2$ and 0 otherewise. In the previous equation, we assumed that the Fermi velocities are the same for the two channels. We would like now to relate the plasmon scattering matrix to the capacitance matrix $(\mathcal{C}_{\alpha\beta})_{\alpha\beta}$. Let us introduce the vector notation :

$$\Phi(\omega)^{(in/out)} = \frac{e}{\sqrt{\pi}} \left(\phi_\alpha(\pm l/2, t)\right)_\alpha \text{ and } U(\omega) = \left(U_\alpha(\omega)\right)_\alpha\,. \tag{B.52}$$

[2]Or the renormalized velocities in the edge channels are the same, a case that we cannot consider here.

Then eq. (B.50) rewrites :

$$\Phi(\omega)^{(in)} - \Phi(\omega)^{(out)} = \mathcal{C} \cdot U(\omega)\,. \tag{B.53}$$

The capacitance matrix is symmetric [84]. Thus, it can be diagonalized by a rotation :

$$\mathcal{C} = \begin{pmatrix} C_1 & -C \\ -C & C_2 \end{pmatrix} = R(\theta)^{-1} \begin{pmatrix} C_+ & 0 \\ 0 & C_- \end{pmatrix} R(\theta)\,. \tag{B.54}$$

The eigenvalues and the angle θ are given by :

$$C_\pm = \frac{C_1 + C_2}{2} + \sqrt{C^2 + \frac{(\Delta C)^2}{4}} \text{ and } \cos\theta = \frac{\Delta C}{\sqrt{C^2 + \frac{(\Delta C)^2}{4}}}\,, \tag{B.55}$$

where $\Delta C = C_1 - C_2$. The plasmon scattering matrix relating $\Phi(\omega)^{(in)}$ and $\Phi(\omega)^{(out)}$ is found by solving the equations of motion. At low energies, it reads :

$$\mathcal{S}(\omega) = \frac{1}{2}\left(e^{i\omega l/v_+} + e^{i\omega l/v_-}\right)\mathbf{1} + \frac{1}{2}\left(e^{i\omega l/v_+} - e^{i\omega l/v_-}\right)\left(\cos\theta\sigma^z - \sin\theta\sigma^x\right)\,, \tag{B.56}$$

where the eigenmode velocities $v_\pm$ are given by:

$$v_\pm = v + (R_K \partial_l C_\pm)^{-1}\,. \tag{B.57}$$

Since the capacitances are proportional to the length l of the interacting region, the eigenmode velocities are independent of l. Thus, we have derived the scattering matrix for plasmon modes, and found that in the infrared limit it has the same universal expression as in the short range coupling case.
Here, the limit $\cos\theta = 0$ is reached for $C \gg |\Delta C|$. It can also be checked that gauge invariance is satisfied by the admittance matrix only if the capacitance matrix $\mathcal{C}$ satisfies the same condition : it means that each edge channel must be totally screened by the other within the interaction region.

Phase scattering

In this section, we consider two examples which lead to a pure phase transmission of plasmons corresponding to the absence of nergy leak outside of the edge channel. These include the casse of a single channel with intrachannel interactions and also the coupling of an open channel to a closed one.

Coupling with a closed channel

In fig B.4, the closed edge channel is described by a spatially periodic bosonic field :

$$\Phi_2(-l/2, t) = \Phi_2(l/2, t), \forall t. \tag{B.58}$$

The former equality means that there is no charge stored in the closed channel, since $Q = \int(\partial_x \Phi)dx = \Phi(l/2) - \Phi(-l/2)$. This assumes the absence of interaction with a zero mode, and thus the equality of the chemical potentials of the two channels : $\mu_F^{(1)} = \mu_F^{(2)}$.Apart from

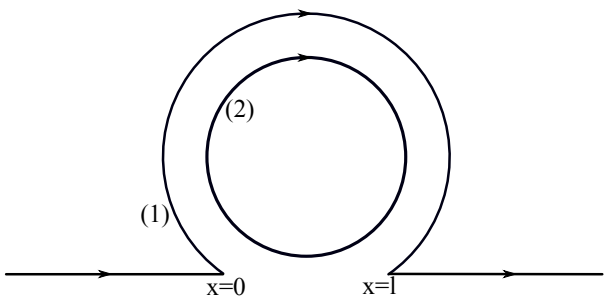

Figure B.4: The edge configuration considered here. There is no tunneling between positions $x = 0$ and $x = L$ of the channel (1). The coupling is assumed to be local all along the closed channel.

this specificity, the derivation of the scattering matrix follows the same line of arguments as for the low energy scattering for $\nu = 2$ edge channels. The supplementary condition comes from the closed channel (2) whose bosonic field satisfies :

$$\phi_2(x = 0, t) = \phi_2(x = l, t)\,. \tag{B.59}$$

Thus, the transmission coefficient has the following expression :

$$t_b(\omega) = \exp\left(-i\phi(\omega)\right) \tag{B.60}$$

with

$$\phi(\omega) = \omega(\tau_+ + \tau-) - 2\arctan\left[\frac{1 - p\cos\omega\tau_+ - (1-p)\cos\omega\tau_-}{p\sin\omega\tau_+ + (1-p)\sin\omega\tau_-}\right], \tag{B.61}$$

and

$$\tau_+ = \frac{l}{v_+}, \quad \tau_+ = \frac{l}{v_-}, \quad p = \frac{1}{2}(1 + cos(\theta)),$$

where v_- (resp.v_+) is the velocity of the dipolar (resp. charge) plasmonic mode.
One has $|t_b(\omega)|^2 = 1, \forall\omega$: since the closed edge has a finite length, there is no energy loss from the first edge to the other one. Two physically relevant parameters appear, which are the ratio between the travel times for slow (dipolar) and fast (charge) modes $\gamma = \frac{\tau_-}{\tau_+}$, and the interaction parameter p or equivalently θ. It should be noticed that $\gamma \in [0, 1]$ since the dipolar mode is slower than the charge one.

The appearance of phase resonances in the transmission coefficient is linked to the presence of the closed channel, and they will be responsible for a step structure in the elastic scattering probability, as seen in chapter 5.

Intrachannel interactions

We now turn to the case of intrachannel interactions. These are responsible for a modification of the plasmon dispersion relation :

$$\omega(q) = v_F q\left(1 + \frac{\tilde{U}(q)}{2\pi\hbar v_F}\right), \tag{B.62}$$

where $\tilde{U}$ is the Fourier transform of the interactin potential.
The screened Coulomb interaction could be modeled by different expressions :

- Contact potential : $U(x,y) = U_0\delta(x-y)$. In this case, $\tilde{U}(q) = U_0$.
- Finite range potential $U(x,y) = U_0 e^{-|x-y|/\xi}$, where ξ is the screening length. Here, $\tilde{U}(q) = \frac{2U_0\xi}{1+(q\xi)^2}$.
- A regularized Coulomb potential : $U(x,y) = \frac{U_0}{\sqrt{a^2+(x-y)^2}}$. This potential form corresponds to $\tilde{U}(q) = 2U_0 a K_0(qa)$.

The dispersion relation being written in the form $\omega(q)$, the different operators appearing in bosonization must be written in terms ok the wavevector k. After propagation during a time t, the parameter of the coherent state of an electron introduced at a position x becomes :

$$\lambda_{x,t}(k) = \lambda_{x,t=0}(k)\, e^{-i\omega(k)t} = \lambda_{x,t=0}(k)\, e^{-iv_F kt}\, e^{-i(\omega(k)-v_F k)t}\,. \tag{B.63}$$

Thus, the transmission coefficient is a phase, and is equal to:

$$t_b(k) = \exp\left(-i(\omega(k) - v_f k)\right). \tag{B.64}$$

In such a situation, the nonlinear part of the scattering phase is responsible for decoherence and relaxation.

Dissipative environment

As a last example, we consider an edge channel coupled to a dissipative environment. The losses per unit length are accounted for by a frequency dependent energy loss rate $\kappa(\omega)$. The propagation over an infinitesimal length dl is described by the following equation :

$$\phi_\omega(l+dl) = \phi_\omega(l)\, e^{i\omega dl/v_F} e^{-\kappa(\omega)dl}\,. \tag{B.65}$$

This leads to the evolution equation for the bosonic field :

$$\frac{d\phi_\omega}{dx}(x) = (\omega/v_F - \kappa(\omega))\phi_\omega(x)\,. \tag{B.66}$$

Thus, in this case, the transmission coefficient representing a propagation over a length l is, up to the free propagation phase :

$$t_b(\omega) = e^{-\kappa(\omega)l}\,. \tag{B.67}$$

The dimensionless admittance equivalent to the circuit depicted on the left is:

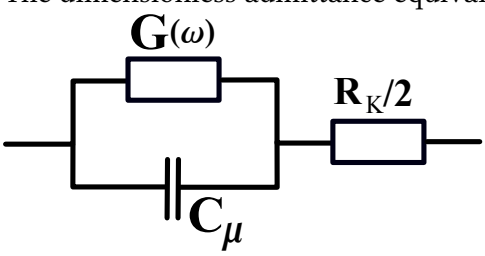

$$y(\omega) = R_K G(\omega) - iR_K C_\mu \omega - \frac{R_K^2}{2}(G(\omega) - iC_\mu\omega)^2\,.$$

If we expand the expression of the admittance obtained from $t_b(\omega)$:

$$y(\omega) = 1 - e^{iR_K C_\mu \omega} e^{-l\kappa(\omega)} \tag{B.68}$$

$$\simeq -iR_K C_\mu \omega - l\kappa(\omega) + \frac{1}{2}(R_K C_\mu \omega)^2 + \frac{1}{2} l^2 \kappa^2(\omega)\,, \tag{B.69}$$

then we have the relation between $\kappa(\omega)$ and the leak conductance $G(\omega)$:

$$l\kappa(\omega) = R_K G(\omega)\,. \tag{B.70}$$

In the case of an ohmic environment $G(\omega) \propto \omega$, the dissipation rate κ is linear in ω.

Appendix C

Auxiliary relaxation functions and modified Wick theorem

In this appendix, the auxiliary functions needed to compute the relaxation of electrons in chapters 5 and 6 are presented. We also give the derivation of a generalization Wick's theorem in a coherent plasmonic state which is necessary to split the coherence function into its modified vacuum and wavepacket parts.

The $\Gamma_\pm$ functions and their properties

The $\Gamma_\pm$ functions are defined by :

$$\Gamma_\pm(q) = \int e^{-iqx} \exp\left(\pm \int_0^\infty (1 - t_b(\omega))(e^{-\frac{i\omega x}{v_F}} - 1)\frac{d\omega}{\omega}\right) dx \tag{C.1}$$

They satisfy the following sum rule :

$$\int \Gamma_\pm(q)\,\frac{dq}{2\pi} = \exp\Big(\pm \int_0^\infty (1 - t_b(\omega))(e^{-\frac{i\omega x}{v_F}} - 1)\frac{d\omega}{\omega}\Big)\Big|_{x=0} = 1\,. \tag{C.2}$$

These functions also satisfy $\Gamma_+ \star \Gamma_- = \delta$, where $\star$ denotes the convolution product. Expanding the exponential integrand in series shows that each of them can be decomposed into a $\delta(q)$ singularity and a regular part $A_\pm(q)$:

$$\frac{\Gamma_\pm(q)}{2\pi\Lambda_\pm} = \delta(q) + A_\pm(q) \tag{C.3}$$

where

$$\Lambda_\pm = \exp\left(\mp \int_0^\infty (1 - t_b(\omega))\frac{d\omega}{\omega}\right) \tag{C.4}$$

and $A_\pm(q) = 0$ for $q > 0$ (since the integration goes from zero to infinity in the exponential in (C.1)). Note that it is assumed that the transmission coefficient $t_b(\omega)$ tends to 1 at infinity fast enough so that $\Lambda_\pm \neq 0$. The property $\Gamma_+ \star \Gamma_- = \delta$ rewrites as:

$$A_+ + A_- + A_+ \star A_- = 0\,. \tag{C.5}$$

The regular part can be obtained as a solution of an inhomogeneous linear integrodifferential equation, in the spirit of the P(E) theory of dynamical Coulomb blockade :

$$-qA_\pm(q) = f_\pm(q) + \int_0^{-q} f_\pm(k)A_\pm(k+q)\,dk \tag{C.6}$$

where $f_\pm(k) = \pm(1-t(v_F k))$. Note that for $q \leq 0$, $A_\pm(q)$ only depends on the values of $t_b(\omega)$ for $0 \leq \omega \leq v_F|q|$. The formal solution to each of these equations is the series expansion of $A_\pm(q)$ as a series of convolutions:

$$A_\pm(q) = \sum_{n=1}^{+\infty} \frac{(\pm 1)^n}{n!} \left[\Theta(-k)\frac{1-t(-vk)}{-k}\right]^{(\star n)}(q) \tag{C.7}$$

which represents their perturbative expansion in terms of plasmon scattering. Since $t_b(\omega)$ goes to zero as $O(\omega)$ for $\omega \to 0$, this shows that $A_\pm(q) \mapsto 0$ when $q \to 0^-$. The first terms of this expansion can be used to obtain approximate analytical expressions for $A_\pm(q)$ in the infrared regime from a low frequency expansion of plasmon scattering or equivalently of the finite frequency admittance $y(\omega) = R_K G_{ee}(\omega)$. In chapter 5, section 2, this expansion has been used to find the series expansion of the elastic scattering probability at low energy. Finally, eqs. (C.6) provide a very convenient way to compute $A_\pm$ numerically from the scattering coefficient $t_b(\omega)$.

Time delay symmetry

In the case of a pure phase scattering $t_b(\omega) = e^{il_0\omega/v_F}$, we have:

$$A_+(q) = -il_0\Theta(-q) \tag{C.8}$$
$$A_-(q) = il_0\Theta(-q)\,e^{-il_0 q}\,. \tag{C.9}$$

In this case, $Z(k_0) = 1$ and more generally $\mathcal{G}^{(e)}_{k_0}$ is the sum of the Fermi sea contribution and of a quasi particle peak $\delta(q-k_0)$. This result simply expresses that $t_b(\omega) = e^{i\omega l_0/v_F}$ is a time delay for single electron excitations and thus does not lead to relaxation at all.

More generally, let us consider $t_b(\omega) = e^{i\omega l_0/v_F}\mathcal{T}(\omega)$. The $e^{i\omega l_0/v_F}$ phase introduces a time delay for single electron excitations and therefore should not alter their energy nor their coherence. Integration by parts shows that:

$$\begin{aligned} A_+(q) &= -il_0\Theta(-q)\left(1+\int_q^0 B_+(k)e^{-ikl_0}\,dk)\right) \\ &+ e^{-iql_0}B_+(q) \end{aligned} \tag{C.10}$$

$$\begin{aligned} A_-(q) &= il_0 e^{-iql_0}\Theta(-q)\left(1+\int_q^0 B_-(k)\,dk)\right) \\ &+ e^{-iql_0}B_-(q) \end{aligned} \tag{C.11}$$

where $B_\pm(q)$ denotes the $A_\pm$ functions defined in (C.1) and (C.3) evaluated using $\mathcal{T}(\omega)$. These expressions can then be used to evaluate for the electron distribution. Plugging this back into the epxression for $|\mathcal{Z}(k_0)|^2$ immediately shows that the result does not depend at all on l_0 and can be evaluated using $\mathcal{T}(\omega)$ instead of $t_b(\omega) = e^{i\omega l_0/v_F}\mathcal{T}(\omega)$ as expected on physical grounds.

Wick theorem in plasmon coherent states

This section shows how a generalization of Wick's theorem can be derived for matrix elements in coherent plamonic states. Before deriving the complete expression of Wick's theorem, we recall some results on coherent states and displacement operators.

Coherent states and displacement operators

A single plasmonic mode is described as a quantum harmonic oscillator. Denoting by b and $b^\dagger$ creation and destruction operators ($[b, b^\dagger] = 1$) in such a mode, the displacement operator with complex parameter λ is defined as:

$$D_b(\lambda) = e^{\lambda\, b^\dagger - \lambda^*\, b}\,. \tag{C.12}$$

This operator generates the coherent state $D_b(\lambda)|0\rangle = |\lambda\rangle$.
Displacement operators form a projective representation of translations in phase space :

$$D_b(\lambda)^\dagger.\, b.\, D_b(\lambda) \;=\; b + \lambda \tag{C.13}$$

$$D_b(\lambda).\, D_b(\mu) \;=\; e^{i\Im(\mu^*\lambda)}\, D_b(\lambda + \mu)\,. \tag{C.14}$$

Denoting by $: A :$ the bosonic normal ordering of A, it immediately follows that

$$D_b(\lambda) = e^{-|\lambda|^2/2}\; : D_b(\lambda) :\; . \tag{C.15}$$

Equations (C.14) and (C.15) give access to all average values. In particular:

$$\langle \alpha_-| : D_b(\lambda) : |\alpha_+\rangle = e^{\lambda\alpha_-^* - \lambda^*\alpha_+}\langle \alpha_-|\alpha_+\rangle\,. \tag{C.16}$$

The scalar product of coherent states follows from (C.14) and (C.15):

$$\langle \mu|\lambda\rangle = e^{-|\lambda-\mu|^2/2} \times e^{i\Im(\mu^*\lambda)}\,. \tag{C.17}$$

All in this thesis, we consider infinite dimensional coherent states that are eigenstates of all b_ω for $\omega > 0$. These states are written as formal infinite tensor products:

$$|[\lambda_\omega]\rangle = \bigotimes_{\omega>0} D_{b_\omega}(\lambda_\omega)|0_\omega\rangle \tag{C.18}$$

Correlation functions as well as matrix elements involving such states are derived simply by taking a formal product over all $\omega > 0$ which is equivalent to integrating the argument of exponentials that appear in the above equations (C.14) to (C.17). For example, the scalar product of two infinite dimensional coherent states is given by:

$$\langle[\mu_\omega]|[\lambda_\omega]\rangle = e^{-\frac{1}{2}\int_0^{+\infty}|\lambda_\omega-\mu_\omega|^2 d\omega} \times e^{i\int_0^{+\infty}\Im(\mu_\omega^*\lambda_\omega)\,d\omega} \tag{C.19}$$

and we have:

$$\langle\alpha_\omega| : \bigotimes_{\omega>0} D(\lambda_\omega) : |\beta_\omega\rangle = e^{\int_0^{+\infty}(\lambda_\omega\alpha_-^* - \lambda_\omega^*\beta_\omega)\,d\omega}\langle[\alpha_\omega]|[\beta_\omega]\rangle\,. \tag{C.20}$$

Generalized Wick's theorem

Our goal is to compute the single electron coherence $\mathcal{G}^{(e)}_{\text{out}}(x,y)$ for an initial state formed by two single particle excitations on top of the Fermi sea:

$$\mathcal{G}^{(e)}(x,y) = \int \varphi(y_+)\varphi^*(y_-)\langle\widetilde{\psi}(y_-)\psi^\dagger(y)\psi(x)\widetilde{\psi}^\dagger(y_+)\rangle_F \mathcal{D}_{\text{ext}}(y_-,y_+)\, dy_+ dy_- \ . \tag{C.21}$$

The main difficulty comes from the four point correlator $\langle\widetilde{\psi}(y_-)\psi^\dagger(y)\psi(x)\widetilde{\psi}^\dagger(y_+)\rangle_F$. In the case of free electrons, Wicks theorem can be used to decompose it into a sum of two contributions which respectively correspond to the Fermi sea and wave packet contributions to $\mathcal{G}^{(e)}(x,y)$.

We want to perform a similar decomposition here. As stressed in chapter 5, the operator $\tilde{\psi}(y)$ only differ from a bare electron operator by an e/h pair dressing:

$$\tilde{\psi}^\dagger(y) = e^{i\int_0^{+\infty}\Im(t_b(\omega))\frac{d\omega}{\omega}}\psi^\dagger(y)\left[\bigotimes_{\omega>0} D_{b_\omega}\left(\lambda_\omega(y)(1-t_b(\omega))\right)\right] . \tag{C.22}$$

Evaluating the above mentioned four point functions then boils down to the evaluation of a four fermion operator matrix element between coherent plasmon states:

$$\langle\tilde{\psi}(y_-)\psi^\dagger(y)\psi(x)\tilde{\psi}^\dagger(y_+)\rangle_F = \langle g(y_-)|\psi(y_-)\psi^\dagger(y)\psi(x)\psi^\dagger(y_+)|g(y_+)\rangle \, . \tag{C.23}$$

where

$$|g(y)\rangle = \bigotimes_{\omega>0}|\lambda_\omega(y)(1-t_b(\omega))\rangle \, . \tag{C.24}$$

As we shall see now, using a generalization of Wick's theorem, the four point correlator appearing in (C.21) can be written as a sum of product of two point functions. Then, a careful rewriting of each of these two contributions will be performed to make its physical meaning more explicit.

The result can be generalized to the product of an arbitrary even number of fermionic operators. For the sake of simplicity, let us look at a four point correlator :

$$A(x_1,x_2;x_1',x_2') = \psi(x_1)\psi(x_2).\,\psi^\dagger(x_1')\psi^\dagger(x_2') \, . \tag{C.25}$$

We would like to evaluate its matrix element $\langle g_-|A(x_1,x_2;x_1',x_2')|g_+\rangle$ between two coherent plasmonic states $|g_\pm\rangle$. Up to phases $A(x_1,x_2;x_1',x_2')$ acts as a product of displacement operators in plasmonic phase space. Making use of (C.15), we get:

$$A(x_1,x_2;x_1',x_2') =: A(x_1,x_2;x_1',x_2') : \times\langle A(x_1,x_2;x_1',x_2')\rangle_F \tag{C.26}$$

where $\langle A\rangle_F$ denotes the average value of A in the Fermi sea $|F\rangle$ and $: A(x_1,x_2;x_1',x_2') :$ denotes the bosonic normal ordering of the four fermion operator. Since the normal ordering consists into putting all the bosonic annihilators (resp. creators) on the right and (resp. left), it implies that $: A(x_1,x_2;x_1',x_2') :$ is nothing but the normal ordered displacement operator $: D(\Lambda) :$ where the parameter Λ is obtained by summing all complex parameters that appear in the 4 fermion operator:

$$\Lambda_\omega = \frac{1}{\sqrt{\omega}}\left(e^{-i\omega x_1'/v} - e^{-i\omega x_1/v} + e^{-i\omega x_2'/v} - e^{-i\omega x_2/v}\right) . \tag{C.27}$$

Then, the matrix element of a normal ordered plasmonic displacement operator $:D(\Lambda):$ between two coherent plasmonic states $|g_\pm\rangle$ is obtained as:

$$\langle g_-| : D(\Lambda) : |g_+\rangle = \langle g_-|g_+\rangle \times e^{\int_0^\infty (g_-(\omega)^*\Lambda_\omega - \Lambda_\omega^* g_+(\omega))\, d\omega} . \tag{C.28}$$

In particular for the fermionic two point function, we obtain :

$$\frac{\langle g_-|\psi(x)\psi^\dagger(y)|g_+\rangle}{\langle g_-|g_+\rangle} = \langle\psi(x)\psi^\dagger(y)\rangle_F \times \exp\left(\int_0^\infty \left\{g_-^*(\omega)(e^{-i\frac{\omega y}{v_F}} - e^{-i\frac{\omega x}{v_F}}) - g_+(\omega)(e^{-i\frac{\omega y}{v_F}} - e^{-i\frac{\omega x}{v_F}})\right\} \frac{d\omega}{\sqrt{\omega}}\right) \tag{C.29}$$

Wick's theorem can then be applied to decompose the four point fermionic correlator into a sum of products of two point functions:

$$\langle A(x_1, x_2; x_1', x_2')\rangle_F = \langle\psi(x_1)\psi^\dagger(x_1')\rangle_F\langle\psi(x_2)\psi^\dagger(x_2')\rangle_F + \langle\psi(x_1)\psi^\dagger(x_2')\rangle_F\langle\psi(x_2)\psi^\dagger(x_1')\rangle_F . \tag{C.30}$$

Using eq. (C.28) and then (C.29) to absorb the exponential into a rewriting of two point functions finally leads to the generalization of Wick's theorem to plasmon coherent states:

$$\frac{\langle g_-|A(x_1, x_2; x_1', x_2')|g_+\rangle}{\langle g_-|g_+\rangle} = \frac{\langle g_-|\psi(x_1)\psi^\dagger(x_1')|g_+\rangle\langle g_-|\psi(x_2)\psi^\dagger(x_2')|g_+\rangle + x_1' \leftrightarrow x_2'}{\langle g_-|g_+\rangle\langle g_-|g_+\rangle} . \tag{C.31}$$

This result has been expected. Indeed, since Wick's theorem is verifies in the state $|F\rangle$ (in the absence of interactions), gauge invariance states that it is also true for every plasmon coherent state. The interesting point in (C.31) comes that an equivalent of Wick's theorem can be found for matrix elements between different plasmonic coherent states.

Splitting the coherence function

Let us apply this result to the evaluation of the four point function $\langle\widetilde{\psi}(y_-)\psi^\dagger(y)\psi(x)\widetilde{\psi}^\dagger(y_+)\rangle_F$ and plug it back into (C.21). This leads to the decomposition of $\mathcal{G}^{(e)}_{\text{out}}(x, y)$ as a sum of two terms.

The first one, called the *modified vacuum contribution*, is given by:

$$\mathcal{G}^{(e)}_{\text{mv}}(x, y) = \int dy_+ dy_- \varphi(y_+)\varphi^*(y_-)\mathcal{D}_{\text{ext}}(y_+, y_-)\langle g(y_-)|\psi(y_-)\psi^\dagger(y_+)|g(y_+)\rangle \frac{\langle g(y_-)|\psi^\dagger(y)\psi(x)|g(y_+)\rangle}{\langle g(y_-)|g(y_+)\rangle} \tag{C.32}$$

Since $\langle g(y_-)|\psi(y_-)\psi^\dagger(y_+)|g(y_+)\rangle = \langle\tilde{\psi}(y_-)\tilde{\psi}^\dagger(y_+)\rangle_F$ and remembering that $\mathcal{D}_{\text{ext}}(y_+, y_-)$ is the scalar product of the circuit and edge channel states issued from localized single electron excitations at positions y_+ and y_-, unitarity of the plasmon scattering matrix leads to:

$$\langle\tilde{\psi}(y_-)\tilde{\psi}^\dagger(y_+)\rangle_F\, \mathcal{D}_{\text{ext}}(y_+, y_-) = \langle\psi(y_-)\psi^\dagger(y_+)\rangle_F . \tag{C.33}$$

Consequently, the modified vacuum contribution rewrites as:

$$\mathcal{G}^{(e)}_{\text{mv}}(x, y) = \int dy_+ d_-\varphi(y_+)\varphi^*(y_-)\langle\psi(y_-)\psi^\dagger(y_+)\rangle_F \frac{\text{Tr}\,[\psi(x)|g(y_+)\rangle\langle g(y_-)|\psi(y)]}{\langle g(y_-)|g(y_+)\rangle} \tag{C.34}$$

This suggests that the modified vacuum contribution can be viewed as originating from an effective many body operator that represents the excitation of the Fermi sea by the wave packet φ:

$$\rho_{\text{mv}}[\varphi] = \int dy_+ dy_- \varphi(y_+)\varphi^*(y_-)\langle\psi(y_-)\psi^\dagger(y_+)\rangle_F \frac{|g(y_+)\rangle\langle g(y_-)|}{\langle g(y_-)|g(y_+)\rangle} . \tag{C.35}$$

This statement can be proved as follows: if we compute the reduced n particle coherence or more generally any mixed objects involving electron creation and destruction operators, all contributions involving the (y_+, y_-) contraction in the l.h.s. of the generalized Wick theorem can be resummed and gathered together as a modified vacuum contribution for the coherence function under consideration. Then, eq. (C.34) becomes true provided one replaces the $\psi(x)$ and $\psi^\dagger(y)$ operators by the corresponding product of operators appearing in the definition of the n-particle coherence. This precisely means that all modified vacuum contributions arise from the effective many body operator (C.35).

The second contribution to (C.21), called the *wavepacket contribution*, is given by:

$$\mathcal{G}^{(e)}_{\rm wp}(x,y) = \int dy_+ dy_- \varphi(y_+)\varphi^*(y_-)\mathcal{D}_{\rm ext}(y_+,y_-)\frac{\langle g(y_-)|\psi(x)\psi^\dagger(y_+)|g(y_+)\rangle\langle g(y_-)|\psi(y_-)\psi^\dagger(y)|g(y_+)\rangle}{\langle g(y_-)|g(y_+)\rangle} \tag{C.36}$$

Using equation (C.29), the two point correlators $\langle g(y_-)|\psi(x)\psi^\dagger(y_+)|g(y_+)\rangle$ and $\langle g(y_-)|\psi(y_-)\psi^\dagger(y)|g(y_+)\rangle$ can be rewritten in terms of the usual propagators $\langle\psi(y_-)\psi^\dagger(y)\rangle_F$ and $\langle\psi(y_-)\psi^\dagger(y)\rangle_F$ multiplied by the appropriate exponential factors:

$$\begin{aligned}\mathcal{G}^{(e)}_{\rm wp}(x,y) &= \int dy_+ dy_- \varphi(y_+)\varphi^*(y_-)\mathcal{D}_{\rm ext}(y_+,y_-)\langle g(y_-)|g(y_+)\rangle\langle\psi(y_-)\psi^\dagger(y)\rangle_F\,\langle\psi(x)\psi^\dagger(y_+)\rangle_F \\ &\times \exp\left[\int_0^{+\infty}\frac{d\omega}{\omega}(1-t_b^*(\omega))\left\{1-e^{i\frac{\omega}{v_F}(y_- - y_+)}+e^{i\frac{\omega y_-}{v_F}}\left(e^{-i\frac{\omega x}{v_F}}-e^{-i\frac{\omega y}{v_F}}\right)\right\}\right] \\ &\times \exp\left[\int_0^{+\infty}\frac{d\omega}{\omega}(1-t_b(\omega))\left\{1-e^{i\frac{\omega}{v_F}(y_- - y_+)}+e^{-i\frac{\omega y_+}{v_F}}\left(e^{i\frac{\omega y}{v_F}}-e^{i\frac{\omega x}{v_F}}\right)\right\}\right].\end{aligned} \tag{C.37}$$

Then, remembering that

$$\mathcal{D}_{\rm ext}(y_+,y_-) = \exp\left(\int_0^{+\infty} R(\omega)\left(e^{-i\frac{\omega\,\Delta y}{v_F}}-1\right)\frac{d\omega}{\omega}\right) \tag{C.38}$$

and computing the scalar product $\langle g(y_-)|g(y_+)\rangle$ as:

$$\mathcal{D}_{\rm ext}(y_+,y_-) = \exp\left(\int_0^{+\infty} |1-t_b(\omega)|^2\left(e^{-i\frac{\omega\,\Delta y}{v_F}}-1\right)\frac{d\omega}{\omega}\right) \tag{C.39}$$

we obtain

$$\mathcal{D}_{\rm ext}(y_+,y_-)\langle g(y_-)|g(y_+)\rangle = \exp\left(\int_0^{+\infty} 2\Re(1-t_b(\omega))(1-e^{i\frac{\omega}{v_F}(x-y)})\frac{d\omega}{\omega}\right). \tag{C.40}$$

Thus, the product $\mathcal{D}_{\rm ext}(y_+,y_-)\langle g(y_-)|g(y_+)\rangle$ compensates parts of the exponentials in the r.h.s. of (C.37). This leads to the following expression for the wavepacket contribution:

$$\mathcal{G}^{(e)}_{\rm wp}(x,y) = \int dy_+ dy_- \varphi(y_+)\varphi^*(y_-)\langle\psi(y_-)\psi^\dagger(y)\rangle_F\,\langle\psi(x)\psi^\dagger(y_+)\rangle_F\, C_{y_+}(x,y)C_{y_-}(y,x)^* \tag{C.41}$$

$$C_{y_+}(x,y) = \exp\left(\int_0^{+\infty}(1-t_b(\omega))e^{-\frac{i\omega y_+}{v_F}}\left(e^{i\frac{\omega y}{v_F}}-e^{i\frac{\omega x}{v_F}}\right)\frac{d\omega}{\omega}\right). \tag{C.42}$$

Decomposing the free electron correlators appearing in eq. (C.41) in Fourier space finally leads to:

$$\mathcal{G}^{(e)}_{\rm wp}(x,y) = \int \tilde{\varphi}(k_+)\,\tilde{\varphi}(k_-)^*\, I_{k_+}(x-y)\, I_{k_-}(x-y)^*\, e^{i(k_+x-k_-y)}\,\frac{dk_+dk_-}{(2\pi)^2}\,. \tag{C.43}$$

where $\tilde{\varphi}$ denotes the incident wavepacket in momentum space and

$$I_k(z) = \int (1-n_F(k-p))\, e^{ipu} \exp\left(\int_0^{+\infty} (1-t_b(\omega)) e^{-i\frac{\omega u}{v_F}} (e^{-i\frac{\omega z}{v_F}}-1)\frac{d\omega}{\omega}\right)\frac{dp\,du}{2\pi} \tag{C.44}$$

The physical intepretation of (C.43) is clear: each contribution from coherent plane waves (k_+, k_-) to the coherence has to be multiplied by and effective decoherence coefficient of the form $I_{k_+}(x-y)\, I_{k_-}(y-x)$ which accounts for the effect of interactions and of the external circuit. The presence of the $(1-n_F(k_\pm - p))$ factor precisely accounts for the Pauli principle.

Translation invariance and splitted coherence function

In chapter 5, we considered the case of an energy resolved electronic excitation. In position space, the wavefunction of such an electron is a plane wave, which is a translation invariant state.
An ambiguity remains in the definition of the dressed electron operator (C.22). Indeed, the reference position to define the bare fermion operator can be chosen arbitrarily. Adding a constant b to this position would lead to :

$$\tilde{\psi}^\dagger(y+b) = e^{i\int_0^\infty \frac{d\omega}{\omega}\Im t_b(\omega)}\psi(y+b)|g(y+b)\rangle\,. \tag{C.45}$$

This different decomposition does not affect $\mathcal{G}^{(e)}(x,y)$ in the case of a planewave : a change of variables shows that the total coherence function is left untouched, as expected from translation invariance. Nevertheless, this ambiguity affects the two contributions $\mathcal{G}^{(e)}_{wp}$ and $\mathcal{G}^{(e)}_{mv}$. Hopefully, the oscillations appearing in the two parts of $\mathcal{G}^{(e)}$ cancel out, as seen in fig. C.1.

The UV behaviour of the scattering guides the appropriate choice for the decomposition of the dressed fermion operator (C.22) : the suitable decomposition is the one leading to $t_b(\omega) \to 1$ when $\omega \to \infty$.

Explicit expressions in Fourier space

In this last paragraph, we give the expression of the different contributions to the excess occupation number in terms of the A functions, and perform a low energy expansion of the coherence function. The elastic scattering amplitude $\mathcal{Z}(k_0)$ is given by :

$$\mathcal{Z}(k_0) = 1 + \int_{-k_0}^{0} A_-(p)dp\,. \tag{C.46}$$

The J and G functions in equations (5.31c) and (5.31a) in chapter 5 admit the following expressions :

$$J(p) = A_+(p)\Theta(p+k_0)\mathcal{Z}(p+k_0) \tag{C.47}$$

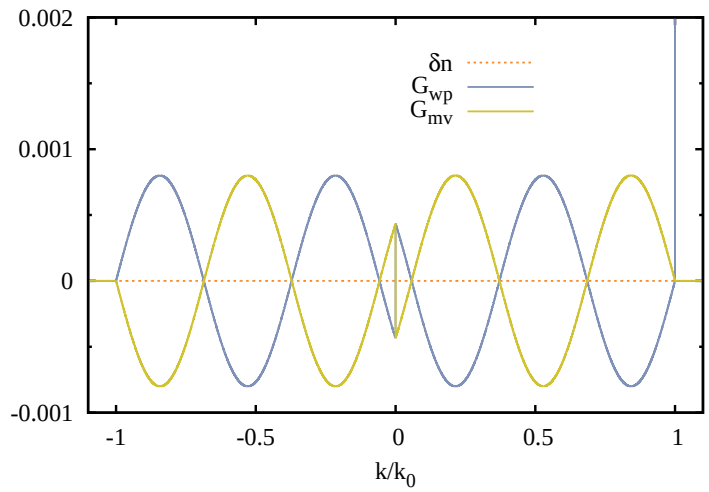

Figure C.1: Effect of a supplementary phase in the scattering. The two contributions $\mathcal{G}^{(e)}_{wp}$ and $\mathcal{G}^{(e)}_{mv}$ are modified by the supplementary phase, but their sum remains untouched (red dashed line). Here, $t_b(\omega) = e^{i\omega L_0/v_F}$, where $L_0 = \frac{6}{k_0}$.

and

$$\frac{G(k_0,q)}{2\pi} = \delta(q)\int_0^{k_0} 2\Re(A_+(p-k_0)A_-^*(p-k_0))\,dp + \Theta(k_0+q)|A_+(q)|^2 + \Theta(k_0-q)|A_-(-q)|^2 + 2\Re\left(A_+(q)\int_0^{k_0} A_+^*(p-k_0)A_-(p-k_0-q)\,dp + A_-(-q)\int_0^{k_0} A_-^*(p-k_0)A_+(p-k_0+q)\,dp\right) + \int_{p\geq 0} A_+\left(\frac{p-k_0+q}{2}+k\right)A_-\left(\frac{p-k_0-q}{2}-k\right)A_+^*\left(\frac{p-k_0+q}{2}-k\right)A_-^*\left(\frac{p-k_0-q}{2}+k\right)dp\,dk\,. \tag{C.48}$$

Low energy approximation

Up to first order in $1-t$, the $A_\pm$ functions read :

$$A_\pm(q) \simeq \mp\theta(-q)\frac{1-t(-v_F q)}{q}\,. \tag{C.49}$$

Thus, in this approximation, the modified vacuum does not contribute to the coherence, since it involves terms containing at least two A functions : the Fermi sea remains spectator. For the same reason, the term $\int J(p)^* J(q-k_0-p)\,dp$ in the expression (5.31a) of $\delta n^{(\mathrm{wp})}(q)$ in chapter 5 does not come into play. Consequently, we are left with

$$\delta n^{(\mathrm{wp})}(q) \simeq |\mathcal{Z}(k_0)|^2\delta(q-k_0) + 2\Re(\mathcal{Z}(k_0)J^*(q-k_0)) \tag{C.50}$$

as an expression for the coherence in Fourier space up to the first order in $1-t$. The second term in the r.h.s. of the equation above can be approximated by $2\Re(\mathcal{Z}(k_0-q)A_+(k_0-q))$, since $\mathcal{Z}(k_0)\simeq 1$. Finally, with $A_+(q)\simeq A_-(q)$ when $q\to 0$, we recover the low energy expression (5.45) of the occupation number at low injection energy :

$$\delta n(k)\begin{cases} \simeq Z(k_0)\delta(k-k_0) - Z'(k-k_0) & \text{for } 0\leq k\leq k_0, \\ = 0 & \text{otherwise}\,. \end{cases} \tag{C.51}$$

List of Figures

1.1 Interfering paths . . . 3
1.2 Landau levels and quantum Hall effect . . . 5
1.3 A Hall bar . . . 6
1.4 QPC sketch and conductance . . . 7
1.5 HBT configuration for noise measurements . . . 8
1.6 LPA single electron source . . . 9
1.7 Elements on the Mach-Zehnder interferometer . . . 10
1.8 Results of Mach-Zehnder interferometry experiment . . . 10

2.1 Schematic view of a photodetector . . . 14
2.2 Photon first order coherence function of a lorentzian wavepacket . . . 17
2.3 First order coherence function in simple cases . . . 19
2.4 Sketch of a coincidence setup for photons . . . 20
2.5 Sketch of first order electronic coherence function in Fourier space . . . 24
2.6 Fourier transform of the first order electronic coherence function for two electrons 26
2.7 First order coherence function for two electrons in position space . . . 27
2.8 First order electronic coherence function for an electron/hole pair . . . 28
2.9 First order electronic coherence function for the coherent superposition of two wavepackets with electron/hole coherences . . . 29
2.10 Tunnel detection setup . . . 30
2.11 Noise for a lorentzian wavepacket . . . 36

3.1 Sketch of a HBT interferometer . . . 41
3.2 The first order coherence function for periodic electronic excitations . . . 43
3.3 Single electron quantum tomography setupl . . . 44
3.4 Floquet matrix elements . . . 49
3.5 Shematic representation of the driven mesoscopic capacitor . . . 50
3.6 Density of states of the quantum dot for a Fabry-Perot model . . . 52
3.7 Sketches of the voltage action . . . 54
3.8 Occupation number and associated noise . . . 55
3.9 Occupation number and associated noise . . . 55
3.10 Excess occupation number with different configurations of the dot's levels . . . 56
3.11 Excess occupation number with decreasing frequency for a sine voltage . . . 57
3.12 Coherence function and χ_n for D=1 . . . 57
3.13 Coherence function and χ_n for D=0.2 . . . 58
3.14 Coherence function and χ_n for D=0.04 . . . 58
3.15 Current pulse for different values of the transparency D . . . 60

3.16 Average electron number per cycle and its fluctuations 61
3.17 Fidelity wrt resonant level model and linear entropy 63
3.18 Summary for chapter 3 64

4.1 Sketch of the $\nu = 2$ edge channel energy relaxation experiment 66
4.2 Setup for energy relaxation 67
4.3 Ajustable relaxation lengths 68
4.4 Measurement of the nonequilibrium electron distribution and excess temperature 69
4.5 Different mechanisms for energy exchanges 70
4.6 Linearized spectrum for electrons 72
4.7 Evolution of the excess temperature wrt bias voltage 80
4.8 Evolution of the excess temperature wrt QPC conductance 81
4.9 Noise measurement setup 82
4.10 Expected excess noise after interchannel coupling 83

5.1 Interaction scheme 86
5.2 Sketch of the excess occupation number 93
5.3 Transmission coefficients 95
5.4 Equivalent circuit 96
5.5 Elastic scattering probability at low energy 98
5.6 Occupation number at low energy 1 99
5.7 Occupation number at low energy 2 100
5.8 Excess occupation number for the closed channel case at low ϵ_0 100
5.9 Occupation number at high energy 1 102
5.10 Occupation number at high energy 2 102
5.11 Excess occupation number for the closed channel case at high ϵ_0 103
5.12 Energy fraction sent to the environment for the RC circuit model 105

6.1 Coherence function of lorentzian pulses at different repetition frequency. . . . 110
6.2 Coherence function of single lorentzian pulses containing different electron numbers. 111
6.3 Time dependence of the average current over one period 113
6.4 Real time coherence function for increasing interaction time 114
6.5 Fourier transform of the coherence function for increasing interaction length . 115
6.6 HBT setup for n electron pulses in the presence of interactions 116
6.7 HBT signals and electron/hole pair counting 117
6.8 HBT signals and interactions 117
6.9 HOM dip for photons 118
6.10 Hong Ou Mandel experiment and interactions 118
6.11 HOM dip in the presence of interactions 120

B.1 Onsager - Büttiker relations 132
B.2 Circuit coupled to an edge channel 133
B.3 Sketch of a mesoscopic RC circuit 134
B.4 Edge channel coupled to a closed loop channel of length l. 140

C.1 Effect of a phase in the scattering 150

Bibliography

[1] I.L. Aleiner and L.I. Glazman. Novel edge excitations of two dimensional electron liquid in a magnetic field. *Phys. Rev. Lett.*, 72:2935, 1994. 80, 84, 123

[2] C. Altimiras, H. Le Sueur, U. Gennser, A. Cavanna, D. Mailly, and F. Pierre. Non-equilibrium edge-channel spectroscopy in the integer quantum hall regime. *Nature Physics*, 6:34, 2009. 11, 31, 64, 65, 66, 67, 68, 123

[3] C. Altimiras, H. Le Sueur, U. Gennser, A. Cavanna, D. Mailly, and F. Pierre. Tuning energy relaxation along quantum hall edge channels. *Phys. Rev. Lett.*, 105:226804, 2010. 11, 64, 65, 66, 87, 99, 123

[4] F. Balibar. *Albert Einstein, oeuvres choisies, T.1.* Seuil/cnrs edition, 1989. 32

[5] L. E. Ballentine. *Quantum mechanics : a modern development.* World Scientific, 1998. 41

[6] Christopher Bauerle, Pascal Degiovanni, and Laurent Saminadayar. Quantum coherence and magnetic scattering. *International Journal of Nanotechnology*, 7:403, 2010. 124

[7] C.W.J. Beenakker. Electron-hole entanglement in the fermi sea. In G. Casati, D.L. Shepelyansky, P. Zoller, and G. Benenti, editors, *Quantum computers, Algorithms and Chaos*, volume 162 of *International School of Physics Enrico Fermi*, pages 307–347, Amsterdam, 2006. IOS Press. 4

[8] C.W.J. Beenakker and H. Schomerus. Counting statistics of photons produced by electronic shot noise. *Phys. Rev. Lett.*, 86:700, 2001. 125

[9] H. Birk, M. J. M. de Jong, and C. Schoenenberger. Shot-noise suppression in the single-electron tunneling regime. *Phys. Rev. Lett.*, 75(8):1610–1613, Aug 1995. 8

[10] Ya.M. Blanter and M. Buttiker. Shot noise in mesoscopic conductors. *Physics Reports*, 336:1, 2000. 7, 45

[11] Ya.M. Blanter, F.W.J. Hekking, and M. Buttiker. Interaction constants and dynamic conductance of a gated wire. *Phys. Rev. Lett.*, 81:1925, 1998. 96

[12] R. Hanbury Brown and R. Q. Twiss. Interferometry of the Intensity Fluctuations in Light. I. Basic Theory: The Correlation between Photons in Coherent Beams of Radiation. *Proceedings of the Royal Society of London. Series A. Mathematical and Physical Sciences*, 242(1230):300–324, 1957. 39, 40

[13] R. Hanbury Brown and R. Q. Twiss. Interferometry of the Intensity Fluctuations in Light II. An Experimental Test of the Theory for Partially Coherent Light. *Proceedings of the Royal Society of London. Series A. Mathematical and Physical Sciences*, 243(1234):291–319, 1958. 39, 40

[14] M. Buttiker. Four terminal phase coherent conductance. *Phys. Rev. Lett.*, 57:1761, 1986. 76, 131

[15] M. Buttiker. Absence of backscattering in the quantum hall effect in multiprobe conductors. *Phys. Rev* **B**, 38:9375, 1988. 5, 6

[16] M. Büttiker. Symmetry of electrical conduction. *IBM J. Res. Dev.*, 32:317–334, May 1988. 94

[17] M. Buttiker. Quantized transmission of a saddle-point constriction. *Phys. Rev. B*, 41(11):7906–7909, Apr 1990. 7

[18] M. Büttiker, A. Prêtre, and H. Thomas. Dynamic conductance and the scattering matrix of small conductors. *Phys. Rev. Lett.*, 70:4114, 1993. 96, 105, 123

[19] M. Buttiker, H. Thomas, and A. Pretre. Current partition in multiprobe conductors in the presence of slowly oscillating external potentials. *Zeitschrift fur physik B-Condensed matter*, 94(1-2):133–137, April 1994. 51

[20] V. Buzek, G. Drobny, R. Derka, G. Adam, and H. Wiedemann. Quantum State Reconstruction From Incomplete Data. 1998. 40

[21] J.T. Chalker, Y. Gefen, and M.Y. Veillette. Decoherence and interactions in an electronic mach-zehnder interferometer. *Phys. Rev.* **B**, 76:085320, 2007. 1, 10, 121

[22] T. Christen and M. Büttiker. Low frequency admittance of a quantum point contact. *Phys. Rev. Lett.*, 77(1):143–146, Jul 1996. 96

[23] S.-W. V. Chung, M. Moskalets, and P. Samuelsson. Quantum pump driven fermionic mach-zehnder interferometer. *Phys. Rev. B*, 75(11):115332, Mar 2007. 121

[24] V.S.-W. Chung, P. Samuelsson, and M. Buttiker. Visibility of current and shot noise in electrical mach-zehnder and hanbury brown twiss interferometers. *Phys. Rev.* **B**, 72(12):125320, Sep 2005. 10, 121

[25] Cl. Cohen-Tannoudji. Décohérence quantique. Cours au Collège de France, 1988–1990. 14

[26] Cl. Cohen-Tannoudji and P. Avan. *Discrete state coupled to a continuum. Continuous transition between the Weisskopf-Wigner exponential decay and the Rabi oscillation*, page 93. Etats atomiques et moléculaires couplés à un continuum. Editions du cnrs edition, 1977. 62

[27] J. Cunningham, V. I. Talyanskii, J. M. Shilton, M. Pepper, M. Y. Simmons, and D. A. Ritchie. Single-electron acoustic charge transport by two counterpropagating surface acoustic wave beams. *Phys. Rev. B*, 60(7):4850–4855, Aug 1999. 8

[28] C. de C. Chamon and X. G. Wen. Sharp and smooth boundaries of quantum hall liquids. *Phys. Rev.* **B**, 49:8227–8241, 1994. 123

[29] P. Degiovanni and S. Peysson. Decoherence of schrödinger cat states in a luttinger liquid. *Phys. Rev. B*, 62(16):10706–10722, Oct 2000. 74

[30] Pascal Degiovanni, Charles Grenier, and Gwendal Feve. Decoherence and relaxation of single electron excitations in quantum hall edge channels. *Physical Review B*, 24:241307, 2009. 63, 87, 132

[31] Pascal Degiovanni, Charles Grenier, Gwendal Feve, Carles Altimiras, Helene Le Sueur, and Frederic Pierre. Plasmon scattering approach to energy exchange and high frequency noise in nu=2 quantum hall edge channels. *Phys. Rev. B*, 81:121302, February 20010. 67, 71, 80, 81, 84, 123

[32] Samuel Deleglise, Igor Dotsenko, Clement Sayrin, Julien Bernu, Michel Brune, Jean-Michel Raimond, and Serge Haroche. Reconstruction of non-classical cavity field states with snapshots of their decoherence. *NATURE*, 455(7212):510–514, SEP 25 2008. 40

[33] M.H. Devoret, D. Esteve, H. Grabert, G.-L. Ingold, H. Pothier, and C. Urbina. Effect of the electromagnetic environment on the coulomb blockade in ultrasmall tunnel junctions. *Phys. Rev. Lett.*, 64:1824, 1990. 90

[34] A. Einstein. *Letter to Niels Bohr reprinted in "Quantum theory and measurement"*. Princeton University Press, May 1920. 2

[35] A. Einstein. Quantentheorie des idealen gases, preussische akademie des wissenschaften. *Phys.- math. Klasse, Sitzungberichte*, 18, 1925. 32

[36] G. Feve, P. Degiovanni, and Th Jolicoeur. Quantum detection of electronic flying qubits. *Physical Review B*, 77:035308, 2008. 87, 132

[37] Gwendal Fève. *Quantization of the AC current : the quantum dot as a subnanosecond single electron source.* PhD thesis, Univ. Paris 6, November 2006. 48, 51

[38] Gwendal Feve, Adrien Mahe, Jean-Marc Berroir, Takis Kontos, Bernard Placais, Christian Glattli, A. Cavanna, Bernard Etienne, and Yong Jin. An on-demand coherent single electron source. *Science*, 316:1169, 2007. 1, 8, 9, 11, 39, 60, 63, 86, 121, 122

[39] R.P. Feynman and A.R. Hibbs. *Quantum Mechanics and Path Integrals.* McGraw-Hill, 1965. 2

[40] R.P. Feynman and F.L. Vernon. The theory of a general quantum system interacting with a linear dissipative system. *Annals of Physics*, 24:118 – 173, 1963. 2, 3

[41] G. Floquet. Sur les équations différentielles linéaires à coefficients périodiques. *Ann. Ecole Norm. Sup.*, 12:47, 1883. 48

[42] H. Forster, S. Pilgram, and M. Müttiker. Decoherence and full counting statistics in a mach-zehnder interferometer. *Phys. Rev. B*, 72:075301, 2005. 10

[43] M. Fox. *Quantum optics : an introduction.* Oxford university press, 2006. 16, 40

[44] J. Gabelli. *Evidence of quantum coherence in dynamical electronic transport.* PhD thesis, Univ. Paris 6, 2006. 51

[45] J. Gabelli, G. Fève, J.M. Berroir, B. Plaçais, A. Cavanna, B. Etienne, Y. Jin, and D.C. Glattli. Violation of kirchhoff's laws for a coherent rc circuit. *Science*, 313:499, 2006. 51, 96

[46] J. Gabelli, G. Fève, T. Kontos, J.-M. Berroir, B. Plaçais, D.C. Glattli, B. Etienne, Y. Jin, and M. Büttiker. Relaxation time of a chiral quantum r-l circuit. *Phys. Rev. Lett.*, 98:166806, 2007. 96

[47] Christopher C. Gerry and Peter L. Knight. *Introductory quantum optics.* Cambridge university press, 2004. 21

[48] Thierry Giamarchi. *Quantum physics in one dimension.* Oxford university press, 2004. 71, 74

[49] D.C. Glattli. Quantum shot noise of conductors and general noise measurement methods. *Eur. Phys. J. Special Topics*, 172:163, 2009. 46

[50] R.J. Glauber. Photon correlations. *Phys. Rev. Lett.*, 10(3):84, Feb 1962. 14, 37

[51] R.J. Glauber. The quantum theory of optical coherence. *Phys. Rev.*, 130(6):2529, Jun 1963. 13, 14, 37, 121

[52] Roy J. Glauber. Coherent and incoherent states of the radiation field. *Phys. Rev.*, 131(6):2766–2788, Sep 1963. 14, 18, 32

[53] A.O. Gogolin, A.A Nersesyan, and A.M. Tsevlik. *Bosonization and strongly correlated systems.* Cambridge University Press, 1998. 71

[54] I.S. Gradshteyn and I.M. Ryzhik. *Table of integrals, series and products (fifth ed.).* Academic Press, Inc, 1994. 111, 130

[55] Ph. Grangier. Experiments with single photons. *Séminaire Poincaré*, 2:1, 2005. 32

[56] Charles Grenier, Rémy Hervé, Erwann Bocquillon, François D. Parmentier, Bernard Plaçais, Jean-Marc Berroir, Gwendal Fève, and Pascal Degiovanni. Single electron quantum tomography in quantum hall edge channels. October 2010. 40, 122

[57] C. Guerlin, J. Bernu, S. Deléglise, C. Sayrin, S. Gleyzes, S. Kuhr, M. Brune, J.-M. Raimond, and S. Haroche. Progressive field-state collapse and quantum non-demolition photon counting. *Nature*, 448:889, 2007. 3

[58] D. B. Gutman, Yuval Gefen, and A. D. Mirlin. Nonequilibrium luttinger liquid: Zero-bias anomaly and dephasing. *Physical Review Letters*, 101(12):126802, 2008. 126

[59] D. B. Gutman, Yuval Gefen, and A. D. Mirlin. Zero bias anomaly out of equilibrium. *Physical Review Letters*, 100:086801, 2008. 84

[60] D. B. Gutman, Yuval Gefen, and A. D. Mirlin. Bosonization of one-dimensional fermions out of equilibrium. *Phys. Rev. B*, 81:085436, 2010. 84, 126

[61] D.B. Gutman, Y. Gefen, and A.D. Mirlin. Bosonization out of equilibrium. *Europhys. Lett.*, 90:37003, 2010. 84, 126

[62] D.B. Gutman, Yu. Gefen, and A.D. Mirlin. Tunneling spectroscopy of luttinger liquid structures far from equilibrium. *Phys. Rev* **B**, 80:045106, 2009. 84, 126

[63] B.I. Halperin. Quantized Hall conductance, current carrying edge states, and the existence of extended states in a two dimensional disordered potential. *Phys. Rev.* **B**, 25:2185 – 2190, 1982. 5

[64] J.H. Han and D.J. Thouless. Dynamics of compressible edge and bosonization. *Phys. Rev.* **B**, 55:R1926, 1997. 123

[65] R. Hanbury Brown and R.Q. Twiss. A test of a new type of stellar interferometer on sirius. *Nature*, 178:1046, 1956. 19, 40

[66] S. Haroche. Lectures at collège de france. 40

[67] S. Haroche and J. M. Raimond. *Exploring the quantum.* Oxford university press, 2006. 14

[68] M. Henny, S. Oberholzer, C. Strunk, T. Heinzel, K. Ensslin, M. Holland, and C. Schönenberger. The fermionic hanbury-brown and twiss experiment. *Science*, 284:296, 1999. 1, 42, 65, 121

[69] M. Heyl, S. Kehrein, F. Marquardt, and C. Neuenhahn. Electron-plasmon scattering in chiral one-dimensional systems with nonlinear dispersion. *Phys. Rev. B*, 82(3):033409, 2010. 103

[70] M. Hofheinz, H. Wang, M. Ansmann, R.C. Biazlczak, E. Lucero, M. Neeley, A.D. O'Connell, D. Sank, J. Wenner, J.M. Martinis, and A.N. Cleland. Synthetizing arbitrary quantum states in a superconducting resonator. *Nature*, 459:546, 2009. 40

[71] C.K. Hong, Z.Y. Ou, and L. Mandel. Measurement of subpicosecond time intervals between two photons by interference. *Phys. Rev. Lett.*, 59:2044, 1987. 117, 118

[72] G.-L. Ingold and Yu.V. Nazarov. *Single charge tunneling*, volume 294 of *NATO ASI Series B*, chapter Charge tunneling rates in ultrasmall junctions, pages 21–107. Plenum Press, New York, 1992. 90

[73] C. Itzykson and J.B. Zuber. *Quantum Field Theory.* Mac Graw Hill, 1980. 25

[74] Y. Ji, Y.C. Chung, D. Sprinzak, M. Heiblum, D. Mahalu, and H. Shtrikman. An electronic mach-zenhder interferometer. *Nature*, 422:415, 2003. 1, 9, 10, 65, 121

[75] E. Joos and H.D. Zeh. The emergence of classical properties through interaction with the environment. *Z. Phys.* **B**, 59:223–243, 1985. 2

[76] J. Keeling, I. Klich, and L.S. Levitov. Minimal excitation states of electrons in one-dimensional wires. *Phys. Rev. Lett.*, 97(11):116403, Sep 2006. 26, 28, 63, 107

[77] J. Keeling, A.V. Shytov, and L.S. Levitov. Coherent particle transfer in an on-demand single-electron source. *Phys. Rev. Lett.*, 101(19):196404, Nov 2008. 51

[78] H. J. Kimble, M. Dagenais, and L. Mandel. Photon antibunching in resonance fluorescence. *Phys. Rev. Lett.*, 39:691, 1977. 40

[79] D. L. Kovrizhin and J. T. Chalker. Exactly solved model for an electronic mach-zehnder interferometer. *Phys. Rev. B*, 80:161306, 2009. 1, 10, 121

[80] D. L. Kovrizhin and J. T. Chalker. Multiparticle interference in electronic mach-zehnder interferometers. *Phys. Rev. B*, 81:155318, 2010. 1, 121

[81] D.L. Kovrizhin and J.T. Chalker. Equilibration of integer quantum hall edge states. arXiv:1009.4555. 80, 123

[82] A. Kumar, L. Saminadayar, D.C. Glattli, Y. Jin, and B. Etienne. Experimental test of the quantum shot noise reduction theory. *Phys. Rev. Lett.*, 76:2778, 1994. 8

[83] L.D. Landau. On the theory of the Fermi liquid. *Sov. Phys. JETP*, 35:70 – 74, 1959. 85, 91, 123

[84] L.D. Landau and E.M. Lifshits. *The electrodynamics of continuous media*, volume 8. Mir editions, 1982. 139

[85] R. Landauer. Johnson-Nyquist noise derived from quantum mechanical transmission. *Physica* **D**, 38:226 – 229, 1989. 7

[86] R. Landauer. The noise is the signal. *Nature*, 392:658, 1998. 7, 8

[87] L.S. Levitov, H.W. Lee, and G.B. Lesovik. Electron counting statistics and coherent states of electric current. *J. Math. Phys.*, 37:4845, 1996. 8, 11, 26, 107, 108, 124

[88] I.P. Levkivskyi and E.V. Sukhorukov. Dephasing in the electronic mach-zehnder interferometer at filling factor $\nu = 2$. *Phys. Rev.* **B**, 78:045322, 2008. 1, 10, 121, 138

[89] Ivan P. Levkivskyi and Eugene V. Sukhorukov. Noise-induced phase transition in the electronic mach-zehnder interferometer. *Phys. Rev. Lett.*, 103:036801, 2009. 1, 121

[90] R.C. Liu, B. Odom, Y. Yamamoto, and S. Tarucha. Quantum interferences in electron collision. *Nature*, 391:263, 1998. 42

[91] Rodney Loudon. *The quantum theory of light.* Oxford science publications, 1983. 19, 20, 22

[92] Anders Mathias Lunde, Simon E. Nigg, and Markus Buttiker. Interaction-induced edge channel equilibration. *Phys. Rev. B*, 81:041311(R), 2010. 80, 81, 84, 123

[93] A. I. Lvovsky and M. G. Raymer. Continuous-variable optical quantum-state tomography. *Rev. Mod. Phys.*, 81(1):299–332, Mar 2009. 40, 41

[94] A. Mahé. *Bruit de charge d'une source d'électrons uniques subnanoseconde.* PhD thesis, Univ. Paris 6, November 2009. 36, 48, 49

[95] A. Mahé, F. D. Parmentier, E. Bocquillon, J.-M. Berroir, D. C. Glattli, T. Kontos, B. Plaçais, G. Fève, A. Cavanna, and Y. Jin. Current correlations of an on-demand single-electron emitter. *Phys. Rev. B*, 82(20):201309, Nov 2010. 36

[96] A. Mahé, F.D. Parmentier, E. Bocquillon, J.M. Berroir, D.C. Glattli, T. Kontos, B. Plaçais, G. Fève, A. Cavanna, and Y. Jin. Current correlations of an on-demand single electron source as an evidence of single particle emission. *Phys. Rev. B*, 82:201309, 2010. Arxiv:1004.1985. 46

[97] N. Maire, F. Hohls, B. Kaestner, K. Pierz, H.W. Schumacher, and R.J. Haug. Noise measurement of a quantized charge pump. *Appl. Phys. Lett.*, 92:082112, 2008. 46

[98] F. Mallet, J. Ericsson, D. Mailly, S. Ünlübayir, D. Reuter, A. Melnikov, A.D. Wieck, T. Micklitz, A. Rosch, T.A. Costi, L. Saminadayar, and C. Bäuerle. Scaling of the low temperature dephasing rate in kondo systems. *Phys. Rev. Lett.*, 97:226804, 2006. 3

[99] L. Mandel. Squeezed states and sub-poissonian photon statistics. *Phys. Rev. Lett.*, 49(2):136–138, Jul 1982. 22

[100] F. Marquardt. Fermionic mach-zehnder interferometer subject to a quantum bath. *Europhys. Lett.*, 72:788, 2005. 10, 121

[101] F. Marquardt. Equations of motion approach to decoherence and current noise in ballistic interferometers coupled to a quantum bath. *Phys. Rev.* **B**, 74:125319, 2006. 10

[102] F. Marquardt and C. Bruder. Effect of dephasing on shot noise in an electronic mach-zehnder interferometer. *Phys. Rev.* **B**, 70:125305, 2004. 10, 121

[103] Th. Martin and R. Landauer. Wave packet approach to noise in multichannel mesoscopic systems. *Phys. Rev.* **B**, 45:1742 – 1755, 1992. 7

[104] J.M. Martinis, S. Nam, J. Aumentado, K.M. Lang, and C. Urbina. Decoherence of a superconducting qubit due to bias noise. *Phys. Rev.* **B**, (67), 2003. 3

[105] F. P. Milliken, S. Washburn, C. P. Umbach, R. B. Laibowitz, and R. A. Webb. Effect of partial phase coherence on aharonov-bohm oscillations in metal loops. *Phys. Rev. B*, 36(8):4465–4468, Sep 1987. 3

[106] B. L. Morgan and L. Mandel. Measurement of Photon Bunching in a Thermal Light Beam. *Physical Review Letters*, 16:1012–1015, May 1966. 40

[107] M. Moskalets and M. Büttiker. Floquet scattering theory of quantum pumps. *Phys. Rev. B*, 66:205320, 2002. 48

[108] M. Moskalets and M. Büttiker. Spectroscopy of electron flows with single- and two-particle emitters. *Phys. Rev. B*, 83:035316, 2011. 47, 56, 63, 121

[109] M. Moskalets, P. Samuelsson, and M. Büttiker. Quantized dynamics of a coherent capacitor. *Phys. Rev. Lett.*, 100(8):086601, Feb 2008. 48

[110] W. Munk and C. Wunsch. *Ocean Acoustic TomographyW*. Cambridge University Press, 1995. 40

[111] I. Neder and F. Marquardt. Coherence oscillations in dephasing by non-gaussian noise. *New Journal of Physics*, 9:112, 2007. 10

[112] I. Neder, N. Ofek, Y. Chung, M. Heiblum, D. Mahalu, and V. Umansky. Interference between two indistinguishable electrons from independent sources. *Nature*, 448:333, 2007. 65, 121

[113] Matthew Neeley, M. Ansmann, Radoslaw C. Bialczak, M. Hofheinz, N. Katz, Erik Lucero, A. O'Connell, H. Wang, A. N. Cleland, and John M. Martinis. Process tomography of quantum memory in a Josephson-phase qubit coupled to a two-level state. *NATURE PHYSICS*, 4(7):523–526, JUL 2008. 40

[114] C. Neuenhahn and F. Marquardt. Dephasing by electron-electron interactions in a ballistic interferometer. *New Journal of Physics*, 10:115018, 2008. 10, 103

[115] C. Neuenhahn and F. Marquardt. Universal dephasing in a chiral 1d interacting fermion system. *Phys. Rev. Lett.*, 102:046806, 2009. 103

[116] M.A. Nielsen and I.L. Chuang. *Quantum computation and quantum information.* Cambridge University Press, 2000. 62

[117] Simon E. Nigg and Markus Büttiker. Universal detector efficiency of a mesoscopic capacitor. *Phys. Rev. Lett.*, 102(23):236801, Jun 2009. 74

[118] Yasuhiro Niimi, Yannick Baines, Thibaut Capron, Dominique Mailly, Fang-Yuh Lo, Andreas D. Wieck, Tristan Meunier, Laurent Saminadayar, and Christopher Bäuerle. Quantum coherence at low temperatures in mesoscopic systems: Effect of disorder. *Phys. Rev. B*, 81(24):245306, Jun 2010. 124

[119] W.D. Oliver, J. Kim, R.C. Liu, and Y. Yamamoto. Handbury brown and twiss experiment with electrons. *Science*, 284:299, 1999. 42

[120] S. Ol'khovskaya, J. Splettstoesser, M. Moskalets, and M. Büttiker. Shot noise of a mesoscopic two-particle collider. *Phys. Rev. Lett.*, 101:166802, 2008. 121

[121] Miguel Orszag. *Quantum optics.* Springer, 2008. 20, 22

[122] F.D. Parmentier, A. Mahé, A. Denis, J.-M. Berroir, D.C. Glattli, B. Plaçais, and G. Fève. A high sensitivity ultra-low temperature rf conductance and noise measurement setup. *Rev. Sci. Instrum.*, 82:013904, 2011. 82

[123] François D. Parmentier. *Short-time Hanbury-Brown and Twiss correlation of a single-electron beam in ballistic conductors.* PhD thesis, Univ. Paris 6, November 2010. 36, 45, 48, 49, 56

[124] J.P. Paz, S. Habib, and W.H. Zurek. Reduction of the wave packet: Preferred observable and decoherence time scale. *Phys. Rev.* **D**, 47:488–501, 1993. 2

[125] Nicholas A. Peters, Tzu-Chieh Wei, and Paul G. Kwiat. Mixed-state sensitivity of several quantum-information benchmarks. *Phys. Rev. A*, 70(5):052309, Nov 2004. 61

[126] D. Pines and Ph. Nozières. *The theory of quantum liquids.* Perseus Book, 1966.

[127] B. Plaçais. Transport dynamique dans les conducteurs mésoscopiques : aspects expérimentaux. Ecole du GDR de physique quantique mesoscopique, Oct 2008. 96

[128] A. Prêtre, H. Thomas, and M. Büttiker. Dynamics admittance of mesoscopic conductors: discrete potential model. *Phys. Rev.* **B**, 54:8130, 1996. 96, 105, 123, 132, 138

[129] Patrik Recher, Eugene V. Sukhorukov, and Daniel Loss. Quantum dot as spin filter and spin memory. *Phys. Rev. Lett.*, 85(9):1962–1965, Aug 2000. 31

[130] A. M. Robinson and V. I. Talyanskii. Shot noise in the current of a surface acoustic-wave-driven single-electron pump. *Phys. Rev. Lett.*, 95(24):247202, Dec 2005. 8

[131] P. Roulleau, F. Portier, D.C. Glattli, P. Roche, A. Cavanna, G. Faini, U. Gennser, and D. Mailly. Finite bias visibility of the electronic mach-zehnder interferometer. *Phys. Rev.* **B**, 76:161309, 2007. 1, 65, 121

[132] P. Roulleau, F. Portier, P. Roche, A. Cavanna, G. Faini, U. Gennser, and D. Mailly. Direct measurement of the coherence length of edge states in the integer quantum hall regime. *Phys. Rev. Lett.*, 100:126802, 2008. 1, 6, 65, 121

[133] P. Roulleau, F. Portier, P. Roche, A. Cavanna, G. Faini, U. Gennser, and D. Mailly. Noise dephasing in edge states of the integer quantum hall regime. *Phys. Rev. Lett.*, 101:186803, 2008. 1, 10, 65, 121

[134] P. Roulleau, F. Portier, P. Roche, A. Cavanna, G. Faini, U. Gennser, and D. Mailly. Tuning decoherence with a voltage probe. *Phys. Rev. Lett.*, 102(23):236802, Jun 2009. 94

[135] I. Safi. A dynamic scattering approach for a gated interacting wire. *Eur. Phys. J.* **D**, 12:451, 1999. 75

[136] I. Safi and H.J. Schulz. Transport in an inhomogeneous interacting one-dimensional system. *Phys. Rev. B*, 52:R1740, 1995. 75

[137] I. Safi and H.J. Schulz. Transport through a single band wire connected to measuring leads. In B. Kramer, editor, *Quantum Transport in Semiconductor Submicron Structures*, page 159. Kluwer Academic Press, Dordrecht, 1995. 75

[138] L. Saminadayar, D.C. Glattli, Y. Jin, and B. Etienne. Observation of the $e/3$ fractionally charged Laughlin quasi-particle. *Phys. Rev. Lett.*, 79:2526 – 2529, 1997. 8

[139] P. Samuelsson and M. Büttiker. Dynamic generation of orbital quasiparticle entanglement in mesoscopic conductors. *Phys. Rev. B*, 71(24):245317, Jun 2005. 121

[140] P. Samuelsson, E.V. Sukhorukov, and M. Büttiker. Two-particle aharonov,bohm effect and entanglement in the electronic hanbury-brown and twiss setup. *Phys. Rev. Lett.*, 92:026805, 2004. 65

[141] G. Seelig and M. Büttiker. Charge fluctuation induced dephasing in a gated mesoscopic conductor. *Phys. Rev.* **B**, 64:245313, 2001. 132

[142] D. Sénéchal. An introduction to bosonization. *Lecture given at the CRM workshop on theoretical methods for strongly correlated electrons, Montreal*, August 1999. 71

[143] R.W. Simmonds, K.M. Lang, D.A. Hite, D.P. Pappas, and J.M. Martinis. Decoherence in josephson phase qubits from junction resonators. *Phys. Rev. Lett.*, (93), 2004. 3

[144] M. Stone, editor. *Bosonization.* World Scientific, 1994. 71

[145] H. Le Sueur, C. Altimiras, U. Gennser, A. Cavanna, D. Mailly, and F. Pierre. Energy relaxation in the integer quantum hall regime. *Physical Review Letters*, 105:056803, 2010. 11, 64, 65, 66, 68, 69, 70, 123

[146] E.V. Sukhorukov and V.V. Cheianov. Resonant dephasing in the electronic mach-zehnder interferometer. *Phys. Rev. Lett.*, 99:156801, 2007. 1

[147] V. I. Talyanskii, J. M. Shilton, M. Pepper, C. G. Smith, C. J. B. Ford, E. H. Linfield, D. A. Ritchie, and G. A. C. Jones. Single-electron transport in a one-dimensional channel by high-frequency surface acoustic waves. *Phys. Rev. B*, 56(23):15180–15184, Dec 1997. 8

[148] U. M. Titulaer and R. J. Glauber. Correlation functions for coherent fields. *Phys. Rev.*, 140(3B):B676–B682, Nov 1965. 16

[149] K. v. Klitzing, G. Dorda, and M. Pepper. New method for high-accuracy determination of the fine-structure constant based on quantized hall resistance. *Phys. Rev. Lett.*, 45(6):494–497, Aug 1980. 5

[150] B. J. van Wees, L. P. Kouwenhoven, E. M. M. Willems, C. J. P. M. Harmans, J. E. Mooij, H. van Houten, C. W. J. Beenakker, J. G. Williamson, and C. T. Foxon. Quantum ballistic and adiabatic electron transport studied with quantum point contacts. *Phys. Rev. B*, 43:12431–12453, 1991. 7

[151] B. J. van Wees, E. M. M. Willems, C. J. P. M. Harmans, C. W. J. Beenakker, H. van Houten, J. G. Williamson, C. T. Foxon, and J. J. Harris. Anomalous integer quantum hall effect in the ballistic regime with quantum point contacts. *Phys. Rev. Lett.*, 62(10):1181–1184, Mar 1989. 70

[152] B.J. van Wees, H. van Houten, C.W.J. Beenakker, J.G. Williamson, L.P. Kouwenhoven, D. van der Marel, and C.T. Foxon. Quantized conductance of point contacts in a two dimensional electron gas. *Phys. Rev. Lett.*, 60:848 – 850, 1988. 7, 65

[153] J. Von Delft. Influence functional for decoherence of interacting electrons in disordered conductors. *Int. J. Mod. Phys. B*, 22:727–833, 2008. 124

[154] Jan von Delft and Herbert Schoeller. Bosonization for beginners â refermionization for experts. *Annalen der Physik*, 7(4):225–305, 1998. 71

[155] S. Washburn, H. Schmid, D. Kern, and R. A. Webb. Normal-metal aharonov-bohm effect in the presence of a transverse electric field. *Phys. Rev. Lett.*, 59(16):1791–1794, Oct 1987. 3

[156] V. Weisskopf and E. Wigner. Berechnung der natürlichen linienbreite auf grund der diracschen lichttheorie. *Zeitschrift für Physik*, 63:54, 1930. 17

[157] X.G. Wen. Chiral Luttinger liquid and the edge excitations in the fractional quantum Hall states. *Phys. Rev.* **B**, 41:12838 – 12844, 1990. 71

[158] W.K. Wootters and W.H. Zurek. A single quantum cannot be cloned. *Nature*, 299:802, 1982. 40

[159] S J Wright, M D Blumenthal, M Pepper, D Anderson, G A C Jones, C A Nicoll, and D A Ritchie. Robust single-parameter quantized charge pumping. *Applied Physics Letters*, 92(19):192106, 2008. 8

[160] Bernard Yurke and John S. Denker. Quantum network theory. *Phys. Rev. A*, 29(3):1419–1437, Mar 1984. 133

[161] E. Zakka-Bajjani, J. Ségala, F. Portier, P. Roche, D.C. Glattli, A. Cavanna, and Y. Jin. Experimental test of the high frequency quantum shot noise theory in a quantum point contact. *Phys. Rev. Lett.*, 99:236803, 2007. 79, 82

[162] H. D. Zeh. On the interpretation of measurement in quantumm theory. *Found. Phys.*, 1:69–76, 1970. 2

[163] W.H. Zurek. Pointer basis of quantum apparatus: into what mixture does the wave packet collapse? *Phys. Rev.* **D**, 24:1516 –1525, 1981. 2

[164] W.H. Zurek. Environment-induced superselection rules. *Phys. Rev.* **D**, 26:1862–880, 1982. 2

[165] W.H. Zurek. Decoherence and the transition from quantum to classical. *Physics Today*, 44:36 – 44, 1991. 2

[166] W.H. Zurek. Decoherence, einselection and the quantum origins of the classical. *Rev. Mod. Phys.*, 75:715, 2003. 2